Dissertation zur Erlangung des Doktorgrades
der Fakultät für Chemie und Pharmazie
der Ludwig-Maximilians-Universität München

Pulsed-Interleaved MINFLUX Super-Resolution Microscopy

Jonas Dominik Junis Zähringer

aus

Heidelberg, Deutschland

2023

Erklärung

Diese Dissertation wurde im Sinne von § 7 der Promotionsordnung vom 28.November 2011 von Herrn Prof. Dr. Philip Tinnefeld betreut.

Eidesstattliche Versicherung

Diese Dissertation wurde eigenständig und ohne unerlaubte Hilfe erarbeitet.
München, 25.09.23

Jonas Zähringer

Dissertation eingereicht am 10.05.2023
1. Gutachter: Prof. Dr. Philip Tinnefeld
2. Gutachter: Prof. Don C. Lamb, PhD
Mündliche Prüfung am 30.06.2023

Summary

Light microscopy has become a powerful tool to investigate structures, dynamics, and interactions in natural science such as cell biology. Especially fluorescence microscopy has seen a rapid development during the last decades. The emergence of far-field fluorescence super-resolution microscopy even overcame the fundamental diffraction limit, enabling imaging with high contrast and specificity of structures below 200 nm. With less than a tenth of the photons needed compared to previous super-resolution methods, MINFLUX is the most recent development to push the resolution limit to truly molecular dimensions. This is achieved by combining the excitation information of a structured illumination featuring a minimum with the respective emission information. While MINFLUX enables the visualization of structures and dynamics with 1 nm precision, the size of a fluorophore, only individual fluorophores are localized, thus information about their environment is missing. The method of choice to report about the environment of a fluorophore is the fluorescence lifetime. To this end, a combination of MINFLUX coupled with the fluorescence lifetime would vastly increase the information wealth of MINFLUX localizations.

In this thesis, I built a pulsed-interleaved MINFLUX (pMINFLUX) that extends the nanometer precise localizations of MINFLUX with the fluorescence lifetime domain while additionally simplifying the technological complexity of pMINFLUX. I demonstrated the performance of this setup using DNA origami structures which act as nanoruler. The unprecedented combination of fluorescence lifetime and nanometer precise localizations was employed in four novel methodologies to make the investigation of structures, interactions, dynamics, and their interplay on the nanometer length scale more accessible.

In combination with graphene energy transfer (GET), I extended the nanometer precise lateral localizations of MINFLUX to the third dimension, by using the fluorescence lifetime encoded axial distance information for nanometer precise 3D super-resolution microscopy. I demonstrated the resolution of GET-pMINFLUX on DNA origami structures using DNA-PAINT with axial precisions below 0.4 nm. DNA-PAINT was used to generate stochastic blinking, which is necessary for the localization method MINFLUX to resolve distances smaller than the diffraction limit. To increase the imaging speed and overcome issues with high fluorescent background of DNA-PAINT, I established local-PAINT (L-PAINT). In contrast to DNA-PAINT, L-PAINT imager strands have two binding sequences with a designed binding hierarchy such that the L-PAINT DNA-strand binds longer on one side. This allows the fluorescent dye-modified second end of the strand to locally scan for binding sites at a rapid rate.

While MINFLUX is able to give insight into structural information, the interplay with the environment remains unknown as only individual fluorophores are localized. I addressed this problem by first combining Förster resonance energy transfer (FRET) with MINFLUX to simultaneously localize the donor dye and map the distance to an acceptor dye. With the multilateration of several donor dye positions I localized the acceptor dye with a full width half maximum of 0.17 nm. To overcome the limited working range of FRET of 2-10 nm, I developed a pMINFLUX lifetime multiplexing approach. pMINFLUX lifetime multiplexing uses the fluorescence lifetime to colocalize two spectrally similar dyes without photo-switching over a large field-of-view. Beyond the FRET range, pMINFLUX lifetime multiplexing enabled the co-localization of two dyes by separating their fluorescence intensities according to their fluorescence lifetimes. I demonstrated this in simulation and experiment using two independent L-PAINT pointer systems, whose dynamics were imaged with nanometer precision. Inside the FRET range, two dyes were co-localized using a newly developed combined phasor-microtime gating approach. As a result, the combination of both multiplexing approaches closed the resolution gap between single-molecule FRET and co-tracking.

Table of Contents

1. Introduction

"It has been said that something as small as the flutter of a butterfly's wing can ultimately cause a typhoon halfway around the world." – Chaos Theory

Chaos is fundamental to our life. It can be found in many aspects in life, the most prominent being the weather.[1] Chaos is based on dynamics which are deterministic but highly volatile and sensitive to perturbations. Such chaotic dynamics can occur at many length scales from black holes[2], over a simple double pendulum[3] down to processes on the microscopic level such as chemical reactions[4, 5]. Examples of chaos on the microscopic scale are numerous and range from dynamics in enzyme complexes[6] to the functionality of extrachromosomal circular DNA[7] and many more[8, 9, 10]. While chaotic processes on all length scales are vital for life, processes on the microscopic scale are particularly critical; only through such dynamics life could emerge.[11]

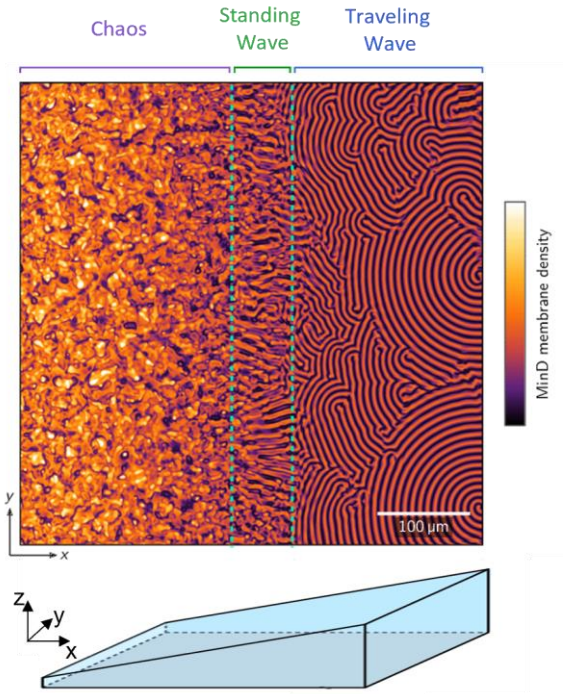

Figure 1: Simulation of different pattern of MinD, depending on the axial height the mixture of MinD and MinE is confined to. The top panel shows the MinD membrane density, the bottom panel indicates the geometry of the chamber. One can observe different regions with chaotic patterns, standing waves and traveling waves. Adapted from [12].

A prominent and well-studied example of chaos is found in the self-organization of Min proteins pattern.[12] Min proteins regulate the division site in *Escherichia Coli* involving oscillations inside the bacterium and are thus a target of interest for life science.[13] Various spatio-temporal patterns can emerge by interactions between the Min proteins and the membrane dictating the division site inside the bacterium.[14, 15] For example, it has been found that geometric restrictions such as the chamber height restrict diffusion modes of different Min proteins and thus stipulate the pattern they form (Figure 1). For low chamber heights, their initial chaotic state persists whereas larger heights result in the emergence of waves or even coexisting stable stationary distributions. As the pattern formation is a chaotic process, sensitive to small perturbations, an understanding of such phenomena comes from the ability to visualize processes on small length scales. For Min proteins but also proteins in general these interactions occur at the nanometer length scale,[16] therefore, it seems evident that research of

life sciences needs to be performed on the smallest of length scales possible. To that end, the tool of choice for Min proteins[17] but also for natural sciences[18] in general is the microscope.

The popular saying “a picture says more than thousand words”, already exemplifies why it is probably not by chance that the beginning of modern natural sciences coincides with the invention of light microscopy.[19, 20] Light microscopy gives a window into the microscopic world and is a fundamental tool for many research fields. Microscopes create understanding, extending knowledge beyond what is visible to the naked eye. Pushing the optical resolution limit down to resolve smaller and smaller structures and dynamics has been mankind’s work over centuries.[21] It started with crude lenses out of spherical flasks filled with water which were able to magnify images and since then has evolved into a tool capable of visualizing structures even at the nanoscale.[22] With advancing scientific and technological development, light microscopy enabled the direct visual proof that every living being consists of cells, the discovery of bacteria and even subcellular organelles.

Nevertheless, the evolution of light microscopy also revealed a fundamental physical limit which prevents the resolution of structures below the diffraction limit of around 200 nm. While this limit can be circumvented using microscopy methods not relying on light such as atomic force microscopy (AFM) or electron microscopy which can reach resolutions of single atoms, these methods suffer from several drawbacks for biological applications.[23, 24, 25] Their invasiveness, lack of specificity and their comparably low temporal resolution make them unsuitable for imaging living biological matter or proteins and dynamic processes occurring in them. Consequently, they are not able to replace the most classical type of microscopy: light microscopy.

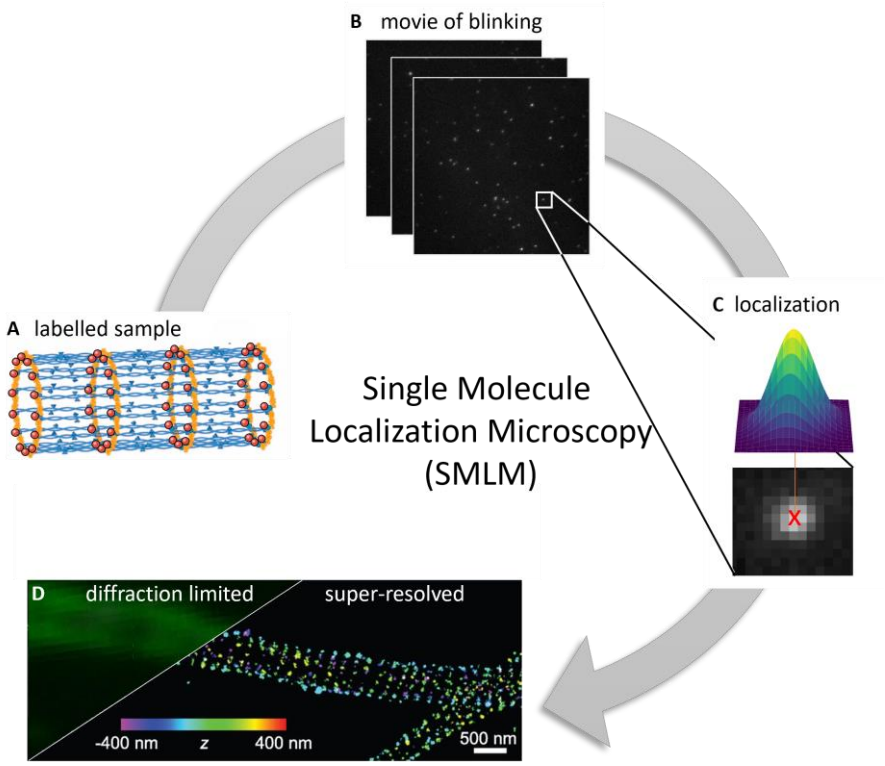

Figure 2: The principle of SMLM. A) A target of interest e.g. adducin in an actin filament is labelled with fluorophores (red spheres) and immobilized. Adapted from [26]. B) For SMLM, the fluorophores are made blinking and a movie of the blinking is acquired. C) In each frame the fit of each individual “on” event localizes the center positions (red cross). D) By plotting the localizations, a super-resolved image of adducin can be generated which enhances the resolution compared to a diffraction limited image of the actin filament. Adapted from [26].

As such, overcoming the diffraction limit in optical microscopy is crucial for observing biological processes between and within living cell organelles. For this the invention of super-resolution (SR) microscopy was crucial and was awarded the Nobel prize in 2014.[27] By controlling and switching fluorescent dyes, structures smaller than the diffraction limit can be resolved. Multiple methods evolved around the switching of fluorophores, that led to two different paradigm of SR microscopy, the targeted-switching and stochastic-switching approaches, respectively.[28]

Stimulated emission depletion (STED) is the most prominent example of targeted-switching techniques and achieves the targeted switching of fluorophores by an excitation and a depletion beam.[29, 30] The excitation remains a standard confocal Gaussian beam. It is superimposed with a second red-shifted beam used to deplete the excited state of the fluorophore by stimulated emission. By saturating with a depletion beam in shape of a donut or more scientific, a vortex-shaped beam, fluorophores outside the center are forced to emit in a stimulated manner. Thus, the area where a fluorophore can spontaneously emit shrinks, making the resolution of fluorophores below the diffraction limit possible. By scanning over the sample thus injecting the coordinates of the superimposition of excitation and depletion beam, a super-resolved image is generated.

The second class, the stochastic-switching techniques, with the prominent examples of photoactivated localization microscopy (PALM)[31, 32] and sub-diffraction-limit imaging by stochastic optical reconstruction microscopy (STORM)[33, 34] use a stochastic approach to switch fluorophores via e.g. buffer. This approach is commonly also referred to as single molecule localization microscopy (SMLM). Here, large areas (80 µm x 80 µm) of immobilized and fluorescently labelled samples are imaged using a camera-based microscope (Figure 2A). To overcome the diffraction limit, stochastic blinking of the fluorophores is introduced to separate them in time such that only one fluorophore per diffraction-limited area is in its emissive state. Then, a movie of the blinking fluorophores is acquired, and the center position of each active fluorophore is localized via a fit in each frame. (Figure 2B-C). By plotting the center positions of all frames, a super-resolved image is reconstructed (Figure 2D). With the first visualization of the periodicity of the membrane skeleton, these methods enabled the discovery of new structural properties for the first time which was a milestone for SR microscopy.[26] Other striking examples of SR microscopy are the discovery of the relation between CD19 expression and CAR-T elimination which is important for leukaemia patients,[35] and the direct visualization of the eight fold symmetry of the nuclear pore complex[36] and many more[37, 38, 39, 40].

Nowadays, both classes of SR and their derivative are widely in use and give insight into many aspects in life sciences and beyond. However, while the impact of this first generation of SR methods is profound, they lack the spatio-temporal resolution necessary to image on the smallest length scales below 10 nm (Figure 3 A). For the targeted-switching techniques, the resolution is directly related to the size of the effective excitation. To reach nanometer resolutions, very high depletion powers of the vortex-shaped beam are needed, which would effectively destroy the sample. For the camera based stochastic-switching techniques, the limiting factor is the photon count of an on-event, as this limits the precision of the localization fit.[41] Thus the first generation of SR methods are limited to ≈20 nm and to ≈30 nm resolution for the stochastic methods of PALM or STORM and for the targeted-switching approach via STED, respectively.[42, 43, 44] While this suffices to resolve a large variety of biological samples, from mitochondria to proteins, it is not sufficient to resolve dynamics and structural features on length scales of 1 nm, the size of a fluorophore (Figure 3 B).

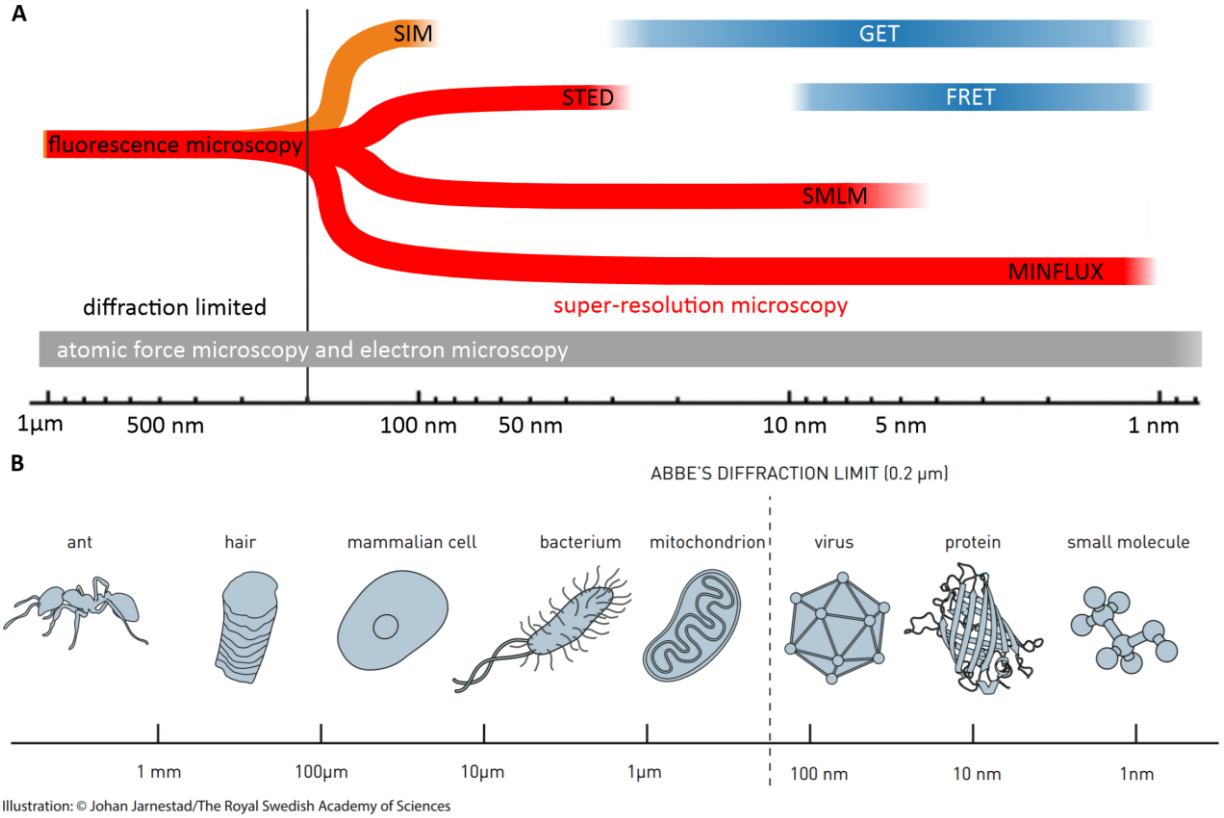

Figure 3: Length scales of common microscopy techniques and structural features. A) Resolution limit of commonly used microscopy techniques. Included are SR methods (red), SIM (orange), energy transfers (blue) and other microscopy techniques (grey). B) Length scale of structural features from [45]. From left to right: bacterium, mitochondrion, virus, protein, and a small molecule.

Over the last decades much effort was put into optimizing the aspects of SR microscopy, both on instrumental and the sample side.[46] On the application side of microscopy the accessibility of components and software increased. Beside commercial companies, many initiatives of open-source microscopy of hardware[47, 48] and software[49, 50, 51] emerged, helping to enormously push the field of microscopy from development towards applications. On the sample side, optimizations were performed for the fluorescent reporters, increasing both their brightness and their photo stability,[52, 53] optimized their linkers[46, 54] and switching properties[55, 56]. Parallel to the improvement of existing techniques, new approaches were developed, pushing the resolution limit further and further. Noteworthy here is the development of DNA-Point Accumulation for Imaging in Nanoscale Topography (PAINT), which is a stochastic-switching technique that uses transient DNA hybridization to regenerate an imager strand modified with a fluorophore thus also its photon budget.[57] This enables squeezing all photons of a single fluorophore into a single localization, reaching a resolution of down to 5 nm.[49, 58, 59] However even with increased photon budget, imaging length scales of 1-2 nm remains challenging.

Beside SR microscopy, other optical methods such as Förster Resonance Energy Transfer (FRET) can be used to measure relative distances between two fluorophores with sub-nanometer precision.[60] FRET uses the fact that two dyes in close proximity transfer an exciton from an donor dye to an acceptor dye. As the energy transfer rate is strongly distance dependent, FRET achieves high spatio-temporal resolution.[61] Coupled with its minimal invasiveness, FRET is an ideal tool for the investigation of protein conformations. However, applications of FRET remain limited due to its small dynamic range of 2-10 nm, leaving protein-protein interactions or multicomponent molecular machineries out of reach. This could be extended using the graphene energy transfer (GET), which instead of an acceptor molecule features a graphene coverslip as an acceptor surface.[62, 63, 64] Nonetheless, only axial distances to graphene are measured and the working range between dye and graphene sheet remains limited

to distances smaller 30 nm. Thus, a SR technique which can routinely image length scales with a precision of 1 nm would be desirable to close the resolution gap between FRET, and SR microscopy.

This is where one of the newest developments of the SR family comes into play: MINFLUX.[65] Requiring less than a tenth of the photons compared to SMLM methods, MINFLUX pushes the field of SR microscopy to precisions of 1 nm, which is the size of a fluorophore. Similar to targeted-switching techniques like STED, MINFLUX is a confocal technique and injects information via their excitation. This is in contrast to camera-based stochastic-switching techniques which use the emitted information. MINFLUX combines both information, the injected excitation of multiple displacements of vortex beam and the respective fluorescence intensity, to increase the information of each emitted photon for more photon efficient localizations. While MINFLUX is typically considered as a SR technique, it is essentially a novel localization technique. To create super-resolved images, MINFLUX requires stochastic-switching of the fluorophores.

It is worth to note, that the combination of fluorescent response and structured illumination follows the works of orbital tracking which was proposed theoretically 20 years ago[66] and demonstrated experimentally later[67, 68, 69, 70]. Orbital tracking localizes a fluorophore by measuring the fluorescence signal at excitations of a focused Gaussian beam along a circular trajectory around the target molecule. The MINFLUX concept sparked a wave of novel methods reaching the nanometer regime. In this framework, MINSTED was proposed which uses a similar approach to orbital tracking with a STED beam for excitation.[71, 72] Another example of this common framework of structured illumination combined with the fluorescent response includes RASTMIN[73] and the combination of structured illumination microscopy (SIM, Figure 3 A) and SMLM[74] as a wide field approach for nanometer precision.[75, 76, 77]

With the pursuit of better and more precise imaging techniques, the complexity increases. While theoretical models to evaluate the localization performance exist, it remains essential to demonstrate the performance experimentally. Thus, suitable standards to benchmark SR methods are required. Especially with techniques such as MINFLUX, which push the limit of resolution to few nanometers, those tools require small spatial features. Historically, filamentous structures such as actin filaments or microtubule were used to demonstrate the performance of the novel techniques. However, biological systems are prone to chaotic fluctuation, which result in a variable molecular environment.[78] This leads to problems in the reproducibility as there is a strong dependence on the protocol, the linker and the markers. There has been recent work using the nuclear pore complex as SR standards.[79] However, drawbacks are still that labeling positions remain stochastic and are highly volatile on the environment.[56] As an accurate standard for the characterization of SR techniques, control over the stoichiometry as well as the fluorophore positions are key.

These requirements are fulfilled by DNA origami structures as breadboards for modifications such as fluorophores.[80] The DNA origami technique was introduced in 2006 by and uses DNA hybridization of multiple shorter oligonucleotides to a long single stranded scaffold strand.[81] By designing the oligonucleotides, also called staple stands, complementary to the scaffold strand a 2D or 3D structure can be designed.[82] With the placement of fluorophores with nanometer precision, DNA origami structures can serve as precise benchmark tools for SR methods. Especially in light of the novel methods of MINFLUX[65], MINSTED[83] and RASTMIN[73], the resolution of few nanometers has been demonstrated using DNA origami.[65, 84, 85] Applications of DNA origami structures lie even beyond optical microscopy, e.g. as a standard for AFM.[86, 87] In the publication respective to chapter 4.1, the broad range of applications of DNA origami towards nanorulers and reference structures are discussed. Besides nanorulers, the DNA origami technique provides a breadboard for many more applications. Especially in the context of light interaction, DNA origami structures are a versatile platform. As discussed in the publication respective to chapter 4.2, DNA origami can be used to optically control

chemical reactions[88], biosensors[89] or even nanodevices with dynamics on the nanometer length scale[90].

However, while state of the art microscopy such as MINFLUX can resolve dynamics and structural features with nanometer precision (linker error aside), information about the environment is lost.[43] Especially when tracking individual fluorophores, only one fluorophore can be tracked simultaneously. While the interpretation of microscopy data on DNA origami might be straightforward, as the interplay of components is designed, in more complex environments this might not be the case. This restricts the interpretation of results, especially for cellular processes which are typically governed by an interplay of multiple chaotic biological components. In the past it has been demonstrated that spectral multiplexing can give novel insights. But for the already technological complex nanometer precise MINFLUX multicolor tracking experiments create an even higher technological complexity and thus have not been demonstrated.

Another approach is the use of the excited state lifetime of the fluorophore, also called fluorescence lifetime. By using suitable markers, the change in fluorescence lifetime can be used as an intrinsic and quantitative measure on the environment of the fluorophore. Biological applications of reporters on environments range from calcium imaging[91], over local viscosity probes[92] to markers of cell progression[93]. Here, the fluorescence lifetime enables a new dimensionality and gives microscopy a tool to unravel the biological mechanisms. Besides measuring the interaction of the dye with the environment, the fluorescence lifetime can also be utilized as a property to improve microscopy techniques. It can separate spectrally similar fluorophore populations, hence enabling multiplexing capabilities.[94, 95, 96] Beside imaging, the fluorescence lifetime can also distinguish photo-physical on-off switching from lifetime-correlated intensity fluctuations.[97, 98, 99] In combination with fluorescence correlation spectroscopy (FCS) and its high temporal resolution, the fluorescence lifetime can give access to dynamics. While the fluorescence lifetime was used so far for high temporal resolution data and imaging, it was not yet used in the spatial context of SR microscopy with nanometer precision.[100, 101]

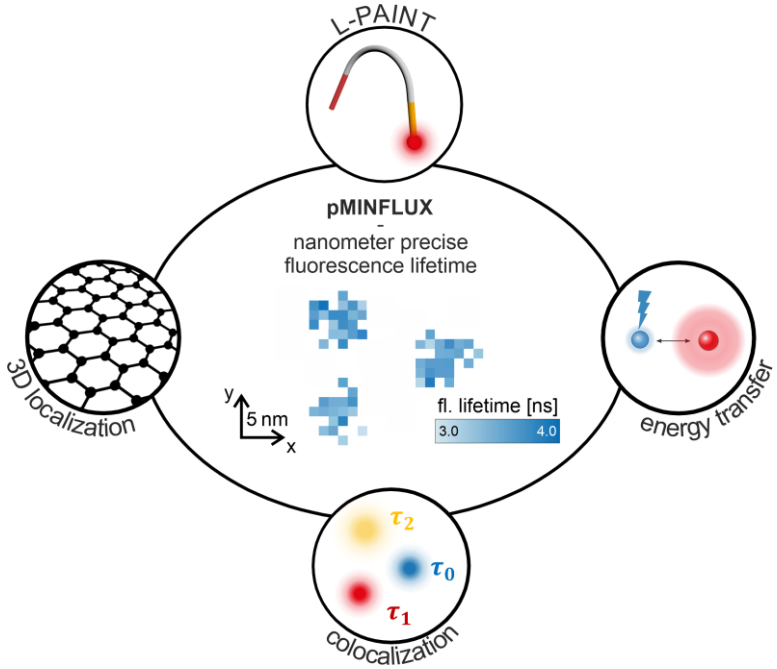

Figure 4: Overview of developments on basis of pMINFLUX with its nanometer precise fluorscence lifetime information. Middle Panel: Simulated pMINFLUX super-resolved fluorescence lifetime image of three fluorophores spaced in 12 nm distance. The length of the black arrows corresponds to 5 nm. Left panel: Schematic of graphene. Top panel: L-PAINT scanning strand. Right Panel: Schematic of FRET between two fluorophores of different color. Bottom panel: Schematic of super-resolved colocalization of three fluorophores with different fluorescence lifetime.

In this thesis, MINFLUX is extended to the fluorescence lifetime domain. To this end a pulsed-interleaved MINFLUX approach (pMINFLUX) which is in comparison to MINFLUX technologically less complicated, is introduced in detail in chapter 4.3. The experimental performance of pMINFLUX is benchmarked experimentally using DNA origami structures and in simulations. Furthermore, the multiplexing capability of the fluorescence lifetime coupled with the nanometer precise localizations is demonstrated. The combination of nanometer precise localization coupled with fluorescence lifetime information enables many applications previously not feasible in SR microscopy. Around this unprecedented combination four novel methods are developed (Figure 4) in this thesis.

The first application is the extension of nanometer precise SR to the third dimension. Up until here, only SR microscopy in lateral direction was contemplated. While it is conceptually easy to extend MINFLUX to the third dimension, the instrumental and engineering requirements increase with dimensionality. 3D MINFLUX has been demonstrated experimentally achieving isotropic nanometer resolution[85], however the fluorescence lifetime of pMINFLUX offers a more elegant approach. By use of the GET to a surface, the axial distance can be determined.[64] In synergy with the lateral localization of pMINFLUX this enables 3D SR with high precision. In chapter 4.4, this is experimentally characterized using DNA origami structures and demonstrated using the stochastic switching of DNA-PAINT.

A major drawback of DNA-PAINT is that high imaging speed require high concentrations of imager strands. Beside double localizations also a high fluorescent background is introduced. Additionally, the MINFLUX excitation is performed in the minimum of the vortex beam, leading to low signal background ratios. The situation is aggravated by the confocal nature of MINFLUX which calls for fast binding kinetics to speed up imaging. However, as MINFLUX is optimized for photon efficient localizations, it does not need the regenerated photon budget of DNA-PAINT for localizations with nanometer precision. The photon can thus be distributed on multiple binding sites. In chapter 4.4, local-PAINT (L-PAINT) is introduced which is an alternative SR technique optimized for the fast localization of multiple binding sites.

While MINFLUX is able to give insight into structural information, the interplay with the environment remains unknown as only individual fluorophores are localized. In GET-pMINFLUX the fluorescence lifetime enables the measurement of an energy transfer to graphene thus giving some direct information about distance and environment. Beside GET, other kinds of energy transfers can be measured. By combining pMINFLUX with FRET, the correlated measurement of nanometer precise tracking of a donor dye and simultaneously the distance to an acceptor becomes possible. Multilateration[102] with multiple donor positions enables the nanometer precise co-localization of both dyes without photo-switching, as it is experimentally demonstrated in chapter 4.5.

One downside of FRET is the small dynamic range of <10 nm. Thus, dynamics occurring at larger distances, cannot be visualized by FRET-pMINFLUX, leaving many other relevant biological dynamics occurring at larger distances out of reach. MINFLUX has the necessary localization precision, temporal resolution and field-of-view, a dual-color MINFLUX approach could independently track multiple dyes simultaneously over a large working range. However, such a dual-color MINFLUX approach is technologically not straightforward as it would be prone to instabilities of drift and misalignment of the independent beams used for MINFLUX excitation, as shown already for STED microscopes.[95] Hence, it is sensible to explore the co-localization with MINFLUX in a single excitation colour and without photo-switching.

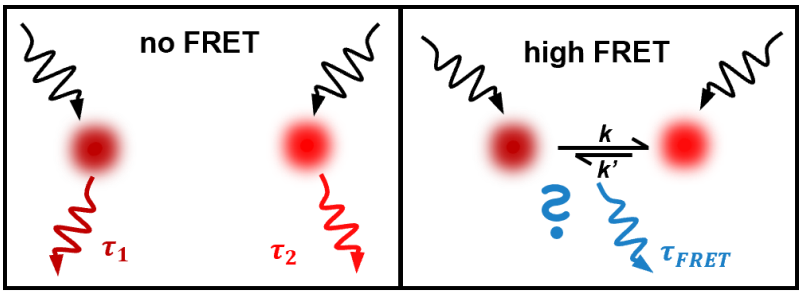

Figure 5: Left panel: For large distances with no FRET between the fluorophores, the fluorescence can be considered independent of each other. Via the fluorescence lifetime τ, an emitted photon cannot be assigned to the fluorophore the photon is absorbed at. Right panel: At distances within the FRET range, the fluorescence of two emitters with similar spectral properties becomes coupled via the rates k and k'. Due to FRET in both direction photons are not necessarily emitted from the fluorophore that absorbed the photon.

To this end, pMINFLUX lifetime multiplexing is developed in this thesis. It uses the fluorescence lifetime as a mean to co-localize two spectrally similar dyes without photo-switching over a large field-of-view. Beyond the FRET range, pMINFLUX lifetime multiplexing enables the co-localization of two dyes by separating their fluorescent responses according to their fluorescence lifetimes. Inside the FRET range, both spectrally similar dyes act as donor and acceptor simultaneously. Thus, photons emitted by one dye cannot be assigned unequivocally, rendering the co-localization inaccurate (Figure 5). The co-localization is recovered by a newly developed combined phasor-microtime gating approach. By combining both multiplexing approaches, the resolution gap between single-molecule FRET and co-tracking can be closed. Using DNA origami structures, pMINFLUX lifetime multiplexing in and beyond the FRET range is demonstrated experimentally and in simulation in chapter 4.5.

2. Theoretical Background

This work extends the field of single molecule fluorescence microscopy, in particular super-resolution microscopy. Therefore, it is crucial to understand the fluorescence properties and the photophysics of a single fluorescent dye. To this end, a model of a single fluorophore with singlet, triplet and radical states is introduced to then exploit the photophysical properties to manipulate a dye for either stable fluorescence trajectories or blinking trajectories. Next, the literal picture of a single dye is extended to two dyes. In imaging, diffraction of light limits the distance where two dyes can be resolved. To overcome this diffraction limit, the field of super-resolution microscopy developed. Beside a brief overview on super-resolution methods, the focus of this chapter lies on the super-resolution method MINFLUX, which is at the core of this work. As MINFLUX can image small distances, energy transfer processes on the same length scales have to be considered. For this purpose, FRET, the energy transfer process of two dyes via dipole-dipole coupling is explained. The concept is extended to explain the graphene energy transfer (GET). Last DNA origami nanotechnology is introduced as a method to place dyes in a controlled fashion and is used as a toolbox to investigate and benchmark super-resolution microscopy and energy transfer processes.

2.1 Fluorescence

The microscopy performed in this work uses the fluorescence of organic dyes. As the literature of fluorescent dyes is very extensive and can be found in textbooks,[103, 104, 105] only the aspects of fluorescent dyes relevant to this work are explained.

Organic dyes are of the size of 1-2 nm and consist mostly out of carbon and hydrogen atoms. The main characteristic of an organic dye is a strongly delocalized π-electron system. This π-electron system can be described as a particle-in-a-box model and mainly defines the fluorescence properties of the dye. Thus, the size of the π-electron system corresponds to the absorption spectrum. Due to energy conservation and non-radiative losses, the emitted fluorescent light is lower in energy resulting in a red-shifted emission spectrum. By introducing heteroatoms like oxygen or nitrogen, the fluorescence properties of a dye can further be tuned.[52, 53]

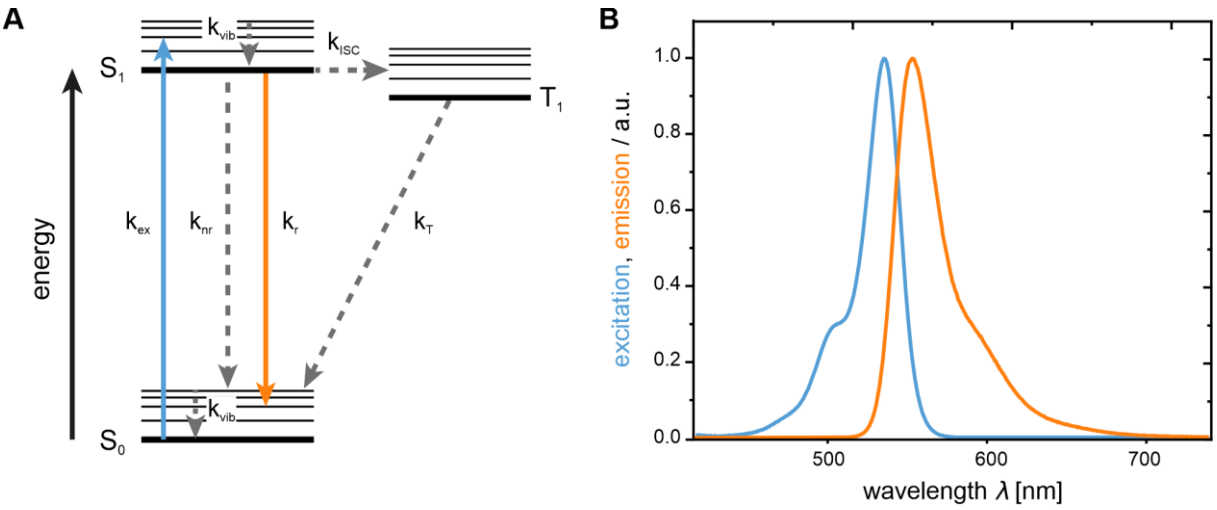

Figure 6: A) Jablonski-diagram of an organic fluorophore. Bold lines represent electronic levels, while thin lines are vibronic levels. The blue arrow depicts the excitation, the orange arrow depicts the fluorescent emission and non-radiative transitions are depicted as grey dashed lines. B) Absorption (blue) and fluorescent emission (orange) spectrum of ATTO542. The shift between both maxima is called Stokes shift.

The Jablonski diagram in Figure 6A depicts the basic photophysical processes in an organic dye. A dye can be described by a number of singlet states S_N and triplet states T_N. N depicts the number of electronically excited state, hence S_0 describes the singlet ground state. For simplification only the first electronically excited states S_1 and T_1 are considered here, where each singlet and triplet state has multiple vibrational states. With an excitation intensity I_{ex}, a dye with an absorption cross section σ is excited from S_0 to S_1 with the rate k_{ex}:

$$k_{ex} = I_{ex}\sigma$$

After excitation, the dye is in a vibrational excited level of S_1 and the vibrational level relaxes within femto-seconds (k_{vib}) to the vibrational ground state of S_1. From there multiple processes can occur. Either it can directly go back to the electronic ground state S_0 via by radiative photon emission (k_r) or non-radiatively via heat dissipation (k_{nr}). As the radiative emission of a photon ends in a vibrational level, the energy of the photon emitted is lower in energy than the energy of the absorbed photon. This energy difference, results in a red shift between absorption and emission and is called Stokes shift (Figure 6 B). The Stokes shift can be used to spectrally separate the emission from the excitation. Another depopulating avenue of the excited S_1 state is via intersystem crossing (k_{ISC}) to the triplet state T_1. The transition of T_1 to the ground state can be either radiatively or non-radiatively and is described by k_T.

An observable to characterize a dye is the lifetime of the excited state S_1, referred as fluorescence lifetime τ_{fl} and is inverse to all depopulating rates of S_1:

$$\tau_{fl} = \frac{1}{k_r + k_{nr} + k_{ISC}}$$

Another important spectroscopic property is the quantum yield Φ of the fluorescence state which describes the efficiency of the fluorescence process.

$$\Phi = k_r\tau_{fl} = \frac{k_r}{k_r + k_{nr} + k_{ISC}}$$

Similarly, the fraction of ISC compared to other states is characterised by the ISC yield Φ_{ISC}:

$$\Phi_{ISC} = \frac{k_{ISC}}{k_r + k_{nr} + k_{ISC}}$$

Typical dyes used in single molecule studies have a low Φ_{ISC}, such rhodamines have Φ_{ISC} of around 0.2 - 1%.[106] As the triplet state is only depopulated by k_T, the lifetime of the triplet τ_T is the inverse of it:

$$\tau_T = \frac{1}{k_T}$$

Even though the triplet state might not be occupied often, it is long lived which leads to intermittence of the fluorescence signal. This is also referred as blinking. While the fluorescence lifetime τ_{fl} is typically in the nanosecond timescale, the triplet lifetime is in the microsecond to millisecond range.

Another important aspect is the role the triplet state plays in photo bleaching. As all excited states have a higher reactivity to e.g. molecular oxygen compared to the electronic ground state, they can irreversibly photo bleach. Even though the ISC yield of a dye might be low, photo bleaching primarily occurs from the triplet state due to its long lifetime.[107] Thus, it is evident that for single molecule studies, the dyes should have a high absorption cross section and a high quantum yield. To further decrease photo bleaching, triplet states should be rare and short-lived.

2.2 Controlling the Photophysics of Dyes

The photo stability of a fluorescent dye can be increased by introducing additives. With an oxygen scavenging system, the molecular oxygen in solution can be removed, minimizing photobleaching. As the molecular oxygen is also a triplet quencher, this also greatly increases the triplet lifetimes.

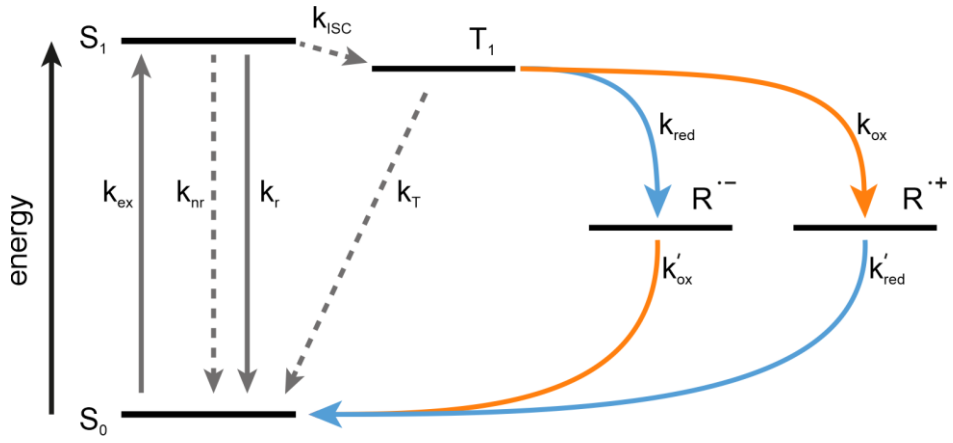

Figure 7: Simplified Jablonski diagram with additional anionic ($R^{\cdot -}$) and cationic ($R^{\cdot +}$) radical states. The reduction and oxidization process predominantly starts from the T_1 state. Reduction is marked as blue, while oxidization in orange. Adapted from [98].

To that end, the concept of a reducing and oxidizing system (ROXS) has been introduced, which provides another pathway to depopulate the triplet state.[108, 109] Additional pathways are via an intermediate radical state ($R^{\cdot -}$ and $R^{\cdot +}$) by oxidizing or reducing the triplet state (Figure 7). A reverse reaction, a respectively reduction or oxidization is then recovering the ground state. A common oxidization and reduction agent for ROXS is trolox (TX) and its oxidized form trolox quinone (TXQ), but also additives like ascorbic acid or methyl viologen can be used.

While the ROXS system is expedient for reporter dyes where stable traces are desired, for super-resolution microscopy it might also be necessary to control the blinking. Here, the ROXS concept explains not only how photobleaching can be minimized, but it can also be used to introduce controlled blinking. By adding only a reduction agent like beta mercaptoethanol (βME), the radical state is not depopulated by an oxidizing additive, leading to long radical hence long off-states.[110, 111, 112] To further decrease photobleaching a triplet quencher e.g. cyclooctatetraene can be added, which additionally depopulates the reactive triplet state. As all these reactions are diffusion limited, the rates can be controlled via the concentrations of the additives.

2.3 The Diffraction Limit

Understanding of the photophysics of organic dyes is the basis for super-resolution microscopy, which is circumventing the diffraction limit in far field fluorescence microscopy. The diffraction limit of light describes the limit where the focused light of two objects cannot be distinguished anymore. This chapter gives a brief overview on the consequences of the diffraction limit, along the argumentation of Lord Rayleigh (1842 - 1919).[113] While other definitions of the diffraction limit such as of Abbe or Sparrow exist, the consequences are similar. For details of the resolution limits, reference to literature is made.[114, 115]

In a fluorescence microscope, light is focused to the sample surface by an objective with a numerical aperture *NA*. The numerical aperture *NA* is dependent on the refractive index *n* of the environment and gives a measure of the range of angles α the objective can emit or collect:

$$NA = n \sin(\alpha).$$

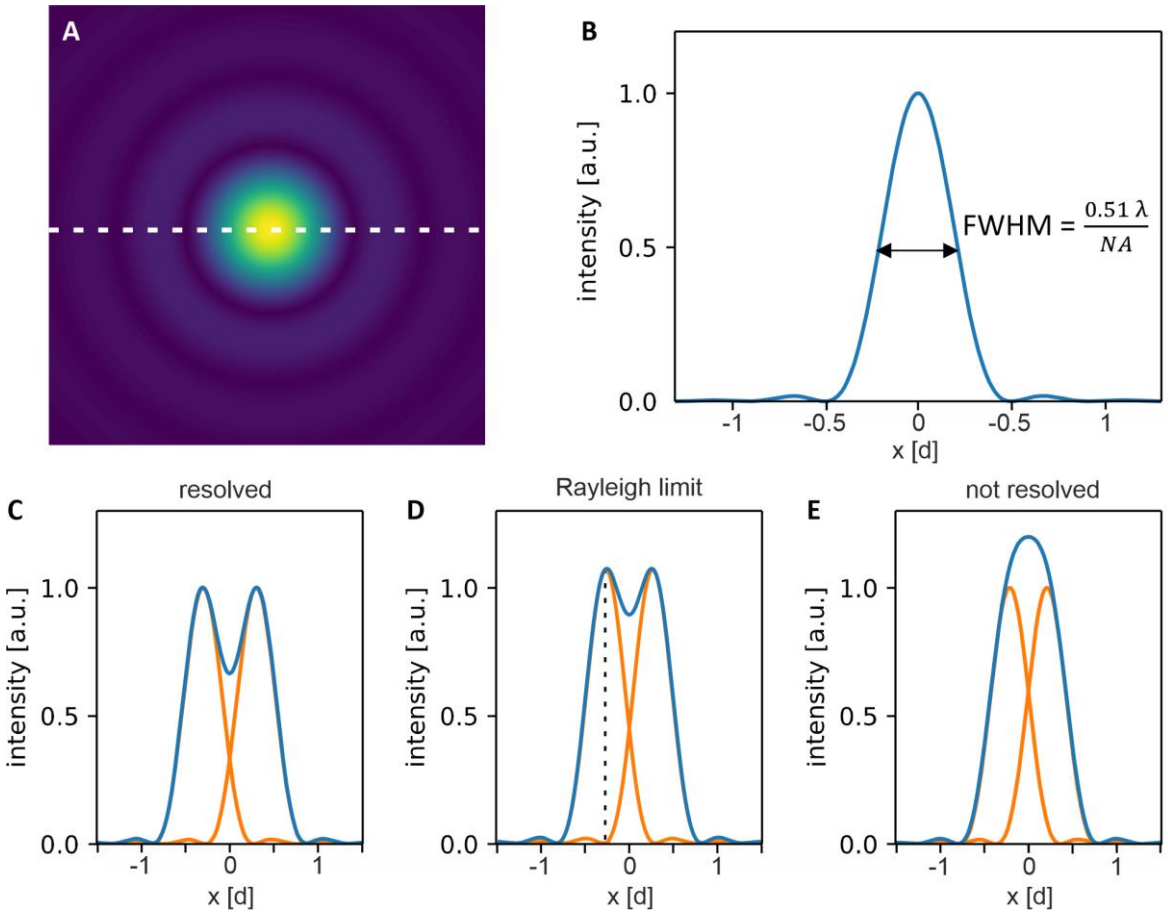

Figure 8: A) 2D plot of an Airy disk. The dashed line indicates the intensity cross section depicted in panel B. B) 1D Intensity profile of an individual Airy disk. The x-axis is in units of d the lateral extent between both minima of an Airy disk. The arrow indicates the full width half maximum (FWHM). C) 1D intensity profile of two individual emitters in a distance larger than the diffraction limit. The individual emitters are depicted in orange, while the resulting emission profile of both emitters is depicted in blue. The x-axis is units of d the lateral extent of an Airy disk. D) 1D intensity profile of two individual emitters in a distance below the diffraction limit. The individual emitters are depicted in orange, while the resulting emission profile of both emitters is depicted in blue. As indicated by the black line, at the Rayleigh diffraction limit the maximum and the first minimum of respective emitters coincide. The x-axis is units of d the lateral extent of an Airy disk. E) 1D intensity profile of two individual emitters in the distance not resolvable according to the Rayleigh limit. The individual emitters are depicted in orange, while the resulting emission profile of both emitters is depicted in blue. The x-axis is units of d the lateral extent of an Airy disk.

Due to the wave nature of light, the shape of light focused with such a lens is diffraction limited and can be described by an Airy disk (Figure 8 A-B). The lateral extent *d* of an Airy disk, the distance between the first minima, is given by the numerical aperture and the wavelength of light λ:

$$d = \frac{1.22\,\lambda}{NA}$$

For two independent emitters the resulting intensity profile is the sum of both (Figure 8 C). The minimal distance resolvable was deduced by Lord Rayleigh. (Figure 8 D). At the Rayleigh diffraction limit, the position of the first emitter is in the minimum of the second emitter's profile. If the distance of both emitters is too small, the emitters become unresolvable (Figure 8 E). When the center of one Airy disk falls on the first minimum of the Airy pattern, both emitters become just resolved. This formulates to the Rayleigh diffraction limit:

$$d_{Rayleigh} = \frac{1.22\,\lambda}{2\,NA} = \frac{0.61\,\lambda}{NA}$$

Along the axial direction, the Airy disc has a larger extent, resulting in the following axial diffraction limit:

$$d_{axial} = \frac{2\,n\,\lambda}{NA^2}$$

While Lord Rayleigh gives a simple measure for the diffraction limit, it still falls short as slightly smaller distances can be resolved. By using the full width half maximum (FWHM) of the Airy disk, instead of the first minima, a more modern formulation is achieved.[115, 116] The lateral diffraction limit then can be rewritten as:

$$d_{FWHM} = \frac{0.51\,\lambda}{NA}$$

This slightly smaller distance is practically identical to other formulations of the diffraction limit such as Abbe's or Sparrow's diffraction limit. While their arguments differ, the results are equivalent: using green light (λ = 532 nm) and a modern objective (*NA* = 1.4), laterally and axially distances smaller than ≈200 nm or ≈800 nm respectively become unresolvable. Smaller distances might be resolved using shorter wavelength such as blue light, however ultimately this becomes unfeasible for fluorescence microscopy. So other ways to overcome the diffraction limit are needed. This is where the field of "super-resolution" microscopy evolved.

2.4 Super-Resolution Microscopy

Super-resolution techniques break or more specifically circumvent the diffraction limit. Two classes of super-resolution techniques emerged[117]: the targeted-switching and the stochastic-switching techniques.

The targeted-switching techniques such as stimulated emission depletion (STED)[29, 118] or ground state depletion microscopy followed by individual molecule return (GSDIM)[119] rely on the targeted-switching of the fluorescence and non-fluorescence state. A fluorophore is excited in a diffraction limited confocal volume. Additionally, a depletion beam in the shape of a vortex is used to supress the fluorescence of dyes. Fluorophore saturated by this additional depletion beam are switched to the ground state by stimulated emission. Only in the vortex-beam center, where dyes are not saturated by the depletion beam, fluorescence is observed. Thus, in STED the position information is inferred by scanning the overlay of both beams over the sample (Figure 9 A). For STED, the precision σ is dependent on the ratio between the intensity of the depletion beam I_{STED} and the intensity of saturation I_{sat}, at which the probability of fluorescent emission is halved:[20]

$$\sigma_{STED} \approx \frac{0.5\,\lambda}{NA\sqrt{1 + \frac{I_{STED}}{I_{Sat}}}}$$

Typical attainable lateral precisions with STED are in the range of 20-40 nm.[43] Higher precision would require very high depletion beam intensity, hence destroying the sample.

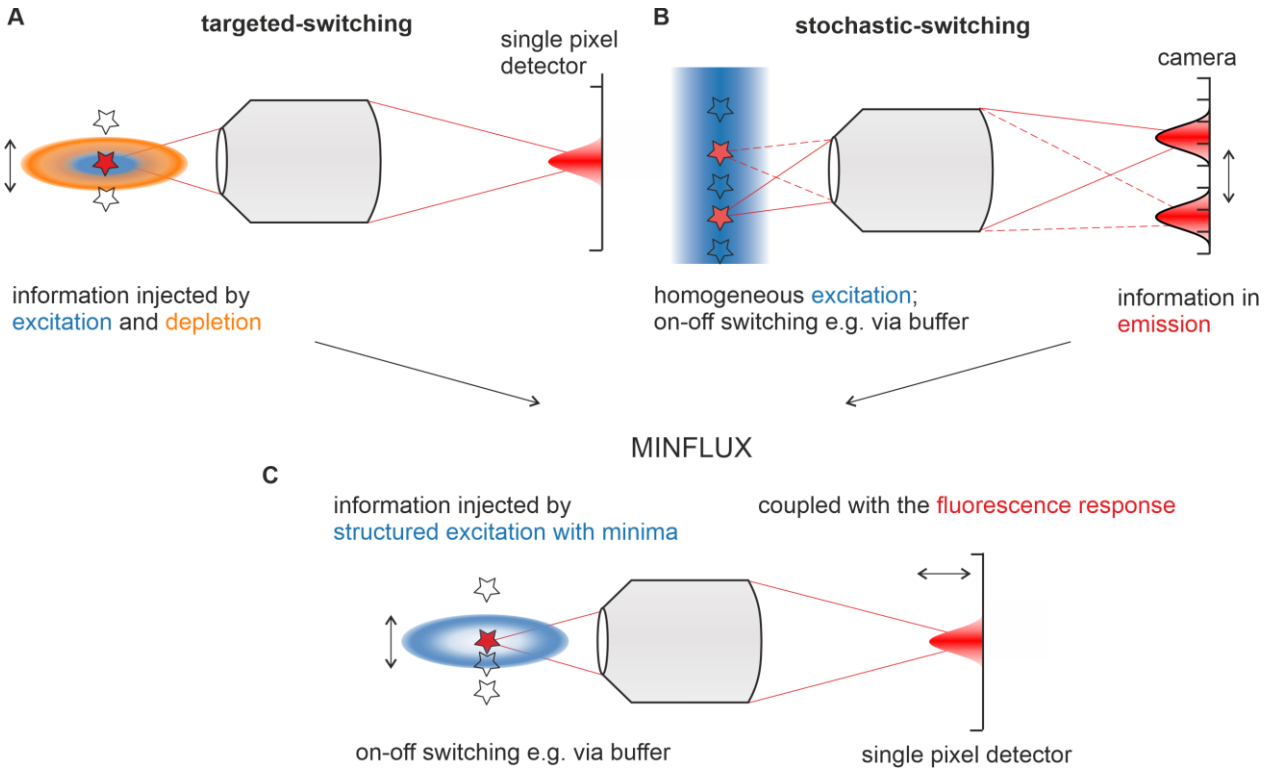

Figure 9: Information in different super-resolution approaches. A) Schematic of targeted-switching approaches. The targeted-switching uses a gaussian excitation beam (blue) overlayed with a depletion beam in shape of vortex beam (orange) and detects the fluorescence (red) on a single pixel detector. By scanning the overlaid beams over the sample, information is injected, and a super-resolution image is generated. B) Schematic of stochastic-switching approaches. The excitation (blue) is homogeneous. Super-resolution is achieved by the stochastic on-off switching of the fluorophores. The position information is obtained solely from the localization of the fit (black) of the fluorescence emission (red). C) Schematic of the MINFLUX approach. In MINFLUX both information are used, the information injected in excitation and the emission information. MINFLUX injects information via a structured excitation with minima which is displaced and combines this information with the fluorescence response at different displacements to localize a fluorophore ratiometrically.

The second class of super-resolution techniques are based on the stochastic-switching of fluorophores. Typical widefield setups homogenously illuminate the sample, whose fluorescence is imaged by a camera. Here, the information is only encoded in the emission information, which is remains diffraction limited (Figure 9 B). Thus, blinking is needed to separate the emission of fluorophores in time. Fluorophores separated by a distance smaller than the diffraction limit, can then be localized independently. The center position of the fluorophore is then determined by a 2D gaussian fit. By fitting a sequence of frames and plotting the center positions, a structure below the diffraction limit can be reconstructed. The precision of a camera-based localization is dependent on the goodness of the gaussian fit.[41, 120] Here, the best attainable localization precision σ is given by the Cramér-Rao bound (CRB):

$$\sigma^2 = \frac{s^2 + \frac{a^2}{12}}{N} + \frac{8\pi s^4 b^2}{a^2 N^2}$$

with *b* background, *a* pixel size, *s* standard deviation of the emission and *N* the number of photons. Here, the number of photons underlying the gaussian fit is a determining factor of the precision and hence the resolution of the image. In the approximation of moderate and high photon numbers (N >100), σ is proportional to $\frac{1}{\sqrt{N}}$.

Microscopy techniques based on stochastic switching are commonly referred under single molecule localization microscopy (SMLM). Common SMLM methods are Photoactivated Localization Microscopy

(PALM)[32], (direct) Stochastic Optical Reconstruction Microscopy ((d)STORM)[33, 121], DNA Point Accumulation for Imaging in Nanoscale Topography (DNA-PAINT)[57] or blink microscopy[110]. They all rely on imaging blinking of fluorophores with a camera. The difference between those methods is how the blinking is achieved. This effects the photon number usable for each fit, hence the precision.

There have been advances in precision, by combining SMLM with a patterned illumination. Noteworthy here is structured illumination microscopy (SIM).[122, 123] SIM illuminates the sample with standing waves in different rotations and phases. By combining those images, higher frequencies can be imaged thus achieving resolutions of 100 nm even without SMLM. Contrary to popular beliefs, while the resolution is below the diffraction limit, SIM does not break the diffraction limit. By imaging higher orders of diffraction, the above named diffraction limits such as Abbe's or Rayleigh's are not applicable to SIM.[124]

While SMLM by itself can reach precisions below 10 nm, it needs a considerable photon budget.[59] This limits the spatiotemporal resolution, making the precise observation of fast processes unfeasible or even impossible. The combination of SMLM with SIM can improve this and enable more photon efficient localizations.[74]

2.5 MINFLUX

Another approach to increase the information of each photon is by combining SMLM with a known structured illumination in a coordinate-targeted fashion. This approach is called MINFLUX.[65] MINFLUX uses a known vortex-beam-shaped excitation pattern. Vortex beams feature a minimum in their intensity profile and the resulting fluorescence indicates the distance of the molecule to the minimum. By sequentially illuminating the target with a known and displaced excitation profile and combining it with the emission information, the fluorophore can be unambiguously localized, resulting in photon efficient localizations. (Figure 9 C).

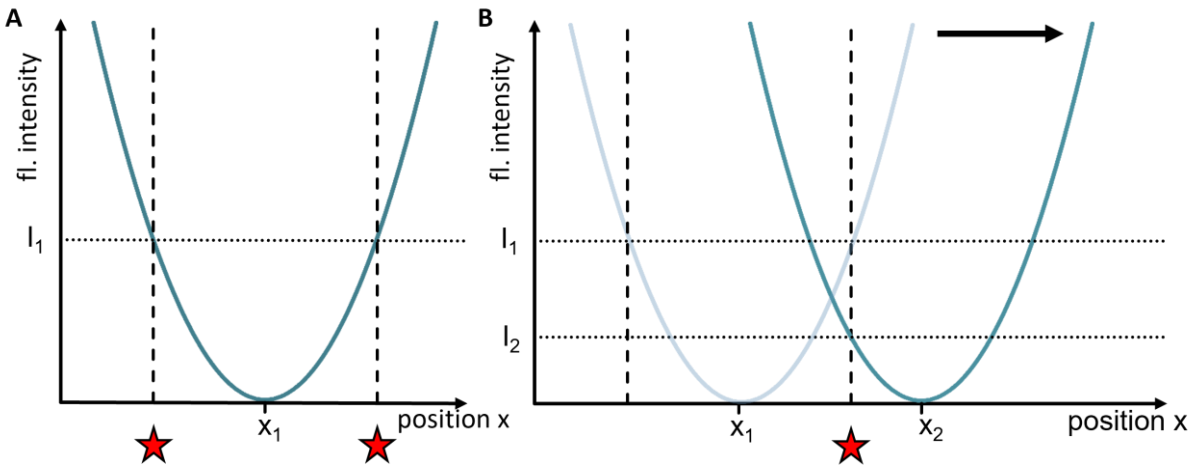

Figure 10: Principle of MINFLUX in 1D. A) In the 1D case MINFLUX utilizes a known parabolic illumination profile (blue line). By measuring the intensity of a fluorophore (I_1) and comparing it with known excitation profile, the fluorophore can be localized to two positions (red stars). B) With a second spatially displaced illumination (darker blue), a respective intensity I_2 is measured. By combining this information with the first illumination (light blue) the fluorophore (red star) can be unambiguously localized.

To explain the principle, MINFLUX is first described in a one-dimensional Gedankenexperiment. A known parabolic laser beam excites a fluorophore. This results in a fluorescence intensity, and with the known intensity profile the fluorophore can be localized to two possible positions (Figure 10 A). In a second step the parabolic intensity profile is displaced to a second position. By measuring the second fluorescence intensity, the fluorophore can be unambiguously localized (Figure 10 B). Condensed: The combination of a series of known structured illuminations with the fluorescent response is needed to localize a fluorophore.

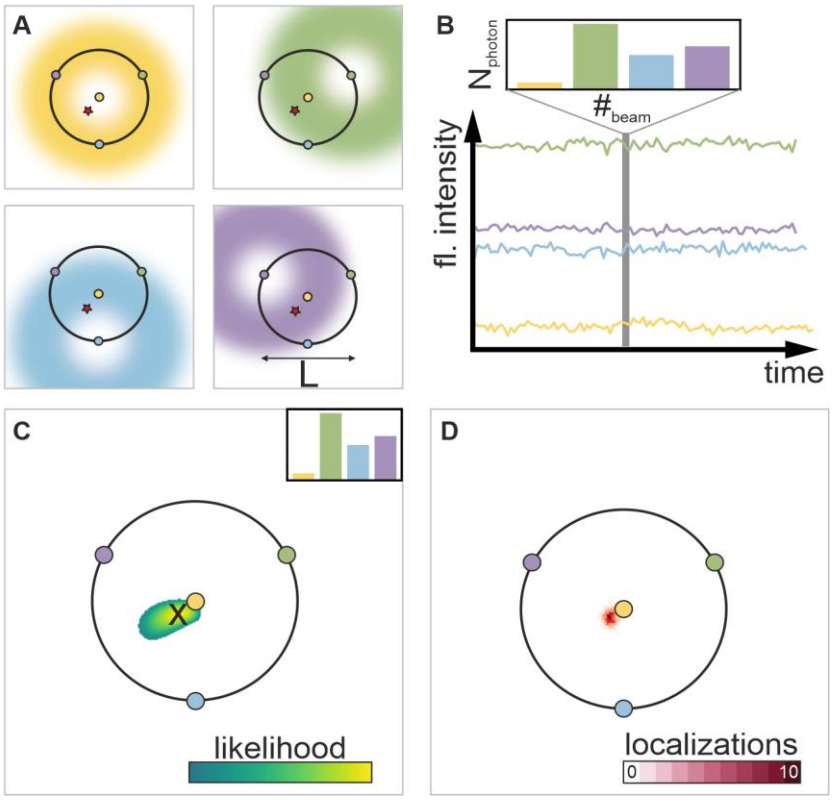

Figure 11: Principle of 2D MINFLUX. A) In the 2D case vortex beams are used. A typical excitation beam pattern is a trianglular displacement with an additional illumination in the middle. Here, the colored circles depict the vortex beam center positions. The triangular pattern of the excitation beam profile has a diameter of L. The fluorophore is depicted as a red star. B) In MINFLUX the photon stream of all excitations is measured. By binning this fluorescence trace, a certain number of photons can be assigned to each illumination beam. C) With the combination of the number of photons with the known excitation profile, a likelihood surface can be generated. A position of the fluorophore is then estimated using a maximum likelihood estimator, denoted by the black x. D) A 2D histogram is generated by localizing all bins of the trace.

In the two-dimensional case, not a parabolic but a vortex-beam is used. The arrangement of the vortex-beams is called excitation beam pattern (EBP). It is quantified with the diameter *L* of the circumference of the beam center position. Typically, the vortex-beam positions are arranged in a triangular pattern with one vortex-beam in the center (Figure 11 A). This center vortex-beam not only removes ambiguities of the localization outside and inside the EBP, but also increases the photon efficiency of the precision. MINFLUX is a targeted approach, with the best photon efficiency around the center of the EBP.

To localize a fluorophore, the fluorescent response needs to be known to each vortex-beam (Figure 11 B). By binning the fluorescence intensity signal, each excitation beam is associated to a respective number of emitted photons which depends on the position in the beam profile. Together with the known intensity profile a likelihood surface is then calculated (Figure 11 C). The maximum of the likelihood surface is the localization of the time bin. In analogy to other SMLM methods, the localizations of all bins are added, and a localization histogram is generated (Figure 11 D).

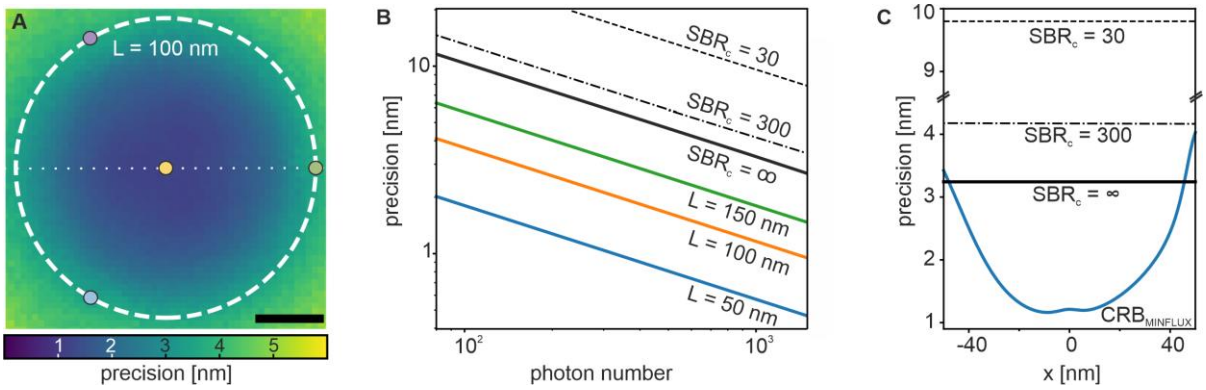

Figure 12: Localization precision of MINFLUX A) Simulated 2D histogram of the lower Cramér-Rao bound precision of MINFLUX as a function of the lateral position. The colored spots and the circle represent the EBP with L = 100 nm. The scale bar is 20 nm. B) Theoretical precision in dependence of the number of photons for different sizes of the EBP L at the center position. Additionally, the lower Cramér-Rao bounds for camera localizations at a Signal Background Ratio (SBR) of 30, 300 and ∞ are shown. C) Simulated precision of the localization along the dotted line in A). The lowest precision for 1000 photons, a SBR of 30 and a L of 100 nm is 1.2 nm. Additionally, the lower Cramér-Rao bounds of camera localizations for 1000 photons at a SBR of 30, 300 and ∞ are given.

One advantage of MINFLUX is that the Cramér-Rao-bound is not only dependent on the number of photons but also on the size *L* of the EBP:

$$\sigma(r = 0)^2_{CRB} = \frac{L}{2\sqrt{2N}}\left(1 - \frac{L^2 \ln(2)}{fwhm^2}\right)^{-1}\sqrt{\left(1 + \frac{1}{SBR(0)}\right)\left(1 + \frac{3}{4\,SBR(0)}\right)}$$

The precision with typical values of the full width half maximum (*FWHM*) of 200 nm, *L* = 100 nm, Signal Background Ratio (SBR) of 30 and moderate photon number *N* = 1000 already reaches less than 1.2 nm. This is 10x more photon efficient than a comparable CRB of a homogeneous illumination (Figure 12 A-B). It is worth noting that the CRB is dependent on the dye position within the EBP (Figure 12 C). Closer to the edge, the localization precision gets worse. Here, iterative approaches have been developed to increase the localization precision. By iteratively centering the fluorophore in the EBP and consecutively shrinking the size *L* of EBP prior information is used and the CRB does not apply anymore. The resulting precision dependence of four iterations cycles scales with $\frac{1}{N^2}$.[85]

To extend MINFLUX to the third dimension, an excitation profile of a 3D tophat is used.[85] By adding displacements in the axial direction to the EBP, a localization in 3D is possible. However, photons of axial displacements only significantly contribute to the axial localization, thus at a fixed number of photons the lateral precision decreases. This is due to photons from the excitation along the axial direction yield predominantly information for the localization along the axial axis.

2.6 Förster Resonance Energy Transfer

Up until here, fluorescent dyes were considered as independent. As the super-resolution techniques get more and more photon efficient, the resolution thus the distance between two dyes that can be individually localized shrinks. However, if two fluorescent dyes are in close proximity, interactions between fluorophores may occur.[125, 126] A prominent example is the case of resonant dipole-dipole coupling, referred to as Förster Resonance Energy Transfer (FRET).[61, 127] In FRET, an exciton can be non-radiatively transferred from a donor to an acceptor dye.

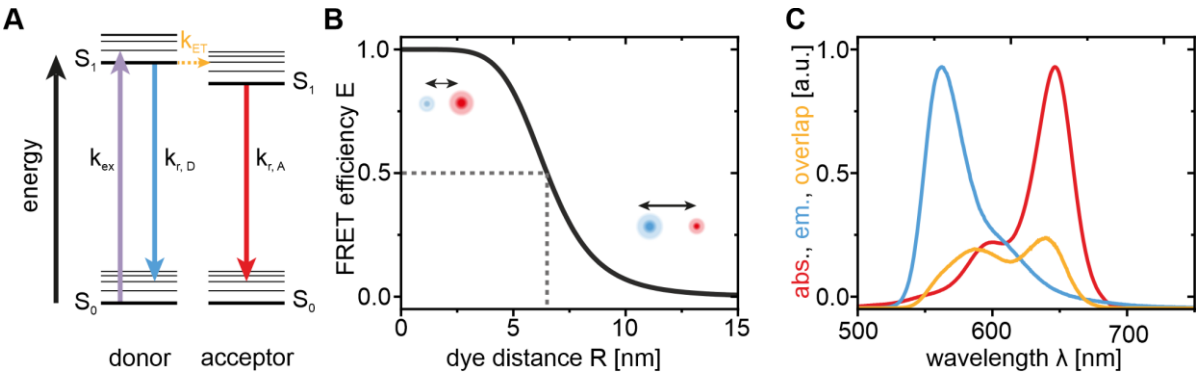

Figure 13: A) Simplified Jablonski diagram of FRET between a donor and acceptor dye. B) Distance dependence of the FRET efficiency E for a dye pair of ATTO542 and ATTO647N with R_0=6.3 nm. Under donor excitation and small interdye distances, mostly the acceptor dye emits, while for larger interdye distances mostly the donor dye emits. C) Spectra of the fluorescent emission of the donor ATTO542 (blue), the absorption of ATTO647N (red) and their spectral overlap density (yellow).

The energy transfer introduces a depopulating rate (k_{ET}) of the excited singlet state S_1 in the donor dye (Figure 13 A). k_{ET}, as well as the energy transfer efficiency E, are strongly distant dependent, scaling with the inverse sixth power law of the interdye distance R:

$$E = \frac{k_{ET}}{k_r + k_{nr} + k_{ISC} + k_{ET}} = \frac{1}{1 + \left(\frac{R}{R_0}\right)^6}$$

The Förster radius R_0 indicates the distance of 50 % energy transfer efficiency (Figure 13 B) and is characteristic for each FRET-pair. The Förster radius is dependent multiple parameters, such as the quantum efficiency of the donor Φ_D, the overlap integral of the emission spectrum of the donor ε_A and the absorption spectrum of the acceptor I_D (Figure 13 C), describing the nearfield coupling of both dyes.

$$R_0 = \frac{9\ ln10\ \kappa^2\ \Phi_D}{128\ \pi^5 N_A\ n^4} \int_0^\infty I_D(\lambda)\varepsilon_A(\lambda)\lambda^4 d\lambda$$

Due to the dipole nature of the energy transfer, the relative orientation κ^2 of both transition-dipole-moments affects R_0. For two freely rotating dipoles the orientation factor is $\kappa^2 = \frac{2}{3}$. Typical FRET pair feature R_0 in the range of 5-7 nm, hence limiting FRET to distances of 2-10 nm.[128] While FRET is very sensitive within its working range, measuring larger distances requires other approaches. One possible approach features the modification of the dynamic range of FRET by placing multiple FRET dyes in a sheet.[129] The extension to a 2D layer decreases the dimensionality of FRET up to a fourth power law allowing larger distances to be measured. However, FRET is commonly used to measure the distance of two position labeled with single dyes. In these kinds of experiments, the approach of adding multiple dyes in order to reduce the dimensionality of FRET is not feasible.

2.7 Graphene Energy Transfer

Another approach to extend FRET is the use of other types of acceptor molecules. In contrast to fluorescent dyes, quencher convert the energy non-radiatively to heat. Dark acceptor molecules can improve concentration and multiplexing limitations of FRET.[128] However their working distance remains limited comparable to FRET with two fluorescent dyes. To extend the working distance of the FRET mechanism, the 2D layer approach would synergistically couple with dark quenchers as acceptors molecules. While this could be designed in bottom-up approach e.g. using DNA origami, graphene is an ideal material to synergistically combining both approaches (Figure 14 A).[62, 63, 64, 130]

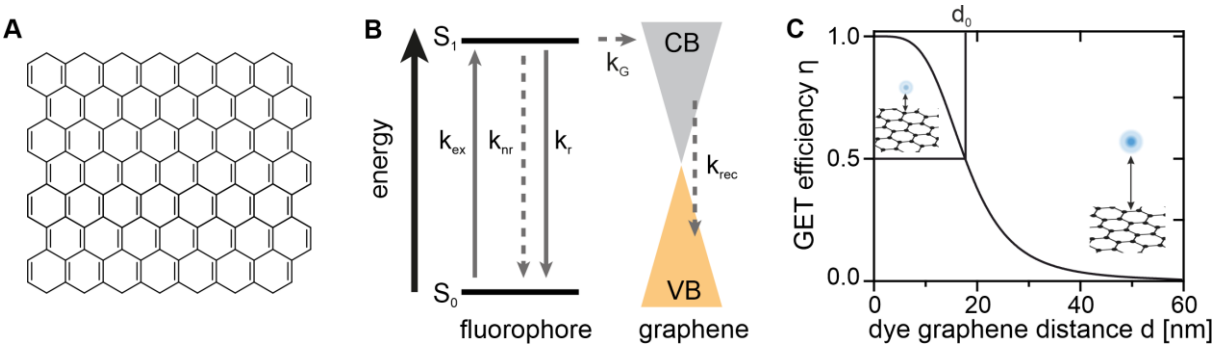

Figure 14: A) Chemical structure of a graphene carbon lattice. B) Simplified Jablonski diagram in presence of graphene. Graphene additionally depopulates the excited state of the fluorophore S_1 with a non-radiative rate k_G. The exciton transfers to the conduction band of graphene, from where it recombines non-radiatively. C) Distance dependence of the GET efficiency for ATTO542 with a 50% quenching distance d_0 of 17.7 nm.

Here, graphene introduces an additional non-radiative rate k_G for the donor dye, depopulating the excited state of the donor (Figure 14 B). This graphene energy transfer (GET) is in analogy to FRET, as the depopulating rate k_G is strongly dependent on the graphene-dye distance d. However, graphene acts as a dark quencher, and the graphene exciton recombines non-radiatively.[131, 132, 133] Graphene is a 2D material, hence acceptor transition-moment-dipoles are orientated along the 2D surface, causing a fourth power law (Figure 14 C).[62, 133, 134] The GET efficiency η can be described with a 50% quenching distance d_0:

$$\eta = \frac{k_G}{k_r + k_{nr} + k_{ISC} + k_G} = \frac{1}{1 + \left(\frac{d}{d_0}\right)^4}$$

With a 50% quenching distance d_0 of around 17-18 nm, the working range of graphene covers dye-graphene distances of 3-35 nm.[62] As GET is a dipole-dipole interaction, the transition-dipole-moment orientation of the donor is important and causes a shift of the d_0 value.[62, 63] Hence it is important to also consider the transition-dipole-moment orientation of the donor dye.

2.8 DNA origami

In order to validate and characterize new methods, like MINFLUX or GET, reference structures with spatial features of few nanometer in three dimension are needed.[78, 80, 135] This can be realized using the DNA origami technique introduced in 2006 by Paul Rothemund.[81]

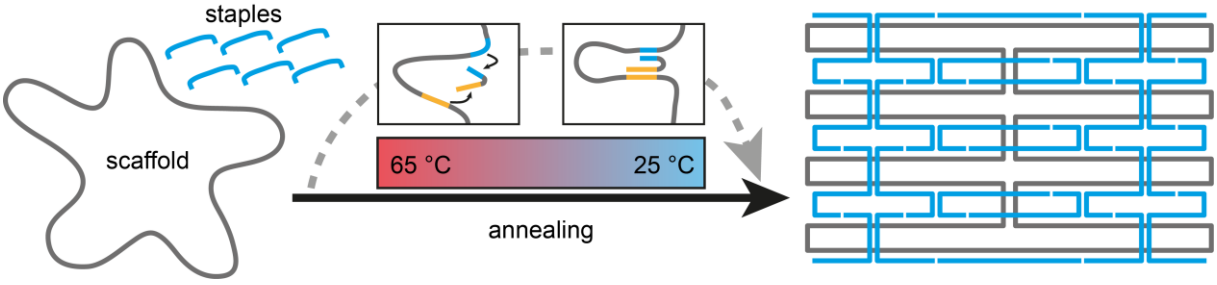

Figure 15: Principle of DNA origami folding. A circular ssDNA scaffold strand (grey) is mixed with shorter ssDNA staple strands. During a temperature ramp, the staples anneal to their designed complimentary (blue and yellow) scaffold position. After the annealing process, a DNA origami structure in a designed 2D shape is formed. From [98].

DNA origami utilizes the fact that two respective complementary nucleotides (nt) adenine (A) and tymine (T) or cytosine (C) and guanine (G) can hybridize and form base pairs via stacking. To this end a 7000-8000 nt long single stranded (ss) circular virus DNA is used as a scaffold (Figure 15). The scaffold is folded into a designed shape by use of ≈200 short (≈60 nt) single stranded staple strands. These

staple strands are complementary to segments of the scaffold, and by use of crossovers between helices, the scaffold is folded into the designed shape. For the design and visualization of the DNA origami structure, the open-source software caDNAno is used.[136]

To ensure correct folding of the DNA origami structure, a buffer containing magnesium ions is used to shield the negative charges of the DNA backbone. The final folding mixture consists out of the scaffold, the buffer and an excess of staple which is heated to 65°C. A slow cooling ramp to room temperature ensures that the domains and hence the overall structure of the origami can form correctly.[137] Depending on the dimensionality of the structure, this temperature ramp can be done within an hour for simple 2D origami or can take up to days for more complex 3D origami.

3. Materials and Methods

The heart of this thesis is a pulsed-interleaved MINFLUX (pMINFLUX) setup. pMINFLUX is based on a confocal microscope and centers around the detection of photons excited by laser pulses, interleaved in the nanosecond time domain. Thus time-correlated single photon counting (TCSPC) is introduced first, which lays the foundation for pMINFLUX. To validate and characterize the setup, fluorescence trajectories of individual immobilized DNA origami structures were acquired. Depending on the measurement, buffers were chosen to either stabilize fluorophores using ROXS or enable stochastic on-off switching by radical blinking or DNA-PAINT.

3.1 Concept of TCSPC and Fluorescence Lifetime

Already 1972 time correlated single photon counting (TCSPC) was used to measure fluorescence lifetime together with photomultipliers.[138, 139] Nowadays in single molecule spectroscopy, a fluorescent dye is excited by a pulsed laser and the emitted single photons of the fluorescence are detected by an avalanche photodiode (APD). TCSPC measures the time between and the output pulse of the APD and the laser excitation pulse. The difference is typically referred to microtime and is in the picosecond to nanosecond regime. Beside the microtime, TCSPC units also tags the absolute time from the beginning of the experiment, which corresponds to the macrotime and the channel, relating to the APD the photon was detected on.

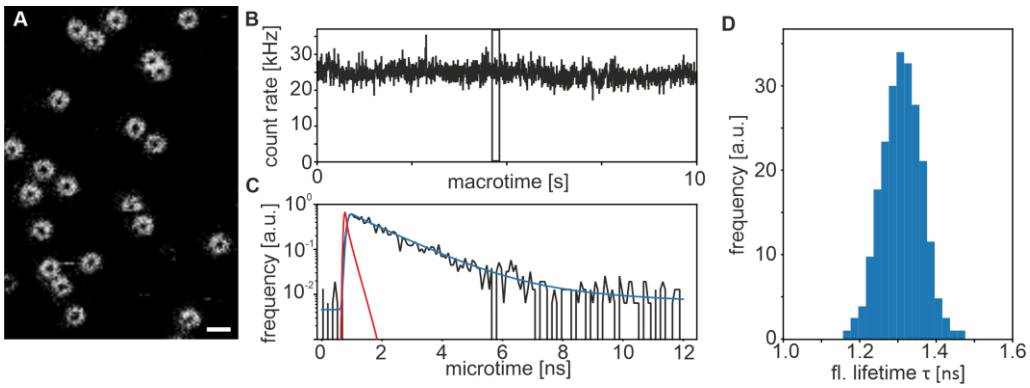

Figure 16: Concept of TCSPC and fluorescence lifetime fitting. A) Example of a confocal scan image with a vortex beam of immobilized DNA origami structures. The scale bar is 500 nm. B) An exemplary fluorescence trajectory of a single fluorophore. The black box indicates the photons used for the microtime histogram in panel C. C) Microtime histogram of the photons indicated in panel B. The black line indicates the histogram. The red line is an IRF and in blue is an IRF reconvonvoluted fluorescence lifetime fit with an additional background function. D) Fluorescence lifetime histogram. This histogram is created by binning and fitting each bin of panel B.

For immobilized samples, a confocal scan is performed first (Figure 16 A). Then individual fluorophores are picked and individual fluorescence intensity traces are measured, which can be binned according to their macrotimes (Figure 16 B). The fluorescence lifetime is extracted by the fit over the histogram of the microtimes (Figure 16 C). As the fluorescence lifetime is in the ns regime, the instrument response function (IRF) also has to be considered. To this end an adapted fit model is used in which the exponential decay is convoluted with the IRF. The IRF has to be known a priori, thus it needs to be independently measured. By extracting the fluorescence lifetime for each bin of the full fluorescence trace, a fluorescence lifetime histogram is created (Figure 16 D). The width of this histogram, hence the precision of the lifetime estimation, is dependent on the number of photons, but also on the background level, the repletion time and the lifetime itself. An estimation can again be given by the lower Cramer-Rao bound for the fluorescence lifetime.[A,140]

[A] As the complete formula of the Cramer-Rao bound is long, it will only be referenced here.

3.2 Pulsed interleaved MINFLUX

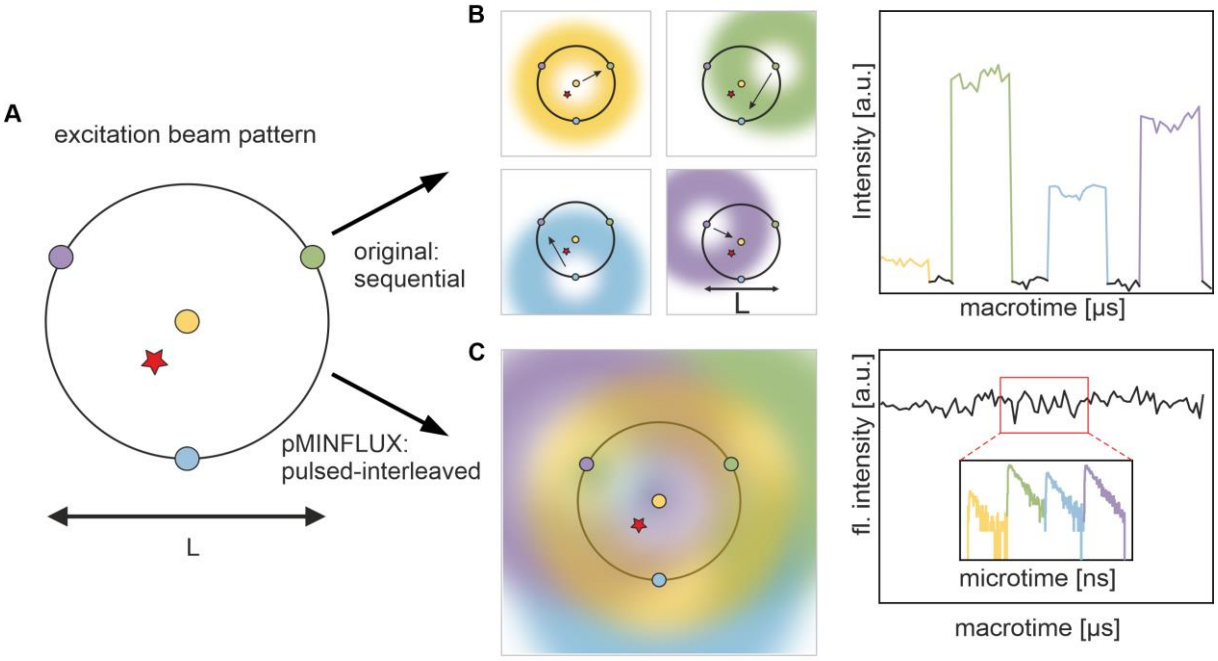

Figure 17: Principle of pulsed interleaved MINFLUX. A) Excitation beam pattern of 2D MINFLUX. The red star represents the position of a fluorophore. B) MINFLUX performs a sequential displacement of a single beam and reads the fluorescent response out of the µs or ms binned fluorescence trace. C) In pMINFLUX, four individual vortex beams with a fixed spatial and temporal displacement are pulsed-interleaved and create the EBP. The fluorescent response is read out of the microtime histogram.

In MINFLUX the fluorophore is localized, by exciting the dye with displaced vortex beams and measuring the fluorescent response (Figure 17 A). Originally Balzarotti *et al.*[65] displace the vortex beams sequentially by two electro-optical deflectors and the emission information was extracted from the fluorescence intensity trace (Figure 17 B). In this work, pulsed-interleaved MINFLUX (pMINFLUX) was developed (Figure 17 C, Chapter 4.3).[141] In pMINFLUX, each excitation in the EBP is an individual vortex beam. The vortex beams are pulsed-interleaved and the corresponding fluorescence emission information is then extracted out of the microtime histogram. This is advantageous in two aspects: On the one hand during the measurement no beam must be actively displaced, making pMINFLUX simpler. On the other hand, pMINFLUX intrinsically gets access to the fluorescence lifetime information.

In this thesis a dual color pMINFLUX setup was built (Figure 18). The setup is controlled with an extensive self-written python software. At the heart of the pMINFLUX system is a pulsed white-light source with a repetition rate T = 19.5 MHz. The light is split into three beams: the infrared (IR) light, which is used for drift correction and two excitation paths with green and red light. An accousto-optic tunable filter (AOTF) is used to switch the excitation color of pMINFLUX to either green, red or both.

For pMINFLUX, the red and green paths are split spectrally with a dichroic mirror. The green light then is then split with three 50:50 beam splitters into four beams and each is coupled into a fiber individually. The four fibers are different in length resulting in time delays of $\Delta t = T/4$, such that all four beams are delayed evenly within one repletion of the laser. After decoupling the beam from the fiber, three additional 50:50 beam splitters are used to recombine the four pulsed-interleaved beams. In the following common path, a vortex phase plate (VPP) and polarization optics (pol) are used for the generation of the m = 1 vortex mode.

An independent second beam path for red MINFLUX illumination is built in analogy to the green. After the polarization optics, the three laser paths, IR, green and red, are recombined using dichroic mirrors.

With a high NA objective, the light is then focused on the sample which can be moved using an 3D Piezo stage. A dichroic mirror is used to split the fluorescence from the exciting light. A pinhole blocks the off-axis fluorescence by optical sectioning, increasing SBR. The fluorescence is afterwards split onto two APDs used for the multimodal detection e.g. via a dichroic mirror to differentiate between green and red fluorescence.

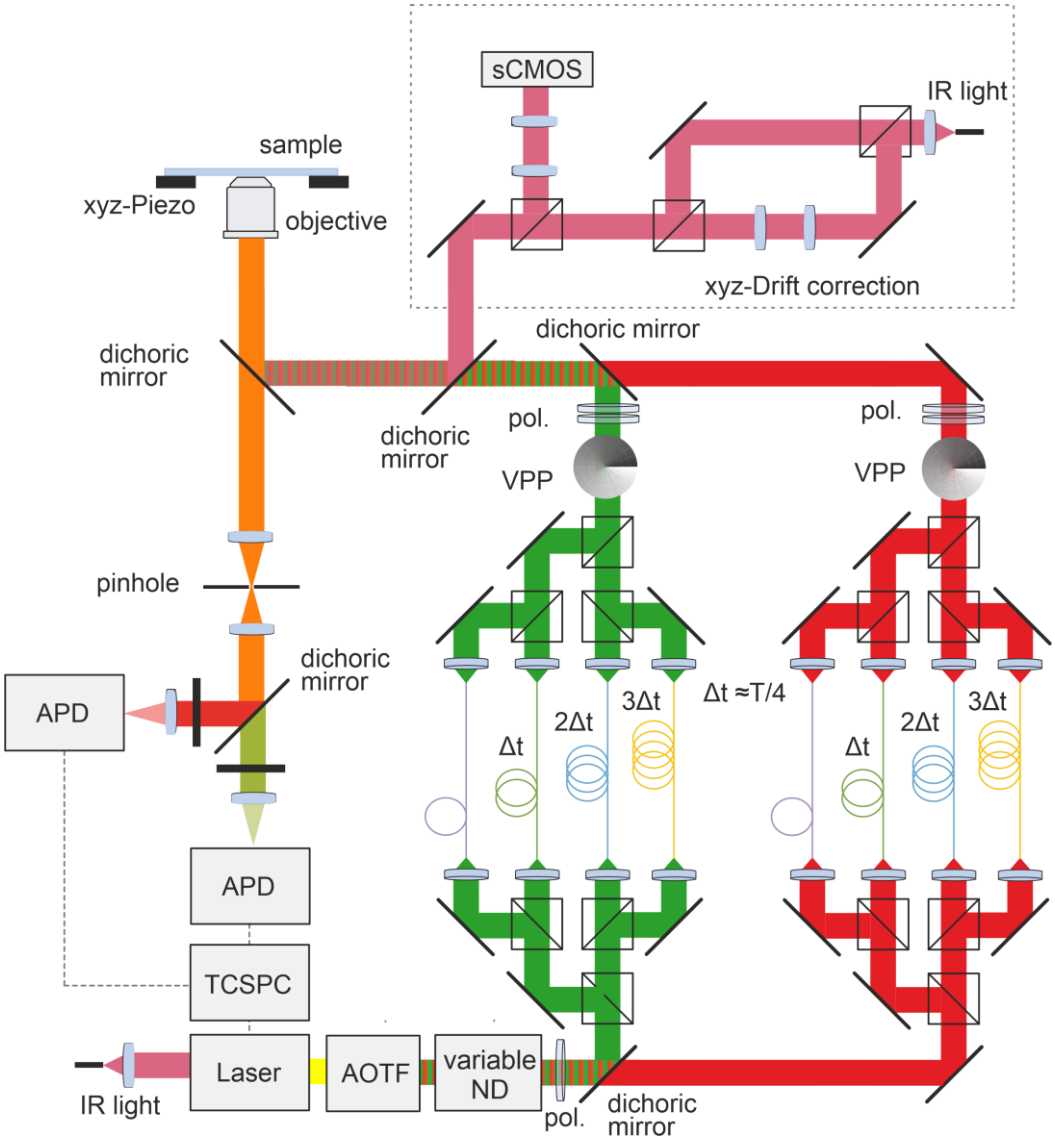

Figure 18: Simplified schematic drawing of the dual color pMINFLUX setup built in this thesis. T is the repetition time of the pulsed white-light laser, VPP vortex phase plate, and pol. Is a combination of λ/2 and λ/4 wave plates for circular polarization.

As MINFLUX achieves localizations with nanometer precision, a xyz-drift correction is needed. To that end the IR light is used in combination with a sCMOS camera. The IR beam is split into two more paths: a confocal path and a wide-field path. The IR confocal beam is reflected in an angle on the sample and can be used for z-drift correction. For xy-drift correction, the IR wide-field path is used to track scattering gold nanorods which act as fiducial markers in the sample. The scattered light of the nanorods, as well as the reflected confocal beam are detected on the same sCMOS camera.

3.3 DNA-PAINT

Typically, stochastic-switching methods such as (d)STORM or blink microscopy rely on induced blinking of the dye. However, such methods lack resolution, as the photon budget is split on multiple localizations. For localizations with a high precision commonly DNA-PAINT is used. In contrast DNA-PAINT prefers photostable dyes, as the stochastic switching of the fluorescence signal is induced by the transient binding of a fluorophore-modified imager strand to a docking strand (Figure 19 A). Here, the imager strand and the docking strand are ssDNA strands, which are reverse-complementary to each other. By hybridization, freely diffusing imager strands can bind to the target, resulting in an “on”-event. As the imager strand, thus the dye, is regenerated the photon budget of an individual fluorophore does not have to be split on multiple blink events. This leads to a higher localization precision compared to e.g. (d)STORM or blink microscopy. The length and sequence of the complementary sequence is chosen such that this hybridization is transient. Consequently, the imager strand can dehybridize resulting in an “off”-event.

The hybridization event is stochastic, and the hybridization rate depends on many factors. One major contribution is the concentration of the imager strand. With more imager strands in solution, the probability of binding increases, hence more on-events in the same timeframe are expected. On the downside more imager strands result in a higher fluorescent background. Due to the excitation with a minimum, this is in particular problematic for MINFLUX. Beside the imager strand concentration, an optimization of buffer conditions and sequence have also shown to increase the hybridization kinetics.[142]

It has been shown that overlapping repetitions on the docking site further increases the binding kinetics to a factor of additional docking motifs (Figure 19 B).[143] Beside an increase in speed, multiple docking sites increase the redundancy within a docking site. This enables a more complete sample frequency as errors in the sequence of the binding site do not lead to a loss of hybridization at the binding site.

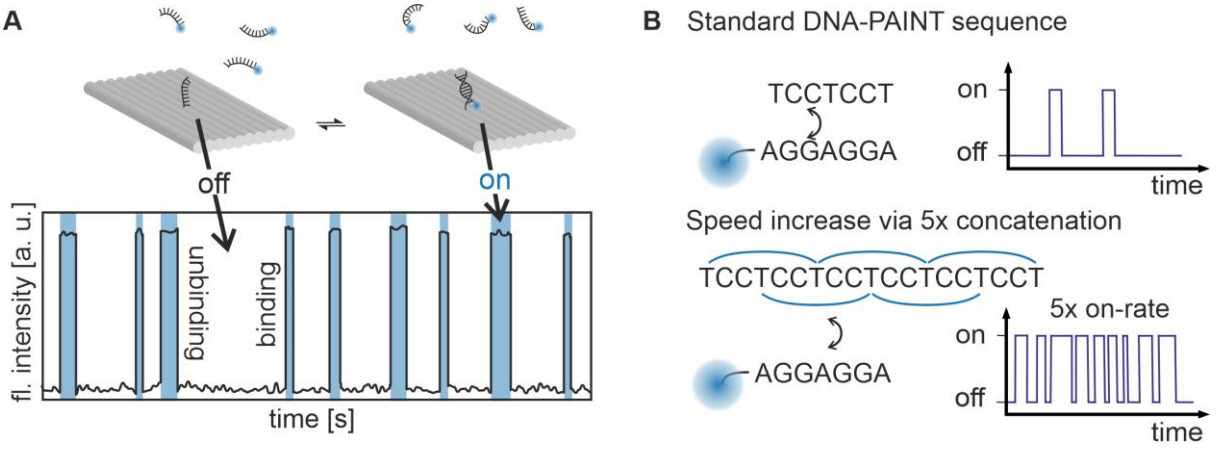

Figure 19: Principle of DNA-PAINT. A) Schematic overview of DNA PAINT on a DNA origami. Imager strands, modified with a fluorescent dye (blue) can transiently hybridize to a docking site. The resulting fluorescence intensity trace exhibits corresponding on and off states. B) To increase the speed of DNA-PAINT, the docking site can be extended with multiple repetitions of the binding sequence.

3.4 Experiments with DNA Origami Structures

DNA origami structures are used for a broad range of applications in super-resolution. A comprehensive review of the use of DNA origami for super-resolution microscopy is given in the publication corresponding to chapter 4.1.

In this work DNA origami structures act as a benchmark tool for the accuracy and precision of pMINFLUX, but also as a tool to validate the new methodology developed in this work. As a benchmark for the validation of pMINFLUX, traces of fluorescent dyes at fixed positions are needed, hence DNA origami structures are immobilized (Figure 20). For this self-built flow chamber are first cleaned with Hellmanex®. After washing, the glass surface is covered with bovine serum albumin (BSA). This on the one hand passivates the surface, on the other hand creates a homogeneous nano environment for the DNA origami structure. For a controlled immobilization of DNA origami structures a biotin-NeutrAvidin-biotin coupling is used. To that end, the BSA is stochastically modified with biotin, such that every ≈15th BSA molecule is modified. By use of NeutrAvidin with its four biotin binding pockets, the immobilized BSA-biotin on the surface can be connected to biotin modified staples of the DNA origami. This enables an orientation-controlled immobilization of the origami. Next, gold nanorods are immobilized to the surface providing as fiducial markers for the pMINFLUX measurement.

Last the appropriate imaging buffer is added. For measurements, where a stable fluorescence trace is desired, a ROXS buffer with Trolox/Trolox quinone is used in combination with protocatechuic acid (PCA) and protocatechuate dioxygenase (PCD) as an oxygen scavenging system. [108, 109, 144] For stochastic blinking via radical blinking, also called blink microscopy, a buffer consisting of glucose oxidase catalase and glucose as an oxygen scavenger system, beta-mercaptoethanol (β-ME) as a reduction agent and cyclooctatetraene as a triplet quencher is used.[110, 112] For stochastic blinking via DNA-PAINT or local-PAINT (L-PAINT) an ROXS buffer of Trolox/Trolox quinone and PCA/PCD as an oxygen scavenging system is used.

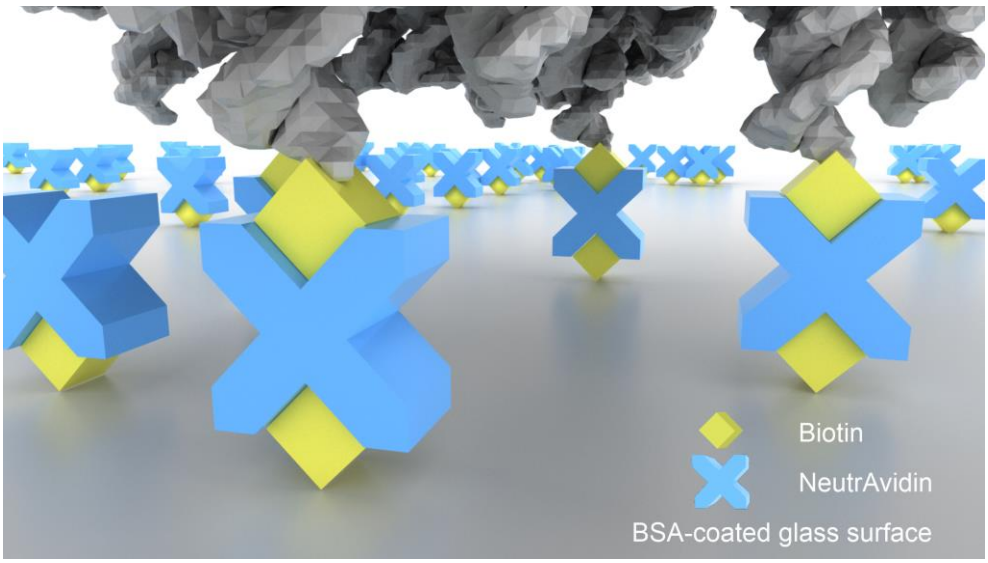

Figure 20: DNA origami structures immobilized by BSA-biotin-NeutrAvidin-biotin coupling. The glass is coated with BSA which is stochastically modified with biotin.

4. Publications

4.1 DNA origami nanorulers and emerging reference structures

Michael Scheckenbach*, Julian Bauer*, **Jonas Zähringer*,** Florian Selbach, and Philip Tinnefeld

(* equal contribution)

APL Materials 8, 110902 (2020); DOI: 10.1063/5.0022885

Novel developments in light microscopy require experimental demonstration and benchmarking. Historically, filamentous structures such as actin filaments or microtubule were used for super-resolution microscopy. However, such biological systems are prone to variation, which result in fluctuations of the molecular environment. The resulting dependence on the protocol, the linker and the markers leads to problems in the reproducibility. An accurate standard for the characterization of SR techniques should have control over the stoichiometry as well as the fluorophore position. The DNA origami technique as a breadboard for modifications such as fluorophores fulfills those requirements. With the placement of modifications such as fluorophores with nanometer precision on DNA origami structures can serve as a universal tool for microscopy.

In the associated review (Appendix 7.1), applications of DNA origami structures as nanoruler are discussed. A special focus lies on applications for super-resolution techniques. Nanoruler are used for distance measurements in two or three dimensions, as correction tool for multicolor-SR microscopy and as a tool to demonstrate novel developments of SR such as MINFLUX with resolutions of a few nanometers. DNA origami structures enable the investigation of energy transfers to plasmonic nanoparticles, gold surfaces and graphene surfaces. The defined stoichiometry of dye modifications also allows DNA origami structures as brightness rulers needed for novel applications of chromophore counting or as a calibration for smartphone-based microscopy. But applications lie even beyond optical microscopy, e.g. as a standard for AFM.

All in all, nanoruler of DNA origami structures offer a broad range of applications as reference structures. Their defined but designable properties make them an ideal tool in the development of novel microscopy methods.

4.2 The Art of Molecular Programming – Optical Control

Jonas Zähringer, Michael Scheckenbach and Philip Tinnefeld

Book chapter accepted.

Light has many avenues to interact and control with nanostructures. Typically, light is used as a tool to image structures using fluorophores. However, beside fluorescence of fluorophores many other light-matter interactions exist which can be exploited to optically control nanodevices. The associated book chapter (Appendix 7.2) highlights different interactions between light and matter on the nanoscale.

Fluorophores are the most common reporter to generate an optical output signal. In fluorescence microscopy, fluorophores are utilized to image dynamics or structural features. However, depending on the environment, such as plasmonic nanoparticles or other fluorophores their fluorescent response can be controlled. This depends on the exact, nanometer precise placement of the fluorophore. To assemble structures in a nanometer-controlled way, DNA origami structures are the tool of choice. With the nanometer precise placement, the interplay between components can be well controlled. Commonly used examples of optical active materials are plasmonic nanoparticles. The proximity of plasmonic particles leads to a coupling of their localized surface plasmons, which can create easily detectable plasmonic shifts as well as several other effects. Depending on the shape and arrangement, plasmonic nanoparticles can enhance the fluorescence or even steer the direction of the fluorescence emission as a nanoantenna.

By use of other optically active modifications, the mechanic state of DNA nanodevices can be optically control. Commonly used are azobenzenes, which under exposure of UV or visible light switch their conformation from the cis- to trans-state respectively. Thus, using photoinduced hybridization and dissociation DNA nanodevices can reversibly switch between a closed state, locked by the duplex formation of trans-azobenzene DNA, and an open state after strand dissociation. Such azobenzene-modified DNA devices were employed as building blocks to design photo-switchable supramolecular self-assemblies at the micrometer scale. Another domain of photo-active modifications is the photo-cleavable o-nitrobenzene. An optical input in form of UV light can break the photo-cleavable, with which cargo is fixed to a DNA nanodevice. The optical input controls the time and space at which cargo is released.

In a nutshell, light can be used as a tool in a variety of applications. By decorating DNA origami structures with light sensitive modifications, a toolbox is created to design and control interactions at the nanoscale.

4.3 Pulsed interleaved MINFLUX

Luciano A. Masullo*, Florian Steiner*, **Jonas Zähringer**, Lucía F. Lopez, Johann Bohlen, Lars Richter, Fiona Cole, Philip Tinnefeld, Fernando D. Stefani
(* equal contribution)

Nano Letters, 2021, 21, 840-846 (**2021**) DOI: 10.1021/acs.nanolett.0c04600

With MINFLUX, super-resolution microscopy routinely accesses length scales of 1-2 nm, the size of a fluorophore. This enabled the tracking and imaging with unprecedented precision in light microscopy. However, while MINFLUX can investigate structures with high precision, it comes at the cost of high technical complexity. In a MINFLUX setup, the fluorophore position is interrogated by a sequence of four spatially displaced excitations with a vortex beam profile. Originally, Balzarotti *et al.* steered a single vortex-beam beam sequentially in the micro- to millisecond timescale. This fast displacement is performed with electro-optical deflectors and FPGAs which introduces an high technological complexity and reduces the accessibility of MINFLUX.

In the associated publication (Appendix 7.3), we realized a novel approach to facilitate a simpler implementation of MINFLUX. With a pulsed-interleaved excitation scheme for MINFLUX (pMINFLUX), four displaced vortex beams at fixed positions can be used, thus simplifying the setup. Here, the fluorescence intensity respective to each vortex beam is extracted via the TCSPC histogram. pMINFLUX improves MINFLUX in two aspects: On one hand, the technological complexity is reduced, as no beam steering optics are needed. On the other hand, pMINFLUX intrinsically provides access to the fluorescence lifetime information.

To demonstrate the pMINFLUX concept, I built a pMINFLUX setup with green excitation. I first characterized the accuracy and precision of the setup. For the benchmark of the precision, I localized an individual ATTO532 fluorophore fixed to a DNA origami. pMINFLUX follows the expected photon efficient precision inherent to the MINFLUX concept. With 1000 photons precisions of ≈ 1-2 nm were demonstrated which are on par with the theoretical precision predicted by the Cramer-Rao bound and two orders of magnitude more photon efficient than camera-based SMLM techniques. For accuracy, a GattaBead® with multiple ATTO542 fluorophores was displaced in a grid of 10 nm steps. The resulting grid is localized with an accuracy of ≈1 nm. Therefore, pMINFLUX reaches accuracies and precisions of ≈1 nm comparable to the original MINFLUX system.

Next, I combined pMINFLUX with blink microscopy as a mean for super-resolution. To this end I designed a DNA origami structure with three dyes in a triangular pattern in 12 nm distance. By using a reducing buffer, the fluorophore is switched to long-lived radical states and providing stochastic on-off blinking needed for super-resolution microscopy. The localization of on-events in pMINFLUX resolves the triangular arrangement of dyes with 1-2 nm precision. Besides the precision, pMINFLUX provides also the fluorescence lifetime information. Hence, by combining the fluorescence lifetime information for each localization, a super-resolved fluorescence lifetime image (FLIM) with nanometer precision is generated.

Last the fluorescence lifetime information is used as an identifier for multiplexing. To this end I designed a dynamic DNA origami. Here, a fluorescently marked pointer strand is transiently hybridizing to two binding sites, distanced 12 nm. I designed two DNA origami structures, differing in their

fluorescence lifetime and their kinetic fingerprint of the transient hybridization. One type of structure incorporates a Cy3B fluorophore with a fluorescence lifetime of $\tau_{fl} = 2.6\,\text{ns}$ and a complimentary sequence of 7 nt, while the other has an ATTO542 fluorophore with $\tau_{fl} = 3.2\,\text{ns}$ and an 8 nt complimentary sequence. With pMINFLUX, I could distinguish both types of structures according to their fluorescence lifetime, which was independently confirmed by the kinetic information.

In summary, pMINFLUX simplifies the technological complexity of a MINFLUX setup, while intrinsically probing the fluorescence lifetime domain with nanometer precision. This unique combination lays the foundation for a broad range of novel applications.

4.4 Combining pMINFLUX, Graphene Energy Transfer and DNA-PAINT for Nanometer Precise 3D Super-Resolution Microscopy

Jonas Zähringer, Fiona Cole, Johann Bohlen, Florian Steiner, Izabela Kamińska, Philip Tinnefeld

Light: Science and Applications, 70 (**2023**) DOI: 10.1038/s41377-023-01111-8

Open Access Article

Up until here, super-resolution only in lateral direction was contemplated. While it is conceptually straightforward to extend MINFLUX to 3D, the technical complexity increases with dimensionality. 3D tophat beams are used which beam profiles need to be either assumed ideal or their shape measured in 3D with nanometer precision and without photobleaching.[85] Additionally the vortex beam needs to be displaced along the axial direction, where photons of the axial displacements only contribute significantly to axial localizations, thus splitting the photon budget.

Here, the fluorescence lifetime intrinsic to pMINFLUX facilitates the use of graphene energy transfer (GET) for axial localizations. By measuring the fluorescence lifetime, the energy transfer to the graphene surface, thus the axial distance can be determined. In synergy with the lateral localization of pMINFLUX this enables 3D super-resolution with high precision in all three dimensions. Other metal induced energy transfer (MIET) with materials like gold induce a significant amount of scattering, which in combination with the low signal background ratio of MINFLUX are not suitable.

In the associated publication (Appendix 7.4), I experimentally characterized GET-pMINFLUX using DNA origami with fixed dyes at different heights demonstrating axial precision below 0.3 nm at moderate photon counts of 1000 photons. To show the applicability for super-resolution imaging, distances smaller than 3 nm were resolved with down to 0.4 nm axial precision using DNA-PAINT. DNA-PAINT is chosen due to its applicability to resolve small distances. By use of hybridization of a modified imager strand with a fluorophore attached to it, only one dye is bound at the same time. Consequently, no interaction between dyes can occur. This is in contrast to other stochastic-switching approaches with fixed dyes such as blink microscopy, where two dyes in proximity below 10 nm can couple and reactivate each other, hence no temporal separation hence spatial resolution is possible.

A major drawback of DNA-PAINT is that high imaging speeds require high concentrations of imager strands. The situation is aggravated by the confocal nature of MINFLUX which calls for fast binding kinetics to speed up imaging which comes at the cost of a high fluorescent background. Additionally, the MINFLUX excitation is performed in the minimum of the vortex beam, leading to low signal background ratio, making fast imaging speeds unfeasible. However, as MINFLUX is optimized for photon efficient localizations, it does not need the regenerated photon budget of DNA-PAINT for a single localization with nanometer precision. The photon budget can thus be distributed on multiple binding sites. Subsequently, local-PAINT (L-PAINT) is developed which is an alternative super-resolution technique optimized for the efficient localization of multiple binding sites. L-PAINT introduces a hierarchy of two binding sequences, which enables an imager strand to scan the local environment for binding sites. Using GET-pMINFLUX, L-PAINT is demonstrated experimentally on DNA origami structures with less than two nanometer precision in 3D. As a result, GET-pMINFLUX is used to resolve a 6 nm triangular structure of L-PAINT binding sites in 3D in under 2 s.

In brief, GET-pMINFLUX enables ultraprecise 3D localizations which with the help of DNA-PAINT also translates in 3 nm resolution. As GET-pMINFLUX is very photon-efficient, I developed L-PAINT to enable fast scanning of dense clusters.

4.5 Super-Resolved FRET and Co-Tracking in pMINFLUX

Fiona Cole*, **Jonas Zähringer***, Johann Bohlen, Tim Schröder, Florian Steiner, Fernando Stefan and Philip Tinnefeld

(* equal contribution)

bioRxiv 2023.03.24.534096; DOI: 10.1101/2023.03.24.534096

With the advent of nanoscopy methods such as MINFLUX, MINSTED or RASTMIN, localization precisions of the size of the reporter fluorophore are possible. These methods were applied to image structures as well as to track single fluorophores. While MINFLUX is able to give insight into structural distribution of e.g. proteins or the movement of motor proteins, only individual dyes are imaged. Thus, the interplay with the environment remains unknown. Multiplexed MINFLUX was demonstrated for imaging using spectral splitting or Exchange-PAINT, but the simultaneous tracking remains restricted to single fluorophores.

In the associated publication (Appendix 7.5), the fluorescence lifetime enables a novel approach for multiplexed localization on the nanometer length scale. In combination of pMINFLUX with FRET, the correlated measurement of nanometer precise tracking of a donor dye and simultaneously the distance to an acceptor becomes possible. Multilateration even enables the nanometer precise co-localization of both dyes without photo-switching, as it is experimentally demonstrated in the associated publication.

However, FRET has a small dynamic range of <10 nm. Dynamics occurring at larger distances cannot be visualized by FRET-pMINFLUX, hence leaving many relevant biological dynamics such as protein-protein interactions in dimerization or multicomponent molecular machineries occurring at larger distances out of reach. A dual-color MINFLUX approach could independently track both dyes simultaneously over a large working range. However, such a dual-color MINFLUX approach is technologically not straightforward. On the one hand, a second color will make the already complex MINFLUX even more complex, thereby reducing accessibility of such a setup further. On the other hand, the overlap of dual color MINFLUX needs to be stable with nanometer precision. This makes a dual MINFLUX system even more prone to instabilities of drift and misalignment of the independent beams used for MINFLUX excitation, as shown already for STED microscopes. Hence it is sensible to explore simultaneous localization of two spectrally similar fluorophores with pMINFLUX without photo-switching.

To this end, pMINFLUX lifetime multiplexing is developed. Outside the FRET range, the fluorescence lifetime is used to assign the detected photons emitted from two fluorophores with similar emission spectrum, but different fluorescence lifetimes. Using a biexponential lifetime fit, the photon numbers for each emitter and each displaced illumination is extracted which is then used to localize two dyes simultaneously. The co-localization is demonstrated in simulations and experiments on DNA origami structures. As a high fluorescence lifetime contrast is required, the DNA origami structures are designed with Alexa Fluor 647 (AF647) and ATTO647N which have a fluorescence lifetime of 1.1 ns and 4.3 ns respectively. First, both dyes are placed in a fixed distance of 15 nm, which are recovered with better than 2 nm precision and better than 1 nm accuracy. Only a loss of precision of 40 % due to the photon assignment with a biexponential fit compared to the localization with a single emitter is observed. Next, we demonstrate the multiplexing approach using two dynamic L-PAINT pointer systems, which transiently hybridize to two binding sites each. The distances between the binding sites of each pointer of 12 nm were well resolved, and individual kinetics could be extracted. pMINFLUX multiplexing allows individual time resolution for each kinetic, thus giving the flexibility of optimizing spatio-temporal resolution in post-processing.

While pMINFLUX multiplexing enables the simultaneous localization of two dyes beyond the FRET range, the photons emitted within the FRET range cannot be assigned unequivocally to one dye. Consequently, the co-localization inside the FRET range holds systematic errors. To recover the localization inside the FRET range, a combined phasor-microtime gating approach is developed. The positions of both dyes are deduced from the separation distance, the direction of the connecting vector of both dyes and the center of mass of both emitters.

Here, the phasor approach yields the separation distance of both dyes, by measuring the resonant coupling of the two-emitter system. A calibration is performed using multiple distances of the two dyes designed on DNA origami structures. The resulting distance dependence of the geometric mean of the phasor coordinates can be described theoretically by the FRET relation. Experiments and simulations agree well, enabling the nanometer precise distance determination.

In a subsequent step the direction between both emitters is determined by combining the standard pMINFLUX localization algorithm with a microtime-gated detection. Early photons are more likely to be absorbed and emitted by AF647 with a short fluorescence lifetime, while late photons are mostly assigned to ATTO647N, which has a long fluorescence lifetime. Thus, the localizations are displaced towards either AF647 or ATTO647N, respectively for early or late photons, resulting in a vector along the connection of both dyes. By combining the distance information and the directionality information with the center of mass obtained by the localization of all photons, the co-localization of both dyes can be recovered with nanometer precision above distances of 4 nm. The pMINFLUX phasor-microtime gating approach is demonstrated in kinetic Monte Carlo simulations as well as in experiments.

In this publication, we show that pMINFLUX enables the co-tracking via FRET. In a next step we developed a co-localization algorithm, which uses the fluorescence lifetime to recover the photons emitted by each emitter. We demonstrate nanometer precise co-localization of two emitters without photo-switching. Inside the FRET range, a combined phasor microtime-gating approach allows the simultaneous localization. By combining both approaches, the resolution gap between single-molecule FRET and co-tracking is closed, extending the working range for nanometer precise distance determination from 10 nm of FRET up to 100 nm for pMINFLUX lifetime multiplexing.

5. Conclusion and Outlook

This work extends the vista of nanometer precise super-resolution microscopy to the fluorescence lifetime domain. To this end a dual-color pMINFLUX setup was constructed and benchmarked using DNA origami structures. The pulsed-interleaved MINFLUX approach enables the measurement of the fluorescence lifetime on molecular length scales while simultaneously simplifying the technological complexity. The unprecedented combination of fluorescence lifetime and nanometer localization precision was fundamental to a variety of novel approaches developed in this work. They can be grouped into three themes: energy transfer, co-localization and L-PAINT.

5.1 Energy Transfer

The first theme in this thesis was the use and investigation of energy transfers. To enable a technically simple 3D approach, the axial distance information from graphene energy transfer (GET) was combined with the lateral nanometer precise localization of pMINFLUX. GET-pMINFLUX was demonstrated using DNA-PAINT and L-PAINT to resolve structural details of less than 3 nm with axial precisions down to 0.4 nm. In the future, GET-pMINFLUX enables the investigation of cellular processes close to the cover slip with nanometer precision in all three dimensions. Open questions that could be addressed are the study of the arrangement of cellular machineries e.g. in parasites such as of toxoplasma[145] or chaotic biochemical pathways within plants[146, 147].

The second energy transfer investigated in this work was FRET. With the *a priori* known Förster radius R_0 of a fluorophore pair, the fluorescence lifetime was converted to a relative interdye distance. By mapping three positions of the donor and measuring the respective fluorescence lifetime, FRET enables a multiateration of the acceptor fluorophore.

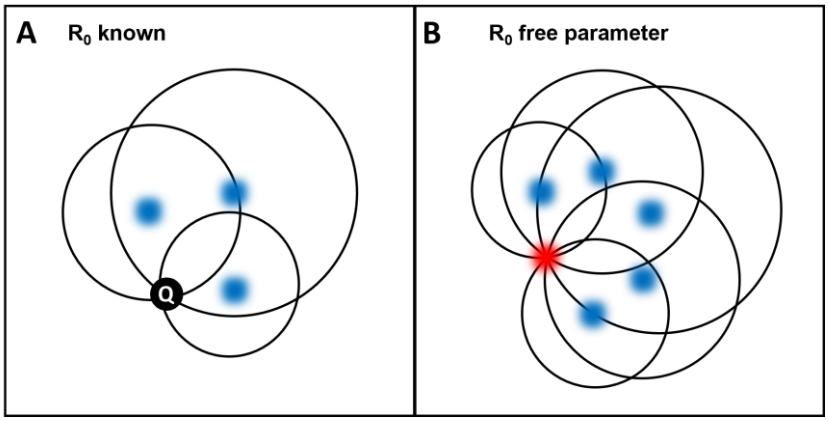

Figure 21: FRET localizations. A) Using multilateration, dark quencher can be localized. With three binding sites, R_0 needs to be known. B) By adding more binding sites, R_0 can be treated as a free parameter in the localization of an acceptor position.

In the future, the combination of pMINFLUX with its nanometer precise localization and the fluorescence lifetime can be used to investigate energy transfers. As only the donor properties, in particular position and fluorescence lifetime are needed, even non-fluorescent acceptors such as quenchers can be localized and investigated without any direct emission (Figure 21 A). By extending the multilateration to more positions, no *a priori* knowledge of R_0 is needed (Figure 21 B). The only requirement is that the energy transfer originates from a single location. R_0 can be determined as a free parameter of the localizations on a single structure. This could simplify prior methods, where the interdye distance was varied employing multiple structures.[148]

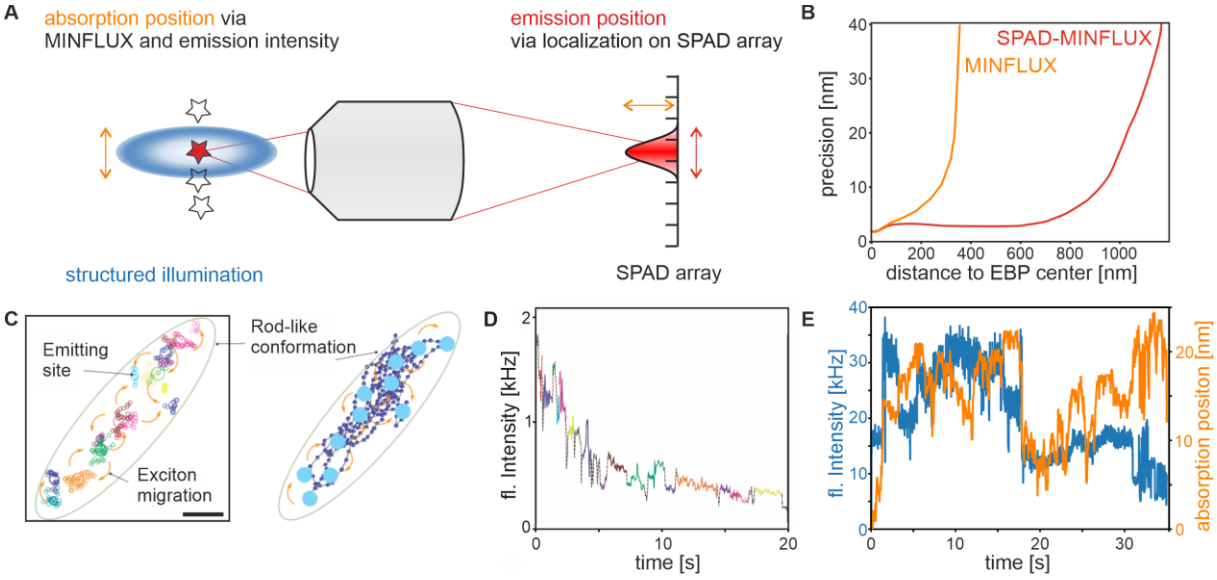

Figure 22: Experiments using a SPAD array as a detector in MINFLUX. A) Schematic of MINFLUX with a SPAD array. B) For an absorption position which equals the emission position, SPAD-MINFLUX enables a larger field of view compared to typical MINFLUX setup. Both simulations were performed with 100 photons per localization. Adapted from [149]. C) Localizations of multiple emitting sites in a conjugated polymer of MEH-PPV. The scale bar corresponds to 20 nm. Adapted from [150]. D) Corresponding fluorescence intensity trace to the localizations of panel C. The color code corresponds to the emitting sites. Adapted from [150]. E) Experimental pMINFLUX data of MEH-PPV polymer. In blue the fluorescence intensity and in orange is the mean square displacement. Correlated jumps of both can be observed.

Further MINFLUX experiments could feature an array of single-photon avalanche diodes (SPAD array) in detection (Figure 22 A).[151] By replacing the single pixel detector with a camera, the position of the emission can be determined similar to SMLM methods. Here, the absorption would be determined via MINFLUX and the emission via the localization of the emission on the SPAD array. If the absorption and emitter position are identical, simulations predict a significant increase in the field of view of MINFLUX (Figure 22 B).[149] This could especially be beneficial for the fast resolution of large structure such as actin filaments using e.g. DNA-PAINT or L-PAINT.

However, if the absorption and emission position are not identical, e.g. due to energy transfer, both can be measured simultaneously and independently. Here, the previously used DNA origami structure for FRET co-localization featuring a L-PAINT system could act as a demonstration. This approach could not only be powerful for life science application but even more so for material science.[152]

Later, this approach could be used to investigate links between the structure and photophysical properties of conjugated polymers such as MEH-PPV.[153] With illumination of the conjugated polymer, photobleaching of individual emission sites occurs by photooxidation. It is known that this leads to a change of emission position which also correlates with a change of fluorescence intensity (Figure 22 C,D).[150, 154, 155, 156] Experimental MINFLUX data suggests that the jump of fluorescence intensity also correlates with a change in absorption position (Figure 22 E). In the future, open structural questions using the change of absorption center position and the emitter position could be investigated, by correlating the absorption position measured via MINFLUX and the emitter position measured via the SPAD array. Additionally, a bleaching step analysis could give more structural information of the conjugated polymers.[157, 158]

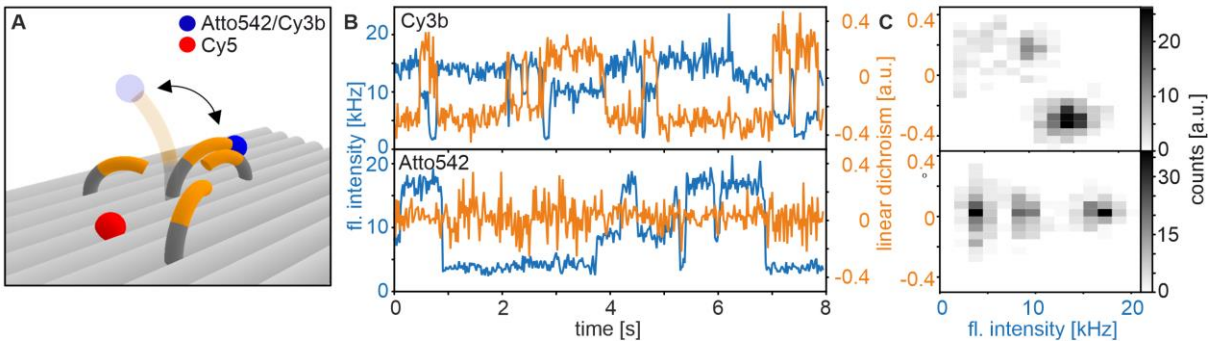

Figure 23: A) FRET pointer system with three binding sites distanced in 6 nm. Adapted from [159]. B) Experimental traces of the FRET pointer system with Cy3b and ATTO542 respectively. The trace shows the fluorescence intensity in blue and the linear dichroism in orange. C) 2D histogram of the fluorescence intensity and the linear dichroism for Cy3b (top) and ATTO542 (bottom) labelled pointer.

Further insight into energy transfer processes of conjugated polymers could be given by polarization measurements such as linear dichroism.[160, 161] Here, the multimodality of the MINFLUX setup can give access to linear dichroism with nanometer precision. Confocal experiments demonstrate that L-PAINT coupled with FRET gives an ideal benchmark structure (Figure 23 A). A clear distinction is found between an ATTO542 pointer with nearly no linear dichroism and a Cy3B pointer which shows a clear correlation between linear dichroism and binding site thus FRET and intensity state (Figure 23 B-C).

5.2 Co-localization

The second theme of this thesis was the use of fluorescence lifetime information to enable the co-localization of fluorophores with nanometer precision without photo-switching inside and beyond the FRET range. Outside the FRET range, a multi-exponential fit recovered the assignment of photons to their respective emitter. As a result, two fluorophores were localized within the same diffraction-limited area without photo-switching with a precision of better than 2 nm. Inside the FRET range, a novel microtime gating-phasor approach was developed to recover the co-localization. By combining both approaches the resolution gap between single-molecule FRET and co-tracking was closed.

In the future, the pMINFLUX lifetime multiplexing beyond the FRET range could be extended to three fluorophores, by use of a phasor-based approach to assign the number of the emitted photons to their fluorophores more efficiently. The multiplexing approach would also benefit with the application of SPAD arrays as detectors. This combination could increase the distance, two fluorophores can be nanometer precisely localized, nearly tenfold to over 1000 nm, two orders of magnitude greater than FRET. Applications of the pMINFLUX multiplexing approach could be the investigation and visualization of the interplay between multiple components. Examples could be the co-tracking of both heads of a motor protein such as kinesin-1. Here, MINFLUX revealed the motion of an individual head, but the direct visualization of both heads remains elusive for photon efficient super-resolution.[162, 163] Another target of interest could be the nuclear pore complex. While the understand of the structure and function progressed, many questions remain. One question could be the interplay of structural features and their interplay with functionality of the diffusion through the nuclear pore complex. [164]

More examples lie in the area of drug delivery. While polyethylenimine (PEI) is a gold standard for the delivery of therapeutic siRNA (small interfering ribonucleic acid) in polycationic drug carrier systems, their interaction is poorly understood, making the optimization by rational design impossible.[165] Here, tracking labelled siRNA packed in PEI polyplexes, can contribute to the understanding of their interplay and open the door for more efficient drug delivery systems.

5.3 L-PAINT

The photon efficiency of novel localization techniques, such as MINFLUX, enabled the development of L-PAINT. L-PAINT introduces a binding hierarchy between docking sites; thus L-PAINT can locally scan dense clusters of docking sites. Due to the high local concentration the imaging is sped-up, as demonstrated on DNA-origami structures. In the future, L-PAINT could be useful for a broad range of applications (Figure 24).

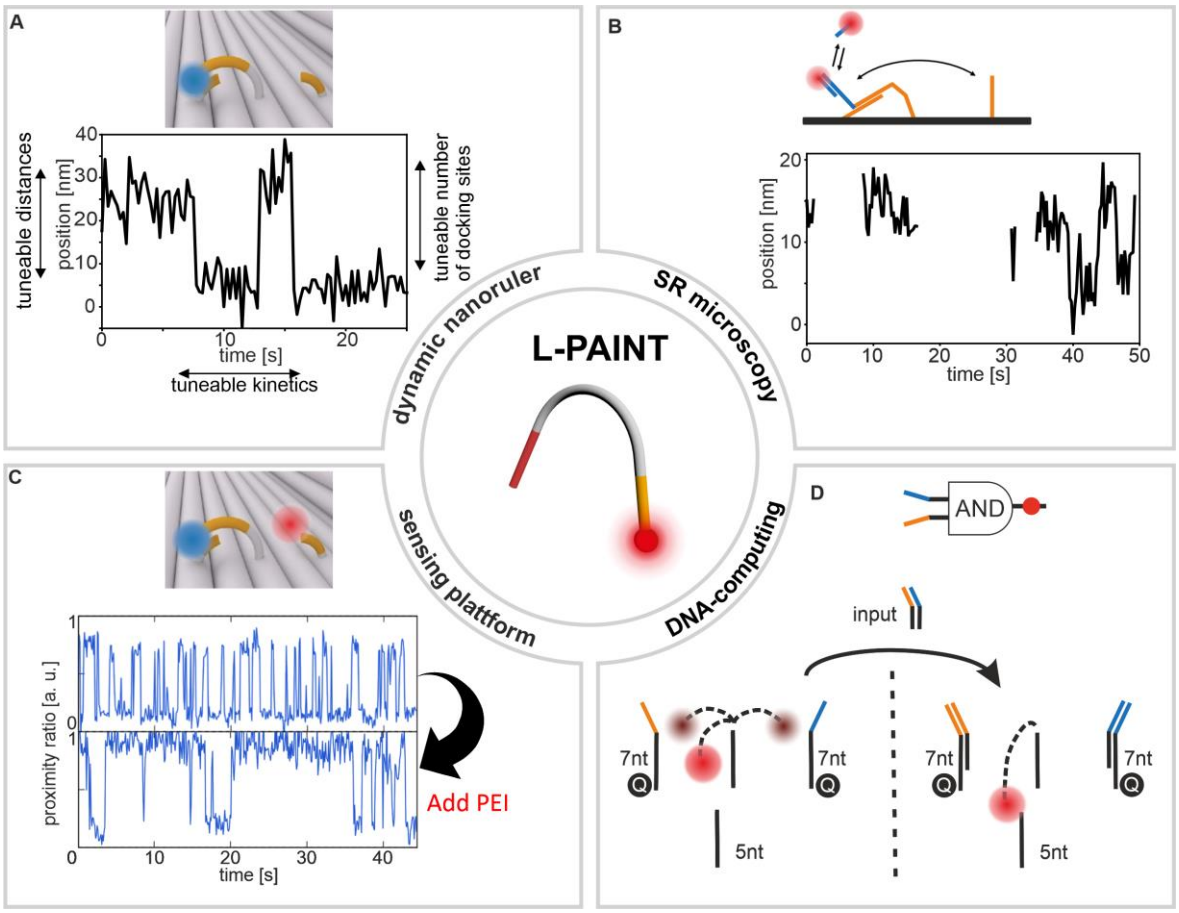

Figure 24: Outlook on the application of L-PAINT. Middle panel: Schematic view of a L-PAINT scanning strand A) Experimental localization data of L-PAINT between two binding sites distanced ≈40 nm. The distance, the kinetics and the number of binding sites for L-PAINT can be tuned. B) Schematic and experimental data of L-PAINT combined with DNA-PAINT. The L-PAINT strand is modified with a sequence for an imager strand (blue) which is modified with a fluorophore (red). Experimental data of the position against time reveals the blinking and the localization of both binding sites in a distance of 12 nm. C) Schematic of L-PAINT on a DNA origami with an additional FRET acceptor at one binding site. Experimental proximity ratio of L-PAINT without and with addition of 10 µM PEI. D) Schematic of an AND Gate based on L-PAINT. L-PAINT enables a logic by adding a hierarchy of binding sites, a fluorophore modified pointer (red, quenched fluorophore: brown) and quencher (black).

The distances and the kinetics of L-PAINT are well reproduceable over many publications[64, 99, 166, 167, 168]; thus one application of L-PAINT could be as a dynamic nanoruler (Figure 24 A). Here, it can either act as a reference structure[78, 135] for super-resolution microscopy, such as MINFLUX, but also for wide-field microscopy. With an acceptor dye close to one binding site, L-PAINT can even serve as a reference structure for dynamic FRET experiments[61, 169]. Experiments also already demonstrated the applicability of L-PAINT to multiple colors and binding sites.

The principle of L-PAINT could further be applied to image densely labelled clusters with a significant speed advantage. To this end, stochastic blinking needs to be introduced to L-PAINT. First experiments on DNA origami structures have shown that L-PAINT can be extended in combination with DNA-PAINT (Figure 24 B). Here, the L-PAINT scanning strand was prolonged with a reverse-complimentary

sequence to the DNA-PAINT imager strand. A combined DNA-PAINT and L-PAINT experiment could resolve both binding sites of the scanning strand. This lays the foundation to apply L-PAINT on biological structures. In the future, a possible approach is the use of labelling units e.g. antibodies or nanobodies with a stochastic mixture of binding sites and L-PAINT scanning strands. This could enable the super-resolved scanning of local cluster, for example of actin filaments with significant speed increases.

The combination of L-PAINT and FRET achieves the differentiation of two binding sites with a high contrast, yielding an easy and photon efficient access to the kinetics of L-PAINT. L-PAINT can act as a molecular balance, to reveal subtle differences between the binding sites (Figure 24 C). A single nucleotide difference between the binding site results in a change of more than one order of magnitude of the binding time, enabling many sensing applications.[64, 99] While this has been performed on more simplistic DNA constructs to measure subtle changes to the energy landscape,[170, 171] the DNA origami approach gives significant advantages. It enables the measurement of steric hinderance, as e.g. the binding of antibodies between scanning and one binding site should significantly disturb the L-PAINT kinetics. Beside such specific interactions, L-PAINT also enables the measurement of more unspecific interactions. Here, experiments using PEI, have shown to significantly change the L-PAINT kinetics as well. As a result, molecular balances on basis on L-PAINT enable the investigation of the interaction between PEI and DNA or RNA, which is important for optimizing PEI nanoparticles as vectors for drug delivery.

Leaving the realm of imaging and sensing, L-PAINT on DNA origami structures offers the ability to link multiple L-PAINT sites. On a single DNA origami structure, a network of L-PAINT can be created. As mentioned before the thermodynamic equilibrium of L-PAINT results in a high sensitivity to subtle changes on the binding sites. Thus, the creation of a hierarchy between binding sites inside this network is easily achievable by altering the length of complementary bases on the binding sites. Thereby, logic gates can be designed on basis of L-PAINT which can be linked to each other creating a new approach to DNA computing (Figure 24 D).[172, 173] The inputs of two DNA staples blocking binding sites of higher hierarchy can force the pointer to bind to the remaining third binding site of lower hierarchy. This binding site can be part of the next L-PAINT logic gate thereby enabling the creation of DNA computing logic gates. A potential read out could be via fluorophore and quencher combinations. Working at the thermodynamic equilibrium offers multiple advantages compared to existing DNA computing techniques. First it enables the resetting of the system, by removing input strands e.g. by strand displacement reactions. The second advantage is its computational speed. L-PAINT kinetics of few milliseconds are feasible thus enabling switching rates in the kHz regime. The versality of the L-PAINT approach also offers possibilities beside digital outputs of “0” corresponding to no or strongly quenched fluorescence and “1” high fluorescence. Due to the high FRET contrast, a third half-quenched state can also be well differentiated[159] and could offer novel algorithmic applications. All in all, L-PAINT offers new and exciting approaches for DNA computing, sensing and super-resolution microscopy.

In this thesis, pMINFLUX was developed to offer novel methodologies to probe the nanoscale world. The fluorescence lifetime enables the mapping of energy transfer rate constants as of FRET or GET for 3D super-resolution microscopy. Another application of the fluorescence lifetime was the co-localization of two dyes, which was achieved without photo-switching of the fluorophores. To investigate structural features with a speed increase, the photon efficiency of MINFLUX enables a novel concept of L-PAINT. In combination, all those methods enable a toolbox to investigate life science and material science for their structures, dynamics, interactions and their interplay on the smallest length scales, the molecular level, thus bringing light into the realm of chaos.

6. References

1. Shen B-W, Pielke Sr R, Zeng X, Baik J-J, Faghih-Naini S, Cui J*, et al.* Is Weather chaotic? Coexisting chaotic and non-chaotic attractors within Lorenz models. Chaotic Modeling and Simulation International Conference; 2020: Springer; 2020. p. 805-825.

2. Magán JM. Black holes, complexity and quantum chaos. *Journal of High Energy Physics* 2018, **2018**(9)**:** 1-34.

3. Shinbrot T, Grebogi C, Wisdom J, Yorke JA. Chaos in a double pendulum. *American Journal of Physics* 1992, **60**(6)**:** 491-499.

4. Gaspard P. Microscopic chaos and chemical reactions. *Physica A: Statistical Mechanics and its Applications* 1999, **263**(1-4)**:** 315-328.

5. Komatsuzaki T, Berry RS. Chemical reaction dynamics: many-body chaos and regularity. *Advances in Chemical Physics* 2002, **123:** 79-152.

6. Arora Verasztó H, Logotheti M, Albrecht R, Leitner A, Zhu H, Hartmann MD. Architecture and functional dynamics of the pentafunctional AROM complex. *Nature Chemical Biology* 2020, **16**(9)**:** 973-978.

7. Zuo S, Yi Y, Wang C, Li X, Zhou M, Peng Q*, et al.* Extrachromosomal Circular DNA (eccDNA): From Chaos to Function. *Frontiers in Cell and Developmental Biology* 2022, **9**.

8. Kriechbaumer V, Brandizzi F. The plant endoplasmic reticulum: an organized chaos of tubules and sheets with multiple functions. *Journal of Microscopy* 2020, **280**(2)**:** 122-133.

9. Corker A, Neff LS, Broughton P, Bradshaw AD, Deleon-Pennell KY. Organized Chaos: Deciphering Immune Cell Heterogeneity's Role in Inflammation in the Heart. *Biomolecules* 2021, **12**(1)**:** 11.

10. Pham TD. The chaotic behavior of the endoplasmic-reticulum network in time-lapse microscopy images. 2013 IEEE International Conference on Bioinformatics and Biomedicine 18-21 Dec. 2013. p. 22-25.

11. Priye A, Yu Y, Hassan YA, Ugaz VM. Synchronized chaotic targeting and acceleration of surface chemistry in prebiotic hydrothermal microenvironments. *Proceedings of the National Academy of Sciences* 2017, **114**(6)**:** 1275-1280.

12. Würthner L, Brauns F, Pawlik G, Halatek J, Kerssemakers J, Dekker C*, et al.* Bridging scales in a multiscale pattern-forming system. *Proceedings of the National Academy of Sciences* 2022, **119**(33).

13. Wettmann L, Kruse K. The Min-protein oscillations in Escherichia coli: an example of self-organized cellular protein waves. *Philosophical Transactions of the Royal Society B: Biological Sciences* 2018, **373**(1747)**:** 20170111.

14. Halatek J, Frey E. Rethinking pattern formation in reaction–diffusion systems. *Nature Physics* 2018, **14**(5)**:** 507-514.

15. Brauns F, Pawlik G, Halatek J, Kerssemakers J, Frey E, Dekker C. Bulk-surface coupling identifies the mechanistic connection between Min-protein patterns in vivo and in vitro. *Nature Communications* 2021, **12**(1).

16. Miyagi A, Ramm B, Schwille P, Scheuring S. High-Speed Atomic Force Microscopy Reveals the Inner Workings of the MinDE Protein Oscillator. *Nano Letters* 2018, **18**(1)**:** 288-296.

17. Loose M, Fischer-Friedrich E, Herold C, Kruse K, Schwille P. Min protein patterns emerge from rapid rebinding and membrane interaction of MinE. *Nature Structural & Molecular Biology* 2011, **18**(5)**:** 577-583.

18. Morris JD, Payne CK. Microscopy and Cell Biology: New Methods and New Questions. *Annual Review of Physical Chemistry* 2019, **70**(1)**:** 199-218.

19. Ratcliff MJ. *The quest for the invisible: microscopy in the Enlightenment*. Routledge, 2016.

20. Sahl SJ, Hell SW. High-Resolution 3D Light Microscopy with STED and RESOLFT. In: Bille JF (ed). *High Resolution Imaging in Microscopy and Ophthalmology: New Frontiers in Biomedical Optics*. Springer International Publishing: Cham, 2019, pp 3-32.

21. Rochow TG, Tucker PA. A Brief History of Microscopy. *Introduction to Microscopy by Means of Light, Electrons, X Rays, or Acoustics*. Springer US: Boston, MA, 1994, pp 1-21.

22. Jacker C. *Window on the unknown : a history of the microscope*. Scribner: New York, 1966.

23. Heath GR, Kots E, Robertson JL, Lansky S, Khelashvili G, Weinstein H*, et al.* Localization atomic force microscopy. *Nature* 2021, **594**(7863)**:** 385-390.

24. Yip KM, Fischer N, Paknia E, Chari A, Stark H. Atomic-resolution protein structure determination by cryo-EM. *Nature* 2020, **587**(7832)**:** 157-161.

25. Nakane T, Kotecha A, Sente A, McMullan G, Masiulis S, Brown PMGE*, et al.* Single-particle cryo-EM at atomic resolution. *Nature* 2020, **587**(7832)**:** 152-156.

26. Xu K, Zhong G, Zhuang X. Actin, Spectrin, and Associated Proteins Form a Periodic Cytoskeletal Structure in Axons. *Science* 2013, **339**(6118)**:** 452-456.

27. Van Noorden R. Nobel for microscopy that reveals inner world of cells. *Nature* 2014, **514**(7522)**:** 286-286.

28. Vogelsang J, Steinhauer C, Forthmann C, Stein IH, Person-Skegro B, Cordes T*, et al.* Make them Blink: Probes for Super-Resolution Microscopy. *ChemPhysChem* 2010, **11**(12)**:** 2475-2490.

29. Hell SW, Wichmann J. Breaking the diffraction resolution limit by stimulated emission: stimulated-emission-depletion fluorescence microscopy. *Opt Lett* 1994, **19**(11)**:** 780-782.

30. Klar TA, Hell SW. Subdiffraction resolution in far-field fluorescence microscopy. *Opt Lett* 1999, **24**(14)**:** 954-956.

31. Dickson RM, Cubitt AB, Tsien RY, Moerner WE. On/off blinking and switching behaviour of single molecules of green fluorescent protein. *Nature* 1997, **388**(6640)**:** 355-358.

32. Betzig E, Patterson GH, Sougrat R, Lindwasser OW, Olenych S, Bonifacino JS*, et al.* Imaging Intracellular Fluorescent Proteins at Nanometer Resolution. *Science* 2006, **313**(5793)**:** 1642-1645.

33. Rust MJ, Bates M, Zhuang X. Sub-diffraction-limit imaging by stochastic optical reconstruction microscopy (STORM). *Nature Methods* 2006, **3**(10)**:** 793-796.

34. Heilemann M, Margeat E, Kasper R, Sauer M, Tinnefeld P. Carbocyanine Dyes as Efficient Reversible Single-Molecule Optical Switch. *Journal of the American Chemical Society* 2005, **127**(11)**:** 3801-3806.

35. Nerreter T, Letschert S, Götz R, Doose S, Danhof S, Einsele H*, et al.* Super-resolution microscopy reveals ultra-low CD19 expression on myeloma cells that triggers elimination by CD19 CAR-T. *Nature Communications* 2019, **10**(1).

36. Löschberger A, Van De Linde S, Dabauvalle M-C, Rieger B, Heilemann M, Krohne G*, et al.* Super-resolution imaging visualizes the eightfold symmetry of gp210 proteins around the nuclear pore complex and resolves the central channel with nanometer resolution. *Journal of Cell Science* 2012, **125**(3)**:** 570-575.

37. Mund M, Van Der Beek JA, Deschamps J, Dmitrieff S, Hoess P, Monster JL*, et al.* Systematic Nanoscale Analysis of Endocytosis Links Efficient Vesicle Formation to Patterned Actin Nucleation. *Cell* 2018, **174**(4)**:** 884-896.e817.

38. Von Appen A, Kosinski J, Sparks L, Ori A, Diguilio AL, Vollmer B*, et al.* In situ structural analysis of the human nuclear pore complex. *Nature* 2015, **526**(7571)**:** 140-143.

39. Pape JK, Stephan T, Balzarotti F, Büchner R, Lange F, Riedel D*, et al.* Multicolor 3D MINFLUX nanoscopy of mitochondrial MICOS proteins. *Proceedings of the National Academy of Sciences* 2020, **117**(34)**:** 20607-20614.

40. Sabinina VJ, Hossain MJ, Hériché J-K, Hoess P, Nijmeijer B, Mosalaganti S*, et al.* Three-dimensional superresolution fluorescence microscopy maps the variable molecular architecture of the nuclear pore complex. *Molecular Biology of the Cell* 2021, **32**(17)**:** 1523-1533.

41. Thompson RE, Larson DR, Webb WW. Precise Nanometer Localization Analysis for Individual Fluorescent Probes. *Biophysical Journal* 2002, **82**(5)**:** 2775-2783.

42. Endesfelder U, Heilemann M. Direct Stochastic Optical Reconstruction Microscopy (dSTORM). In: Verveer PJ (ed). *Advanced Fluorescence Microscopy: Methods and Protocols*. Springer New York: New York, NY, 2015, pp 263-276.

43. Schermelleh L, Ferrand A, Huser T, Eggeling C, Sauer M, Biehlmaier O*, et al.* Super-resolution microscopy demystified. *Nature Cell Biology* 2019, **21**(1)**:** 72-84.

44. Kasper R, Harke B, Forthmann C, Tinnefeld P, Hell SW, Sauer M. Single-Molecule STED Microscopy with Photostable Organic Fluorophores. *Small* 2010, **6**(13)**:** 1379-1384.

45. NobelPrize.org Nobel Prize Outreach 2014 [cited 30.01.2023]Available from: https://www.nobelprize.org/prizes/chemistry/2014/press-release/

46. Lelek M, Gyparaki MT, Beliu G, Schueder F, Griffié J, Manley S*, et al.* Single-molecule localization microscopy. *Nature Reviews Methods Primers* 2021, **1**(1).

47. Holm T, Klein T, Löschberger A, Klamp T, Wiebusch G, van de Linde S*, et al.* A Blueprint for Cost-Efficient Localization Microscopy. *ChemPhysChem* 2014, **15**(4)**:** 651-654.

48. Ambrose B, Baxter JM, Cully J, Willmott M, Steele EM, Bateman BC*, et al.* The smfBox is an open-source platform for single-molecule FRET. *Nature Communications* 2020, **11**(1).

49. Schnitzbauer J, Strauss MT, Schlichthaerle T, Schueder F, Jungmann R. Super-resolution microscopy with DNA-PAINT. *Nature Protocols* 2017, **12**(6)**:** 1198-1228.

50. Schindelin J, Arganda-Carreras I, Frise E, Kaynig V, Longair M, Pietzsch T*, et al.* Fiji: an open-source platform for biological-image analysis. *Nature Methods* 2012, **9**(7)**:** 676-682.

51. Stuurman N, Amdodaj N, Vale R. µManager: Open Source Software for Light Microscope Imaging. *Microscopy Today* 2007, **15**(3)**:** 42-43.

52. Grimm JB, English BP, Chen J, Slaughter JP, Zhang Z, Revyakin A*, et al.* A general method to improve fluorophores for live-cell and single-molecule microscopy. *Nature Methods* 2015, **12**(3)**:** 244-250.

53. Wang L, Frei MS, Salim A, Johnsson K. Small-Molecule Fluorescent Probes for Live-Cell Super-Resolution Microscopy. *Journal of the American Chemical Society* 2019, **141**(7)**:** 2770-2781.

54. Mihaila TS, Bäte C, Ostersehlt LM, Pape JK, Keller-Findeisen J, Sahl SJ*, et al.* Enhanced incorporation of subnanometer tags into cellular proteins for fluorescence nanoscopy via optimized genetic code expansion. *Proceedings of the National Academy of Sciences* 2022, **119**(29).

55. Dempsey GT, Vaughan JC, Chen KH, Bates M, Zhuang X. Evaluation of fluorophores for optimal performance in localization-based super-resolution imaging. *Nature Methods* 2011, **8**(12)**:** 1027-1036.

56. Remmel M, Scheiderer L, Butkevich AN, Bossi ML, Hell SW. Accelerated MINFLUX Nanoscopy, through Spontaneously Fast-Blinking Fluorophores. *Small* 2023, **n/a**(n/a)**:** 2206026.

57. Jungmann R, Steinhauer C, Scheible M, Kuzyk A, Tinnefeld P, Simmel FC. Single-Molecule Kinetics and Super-Resolution Microscopy by Fluorescence Imaging of Transient Binding on DNA Origami. *Nano Lett* 2010, **10:** 4756-4761.

58. Jungmann R, Avendaño MS, Woehrstein JB, Dai M, Shih WM, Yin P. Multiplexed 3D cellular super-resolution imaging with DNA-PAINT and Exchange-PAINT. *Nature Methods* 2014, **11**(3)**:** 313-318.

59. Raab M, Schmied JJ, Jusuk I, Forthmann C, Tinnefeld P. Fluorescence Microscopy with 6 nm Resolution on DNA Origami. *ChemPhysChem* 2014, **15**(12)**:** 2431-2435.

60. Förster T. Zwischenmolekulare Energiewanderung und Fluoreszenz. *Annalen der Physik* 1948, **437**(1-2)**:** 55-75.

61. Hellenkamp B, Schmid S, Doroshenko O, Opanasyuk O, Kühnemuth R, Rezaei Adariani S*, et al.* Precision and accuracy of single-molecule FRET measurements—a multi-laboratory benchmark study. *Nature Methods* 2018, **15**(9)**:** 669-676.

62. Kaminska I, Bohlen J, Rocchetti S, Selbach F, Acuna GP, Tinnefeld P. Distance Dependence of Single-Molecule Energy Transfer to Graphene Measured with DNA Origami Nanopositioners. *Nano Letters*; 2019. pp. 4257-4262.

63. Ghosh A, Sharma A, Chizhik AI, Isbaner S, Ruhlandt D, Tsukanov R*, et al.* Graphene-based metal-induced energy transfer for sub-nanometre optical localization. *Nature Photonics* 2019, **13**(12)**:** 860-865.

64. Kaminska I, Bohlen J, Yaadav R, Schuler P, Raab M, Schroder T*, et al.* Graphene Energy Transfer for Single-Molecule Biophysics, Biosensing, and Super-Resolution Microscopy. *Adv Mater* 2021, **33**(24)**:** e2101099.

65. Balzarotti F, Eilers Y, Gwosch KC, Gynna AH, Westphal V, Stefani FD*, et al.* Nanometer resolution imaging and tracking of fluorescent molecules with minimal photon fluxes. *Science* 2017, **355**(6325)**:** 606-612.

66. Enderlein J. Tracking of fluorescent molecules diffusing within membranes. *Applied Physics B* 2000, **71**(5)**:** 773-777.

67. Levi V, Ruan Q, Kis-Petikova K, Gratton E. Scanning FCS, a novel method for three-dimensional particle tracking. *Biochemical Society Transactions* 2003, **31**(5)**:** 997-1000.

68. Lanzanò L, Gratton E. Orbital single particle tracking on a commercial confocal microscope using piezoelectric stage feedback. *Methods and Applications in Fluorescence* 2014, **2**(2)**:** 024010.

69. Mieskes F, Ploetz E, Wehnekamp F, Rat V, Lamb DC. Multicolor 3D Orbital Tracking. *Small* 2023**:** 2204726.

70. Wehnekamp F, Plucińska G, Thong R, Misgeld T, Lamb DC. Nanoresolution real-time 3D orbital tracking for studying mitochondrial trafficking in vertebrate axons in vivo. *eLife* 2019, **8**.

71. Weber M, Leutenegger M, Stoldt S, Jakobs S, Mihaila TS, Butkevich AN*, et al.* MINSTED fluorescence localization and nanoscopy. *Nat Photonics* 2021, **15**(5)**:** 361-366.

72. Masullo LA, Lopez LF, Stefani FD. A common framework for single-molecule localization using sequential structured illumination. *Biophysical Reports* 2022, **2**(1)**:** 100036.

73. Masullo LA, Szalai AM, Lopez LF, Pilo-Pais M, Acuna GP, Stefani FD. An alternative to MINFLUX that enables nanometer resolution in a confocal microscope. *Light Sci Appl* 2022, **11**(1)**:** 199.

74. Gartenmann L, Wainman A, Qurashi M, Kaufmann R, Schubert S, Raff JW*, et al.* A combined 3D-SIM/SMLM approach allows centriole proteins to be localized with a precision of ∼4–5 nm. *Current Biology* 2017, **27**(19)**:** R1054-R1055.

75. Gu L, Li Y, Zhang S, Xue Y, Li W, Li D*, et al.* Molecular resolution imaging by repetitive optical selective exposure. *Nature Methods* 2019, **16**(11)**:** 1114-1118.

76. Reymond L, Ziegler J, Knapp C, Wang F-C, Huser T, Ruprecht V*, et al.* SIMPLE: Structured illumination based point localization estimator with enhanced precision. *Optics Express* 2019, **27**(17)**:** 24578.

77. Cnossen J, Hinsdale T, Thorsen RØ, Siemons M, Schueder F, Jungmann R*, et al.* Localization microscopy at doubled precision with patterned illumination. *Nature Methods* 2020, **17**(1)**:** 59-63.

78. Schmied JJ, Gietl A, Holzmeister P, Forthmann C, Steinhauer C, Dammeyer T*, et al.* Fluorescence and super-resolution standards based on DNA origami. *Nature Methods* 2012, **9**(12)**:** 1133-1134.

79. Thevathasan JV, Kahnwald M, Cieśliński K, Hoess P, Peneti SK, Reitberger M*, et al.* Nuclear pores as versatile reference standards for quantitative superresolution microscopy. *Nature Methods* 2019, **16**(10)**:** 1045-1053.

80. Schmied JJ, Raab M, Forthmann C, Pibiri E, Wünsch B, Dammeyer T*, et al.* DNA origami–based standards for quantitative fluorescence microscopy. *Nature Protocols* 2014, **9**(6)**:** 1367-1391.

81. Rothemund PWK. Folding DNA to create nanoscale shapes and patterns. *Nature* 2006, **440:** 297-302.

82. Wagenbauer KF, Engelhardt FAS, Stahl E, Hechtl VK, Stömmer P, Seebacher F*, et al.* How We Make DNA Origami. *ChemBioChem* 2017, **18**(19)**:** 1873-1885.

83. Weber M, Von Der Emde H, Leutenegger M, Gunkel P, Sambandan S, Khan TA*, et al.* MINSTED nanoscopy enters the Ångström localization range. *Nature Biotechnology* 2022.

84. Eilers Y, Ta H, Gwosch KC, Balzarotti F, Hell SW. MINFLUX monitors rapid molecular jumps with superior spatiotemporal resolution. *Proc Natl Acad Sci U S A* 2018, **115**(24)**:** 6117-6122.

85. Gwosch KC, Pape JK, Balzarotti F, Hoess P, Ellenberg J, Ries J*, et al.* MINFLUX nanoscopy delivers 3D multicolor nanometer resolution in cells. *Nat Methods* 2020, **17**(2)**:** 217-224.

86. Helmig S, Rotaru A, Arian D, Kovbasyuk L, Arnbjerg J, Ogilby PR*, et al.* Single Molecule Atomic Force Microscopy Studies of Photosensitized Singlet Oxygen Behavior on a DNA Origami Template. *ACS Nano* 2010, **4**(12)**:** 7475-7480.

87. Kolbeck PJ, Dass M, Martynenko IV, Van Dijk-Moes RJA, Brouwer KJH, Van Blaaderen A*, et al.* DNA Origami Fiducial for Accurate 3D Atomic Force Microscopy Imaging. *Nano Letters* 2023.

88. Winterwerber P, Harvey S, Ng DYW, Weil T. Photocontrolled Dopamine Polymerization on DNA Origami with Nanometer Resolution. *Angewandte Chemie International Edition* 2020, **59**(15)**:** 6144-6149.

89. Trofymchuk K, Glembockyte V, Grabenhorst L, Steiner F, Vietz C, Close C*, et al.* Addressable nanoantennas with cleared hotspots for single-molecule detection on a portable smartphone microscope. *Nat Commun* 2021, **12**(1)**:** 950.

90. Pumm A-K, Engelen W, Kopperger E, Isensee J, Vogt M, Kozina V*, et al.* A DNA origami rotary ratchet motor. *Nature* 2022, **607**(7919)**:** 492-498.

91. Wilms CD, Schmidt H, Eilers J. Quantitative two-photon Ca2+ imaging via fluorescence lifetime analysis. *Cell Calcium* 2006, **40**(1)**:** 73-79.

92. Kuimova MK, Yahioglu G, Levitt JA, Suhling K. Molecular Rotor Measures Viscosity of Live Cells via Fluorescence Lifetime Imaging. *Journal of the American Chemical Society* 2008, **130**(21)**:** 6672-6673.

93. Pliss A, Zhao L, Ohulchanskyy TY, Qu J, Prasad PN. Fluorescence Lifetime of Fluorescent Proteins as an Intracellular Environment Probe Sensing the Cell Cycle Progression. *ACS Chemical Biology* 2012, **7**(8)**:** 1385-1392.

94. Betzig E. Proposed method for molecular optical imaging. *Opt Lett* 1995, **20**(3)**:** 237-239.

95. Bückers J, Wildanger D, Vicidomini G, Kastrup L, Hell SW. Simultaneous multi-lifetime multi-color STED imaging for colocalization analyses. *Optics Express* 2011, **19**(4)**:** 3130-3143.

96. Heilemann M, Herten DP, Heintzmann R, Cremer C, Müller C, Tinnefeld P*, et al.* High-Resolution Colocalization of Single Dye Molecules by Fluorescence Lifetime Imaging Microscopy. *Analytical Chemistry* 2002, **74**(14)**:** 3511-3517.

97. Böhmer M, Wahl M, Rahn H-J, Erdmann R, Enderlein J. Time-resolved fluorescence correlation spectroscopy. *Chemical Physics Letters* 2002, **353**(5)**:** 439-445.

98. Schröder T. Connecting Excited State Lifetime and Intensity Correlations for Quantitative Analysis of Chromophore Interactions. PhD thesis, Ludwig-Maximilians-Universität München, 2022.

99. Schröder T, Bohlen J, Ochmann SE, Schüler P, Krause S, Lamb DC*, et al.* Shrinking gate fluorescence correlation spectroscopy yields equilibrium constants and separates photophysics from structural dynamics. *Proceedings of the National Academy of Sciences* 2023, **120**(4).

100. Oleksiievets N, Sargsyan Y, Thiele JC, Mougios N, Sograte-Idrissi S, Nevskyi O*, et al.* Fluorescence lifetime DNA-PAINT for multiplexed super-resolution imaging of cells. *Commun Biol* 2022, **5**(1)**:** 38.

101. Castello M, Tortarolo G, Buttafava M, Deguchi T, Villa F, Koho S*, et al.* A robust and versatile platform for image scanning microscopy enabling super-resolution FLIM. *Nature Methods* 2019, **16**(2)**:** 175-178.

102. Mahalingam M, Girgenrath T, Svensson B, David, Razvan, James. Structural Mapping of Divergent Regions in the Type 1 Ryanodine Receptor Using Fluorescence Resonance Energy Transfer. *Structure* 2014, **22**(9)**:** 1322-1332.

103. Lakowicz JR. *Principles of fluorescence spectroscopy*, 1st 1983. edn. Plenum Press: New York ; London, 1983.

104. Haken H, Wolf HC, Wolf HC. *Atom- und Quantenphysik : Einführung in die experimentellen und theoretischen Grundlagen*, 6. verb. u. erw. Aufl. edn. Springer: Berlin, 1996.

105. Haken H, Wolf HC. Molekülphysik und Quantenchemie : Einführung in die experimentellen und theoretischen Grundlagen. *Springer-Lehrbuch*. Fünfte, völlig neubearbeitete und erweiterte Auflage. ed. Heidelberg: Springer-Verlag Berlin Heidelberg; 2006.

106. Van De Linde S, Krstić I, Prisner T, Doose S, Heilemann M, Sauer M. Photoinduced formation of reversible dye radicals and their impact on super-resolution imaging. *Photochemical & Photobiological Sciences* 2011, **10**(4)**:** 499-506.

107. Song L, Varma CA, Verhoeven JW, Tanke HJ. Influence of the triplet excited state on the photobleaching kinetics of fluorescein in microscopy. *Biophys J* 1996, **70**(6)**:** 2959-2968.

108. Vogelsang J, Kasper R, Steinhauer C, Person B, Heilemann M, Sauer M*, et al.* A Reducing and Oxidizing System Minimizes Photobleaching and Blinking of Fluorescent Dyes. *Angewandte Chemie International Edition* 2008, **47**(29)**:** 5465-5469.

109. Cordes T, Vogelsang J, Tinnefeld P. On the mechanism of Trolox as antiblinking and antibleaching reagent. *J Am Chem Soc* 2009, **131**(14)**:** 5018-5019.

110. Steinhauer C, Forthmann C, Vogelsang J, Tinnefeld P. Superresolution Microscopy on the Basis of Engineered Dark States. *Journal of the American Chemical Society* 2008, **130**(50)**:** 16840-16841.

111. Vogelsang J, Cordes T, Forthmann C, Steinhauer C, Tinnefeld P. Controlling the fluorescence of ordinary oxazine dyes for single-molecule switching and superresolution microscopy. *Proceedings of the National Academy of Sciences* 2009, **106**(20)**:** 8107-8112.

112. Holzmeister P, Gietl A, Tinnefeld P. Geminate Recombination as a Photoprotection Mechanism for Fluorescent Dyes. *Angewandte Chemie International Edition* 2014, **53**(22)**:** 5685-5688.

113. Rayleigh. XXXI. Investigations in optics, with special reference to the spectroscope. *The London, Edinburgh, and Dublin Philosophical Magazine and Journal of Science* 1879, **8**(49)**:** 261-274.

114. Masters BR, SpringerLink. *Superresolution Optical Microscopy: The Quest for Enhanced Resolution and Contrast*, 1st 2020. edn. Springer International Publishing: Imprint: Springer: Cham, 2020.

115. Lauterbach MA. Finding, defining and breaking the diffraction barrier in microscopy – a historical perspective. *Optical Nanoscopy* 2012, **1**(1)**:** 8.

116. Houston WV. A Compound Interferometer for Fine Structure Work. *Physical Review* 1927, **29**(3)**:** 478-484.

117. Scheckenbach M, Bauer J, Zähringer J, Selbach F, Tinnefeld P. DNA origami nanorulers and emerging reference structures. *APL Materials* 2020, **8**(11)**:** 110902.

118. Klar TA, Jakobs S, Dyba M, Egner A, Hell SW. Fluorescence microscopy with diffraction resolution barrier broken by stimulated emission. *Proc Natl Acad Sci U S A* 2000, **97**(15)**:** 8206-8210.

119. Folling J, Bossi M, Bock H, Medda R, Wurm CA, Hein B*, et al.* Fluorescence nanoscopy by ground-state depletion and single-molecule return. *Nat Methods* 2008, **5**(11)**:** 943-945.

120. Mortensen KI, Churchman LS, Spudich JA, Flyvbjerg H. Optimized localization analysis for single-molecule tracking and super-resolution microscopy. *Nature Methods* 2010, **7**(5)**:** 377-381.

121. Heilemann M, van de Linde S, Schüttpelz M, Kasper R, Seefeldt B, Mukherjee A*, et al.* Subdiffraction-Resolution Fluorescence Imaging with Conventional Fluorescent Probes. *Angewandte Chemie International Edition* 2008, **47**(33)**:** 6172-6176.

122. Gustafsson MGL. Surpassing the lateral resolution limit by a factor of two using structured illumination microscopy. SHORT COMMUNICATION. *Journal of Microscopy* 2000, **198**(2)**:** 82-87.

123. Gustafsson MGL, Shao L, Carlton PM, Wang CJR, Golubovskaya IN, Cande WZ*, et al.* Three-Dimensional Resolution Doubling in Wide-Field Fluorescence Microscopy by Structured Illumination. *Biophysical Journal* 2008, **94**(12)**:** 4957-4970.

124. Manton JD. Answering some questions about structured illumination microscopy. *Philos Trans A Math Phys Eng Sci* 2022, **380**(2220)**:** 20210109.

125. Jelley EE. Spectral Absorption and Fluorescence of Dyes in the Molecular State. *Nature* 1936, **138**(3502)**:** 1009-1010.

126. Schröder T, Scheible MB, Steiner F, Vogelsang J, Tinnefeld P. Interchromophoric Interactions Determine the Maximum Brightness Density in DNA Origami Structures. *Nano Letters* 2019, **19**(2)**:** 1275-1281.

127. Ha T, Enderle T, Ogletree DF, Chemla DS, Selvin PR, Weiss S. Probing the interaction between two single molecules: fluorescence resonance energy transfer between a single donor and a single acceptor. *Proceedings of the National Academy of Sciences* 1996, **93**(13)**:** 6264-6268.

128. Fang B, Shen Y, Peng B, Bai H, Wang L, Zhang J*, et al.* Small-Molecule Quenchers for Forster Resonance Energy Transfer: Structure, Mechanism, and Applications. *Angew Chem Int Ed Engl* 2022, **61**(41)**:** e202207188.

129. Mathur D, Samanta A, Ancona MG, Díaz SA, Kim Y, Melinger JS*, et al.* Understanding Förster Resonance Energy Transfer in the Sheet Regime with DNA Brick-Based Dye Networks. *ACS Nano* 2021, **15**(10)**:** 16452-16468.

130. Krause S, Ploetz E, Bohlen J, Schuler P, Yaadav R, Selbach F*, et al.* Graphene-on-Glass Preparation and Cleaning Methods Characterized by Single-Molecule DNA Origami Fluorescent Probes and Raman Spectroscopy. *ACS Nano* 2021, **15**(4)**:** 6430-6438.

131. Bostwick A, Ohta T, McChesney JL, Seyller T, Horn K, Rotenberg E. Band structure and many body effects in graphene. *The European Physical Journal Special Topics* 2007, **148**(1)**:** 5-13.

132. Gierz I, Petersen JC, Mitrano M, Cacho C, Turcu ICE, Springate E*, et al.* Snapshots of non-equilibrium Dirac carrier distributions in graphene. *Nature Materials* 2013, **12**(12)**:** 1119-1124.

133. Federspiel F, Froehlicher G, Nasilowski M, Pedetti S, Mahmood A, Doudin B*, et al.* Distance Dependence of the Energy Transfer Rate from a Single Semiconductor Nanostructure to Graphene. *Nano Letters* 2015, **15**(2)**:** 1252-1258.

134. Swathi RS, Sebastian KL. Resonance energy transfer from a dye molecule to graphene. *The Journal of Chemical Physics* 2008, **129**(5)**:** 054703.

135. Schmied JJ, Forthmann C, Pibiri E, Lalkens B, Nickels P, Liedl T*, et al.* DNA Origami Nanopillars as Standards for Three-Dimensional Superresolution Microscopy. *Nano Letters* 2013, **13**(2)**:** 781-785.

136. Douglas SM, Marblestone AH, Teerapittayanon S, Vazquez A, Church GM, Shih WM. Rapid prototyping of 3D DNA-origami shapes with caDNAno. *Nucleic Acids Research* 2009, **37**(15)**:** 5001-5006.

137. Nickels PC, Wunsch B, Holzmeister P, Bae W, Kneer LM, Grohmann D*, et al.* Molecular force spectroscopy with a DNA origami-based nanoscopic force clamp. *Science* 2016, **354**(6310)**:** 305-307.

138. Binkert T, Tschanz HP, Zinsli PE. The measurement of fluorescence decay curves with the single-photon counting method and the evaluation of rate parameters. *Journal of Luminescence* 1972, **5**(3)**:** 187-217.

139. Bachrach RZ. A Photon Counting Apparatus for Kinetic and Spectral Measurements. *Review of Scientific Instruments* 1972, **43**(5)**:** 734-737.

140. Thiele JC, Nevskyi O, Helmerich DA, Sauer M, Enderlein J. Advanced Data Analysis for Fluorescence-Lifetime Single-Molecule Localization Microscopy. *Front Bioinform* 2021, **1:** 740281.

141. Masullo LA, Steiner F, Zahringer J, Lopez LF, Bohlen J, Richter L*, et al.* Pulsed Interleaved MINFLUX. *Nano Letters* 2021, **21**(1)**:** 840-846.

142. Schueder F, Stein J, Stehr F, Auer A, Sperl B, Strauss MT*, et al.* An order of magnitude faster DNA-PAINT imaging by optimized sequence design and buffer conditions. *Nat Methods* 2019, **16**(11)**:** 1101-1104.

143. Strauss S, Jungmann R. Up to 100-fold speed-up and multiplexing in optimized DNA-PAINT. *Nat Methods* 2020, **17**(8)**:** 789-791.

144. Aitken CE, Marshall RA, Puglisi JD. An Oxygen Scavenging System for Improvement of Dye Stability in Single-Molecule Fluorescence Experiments. *Biophysical Journal* 2008, **94**(5)**:** 1826-1835.

145. Li W, Grech J, Stortz JF, Gow M, Periz J, Meissner M*, et al.* A splitCas9 phenotypic screen in Toxoplasma gondii identifies proteins involved in host cell egress and invasion. *Nature Microbiology* 2022, **7**(6)**:** 882-895.

146. Roeder AHK, Otegui MS, Dixit R, Anderson CT, Faulkner C, Zhang Y*, et al.* Fifteen compelling open questions in plant cell biology. *The Plant Cell* 2021, **34**(1)**:** 72-102.

147. Alamos S, Reimer A, Niyogi KK, Garcia HG. Quantitative imaging of RNA polymerase II activity in plants reveals the single-cell basis of tissue-wide transcriptional dynamics. *Nature Plants* 2021, **7**(8)**:** 1037-1049.

148. Bohlen J, Cuartero-González Á, Pibiri E, Ruhlandt D, Fernández-Domínguez AI, Tinnefeld P*, et al.* Plasmon-assisted Förster resonance energy transfer at the single-molecule level in the moderate quenching regime. *Nanoscale* 2019, **11**(16)**:** 7674-7681.

149. Slenders E, Vicidomini G. ISM-FLUX: MINFLUX with an array detector. *Physical Review Research* 2023, **5**(2).

150. Vacha M, Habuchi S. Conformation and physics of polymer chains: a single-molecule perspective. *NPG Asia Materials* 2010, **2**(4)**:** 134-142.

151. Slenders E, Castello M, Buttafava M, Villa F, Tosi A, Lanzanò L*, et al.* Confocal-based fluorescence fluctuation spectroscopy with a SPAD array detector. *Light: Science & Applications* 2021, **10**(1).

152. Pujals S, Feiner-Gracia N, Delcanale P, Voets I, Albertazzi L. Super-resolution microscopy as a powerful tool to study complex synthetic materials. *Nature Reviews Chemistry* 2019, **3**(2)**:** 68-84.

153. Lee YJ, Kim DY, Grey JK, Barbara PF. Variable Temperature Single-Molecule Dynamics of MEH-PPV. *ChemPhysChem* 2005, **6**(11)**:** 2404-2409.

154. Habuchi S, Onda S, Vacha M. Mapping the emitting sites within a single conjugated polymer molecule. *Chemical Communications* 2009(32)**:** 4868.

155. Lin H, Tian Y, Zapadka K, Persson G, Thomsson D, Mirzov O*, et al.* Fate of Excitations in Conjugated Polymers: Single-Molecule Spectroscopy Reveals Nonemissive "Dark" Regions in MEH-PPV Individual Chains. *Nano Letters* 2009, **9**(12)**:** 4456-4461.

156. Habuchi S, Onda S, Vacha M. Molecular weight dependence of emission intensity and emitting sites distribution within single conjugated polymer molecules. *Phys Chem Chem Phys* 2011, **13**(5)**:** 1743-1753.

157. Gordon MP, Ha T, Selvin PR. Single-molecule high-resolution imaging with photobleaching. *Proceedings of the National Academy of Sciences* 2004, **101**(17)**:** 6462-6465.

158. Park H, Hoang DT, Paeng K, Kaufman LJ. Localizing Exciton Recombination Sites in Conformationally Distinct Single Conjugated Polymers by Super-resolution Fluorescence Imaging. *ACS Nano* 2015, **9**(3)**:** 3151-3158.

159. Cole F, Zähringer J, Bohlen J, Schröder T, Steiner F, Stefani FD*, et al.* Super-Resolved FRET and Co-Tracking in pMINFLUX. Cold Spring Harbor Laboratory; 2023.

160. Wöll D, Braeken E, Deres A, De Schryver FC, Uji-I H, Hofkens J. Polymers and single molecule fluorescence spectroscopy, what can we learn? *Chem Soc Rev* 2009, **38**(2)**:** 313-328.

161. Aggarwal AV, Thiessen A, Idelson A, Kalle D, Würsch D, Stangl T*, et al.* Fluctuating exciton localization in giant π-conjugated spoked-wheel macrocycles. *Nature Chemistry* 2013, **5**(11)**:** 964-970.

162. Deguchi T, Iwanski MK, Schentarra E-M, Heidebrecht C, Schmidt L, Heck J*, et al.* Direct observation of motor protein stepping in living cells using MINFLUX. *Science* 2023, **379**(6636)**:** 1010-1015.

163. Wolff JO, Scheiderer L, Engelhardt T, Engelhardt J, Matthias J, Hell SW. MINFLUX dissects the unimpeded walking of kinesin-1. *Science* 2023, **379**(6636)**:** 1004-1010.

164. Kevin, Thomas. The Nuclear Pore Complex as a Flexible and Dynamic Gate. *Cell* 2016, **164**(6)**:** 1162-1171.

165. Winkeljann B, Keul DC, Merkel OM. Engineering poly- and micelleplexes for nucleic acid delivery – A reflection on their endosomal escape. *Journal of Controlled Release* 2023, **353:** 518-534.

166. Masullo LA, Steiner F, Zähringer J, Lopez LF, Bohlen J, Richter L*, et al.* Pulsed Interleaved MINFLUX. *Nano Letters* 2021, **21**(1)**:** 840-846.

167. Zähringer J, Cole F, Bohlen J, Steiner F, Kamińska I, Tinnefeld P. Combining pMINFLUX, graphene energy transfer and DNA-PAINT for nanometer precise 3D super-resolution microscopy. *Light: Science & Applications* 2023, **12**(1)**:** 70.

168. Wanninger S, Asadiatouei P, Bohlen J, Salem C-B, Tinnefeld P, Ploetz E*, et al.* Deep-Learning Assisted, Single-molecule Imaging analysis (Deep-LASI) of multi-color DNA Origami structures. Cold Spring Harbor Laboratory; 2023.

169. Agam G, Gebhardt C, Popara M, Mächtel R, Folz J, Ambrose B*, et al.* Reliability and accuracy of single-molecule FRET studies for characterization of structural dynamics and distances in proteins. *Nature Methods* 2023, **20**(4)**:** 523-535.

170. Johnson-Buck A, Su X, Giraldez MD, Zhao M, Tewari M, Walter NG. Kinetic fingerprinting to identify and count single nucleic acids. *Nature Biotechnology* 2015, **33**(7)**:** 730-732.

171. Mandal S, Khanna K, Johnson-Buck A, Walter NG. A guide to accelerated direct digital counting of single nucleic acid molecules by FRET-based intramolecular kinetic fingerprinting. *Methods* 2022, **197:** 63-73.

172. Chatterjee G, Dalchau N, Muscat RA, Phillips A, Seelig G. A spatially localized architecture for fast and modular DNA computing. *Nature Nanotechnology* 2017, **12**(9)**:** 920-927.

173. Song T, Eshra A, Shah S, Bui H, Fu D, Yang M*, et al.* Fast and compact DNA logic circuits based on single-stranded gates using strand-displacing polymerase. *Nature Nanotechnology* 2019, **14**(11)**:** 1075-1081.

7 Appendix:

7.1 Publication I: DNA origami nanorulers and emerging reference

by

Michael Scheckenbach*, Julian Bauer*, Jonas Zähringer*, Florian Selbach, and Philip Tinnefeld (* equal contribution)

published in

APL Materials 8, 110902 (2020); doi: 10.1063/5.0022885

Author contribution:
I wrote the section about targeted-switching super-resolution techniques and energy transfers.

APL Materials

DNA origami nanorulers and emerging reference structures

Cite as: APL Mater. **8**, 110902 (2020); https://doi.org/10.1063/5.0022885
Submitted: 29 July 2020 . Accepted: 16 September 2020 . Published Online: 10 November 2020

Michael Scheckenbach, Julian Bauer, Jonas Zähringer, Florian Selbach, and Philip Tinnefeld

DNA origami nanorulers and emerging reference structures

Cite as: APL Mater. 8, 110902 (2020); doi: 10.1063/5.0022885
Submitted: 29 July 2020 • Accepted: 16 September 2020 •
Published Online: 10 November 2020

Michael Scheckenbach,[1] Julian Bauer,[1] Jonas Zähringer,[1] Florian Selbach,[1,2,a)] and Philip Tinnefeld[1,a)]

AFFILIATIONS

[1]Department of Chemistry and Center for NanoScience (CeNS), Ludwig-Maximilians-Universität München, Butenandtstr. 5-13, 81377 München, Germany
[2]GATTAquant GmbH, Lochhamer Schlag 11, 82166 Gräfelfing, Germany

[a)]**Authors to whom correspondence should be addressed:** selbach@gattaquant.com and philip.tinnefeld@lmu.de

ABSTRACT

The DNA origami technique itself is considered a milestone of DNA nanotechnology and DNA origami nanorulers represent the first widespread application of this technique. DNA origami nanorulers are used to demonstrate the capabilities of techniques and are valuable training samples. They have meanwhile been developed for a multitude of microscopy methods including optical microscopy, atomic force microscopy, and electron microscopy, and their unique properties are further exploited to develop point-light sources, brightness references, nanophotonic test structures, and alignment tools for correlative microscopy. In this perspective, we provide an overview of the basics of DNA origami nanorulers and their increasing applications in fields of optical and especially super-resolution fluorescence microscopy. In addition, emerging applications of reference structures based on DNA origami are discussed together with recent developments.

I. INTRODUCTION

Light microscopy techniques are major nondestructive imaging tools in biology, biomedicine, and related life sciences. The diffraction limit, the ultimate resolution limitation in optical microscopy, has been overcome with super-resolution (SR) microscopy.[1–3] Even distances below the diffraction limit of light can now be resolved with a non-invasive optical microscope yielding crisp images. The most prominent super-resolution techniques are stimulated emission depletion[4] (STED) and single-molecule localization-based microscopy (STORM,[5] dSTORM,[6] PALM,[7] PAINT,[8] DNA-PAINT,[9] MINFLUX[10,11]) and derivates thereof. Similarly, structured illumination microscopy[12,13] (SIM) techniques are pushing the limits of resolution. The resolution problem boils down to the ability of distinguishing two point-like objects. Two fluorescent spots in close proximity, for example, could not be differentiated in a wide-field microscope [Fig. 1(a)] as quantitatively described by the Rayleigh criterion. The information of the localization of each spot can, however, be reconstructed when just one fluorophore is visible at a time. In single-molecule localization approaches, the point spread function (PSF) of each emitting spot is fitted by a Gaussian function and the exact position is determined with a precision substantially better than the detector pixel size.

In the early years of super-resolution microscopy, filamentous structures such as microtubules and actin filaments were imaged to demonstrate the new techniques and their variants [Fig. 1(b)].[14] The images were then examined to find the smallest features that could be distinguished. This could, e.g., be two filaments oriented parallel over some distance. Presenting cross sections of these parts of the image demonstrated the achievable resolution. The disadvantages of this approach are obvious. First, the true underlying structure is unknown. The measurements are not reproducible as every location in a cell is different and statistically underpinned resolution measures cannot be deduced. Critically, claimed resolution measures cannot directly be reproduced in another laboratory. The important property of a standard, i.e., providing comparability between labs and instruments was not provided. Furthermore, the molecular environment of the labels is not defined and the number of labels contributing to the signal is not known.

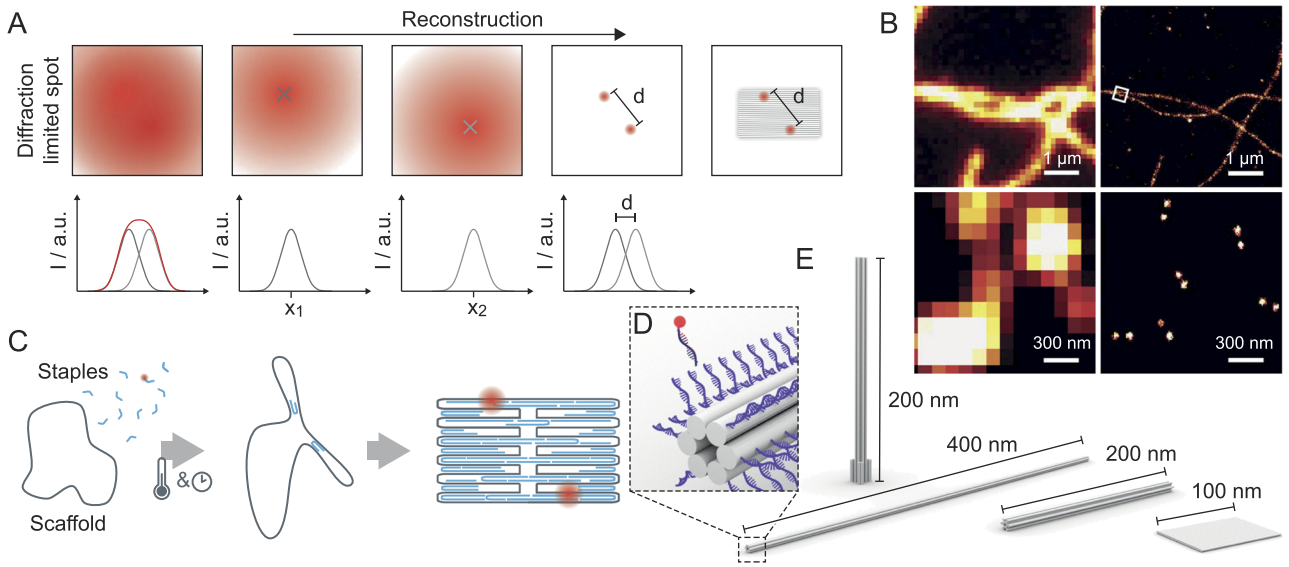

FIG. 1. (a) Sketch explaining super-resolution microscopy by successive single-molecule localizations. Positions of individual, independently switching molecules are determined and the super-resolution image is reconstructed from the density of localizations. (b) Comparison of actin filaments (top row) and DNA origamis (bottom row) as test structures. Right panels show representative super-resolution images and left panels show the corresponding total internal reflection fluorescence (TIRF) images (adapted from Ref. 14). (c) Scheme of folding a dye labeled DNA origami nanoruler. (d) Scheme of addressability of modifications (e.g., fluorophores) on DNA origami nanorulers by DNA hybridization. (e) Scheme of underlying structures successfully used as DNA origami nanoruler breadboards [six helix bundle (400 nm), 12 helix-bundle (200 nm), rectangular structure (100 nm), and pillar (200 nm)].

Nowadays, three approaches have evolved for objective characterization of fluorescence imaging techniques including algorithmic resolution calculation[15] [e.g., Fourier ring correlation (FRC)[16]], defined natural protein structures such as nuclear pores[17,18] or the diameter of microtubules,[18] and artificial structures such as DNA origami nanorulers.[19–23] Among the different approaches which all have their pros and cons, DNA origami nanorulers are the best-defined and most versatile and realistically allow emulating diverse microscopy experiments. As is shown in Fig. 1(b) (bottom panel), the ability to distinguish two point-light sources as required by established resolution criteria is directly visualized for the imaging technique in the bottom right panel compared to the imaging method used for the image in the bottom left panel. Beyond the possibility to quantitatively characterize microscopy techniques, DNA origami nanorulers have become a positive control, calibration tool, and training sample in fluorescence microscopy and beyond.

In this perspective, we outline the development of DNA origami nanorulers, explain the principles of their design and functioning, and provide numerous examples of their application. These applications meanwhile diverge into different fields and an outlook on new directions is given. Emerging applications include fiducial markers (FM), brightness referencing and applications in atomic force microscopy, electron microscopy and their combinations.

A. DNA origami nanorulers - basics

DNA origami nanorulers[14] are building on the DNA origami technique. DNA origami was introduced in 2006 by Rothemund and is seen as a milestone in DNA nanotechnology.[24] With DNA origami, a single person can easily create impressively big DNA nanostructures with programmed geometry and almost atomistic structural control.[24,25] The resulting nanostructures are obtained in high yields and, after folding, they are robust and stable in a variety of conditions and over long timescales. DNA origami nanorulers made early use of DNA origami and led to the first commercial application based on DNA origami technology by the spin-off company GATTAquant.

DNA origami are built from one long single-stranded DNA of ~7300 nucleotides with known sequence, which is called the scaffold strand. The single-stranded, circular scaffold strand was obtained from a bacteriophage (typically M13mp18) and can be folded with ~200 shorter oligonucleotides, so called staple strands into a defined 2D- or 3D-structure [Fig. 1(c)].[25] Scaffold and staple strands are mixed together, heated, and cooled down slowly to room temperature to ensure correct DNA hybridization of the individual parts. DNA origami structures can be designed with open-sourced software like caDNAno[25] or canDo.[26] First, with the aid of caDNAno, the user decides on the geometry of the structure and the scaffold is routed through this geometry to obtain the desired shape. Subsequently, the staple strands are planned so that parallel DNA helices are connected by crossovers and the final structure is stabilized. The conformational flexibility of the planned structure is estimated with the software canDo. At the end of the design process, a list of staple strands to be purchased for synthesis is obtained. To get from DNA origamis to DNA origami nanorulers, certain staples strands are modified, e.g., with fluorescent dyes. As each staple position in the DNA origami is precisely known, the exact position of the fluorescent dyes in the DNA origami is well-defined.[27]

Alternative to fluorescent dyes, a multitude of chemical functionalities including amino- or thiol groups, biotin, cholesterol, pyrene, and click chemistry groups can thus be introduced in pre-defined patterns at well-controlled stoichiometry providing the chemical handles for placing proteins, nanoparticles, and essentially everything that is compatible with the water chemistry of DNA. Another simple and versatile attachment chemistry can be offered by extending the staple strands so that single-stranded DNA oligonucleotides protrude from the DNA origami to which other DNA functionalized moieties can bind.[28] Protruding single-stranded DNA is also used for the super-resolution technique DNA-PAINT that is the basis of one of the most important realizations of DNA origami nanorulers.[9,20,29]

For designing a DNA origami nanoruler, simple geometric considerations are made. Along the direction of the DNA helix, the distance between two adjacent bases is 0.34 nm and the distance between the centers of two neighboring DNA helices is between 2.5 nm and 2.8 nm depending on the exact origami design (e.g., honeycomb or square lattice) and the buffer conditions.[30,31] Still, the finally measured distance in a DNA origami nanoruler rarely exactly meets the designed distance as over larger distances further aspects such as strain, torsion, and bending come into play.[14,19,32] Additional distance inaccuracy comes from incorporation efficiency of modified staple strands, docking site accessibility of external modifications, and length and flexibility of used dye linkers to the DNA.[33] Hence, accurate distances have to be determined by microscopes that are able to resolve the structure and are calibrated to determine the distances.[19,28] With this procedure, accurate placement (<1 nm) can be achieved.[28,32,34]

Fundamentally, fluorescent dyes can be incorporated at every base position of the DNA origami. At very small distance (<5 base pair distance), however, quenching occurs as soon as the dyes physically touch.[35] For larger distances, fluorescence scales perfectly linear with the number of dyes.[19,20] In practice, fluorescent dyes are commonly incorporated by labeling staple strands at the 3′- or 5′-end, which is also more economical. To this end, the number of fluorescent dyes per DNA origami is limited to roughly 1000 for a maximally labeled DNA origami still avoiding quenching and to about 200 dyes for singly labeled staple strands. For a 12 helix-bundle (12 HB), i.e., a typical DNA origami nanoruler structure that has a length of roughly 200 nm and a diameter of ~13 nm, this means that we find one potential dye position every nanometer along its 1D projection [see Fig. 1(d)]. In simple terms, the 12 HB is a DNA origami nanoruler that can be seen as a molecular breadboard with one plug-in position every nanometer.

Besides the 12 HB, typical DNA origami structures used for DNA origami nanorulers are rectangles and rod-like structures such as DNA bundles (e.g., 6 HB) [see Figs. 1(d) and 1(e)]. The rectangular structure enables modifications over the whole 2D breadboard structure and the 6 HB is so long that a nanoruler with marks at its ends can be resolved with conventional fluorescence microscopy.[20] For 3D applications, a pillar-like structure was designed that can specifically be immobilized via its small base using biotin modifications on streptavidin surfaces and stands roughly 200 nm high despite its enormous aspect ratio.[23,36]

In the following, we describe more specific applications of DNA origami nanorulers. We chapter the methods into the more general stochastic switching (also referred to as single-molecule localization methods) and targeted switching super-resolution approaches[37] and report on the strength of these tools in atomic-force microscopy (AFM) and transmission electron microscopy (TEM). Finally, we outline emerging DNA origami applications in which they are used as reference structures.

II. STOCHASTIC SWITCHING BASED SUPER-RESOLUTION MICROSCOPY NANORULERS

The principle of the reconstruction of stochastic single molecule localizations shown in Fig. 1(a) can be accomplished by different approaches as, for example, covered in the following reviews.[1,38,39] Most common single-molecule localization techniques use either the stochastic activation of photoswitchable fluorescent molecules such as fluorescent proteins and certain organic dyes (STORM,[5] PALM,[7] GSDIM,[40] SOFI[41]), or the stochastic binding of fluorescently labeled molecules to a target (PAINT,[8] uPAINT,[42] DNA-PAINT[9]).

All of these SR methods work with image reconstruction, implying that the true image cannot be immediately deduced from the acquired data, but lies beneath layers of data processing, like localizing, un-drifting, and other corrections. Single-molecule localization super-resolution methods especially require optimization of the measurement parameters and the sample preparation. For sample preparation, dense enough labeling and a high enough number of localizations have to fulfill resolution requirements of the Nyquist criterion.[43] Due to the number of factors and the indirect and algorithmic procedure to obtain the final image, resolution is not solely defined by localization precision. It is therefore vital to verify the performance of the setup and to test whether a claimed resolution can indeed be achieved. Further, to ensure only one emitting molecule at a time within a diffraction limited region, the blinking kinetics have to be adapted accordingly. Here, a positive control is helpful for adjusting the photoswitching, blinking or dye binding kinetics to the measurement method that depends amongst others on buffer compositions and laser excitation conditions. The latter requires that the positive control uses the same fluorescent dyes in a similar environment. All these arguments call for reliable and well-defined structures in the nanometer regime that can be adapted to the needs of the specific method and even for the fluorescent dye used. Here, the introduced DNA origami nanorulers serve as an established reference tool, offering a quantitative analysis of the resolution, e.g., a multi-Gaussian fit to the line profile along a 12-helix bundle DNA origami with three equidistant spots is a measure of the optical resolution [Fig. 2(a)].[28] To answer the question of the accuracy of nanorulers, a strategy was developed to quantify the traceability of DNA origami nanorulers in SI units, establishing them as true standards. Accordingly, the accuracy, and not only the precision of the nanorulers, was characterized and found that the accuracy of marks (labeling spots) on DNA origami was commonly better than 2 nm.[28] Many labs meanwhile use DNA origami nanorulers to first check and demonstrate their SR abilities and then present their biological results obtained by SR microscopy.[44–49]

Besides, for the investigation of a new method for the spectral filtering of fluorescent impurities,[50] DNA origami nanorulers are often used to demonstrate the ability of new software and hardware tools. Parameter free resolution estimation in single images[15,51] and data processing methods for cluster analysis[52–54] utilize DNA

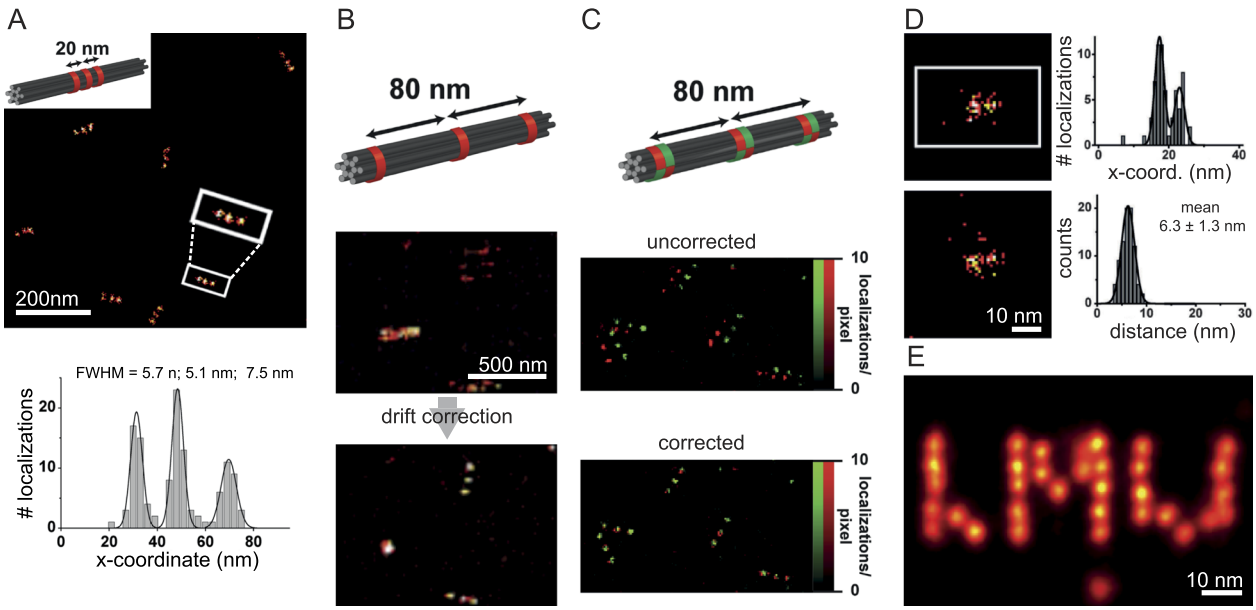

FIG. 2. Super-resolution microscopy with DNA-PAINT. (a) Nanorulers with 20 nm spacing between marks. The histogram shows the accumulated profile of a representative nanoruler (white frame) and is fitted with a triple gaussian.[28] (b) Fiducial marker (FM) and nanorulers with 80 nm spacing imaged simultaneously (upper image). Below, the same image, drift corrected using the positions of the FM.[62] (c) Two-color overlaid super-resolution images of nanorulers with 80 nm spacing between dual-color labeled marks before and after correction of the chromatic shift. The chromatic correction was calculated in a separate measurement of dual-color labeled DNA origami FMs.[28] (d) Single DNA origami structures with docking sites at a designed distance of ~6 nm. The upper histogram shows the accumulated profile of one representative DNA origami (white frame), fitted with a double Gaussian. The bottom histogram shows the distribution of many measured distances fitted with a Gaussian.[21] (e) Average image of 215 DNA origami structures with the letters "LMU." The distance between adjacent spots are ~5 nm.[60]

origami nanorulers as verification tool for their performance. Hardware improvements of microscopy setup components are also demonstrated with nanorulers as reference tool. This includes the introduction of a chip-based waveguide, which decouples the total internal reflection fluorescence (TIRF) illumination from the detection path,[55] the development of SPAD arrays for widefield applications,[56–58] and active stabilization of the sample throughout the measurement to reduce its drift.[59]

Sample drift is a crucial problem in SR microscopy. Whereas focus drift in the axial direction leads to an irretrievable loss in localization precision, a sample drift in the x–y-plane can be corrected for. Freely available and widely used localization software like Picasso[60] or ThunderSTORM[61] can use cross-correlation or fiducial-based alignment algorithms to back-calculate the x–y drift. For sufficient numbers of localizations, the cross-correlation can undrift the sample structures to a certain extent. A more precise and stable approach tracks the continuous signal from additional fiducial markers (FM) in the sample[62] [Fig. 2(b)]. However, the use of FM implies a reduced sample density to guarantee the diffraction limited separation of the continuous signals.

Besides the sample movement induced shifts, experimenters can also be confronted with steady shifts, e.g., chromatic aberrations induced by the optical elements in the detection path. For these shifts, a correction vector map can be generated by measuring dual color FM, or other structures, where fluorophores of both colors can be localized at the same position. This map can be evaluated in calibration measurements for linear shifts[28] [Fig. 2(c)], or, analogously, for radial and combined shifts.[63]

DNA origami FM used for the corrections above can be realized with fluorophores incorporated in a DNA origami structure making them also subject to photobleaching. More elegantly, DNA origami FM can be incorporated with many identical binding strands for DNA-PAINT. Renewal of labeled strands makes them free of photobleaching, maintaining a steady intensity trace, even throughout long measurements.[60] To reduce the background, one can use the same labeled imaging strands as for the structure under investigation.

In general, DNA-PAINT has recently attracted attention as the required dye blinking is separated from the photo-physics of the dyes so that the full photon budget of the brightest dyes can be used and multiplexing is facilitated using orthogonal binding sequences. Moreover, DNA-PAINT provides an additional information channel from examining the binding kinetics.[64,65] In recent publications, optimization of the binding kinetics was used to decrease the SR imaging time to the order of a minute.[66,67] Historically interesting, DNA-PAINT was first developed on DNA origamis and in conjunction with DNA origami rulers.[9,14] With DNA-PAINT labeled DNA origami structures with a spot distance of 6 nm could be resolved already in 2014 [Fig. 2(d)],[21] which was excelled in 2017 with 5 nm distances resolved in grid arrangements of dyes with ~1 nm precision, representing the letters "LMU" [Fig. 2(e)].[60] The latter study showed that the labeled DNA origami structures can

also be used as FM to undrift the sample. Other commonly used FM are gold nanoparticles (AuNPs), quantum dots, and fluorescent microspheres.

Over the last decade, SMLM advanced into the third dimension. Common methods use either the biplane approach[68] or astigmatism[69] to image in an axial range of several hundred nanometers. The ability of resolving several tenth of nanometers adds additional value to well-defined 3D DNA origami structures. The so-called nanopillars with 80 nm spot distance and arbitrary spatial orientation in the sample were first resolved under the use of astigmatism[23] and served as reference tool for a quantitative analysis on the performance of a 3D SR microscopy setup with the biplane approach[63] [Fig. 3(a)]. The option of attaching nanoparticles to DNA origami structures was used for a study of the shift of fluorescent signals induced by plasmonic nanoparticles placed in proximity of a fluorescent dye [Fig. 3(b)].[70] This can be visualized in 2D [red-yellow color code in left panels of Fig. 3(b), gray overlay indicates scattering of the nanoparticle] and 3D [blue-red color code in right panels of Fig. 3(b)], whereas the 3D imaging is essential for the quantitative estimation of the shift. In addition, flow cytometry recently advanced toward 3D imaging [Fig. 3(c)].[71] The SR of the two spots, labeled with different colors with 180 nm distance, was achieved by dual channel acquisition. A reference measurement with beads mapped the astigmatic change of the PSF to an axial position in the flow chamber (indicated with 1, 2, 3). The designed distance could then be recuperated from the distribution of several hundred nanorulers passing the field of view (FOV) one by one.[71]

Standard and customized DNA origami nanorulers are commonly available for all stochastic SMLM techniques mentioned in this paragraph. For TIRF microscopes, independent of the imaging technique of choice, sealed and "ready to image" DNA-PAINT samples can be purchased. A recent publication might even establish DNA-PAINT for HILO or EPI illumination.[72]

III. TARGETED SWITCHING SUPER-RESOLUTION NANORULERS

The second approach of super-resolution microscopy uses targeted switching of fluorescent molecules by using patterns in the excitation pathway and exploiting saturable transitions.[37] Stimulated emission depletion (STED) nanoscopy is a prominent example for these coordinate targeted techniques and overlays a donut-shaped depletion beam on a Gaussian excitation, hence reducing the effective detection volume.[4,73] The requirements for microscopy with targeted readout are different and therefore also need different DNA origami nanorulers. One major difference is that several dyes are allowed to fluoresce at the same time. Here, the versatility of DNA origami nanorulers can be seen in a wide range from diffraction limited to nanometer precise placements of dyes.

The most broadly used microscopy technique with structured illumination is confocal microscopy. Not being a SR technique, it requires diffraction limited samples, hence dyes separated by 386 nm on a six helix-bundle can be resolved [Fig. 4(a)]. For confocal

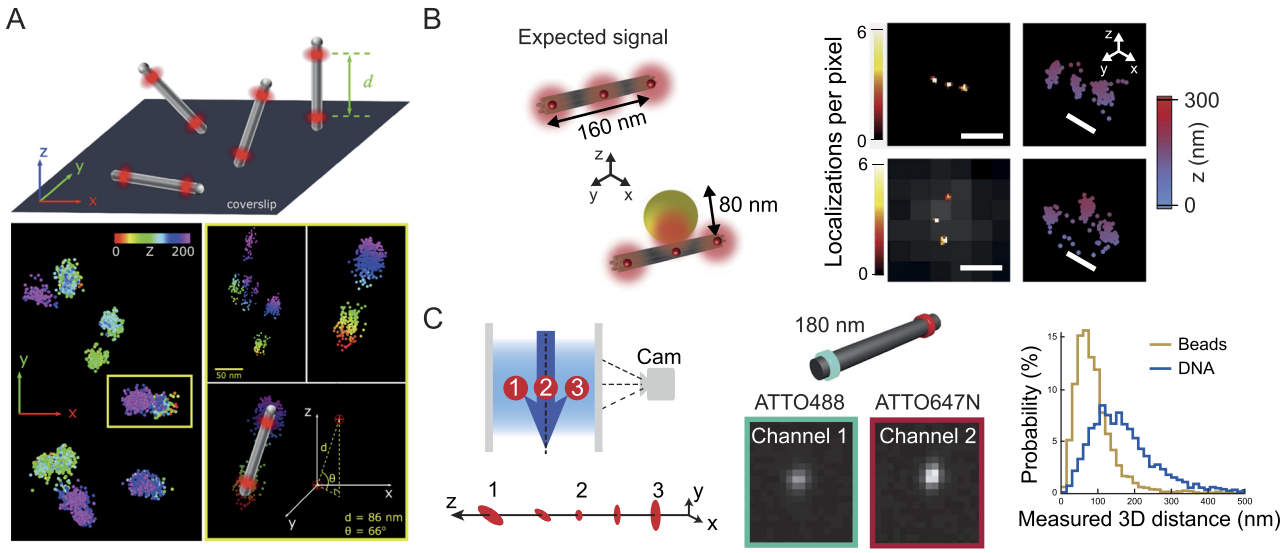

FIG. 3. (a) 3D DNA-PAINT image of 3D nanopillars with 80 nm spacing using the biplane method. The upper sketch shows nanopillars indicating a broad distribution of orientation. On the left is a 2D view of localization clouds in the x–y plane with color encoded z-position. An exemplary nanopillar (yellow frame) is depicted before (left) and after (right) drift correction and analyzed for the spatial separation and the angular orientation of the two spots (bottom).[63] (b) Molecular localization shift by plasmonic coupling. A sketch depicting the expected emission spots with and without the presence of a gold nanoparticle next to the respective 2D DNA-PAINT images (scale bars, 200 nm) and 3D DNA-PAINT images (scale bars, 100 nm).[70] (c) Multicolor 3D localization flow cytometry. A cylindrical lense in the detection pathway resolves the z positions (1, 2, 3) in the flow cell with astigmatism. Nanorulers, labeled with red and green dyes (180 nm distance between marks), are simultaneously detected in two color channels. From the respective x–y position (pinpointed by a gaussian) and the z position (estimated by the ellipticity of the PSF), distances between marks can be calculated in 3D. The histogram shows the measured distances of numerous nanorulers.[71]

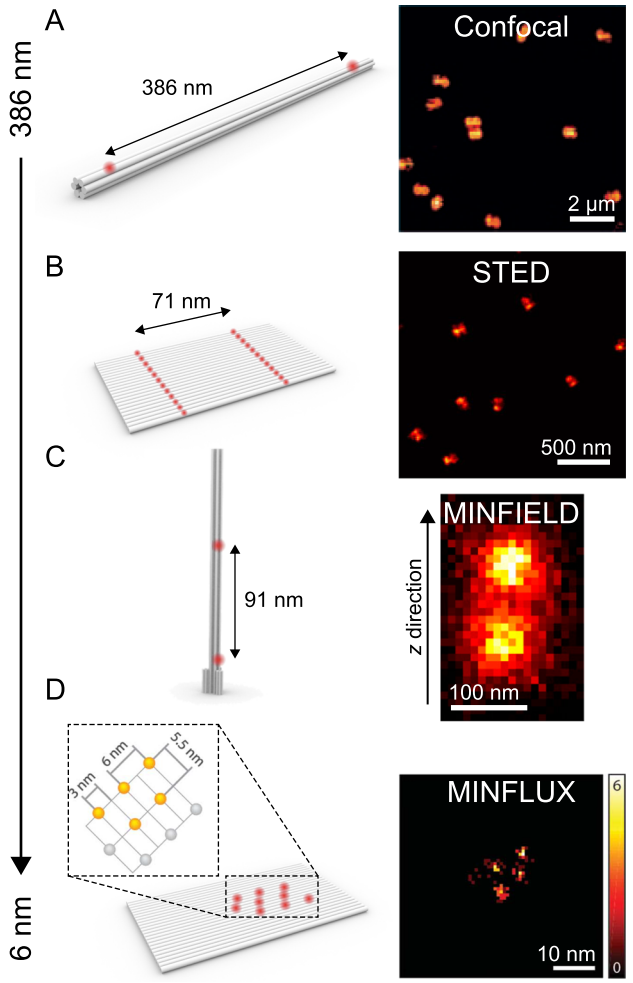

FIG. 4. DNA origami nanorulers across length scales for SR based on targeted switching. (a) Nanoruler for diffraction limited microscopy. On the left, a six helix-bundle labeled with two fluorophores in 386 nm distance is shown. Thus, the DNA origami is resolvable with standard confocal microscopy, which is shown on the right.[20] (b) Nanoruler for 2D STED microscopy: The sketch on the left shows a rectangular DNA origami labeled with two parallel lines of fluorophores at a distance of 71 nm. The panel on the right shows that these lines are resolved with STED microscopy.[20] (c) Nanoruler for 3D MINFIELD-STED microscopy. On the left, an upright 12 helix-bundle is shown and is labeled with single fluorophores at a distance of 91 nm. This 3D structure is resolved using MINFIELD-STED microscopy on the right.[82] (d) Nanoruler for MINFLUX nanoscopy. On the left, the labels on a rectangular DNA origami are indicated. On the right, using MINFLUX nanoscopy, the blinking fluorophores are resolved with 1 nm precision.[10]

microscopy, the applications range from calibration of the setup to training of experimenters.[20]

While the performance of a confocal setup can be calculated via Abbes formulas, this is not as straight-forward for SR setups, like STED microscopes. Here, the resolution is mainly dependent on the power of the depletion beam, however, also sample properties, e.g., the dyes themselves as well as photobleaching have an influence on the resolution.[29] Hence, the effective resolution needs to be accessed experimentally.[74] Thanks to the robustness and homogeneity of DNA origami nanorulers in signal and size, they are routinely used to resolve inter-mark distances down to few tens of nanometers, demonstrating that the SR setup can resolve the structures of interest [Fig. 4(b)]. These samples are mostly of biological nature and gave insights, e.g., in the actin/spectrin organization at synapses using 3-colors multilevel STED,[75] the γ-secretase in neural synapses[76] or topoisomerase in mitochondria.[77]

With increasing STED laser powers and improved resolution, the volume from which fluorescence is still allowed is decreasing so that fewer and fewer molecules are contributing to the signal and the background increases due to the high overall laser power. Resolution can then be limited by the signal-to-noise ratio and common fluorescent beads are either too big or not bright enough for optimal quantification of the STED abilities. To this end, DNA origamis can offer point-light sources with maximized brightness density. A typical DNA origami structure with 23 nm diameter could, e.g., be labeled with ~80 dyes and immobilized for STED imaging. With these DNA origami nanobeads, optimized point-spread-functions for STED deconvolution imaging were obtained that could not be matched with conventional fluorescent beads.[78]

The choice of dyes is another important aspect for optimizing STED microscopy. Using DNA origami nanorulers, different dyes were tested under different conditions.[79] In addition, the multiplexing possibility of DNA-PAINT was exploited in combination with STED by alternating washing and labeling steps of DNA origami structures.[80,81] Importantly, multiplexing was achieved with a single color system by encoding the different labels in the DNA sequences used for labeling.[79]

As DNA origami nanorulers are established, not only resolutions on existing methods are checked but also proof-of-principle measurements of new more powerful techniques are demonstrated with DNA origami nanorulers as the reference structure. One example is the introduction of the STED modality MINFIELD-STED. MINFIELD is an imaging strategy that increases resolution by reducing the exposure and hence the photobleaching.[82] With MINFIELD-STED, 2D objects smaller than 25 nm were resolved, as well as 3D DNA origami nanorulers with an axial precision of 60 nm [Fig. 4(c)]. Furthermore, other advances of STED nanoscopy, e.g., faster STED by parallel sub-second electro-optical-STED,[83] or in extended sample regions[83,84] were first demonstrated with DNA origami structures.[85,86]

The latest step in resolution of optical nanoscopy was the combination of advantages of single-molecule localization microscopy and excitation patterning shown in the so-called minimal photon flux nanoscopy (MINFLUX).[10,11] MINFLUX nanoscopy localizes the dye in the minimum of four donut-shaped beams, reaching localization precision in the single digit nanometer regime with less than 100 photons per localization, as well as enabling the tracking of quickly diffusing molecules. To be precise, MINFLUX requires stochastic switching for superresolution but was classified in this section due to the similarity of laser profiles. Proof-of-principle measurements were performed on DNA origami nanorulers, which resolved several dyes in less than 6 nm distances with a precision of less than 1 nm in 2D as well as 3D.[20] Here, several dyes were placed on a DNA origami nanoruler and activated stochastically and it was demonstrated that better localization precision could be

achieved with fewer detected photons. Similarly, other techniques called SIMFLUX[87] or Rose[88] use the idea to combine a structured illumination and its emission information to enhance the resolution twofold. Again, proof-of-principle measurements were shown with DNA origami nanorulers.

IV. ENERGY TRANSFER NANORULERS

The breadboard character of DNA origami nanorulers makes them an ideal tool to investigate distance dependent energy transfer mechanisms at the single-molecule level. Förster resonance energy transfer (FRET) ensemble studies using donor–acceptor labeled poly-proline were first conducted in 1967, showing higher FRET efficiencies than expected.[89] To investigate this discrepancy, rigid DNA origami blocks have been used as reference structures for quantitative single-molecule FRET studies. Placing donor and acceptor dyes on the surface of a DNA origami block with known distances reduces the influence of the dye linkers and circumvents the need for a multiparametric fit in comparison to commonly used dsDNA constructs.[90] Furthermore, FRET was used in combination with DNA origami nanostructures in 2009 to probe the controlled opening and closing of the dynamic lid of a DNA origami box designed for applications such as drug delivery [Fig. 5(a)].[91] Besides energy transfer between organic dyes, interactions of dyes with different materials ranging from nanoparticles to metallic surfaces are possible to be investigated in a highly controlled manner using DNA origami nanostructures. Analogously to FRET studies, nanoparticle or metallic surface induced quenching effects were examined with respect to fluorescence intensity, as well as fluorescence lifetime.[92] DNA origamis were used to position AuNPs at varying distance to a dye, and the quenching effect and its distance dependence were elucidated. Additionally, the precise positioning of AuNPs in close vicinity to a fluorophore can be used as a plasmonic nanoantenna. Placing a single fluorophore in the plasmonic hotspot induced by a single or multiple AuNPs, the fluorescence brightness is enhanced up to more than 400 fold.[93,94] Even further, a combination of AuNPs and FRET was already investigated and depending on the conditions, an enhancement of FRET rates could be found [Fig. 5(b)].[95,96] In addition, the coupling of plasmons on the DNA origamis itself as nanowires was demonstrated.[97]

A dye in an excited state can transfer its energy not only to metallic nanoparticles, but also to a metallic surface. The immobilization of 3D DNA origami structures with labeled fluorophores on such metallic surfaces enables the investigation of the z dimension due to the height dependent energy transfer [Fig. 5(c)]. This approach was used to study quenching effects of fluorophore labeled nanorulers to a gold surface, which later could be used as a calibration structure to deduce the height information of the labeled fluorophores.[98] Recent advances with the combination of semi-metallic graphene were made to increase the z-resolution to nanometer precision [Fig. 5(d)], which can be combined with SR microscopy techniques like, e.g., DNA-PAINT or MINFLUX to realize highly sensitive 3D SR microscopy.[99,100]

V. BRIGHTNESS REFERENCING AND EMERGING APPLICATIONS

A. Expansion Microscopy

Another approach to SR is physical expansion of the sample so that initially unresolvable distances are increased to values larger than the diffraction limit to achieve SR information. One advantage is that SR is achieved with common diffraction limited microscopy techniques. In expansion microscopy (ExM), the sample is embedded in an electrolytic polymer [Fig. 6(a)] to which the fluorescent labels are crosslinked.[101] After degradation of the sample, the polymer gel is expanded by dialysis with water. With conventional ExM,

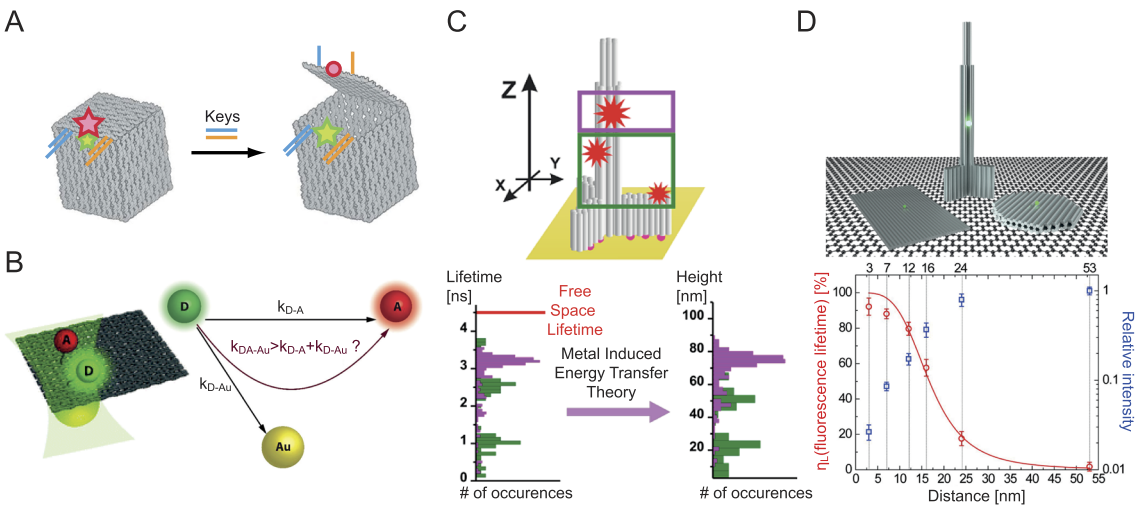

FIG. 5. (a) A box shaped DNA origami with a green and a red dye as a FRET pair, which acts as an opening sensor.[91] (b) Positioning of a donor dye, an acceptor dye, and a gold nanoparticle for the investigation of energy transfer rates. It was shown that an AuNP can enhance the FRET rate.[95] (c) Gold surfaces or semi-metallic surfaces like graphene act as powerful quenchers, which can enable nanometer resolution along the optical axis.[98–100] (d) Positioning of dyes on graphene with DNA origami nanopositioner yields quenching of intensity and fluorescence lifetime of a dye depending on its height with a d^{-4} distance dependence.[99]

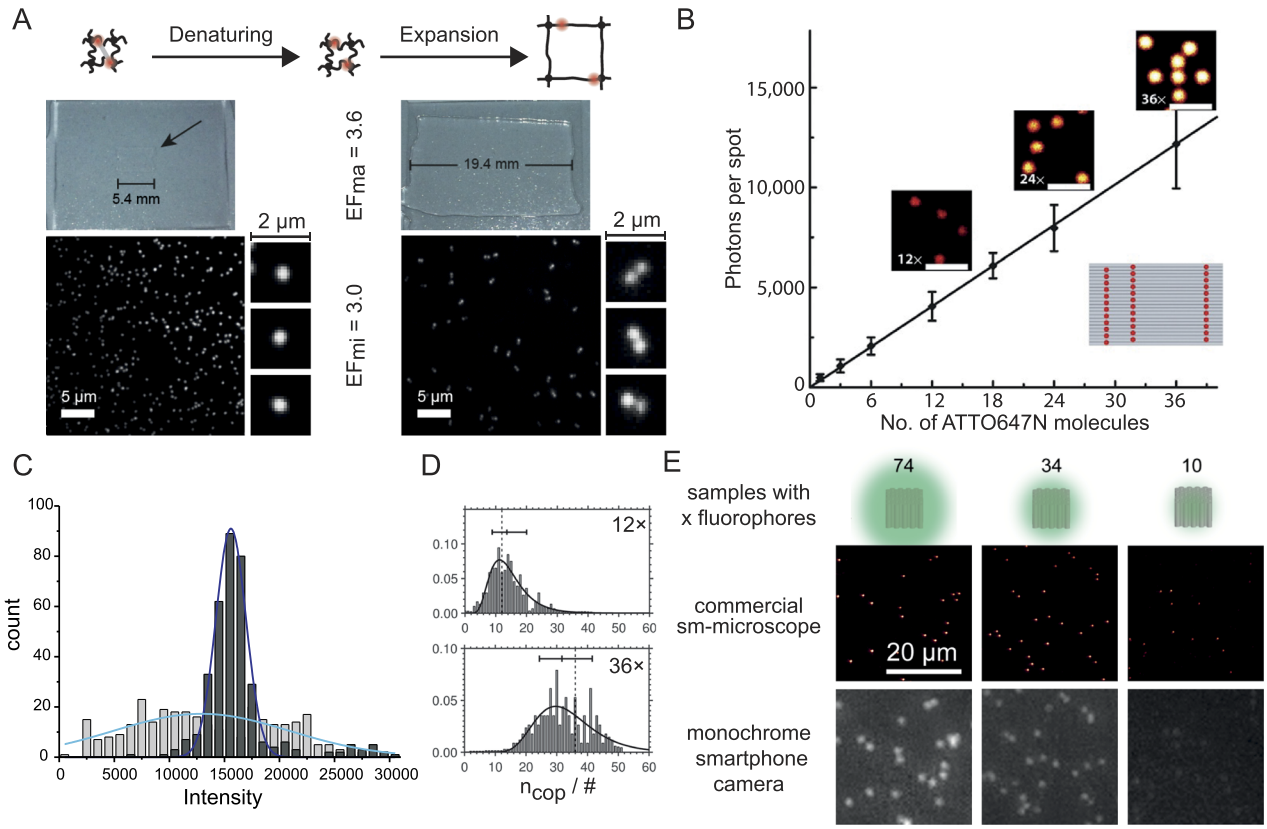

FIG. 6. (a) Top: Polyacrylamide gel before (5.4 mm average width) and after expansion (19.4 mm average width) with a macroscopic expansion factor of 3.6. Bottom: TIRF microscopy image of immobilized nanorulers before gelation and expansion carrying ATTO647N dyes. After expansion nanorulers are imaged in epi-fluorescence and the 160 nm intermark distances are clearly resolved, represented by two adjacent spots (selected zoom-ins).[105] (b) Rectangular DNA origami as fluorescence brightness standard. Top insets, fluorescence images of 12×, 24×, or 36× ATTO647N dyes on the DNA origami. Bottom inset is the sketch of nanoruler with 36× dyes. Scale bars, 2 μm; color scale from 15 to 100 counts.[20] (c) Counting dyes by means of photon statistics. Probability density of estimated emitter numbers from rectangular DNA origami with 12× and 36× ATTO 647N dyes. A log-normal fit to the probability density is depicted as a solid line. Box plot indicates the central 68% quantile about the median of the probability density. The dashed line represents the expected emitter number.[79] (d) Brightness distributions of DNA origami nanobeads (GATTA-Beads, 23 nm) and conventional polystyrene beads (FluoSpheres, 40 nm) reveal the superior homogeneity of DNA origami based nanobeads.[79] (e) Images of highly labeled DNA origami nanobeads (10×, 34×, and 74× dyes) taken with a commercial super-resolution microscope and a monochrome smartphone camera-based fluorescence microscope. The scale bar is applicable to all images.[107]

macroscopic expansion factors of 3–5× are usually achieved, while further increased resolution factors are realized with more sophisticated techniques like iterative ExM (up to 20fold) or by a combination of ExM with SIM.[102–104] Generally, the expansion factor is determined at the macroscopic scale, i.e., by examining the macroscopic swelling of the gel. However, several parameters are critical for characterizing ExM including the expansion factor, cross-linking efficiency, the fraction of active dyes after expansion, and so on. Using nanorulers with inter-mark distances of 160 nm, it could be shown that nanorulers could efficiently be expanded yielding bright marks that could be resolved with conventional microscopy [Fig. 6(a)].[105] Interestingly, the microscopic expansion factor yielded smaller microscopic expansion factors of 3.0 compared to a macroscopic expansion factor of 3.6, which could be explained by the surface immobilization of the DNA origami nanorulers. For a quantitative interpretation of biological expansion microscopy, nanorulers as *in situ* references could also be helpful to reveal anisotropy in the expansion process.

As SR techniques, especially MINFLUX, probe the single nanometer regime, a particular interest of DNA origami nanoruler is how close two dyes can be placed. On one hand, the placement of dyes is DNA-base pair specific, and on the other hand, dye–dye interactions may occur. Hence, DNA origami nanorulers were used as a breadboard to investigate the intensity and lifetime of two dyes in a single base pair precise distance.[35] It was found that, in the case of ATTO 647N at small distances, the lifetimes and intensities of the dyes decrease, which is due to the static quenching of H-type dimer formation. Hence, two independent dyes on a DNA origami nanoruler are limited to a minimal distance of seven base pairs, which equals ~2.3 nm. This leads to the conclusion that in total more than 1000 dyes can be placed on a single DNA origami structure without losing the intensity signal. Together with the highly

controllable breadboard character of DNA origami nanorulers, this naturally leads to DNA origami structures as brightness standards. This is especially interesting for the characterization of the PSF for donut-shaped beams, commonly used in STED and MINFLUX.[11]

B. Brightness referencing

The quantification of labeled dye numbers, i.e., counting the individual fluorophoric labels, plays a key role in the investigation of biological processes as, e.g., in the determination of protein rates and protein complex stoichiometries or the deduction of mathematical models.[106] As discussed in the introduction, appropriately labeled DNA origami structures show a linear dependence of signal intensity on the number of incorporated dyes [Fig. 6(b)].[19,20,107] Together with the stoichiometric control of incorporation, DNA origami nanostructures can thus be used as quantitative signal references. Using DNA origami brightness references, a sensitivity scale of units of fluorescent molecules could be introduced similar to the MESF (molecules of equivalent soluble fluorochrome) that is used in cytometry. In this context, the advantage of DNA origami reference samples (also called DNA origami beads) is that the same dyes as for the sample of interest can be used and the dyes are in a similar chemical buffer environment to the sample in contrast to plastic beads commonly used in flow cytometry.[108] Additionally, recent applications of spectroscopic barcoding in cytometry, i.e., the multicolor and multi-stoichiometric labeling of molecules of interest, require the exact determination of the number of labeled dye molecules with single fluorophore sensitivity.[109]

Counting molecules is also important in microscopy to determine how many labeled molecules contribute to a signal. Counting molecules by intensities has the disadvantage that intensity is an extensive variable. For developing alternative techniques, the photon statistics has for example been used also using DNA origami nanorulers. Techniques like "counting by photon statistics" (CoPS)[110] use the idea of photon antibunching to deduce the number of independent emitters and their molecular brightness [Fig. 6(c)].[85] Here, DNA origami nanorulers with their controllable number of dyes were used as proof-of-principle samples, resolving the number of physical emitters.

The potentially large labeling density of DNA origami nanorulers and the high control over the labeling stoichiometry enable the design of compact and very bright fluorescent beads. Commercially available DNA origami based fluorescent beads show an improved homogeneity and flexibility compared to other conventional beads [Fig. 6(d)]. Such DNA origami nanobeads could be used, e.g., in the determination of PSF in 3D STED microscopy.[79] Highly labeled DNA origami brightness references have also been applied for probing the sensitivity of other types of microscopes. In the recent past, smartphone-based fluorescence microscopy (SBFM) has, for example, evolved as a promising approach to various applications in point-of-care (POC) diagnostics like quantification of immunoassays, detection of microorganisms, or sensing of viruses.[107,111] Although SBFM creates a promising low-cost and field-portable solution, high detection sensitivity comparable to laboratory-based fluorescence microscopes is necessary for the detection of target substances at the single-molecule level. DNA origami nanobeads with up to 74 labeled fluorophores were used to quantify the detection sensitivity of a SBFM [Fig. 6(e)].[107] For the monochrome smartphone camera used in the study, a sensitivity down to 10 fluorophores could be determined. Recently, detection of single emitters on a SBFM could even be achieved by placing single fluorophores in the plasmonic hotspot of a DNA origami based nanoantenna.[94]

The high control over designed geometries and the breadboard character of DNA origami structures enables the creation of reference structures also for other imaging methods besides optical fluorescence microscopy. For example, placing plasmonic nanoparticles on a 24 helix-bundle DNA origami as shown in Fig. 7(a) forms chiral nanorulers especially suitable for 3D tomography or electron microscopy (EM).[112,113] The nanorulers of pure chirality (either left-handed L or right-handed R conformation) can easily be detected with EM due to their high contrast and show circular dichroism (CD) due to plasmonic resonance of the chirally labeled nanoparticles. In electron tomography, such chiral nanorulers were used as reference structures to determine the left-handed chirality of macrofibrils in mammalian hair.[114,115]

Besides placing modifications on DNA origami for nanometrology, the designed structural geometry of the DNA origami itself can

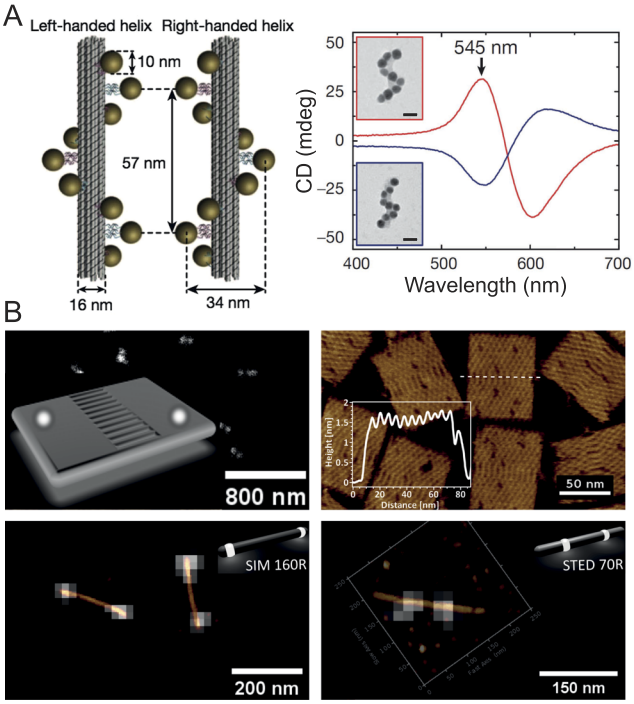

FIG. 7. (a) Left: Left- and right-handed nanohelices with nine gold nanoparticles attached to 24-helixbundle DNA origami. Right: Exemplary corresponding CD spectra of L (red) and R (blue) nanohelices. Insets show TEM images of corresponding nanohelices (scale bars, 20 nm).[112] (b) Top left: Sketch of a DNA rectangular origami (GATTA-AFM) with the theoretical locations for the Atto647N fluorophores. Background shows an STED image of the corresponding nanorulers. Top right: Fast amplitude modulation (AM) AFM image of the DNA origami lattice. The inset represents a cross-section across the central ladder seam of the DNA nanostructure (z-scale: 2 nm). Bottom: Optical correlation of consecutively acquired STED and AFM images of (left) SIM160R and (right) STED70R nanoruler (GATTAquant GmbH) with corresponding sketches.[116]

TABLE I. Overview of typical used DNA origami nanorulers for different fluorescence microscopy techniques.

Microscopy techniques	Distance/nm	Number of fluorophores per spot
MINFLUX 2D[10]/3D[11]	<10	1
STORM 2D[20,55,123]/3D[23]	30, 50, 90/180	6/10
DNA-PAINT 2D[19–21]/3D[63]	<10, 20, 40, 80/30, 80	1–6/10
SIM[122]	140	20
Confocal[20]	270–350	20
STED 2D[75]/3D[82]	50, 70, 90/80	20/15

be used as a nanoruler. By designing the stapling of the scaffold strand, structural characteristics of known geometry can be introduced into the DNA origami. This can be used to design topological nanorulers for scanning probe microscopy (SPM).[27] Figure 7(b) top images show an atomic force microscopy (AFM) nanoruler based on a rectangular DNA origami.[116] The depicted AFM nanoruler exhibits a central ladder seam bridging the crossed halves with a pitch of 6 nm, which can be used as a reference structure for quantitative AFM analysis [Fig. 7(b) top right]. Combining controlled positioning of fluorophores on the DNA origami and the design of the geometrical structure itself makes it a powerful tool for correlating AFM and optical microscopy. Exemplary optical correlation of STED and AFM for 160 nm and 70 nm nanorulers is shown in Fig. 7(b) bottom. The consecutively acquired STED and AFM images underline the accurately designed geometries of the fluorophore marks and the nanoruler itself. Additionally, combining the topographic information of AFM with the tip induced quenching of labeled fluorophores on DNA origami enabled correlative localization studies with sub 5 nm resolution.[117] DNA origami reference structures were also successfully used to investigate the production of singlet oxygen from a single photosensitizer molecule conjugated to the nanoruler. The subsequent diffusion of the singlet oxygen could be visualized by placing singlet oxygen cleavable linker molecules with biotin labels in designed distances to the photosensitizer molecule. After binding of streptavidin to the remaining linker molecules with biotin labels, the diffusion radii of the produced singlet oxygen molecules could be examined via AFM imaging.[118]

Also, the combination of confocal microscopy with an ABEL trap uses DNA origami nanorulers to test the performance of the setup.[119] The ABEL trap is an electrophoretic system, which tracks small particles via fluorescence and applies an electrokinetic feedback, which cancels the Brownian motion of the particle, thus trapping the particle.[120]

On one hand, the fluorophore of the DNA origami nanoruler is used to detect the DNA origami and control the anti-Brownian electrokinetic trap (ABEL trap). On the other hand, the origami aspect was used to explore different hydrodynamic radii, hence diffusion coefficients, and test the performance of this setup.

VI. CONCLUSION

DNA origami nanorulers provide an unprecedented control of shape and stoichiometry of impressively large objects. The simplicity of fabrication and the chemical robustness have enabled DNA origami to become the scaffold for reference structures in several fields of research and technology. In this perspective, we highlight the emerging applications in optical microscopy, scanning probe microscopy, and electron microscopy. In the meantime, even manufacturers of microscopes promote their products using DNA origami nanoruler demonstration.[121,122] On the other hand, DNA origami nanorulers as a ubiquitously available single-molecule standard can help customers to decide which microscope to purchase for a specific application and are frequently used as positive control for training the respective microscopy technique.

Typical and commonly used DNA origami nanorulers for different fluorescence microscopy techniques are listed in Table I with the required distances and fluorophore numbers.

For the future, we expect an ever-growing applicability of DNA origami nanorulers, brightness references, and further emerging applications in the fields of cytometry, microfluidics, and molecular diagnostics as well as fluorescence and correlative microscopy. As new functionalities are easily added for targeting the DNA origami to different local environments and binding partners, DNA reference structures have the potential to report on local events and to work *in situ* in complex chemical environments.

AUTHORS' CONTRIBUTIONS

M.S., J.B., and J.Z. contributed equally to this work.

ACKNOWLEDGMENTS

The authors thank Carsten Forthmann and Jürgen Schmied for their input and discussions. We gratefully acknowledge financial support from the DFG (Grant No. INST 86/1904-1 FUGG, TI 329/9-2, excellence clusters NIM and e-conversion, SFB1032), BMBF (Grant Nos. POCEMON, 13N14336, and SIBOF, 03VP03891), and the European Union's Horizon 2020 research and innovation program under Grant Agreement No. 737089 (Chipscope).

DATA AVAILABILITY

Data sharing is not applicable to this article as no new data were created or analyzed in this study.

REFERENCES

[1]S. W. Hell, S. J. Sahl, M. Bates, X. Zhuang, R. Heintzmann, M. J. Booth, J. Bewersdorf, G. Shtengel, H. Hess, P. Tinnefeld, A. Honigmann, S. Jakobs, I. Testa, L. Cognet, B. Lounis, H. Ewers, S. J. Davis, C. Eggeling, D. Klenerman, K. I. Willig, G. Vicidomini, M. Castello, A. Diaspro, and T. Cordes, J. Phys. D: Appl. Phys. **48**, 443001 (2015).
[2]D. Baddeley and J. Bewersdorf, Annu. Rev. Biochem. **87**, 965 (2018).
[3]G. Jacquemet, A. F. Carisey, H. Hamidi, R. Henriques, and C. Leterrier, J. Cell Sci. **133**, jcs240713 (2020).
[4]T. A. Klar, S. Jakobs, M. Dyba, A. Egner, and S. W. Hell, Proc. Natl. Acad. Sci. U. S. A. **97**, 8206 (2000).
[5]M. J. Rust, M. Bates, and X. Zhuang, Nat. Methods **3**, 793 (2006).
[6]M. Heilemann, S. van de Linde, M. Schüttpelz, R. Kasper, B. Seefeldt, A. Mukherjee, P. Tinnefeld, and M. Sauer, Angew. Chem. **120**, 6266 (2008).
[7]E. Betzig, G. H. Patterson, R. Sougrat, O. W. Lindwasser, S. Olenych, J. S. Bonifacino, M. W. Davidson, J. Lippincott-Schwartz, and H. F. Hess, Science **313**, 1642 (2006).

[8]A. Sharonov and R. M. Hochstrasser, Proc. Natl. Acad. Sci. U. S. A. **103**, 18911 (2006).
[9]R. Jungmann, C. Steinhauer, M. Scheible, A. Kuzyk, P. Tinnefeld, and F. C. Simmel, Nano Lett. **10**, 4756 (2010).
[10]F. Balzarotti, Y. Eilers, K. C. Gwosch, A. H. Gynnå, V. Westphal, F. D. Stefani, J. Elf, and S. W. Hell, Science **355**, 606 (2017).
[11]K. C. Gwosch, J. K. Pape, F. Balzarotti, P. Hoess, J. Ellenberg, J. Ries, and S. W. Hell, Nat. Methods **17**, 217 (2020).
[12]M. G. L. Gustafsson, Proc. Natl. Acad. Sci. U. S. A. **102**, 13081 (2005).
[13]M. G. L. Gustafsson, J. Microsc. **198**, 82 (2000).
[14]C. Steinhauer, R. Jungmann, T. L. Sobey, F. C. Simmel, and P. Tinnefeld, Angew. Chem., Int. Ed. **48**, 8870 (2009).
[15]A. Descloux, K. S. Grußmayer, and A. Radenovic, Nat. Methods **16**, 918 (2019).
[16]N. Banterle, K. H. Bui, E. A. Lemke, and M. Beck, J. Struct. Biol. **183**, 363 (2013).
[17]J. V. Thevathasan, M. Kahnwald, K. Cieśliński, P. Hoess, S. K. Peneti, M. Reitberger, D. Heid, K. C. Kasuba, S. J. Hoerner, Y. Li, Y.-L. Wu, M. Mund, U. Matti, P. M. Pereira, R. Henriques, B. Nijmeijer, M. Kueblbeck, V. J. Sabinina, J. Ellenberg, and J. Ries, Nat. Methods **16**, 1045 (2019).
[18]U. Endesfelder and M. Heilemann, Nat. Methods **11**, 235 (2014).
[19]J. J. Schmied, M. Raab, C. Forthmann, E. Pibiri, B. Wünsch, T. Dammeyer, and P. Tinnefeld, Nat. Protoc. **9**, 1367 (2014).
[20]J. J. Schmied, A. Gietl, P. Holzmeister, C. Forthmann, C. Steinhauer, T. Dammeyer, and P. Tinnefeld, Nat. Methods **9**, 1133 (2012).
[21]M. Raab, J. J. Schmied, I. Jusuk, C. Forthmann, and P. Tinnefeld, ChemPhysChem **15**, 2431 (2014).
[22]C. Steinhauer, R. Jungmann, T. L. Sobey, F. C. Simmel, and P. Tinnefeld, Angew. Chem. **121**, 9030 (2009).
[23]J. J. Schmied, C. Forthmann, E. Pibiri, B. Lalkens, P. Nickels, T. Liedl, and P. Tinnefeld, Nano Lett. **13**, 781 (2013).
[24]P. W. K. Rothemund, Nature **440**, 297 (2006).
[25]S. M. Douglas, H. Dietz, T. Liedl, B. Högberg, F. Graf, and W. M. Shih, Nature **459**, 414 (2009).
[26]C. E. Castro, F. Kilchherr, D.-N. Kim, E. L. Shiao, T. Wauer, P. Wortmann, M. Bathe, and H. Dietz, Nat. Methods **8**, 221 (2011).
[27]Y. Ke, S. Lindsay, Y. Chang, Y. Liu, and H. Yan, Science **319**, 180 (2008).
[28]M. Raab, I. Jusuk, J. Molle, E. Buhr, B. Bodermann, D. Bergmann, H. Bosse, and P. Tinnefeld, Sci. Rep. **8**, 1780 (2018).
[29]S. Beater, M. Raab, and P. Tinnefeld, *Methods in Cell Biology* (Academic Press, Inc., 2014), pp. 449–466.
[30]X.-C. Bai, T. G. Martin, S. H. W. Scheres, and H. Dietz, Proc. Natl. Acad. Sci. U. S. A. **109**, 20012 (2012).
[31]S. Fischer, C. Hartl, K. Frank, J. O. Rädler, T. Liedl, and B. Nickel, Nano Lett. **16**, 4282 (2016).
[32]J. J. Funke and H. Dietz, Nat. Nanotechnol. **11**, 47 (2016).
[33]M. T. Strauss, F. Schueder, D. Haas, P. C. Nickels, and R. Jungmann, Nat. Commun. **9**, 1600 (2018).
[34]A. Shaw, I. T. Hoffecker, I. Smyrlaki, J. Rosa, A. Grevys, D. Bratlie, I. Sandlie, T. E. Michaelsen, J. T. Andersen, and B. Högberg, Nat. Nanotechnol. **14**, 184 (2019).
[35]T. Schröder, M. B. Scheible, F. Steiner, J. Vogelsang, and P. Tinnefeld, Nano Lett. **19**, 1275 (2019).
[36]R. Iinuma, Y. Ke, R. Jungmann, T. Schlichthaerle, J. B. Woehrstein, and P. Yin, Science **344**, 65 (2014).
[37]S. J. Sahl, S. W. Hell, and S. Jakobs, Nat. Rev. Mol. Cell Biol. **18**, 685 (2017).
[38]M. Sauer and M. Heilemann, Chem. Rev. **117**, 7478 (2017).
[39]A. Jimenez, K. Friedl, and C. Leterrier, Methods **174**, 100 (2020).
[40]J. Fölling, M. Bossi, H. Bock, R. Medda, C. A. Wurm, B. Hein, S. Jakobs, C. Eggeling, and S. W. Hell, Nat. Methods **5**, 943 (2008).
[41]T. Dertinger, R. Colyer, G. Iyer, S. Weiss, and J. Enderlein, Proc. Natl. Acad. Sci. U. S. A. **106**, 22287 (2009).
[42]G. Giannone, E. Hosy, F. Levet, A. Constals, K. Schulze, A. I. Sobolevsky, M. P. Rosconi, E. Gouaux, R. Tampé, D. Choquet, and L. Cognet, Biophys. J. **99**, 1303 (2010).
[43]G. Patterson, M. Davidson, S. Manley, and J. Lippincott-Schwartz, Annu. Rev. Phys. Chem. **61**, 345 (2010).
[44]S. Tajada, C. M. Moreno, O. Samantha, S. Woods, D. Sato, M. F. Navedo, and L. F. Santana, J. Gen. Physiol. **149**, 639 (2017).
[45]Y. G. Suárez, J. L. Martínez, D. T. Hernández, H. O. Hernández, A. Pérez-Delgado, M. Méndez, C. D. Wood, J. M. Rendon-Mancha, D. Silva-Ayala, S. López, A. Guerrero, and C. F. Arias, Elife **8**, e42906 (2019).
[46]H. A. T. Pritchard, P. W. Pires, E. Yamasaki, P. Thakore, and S. Earley, Proc. Natl. Acad. Sci. U. S. A. **115**, E9745 (2018).
[47]H. A. T. Pritchard, C. S. Griffin, E. Yamasaki, P. Thakore, C. Lane, A. S. Greenstein, and S. Earley, Proc. Natl. Acad. Sci. U. S. A. **116**, 21874 (2019).
[48]K. J. A. Martens, S. P. B. van Beljouw, S. van der Els, J. N. A. Vink, S. Baas, G. A. Vogelaar, S. J. J. Brouns, P. van Baarlen, M. Kleerebezem, and J. Hohlbein, Nat. Commun. **10**, 3552 (2019).
[49]I. Jayasinghe, A. H. Clowsley, and C. Soeller, *Advances in Biomembranes and Lipid Self-Assembly*, edited by A. Iglič, M. Rappolt, and L. S.-A. García-Sáez (Academic Press, 2018), pp. 167–197.
[50]J. L. Davis, B. Dong, C. Sun, and H. F. Zhang, J. Biomed. Opt. **23**, 1 (2018).
[51]S. Mailfert, J. Touvier, L. Benyoussef, R. Fabre, A. Rabaoui, M.-C. Blache, Y. Hamon, S. Brustlein, S. Monneret, D. Marguet, and N. Bertaux, Biophys. J. **115**, 565 (2018).
[52]R. J. Marsh, K. Pfisterer, P. Bennett, L. M. Hirvonen, M. Gautel, G. E. Jones, and S. Cox, Nat. Methods **15**, 689 (2018).
[53]A. D. Staszowska, P. Fox-Roberts, L. M. Hirvonen, C. J. Peddie, L. M. Collinson, G. E. Jones, and S. Cox, Bioinformatics **34**, 4102 (2018).
[54]M. Fazel, M. J. Wester, B. Rieger, R. Jungmann, and K. A. Lidke, bioRxiv 752287 (2019).
[55]R. Diekmann, Ø. I. Helle, C. I. Øie, P. McCourt, T. R. Huser, M. Schüttpelz, and B. S. Ahluwalia, Nat. Photonics **11**, 322 (2017).
[56]I. Gyongy, A. Davies, N. A. W. Dutton, R. R. Duncan, C. Rickman, R. K. Henderson, and P. A. Dalgarno, Sci. Rep. **6**, 37349 (2016).
[57]I. M. Antolovic, S. Burri, C. Bruschini, R. A. Hoebe, and E. Charbon, Sci. Rep. **7**, 44108 (2017).
[58]M. Caccia, L. Nardo, R. Santoro, and D. Schaffhauser, Nucl. Instrum. Methods Phys. Res., Sect. A **926**, 101 (2019).
[59]S. Coelho, J. Baek, M. S. Graus, J. M. Halstead, P. R. Nicovich, K. Feher, H. Gandhi, J. J. Gooding, and K. Gaus, Sci. Adv. **6**, eaay8271 (2020).
[60]J. Schnitzbauer, M. T. Strauss, T. Schlichthaerle, F. Schueder, and R. Jungmann, Nat. Protoc. **12**, 1198 (2017).
[61]M. Ovesný, P. Křížek, J. Borkovec, Z. Švindrych, and G. M. Hagen, Bioinformatics **30**, 2389 (2014).
[62]J. Schmied, Opt. Photonik **11**, 23 (2016).
[63]R. Lin, A. H. Clowsley, T. Lutz, D. Baddeley, and C. Soeller, Methods **174**, 56 (2020).
[64]R. Jungmann, M. S. Avendaño, M. Dai, J. B. Woehrstein, S. S. Agasti, Z. Feiger, A. Rodal, and P. Yin, Nat. Methods **13**, 439 (2016).
[65]O. K. Wade, J. B. Woehrstein, P. C. Nickels, S. Strauss, F. Stehr, J. Stein, F. Schueder, M. T. Strauss, M. Ganji, J. Schnitzbauer, H. Grabmayr, P. Yin, P. Schwille, and R. Jungmann, Nano Lett. **19**, 2641 (2019).
[66]F. Schueder, J. Stein, F. Stehr, A. Auer, B. Sperl, M. T. Strauss, P. Schwille, and R. Jungmann, Nat. Methods **16**, 1101 (2019).
[67]S. Strauss and R. Jungmann, Nat. Methods **17**, 789 (2020).
[68]M. F. Juette, T. J. Gould, M. D. Lessard, M. J. Mlodzianoski, B. S. Nagpure, B. T. Bennett, S. T. Hess, and J. Bewersdorf, Nat. Methods **5**, 527 (2008).
[69]B. Huang, W. Wang, M. Bates, and X. Zhuang, Science **319**, 810 (2008).
[70]M. Raab, C. Vietz, F. D. Stefani, G. P. Acuna, and P. Tinnefeld, Nat. Commun. **8**, 13966 (2017).
[71]L. E. Weiss, Y. S. Ezra, S. Goldberg, B. Ferdman, O. Adir, A. Schroeder, O. Alalouf, and Y. Shechtman, Nat. Nanotechnol. **15**, 500 (2020).
[72]K. K. H. Chung, Z. Zhang, P. Kidd, Y. Zhang, N. D. Williams, B. Rollins, Y. Yang, C. Lin, D. Baddeley, and J. Bewersdorf, bioRxiv:066886 (2020).
[73]S. W. Hell and J. Wichmann, Opt. Lett. **19**, 780 (1994).

[74]C. A. Combs, D. L. Sackett, and J. R. Knutson, J. Microsc. **274**, 168 (2019).
[75]S. C. Sidenstein, E. D'Este, M. J. Böhm, J. G. Danzl, V. N. Belov, and S. W. Hell, Sci. Rep. **6**, 26725 (2016).
[76]S. Schedin-Weiss, I. Caesar, B. Winblad, H. Blom, and L. O. Tjernberg, Acta Neuropathol. Commun. **4**, 29 (2016).
[77]T. J. Nicholls, C. A. Nadalutti, E. Motori, E. W. Sommerville, G. S. Gorman, S. Basu, E. Hoberg, D. M. Turnbull, P. F. Chinnery, N.-G. Larsson, E. Larsson, M. Falkenberg, R. W. Taylor, J. D. Griffith, and C. M. Gustafsson, Mol. Cell **69**, 9 (2018).
[78]J. J. S. J. J. Schmied, R. Dijkstra, M. Scheible, and G. M. R. De Luca, "Measuring the 3D STED-PSF with a new type of fluorescent beads," available at https://www.leica-microsystems.com/science-lab/measuring-the-3d-sted-psf-with-a-new-type-of-fluorescent-beads/.
[79]S. Beater, P. Holzmeister, E. Pibiri, B. Lalkens, and P. Tinnefeld, Phys. Chem. Chem. Phys. **16**, 6990 (2014).
[80]S. Beater, P. Holzmeister, B. Lalkens, and P. Tinnefeld, Opt. Express **23**, 8630 (2015).
[81]R. Jungmann, M. S. Avendaño, J. B. Woehrstein, M. Dai, W. M. Shih, and P. Yin, Nat. Methods **11**, 313 (2014).
[82]F. Göttfert, T. Pleiner, J. Heine, V. Westphal, D. Görlich, S. J. Sahl, and S. W. Hell, Proc. Natl. Acad. Sci. U. S. A. **114**, 2125 (2017).
[83]J. Alvelid and I. Testa, J. Phys. D: Appl. Phys. **53**, ab4c13 (2020).
[84]A. Girsault and A. Meller, Opt. Lett. **45**, 2712 (2020).
[85]H. Ta, J. Keller, M. Haltmeier, S. K. Saka, J. Schmied, F. Opazo, P. Tinnefeld, A. Munk, and S. W. Hell, Nat. Commun. **6**, 7977 (2015).
[86]M. Oneto, L. Scipioni, M. J. Sarmento, I. Cainero, S. Pelicci, L. Furia, P. G. Pelicci, G. I. Dellino, P. Bianchini, M. Faretta, E. Gratton, A. Diaspro, and L. Lanzanò, Biophys. J. **117**, 2054 (2019).
[87]J. Cnossen, T. Hinsdale, R. Thorsen, M. Siemons, F. Schueder, R. Jungmann, C. S. Smith, B. Rieger, and S. Stallinga, Nat. Methods **17**, 59 (2020).
[88]L. Gu, Y. Li, S. Zhang, Y. Xue, W. Li, D. Li, T. Xu, and W. Ji, Nat. Methods **16**, 1114 (2019).
[89]L. Stryer and R. P. Haugland, Proc. Natl. Acad. Sci. U. S. A. **58**, 719 (1967).
[90]I. H. Stein, V. Schüller, P. Böhm, P. Tinnefeld, and T. Liedl, ChemPhysChem **12**, 689 (2011).
[91]E. S. Andersen, M. Dong, M. M. Nielsen, K. Jahn, R. Subramani, W. Mamdouh, M. M. Golas, B. Sander, H. Stark, C. L. P. Oliveira, J. S. Pedersen, V. Birkedal, F. Besenbacher, K. V. Gothelf, and J. Kjems, Nature **459**, 73 (2009).
[92]G. P. Acuna, M. Bucher, I. H. Stein, C. Steinhauer, A. Kuzyk, P. Holzmeister, R. Schreiber, A. Moroz, F. D. Stefani, T. Liedl, F. C. Simmel, and P. Tinnefeld, ACS Nano **6**, 3189 (2012).
[93]G. P. Acuna, F. M. Möller, P. Holzmeister, S. Beater, B. Lalkens, and P. Tinnefeld, Science **338**, 506 (2012).
[94]K. Trofymchuk, V. Glembockyte, L. Grabenhorst, F. Steiner, C. Vietz, C. Close, M. Pfeiffer, L. Richter, M. L. Schütte, F. Selbach, R. Yaadav, J. Zähringer, Q. Wei, A. Ozcan, B. Lalkens, G. P. Acuna, and P. Tinnefeld, bioRxiv:2020.04.09.032037 (2020).
[95]N. Aissaoui, K. Moth-Poulsen, M. Käll, P. Johansson, L. M. Wilhelmsson, and B. Albinsson, Nanoscale **9**, 673 (2017).
[96]J. Bohlen, Á. Cuartero-González, E. Pibiri, D. Ruhlandt, A. I. Fernández-Domínguez, P. Tinnefeld, and G. P. Acuna, Nanoscale **11**, 7674 (2019).
[97]K. Korobchevskaya, B. Lagerholm, H. Colin-York, and M. Fritzsche, Photonics **4**, 41 (2017).
[98]S. Isbaner, N. Karedla, I. Kaminska, D. Ruhlandt, M. Raab, J. Bohlen, A. Chizhik, I. Gregor, P. Tinnefeld, J. Enderlein, and R. Tsukanov, Nano Lett. **18**, 2616 (2018).
[99]I. Kaminska, J. Bohlen, S. Rocchetti, F. Selbach, G. P. Acuna, and P. Tinnefeld, Nano Lett. **19**, 4257 (2019).
[100]A. Ghosh, A. Sharma, A. I. Chizhik, S. Isbaner, D. Ruhlandt, R. Tsukanov, I. Gregor, N. Karedla, and J. Enderlein, Nat. Photonics **13**, 860 (2019).
[101]F. Chen, P. W. Tillberg, and E. S. Boyden, Science **347**, 543 (2015).
[102]J.-B. Chang, F. Chen, Y.-G. Yoon, E. E. Jung, H. Babcock, J. S. Kang, S. Asano, H.-J. Suk, N. Pak, P. W. Tillberg, A. T. Wassie, D. Cai, and E. S. Boyden, Nat. Methods **14**, 593 (2017).
[103]Y. Wang, Z. Yu, C. K. Cahoon, T. Parmely, N. Thomas, J. R. Unruh, B. D. Slaughter, and R. S. Hawley, Nat. Protoc. **13**, 1869 (2018).
[104]A. R. Halpern, G. C. M. Alas, T. J. Chozinski, A. R. Paredez, and J. C. Vaughan, ACS Nano **11**, 12677 (2017).
[105]M. B. Scheible and P. Tinnefeld, bioRxiv:265405 (2018).
[106]V. C. Coffman and J.-Q. Wu, Mol. Biol. Cell **25**, 1545 (2014).
[107]C. Vietz, M. L. Schütte, Q. Wei, L. Richter, B. Lalkens, A. Ozcan, P. Tinnefeld, and G. P. Acuna, ACS Omega **4**, 637 (2019).
[108]A. Schwartz, A. K. Gaigalas, L. Wang, G. E. Marti, R. F. Vogt, and E. Fernandez-Repollet, Cytometry, Part B **57B**, 1 (2004).
[109]L. D. Smith, Y. Liu, M. U. Zahid, T. D. Canady, L. Wang, M. Kohli, B. T. Cunningham, and A. M. Smith, ACS Nano **14**, 2324 (2020).
[110]A. Kurz, J. J. Schmied, K. S. Grußmayer, P. Holzmeister, P. Tinnefeld, and D.-P. Herten, Small **9**, 4061 (2013).
[111]Q. Wei, G. Acuna, S. Kim, C. Vietz, D. Tseng, J. Chae, D. Shir, W. Luo, P. Tinnefeld, and A. Ozcan, Sci. Rep. **7**, 2124 (2017).
[112]A. Kuzyk, R. Schreiber, Z. Fan, G. Pardatscher, E.-M. Roller, A. Högele, F. C. Simmel, A. O. Govorov, and T. Liedl, Nature **483**, 311 (2012).
[113]A. Briegel, M. Pilhofer, D. N. Mastronarde, and G. J. Jensen, J. Struct. Biol. **183**, 95 (2013).
[114]D. P. Harland, V. Novotna, M. Richena, S. Velamoor, M. Bostina, and A. J. McKinnon, J. Struct. Biol. **206**, 345 (2019).
[115]D. P. Harland, V. Novotná, M. Richena, M. Bostina, S. Velamoor, and A. J. McKinnon, Microsc. Microanal. **25**, 1348 (2019).
[116]T. Neumann, J. Barner, and D. Stamov, JPK Application Note 1, 2014.
[117]O. Schulz, Z. Zhao, A. Ward, M. Koenig, F. Koberling, Y. Liu, J. Enderlein, H. Yan, and R. Ros, Opt. Nanosc. **2**, 1 (2013).
[118]S. Helmig, A. Rotaru, D. Arian, L. Kovbasyuk, J. Arnbjerg, P. R. Ogilby, J. Kjems, A. Mokhir, F. Besenbacher, and K. V. Gothelf, ACS Nano **4**, 7475 (2010).
[119]M. Dienerowitz, F. Dienerowitz, and M. Börsch, J. Opt. **20**, 034006 (2018).
[120]A. E. Cohen and W. E. Moerner, Appl. Phys. Lett. **86**, 093109 (2005).
[121]J. Huff, W. Bathe, R. Netz, T. Anhut, and K. Weisshart, Technology Note by ZEISS 1, 2015.
[122]R. T. Borlinghaus and C. Kappel, Nat. Methods **13**, i (2016).
[123]L. Wang, B. Bateman, L. C. Zanetti-Domingues, A. N. Moores, S. Astbury, C. Spindloe, M. C. Darrow, M. Romano, S. R. Needham, K. Beis, D. J. Rolfe, D. T. Clarke, and M. L. Martin-Fernandez, Commun. Biol. **2**, 74 (2019).

7.2 Publication II: The Art of Molecular Programming – Optical Control

by

Jonas Zähringer, Michael Scheckenbach and Philip Tinnefeld

book chapter accepted in

The Art of Molecular Programming

Author contributions:

I wrote parts of the manuscript and prepared the figures together with Michael Scheckenbach.

Optical Control

Jonas Zähringer, Michael Scheckenbach, Philip Tinnefeld

Primer on optical materials

DNA itself interacts with electromagnetic radiation below 400 nm yielding well-documented and cancerogenous DNA breaks as well as specific photochemistry such as thymine-thymine dimerization, covalently linked by ultraviolet radiation exposure. For DNA nanotechnology, photodimerization has specifically been used to chemically stabilize DNA nanostructures or to relief strain.[1, 2, 3]

More generally, DNA systems with optical control are generated by attaching optically active components to DNA scaffolds, strands and structures. Representative optical components are fluorescent dyes and photosensitizers, photocleavable and photoswitchable molecules often employing the prototypical azo-compounds, and plasmonic nanoparticles (most typically made of gold or silver). Further active compounds are quantum dots, lanthanides, upconverting particles as well as polymers, which are, however, not covered in this chapter.

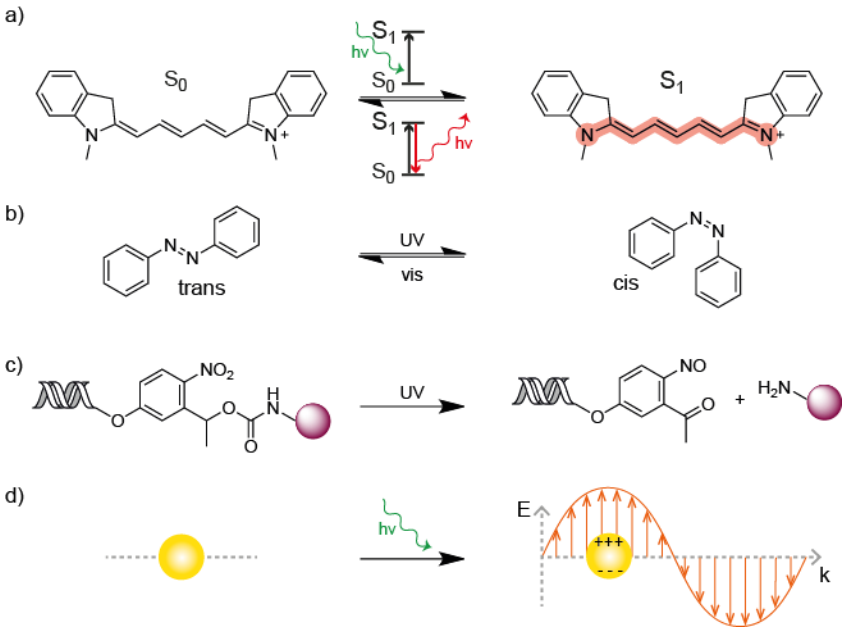

Figure 1. Examples of optically active reporters. a) Exemplary cyanine dye Cy5 in the electronic ground state S_0 and after excitation by a photon of suitable energy to the first excited state S_1. Spontaneous emission of a red shifted photon, i.e. fluorescence, results again in the ground state S_0. b) An azo-benzene photoswitch in the relaxed *trans*-conformation and after UV light triggered isomerization to the *cis*-conformation. c) An *o*-nitrobenzyl motif for an UV light triggered bond

break and cargo release. d) Exemplary plasmonic metal nanoparticle before and after light induced surface plasmon resonance.

Fluorescent dyes are optical reporters that are excited to the first excited singlet state and emit a red-shifted fluorescence photon (Figure 1a). In combination with sensitive microscopy, they report on the location, properties and functioning of DNA nanostructures even on the level of single entities. The whole toolbox of single-molecule spectroscopy can be applied to DNA structures including superresolution and single-molecule FRET.

Conformationally switchable dyes such as azo-benzenes absorb light. In the excited state, they undergo a conformational transition commonly from an energetically favored *trans*-conformation to a *cis*-conformation (Figure 1b). Photocleavable compounds show a programmed breakage of a covalent bond that helps to elicit a molecular function such as the release of a drug from a cage (Figure 1c).[4]

Despite their small size substantially smaller than the optical wavelength, plasmonic nanoparticles have a large cross section for visible light due to the localized excitation of collective electron oscillations (i.e. localized surface plasmons (LSP)). Especially gold and silver are commonly used due to their plasmonic resonances in the visible spectrum and for their chemical accessibility of different shaped nanoparticles and the possibility of the attachment to DNA nanostructures.[5]

Plasmonic nanoparticles offer many possibilities how they report on molecular interactions and can be used to optically control nanoscale interaction. Their resonance wavelength depends, for example, strongly on the dielectric environment so that single-molecule binding events to gold nanorods could be detected by the shift of the resonant plasmon band.[6] Furthermore, the proximity of plasmonic particles leads to coupling of their LSPs, which leads to easily detectable plasmonic shifts as well as a number of other interesting effects discussed below. The enhanced electric fields on the surface of nanoparticles can additionally increase the interaction of the light field with molecules in the proximity of the nanoparticles. The effect is strongly enhanced in gaps between particles (“gap antennas”) which is exploited for surface enhanced spectroscopies (Figure 1d).

Finally, heating of plasmonic particles due to Ohmic losses is a further means of controlling DNA nanostructures at the nanoscale.

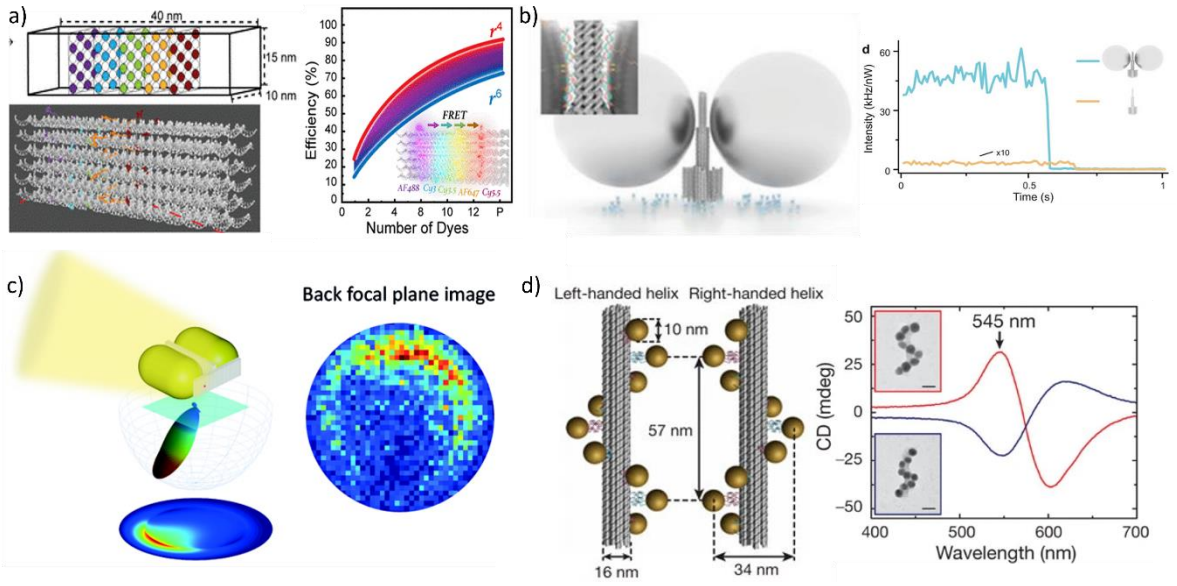

Figure 2. Examples of nanophotonic light control enabled by DNA nanotechnology. a) Schematic of a DNA origami structure with a two-dimensional sheet placement of fluorophores. The placement of fluorophores in two-dimensional sheets enables the modification of the distance dependence of FRET from $1/r^6$ towards $1/r^4$. Adapted from [7] b) Schematic of a DNA origami structure with two plasmonic nanoparticles. The nanoparticles generate plasmonic hotspots which can enhance the fluorescence of fluorophore in the plasmonic hotspot hundreds fold. Adapted from [8] c) Schematic of a DNA origami with two nanorods in a nanoantenna design. The back focal plane image shows the direction of the emitter fluorescence. Adapted from [9] d) Schematic and circular dichroism simulation of a DNA origami structure modified in a rotary pattern of plasmonic nanoparticles. The chirality of the rotary pattern enables tuning of the circular dichroism. Adapted from [10]

DNA plasmonic and photonic circuits

Photonic circuits are believed to replace electronic circuits due to their potentially higher speed and parallelizability. A primary challenge is the compaction of photonic circuits beyond the limits of diffraction using nanophotonics. On the nanoscale, light can, for example be controlled by plasmonic particles and their arrangements or by excitation energy transport in chromophores in analogy to excitation energy transport in light harvesting complexes. To this end, an excited chromophore can transfer its energy to neighboring chromophores by coherent or incoherent (Förster-type) energy transfer. As dyes are commonly attached to DNA by aliphatic linkers, their precise location and orientation is not well controlled but rapid thermal equilibration in liquid buffer solutions can ensure homogeneous Förster energy transfer between dyes in cascades (termed photonic wires)[11], with less energy loss using homo-FRET[12], and for light funneling.[13] More recently, pseudoisocyanine aggregates could be assembled in A-tracts of DNA forming J-aggregates that successfully transmitted excited state energy from a donor through the J-aggregate to an acceptor dye.[14] Interestingly, with many acceptor dyes, the distance dependence can shift from $1/r^6$ (Förster) and approach $1/r^4$ in analogy to true 2D material energy transfer

acceptors (Figure 2a).[7, 15] Similar to dyes, plasmonic nanoparticles can also funnel energy, e.g. to a gap between the particles in DNA-directed plasmonic gap antennas.[16] Here, the resonant electron oscillations of two or more particles couple and create a drastically increased electric field in the hotspot region between the nanoparticles. Surface enhanced spectroscopies such as Raman or fluorescence spectroscopy can yield drastically enhanced signal allowing single molecule detection for Raman active or single fluorescent molecule detection with simple optics including a smartphone camera.[8, 17, 18](Figure 2b). An asymmetric assembly can also steer the direction of the fluorescence emission (Figure 2c)[9, 19]. Coupled particles can also transport energy over long distances after the energy is induced by a donor and it can be transmitted to an acceptor through several particles. A thermo-responsive polymer attached to one of the particles even modulated the degree of energy transfer.[20] Furthermore, DNA origami precisely decorated with plasmonic nanoparticles shows a drastic dependence of the circular dichroism spectrum on their orientation to the light beam.[10] (Figure 2d). Orienting the nanostructures using the polarization of light beam hence allows the switching of the CD spectrum.[21]

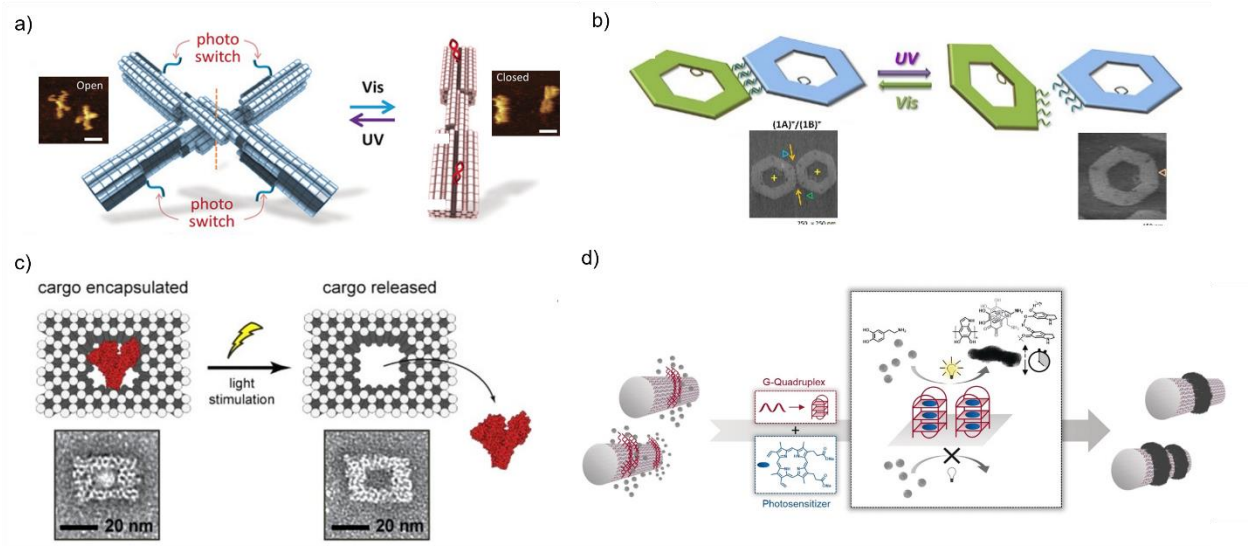

Figure 3. Photocontrolled DNA devices and functionalities. a) Schematic and AFM images of DNA origami modified with azobenzene enables the switching of a cross to a longitudinal state using Visible and UV light respectively. Adapted from [22] b) Schematic and TEM images of a DNA origami assembly modified with azobenzene bonds which can be controlled using UV and visible light. Thus, the formation or disassociation of DNA origami assemblies can be photo controlled respectively. Adapted from [23] c) Schematic and TEM image of a DNA origami structure with encapsulated BSA. By light stimulation the *o*-nitrobenzyl motifs break and the cargo is released in a photocontrolled manner. Adapted from [4] d) Schematic of a photoinduced polymerization process. With photosensitizer embedded in G-Quadruplexes, a chemical reaction which forms a polymerization on the DNA origami structure can be controlled via light. Adapted from [24]

Dynamic control of optical DNA devices

Introducing conformationally switchable dyes into DNA nanodevices enables the reversible photoinduced switching between two designed states or can fuel nano machines. The prototypical photoswitch azobenzene consist of two phenyl rings linked by an azo group and adopt the *trans* conformation in the ground state (Figure 1b). After excitation with UV light, the azo compound can rotate and isomerize to the *cis* isomer. Excitation of the *cis* isomer by visible light induces the reverse rotation and isomerization back to the *trans* state. By introducing azobenzene moieties to the DNA backbone, the hybridization of the two modified DNA strands can be externally controlled. While *trans*-azobenzene favors the DNA duplex formation due to constructive stacking interactions with neighboring nucleobases, the non-planar cis form destabilizes the duplex by steric hindrance and triggers strand dissociation.[19] The photoinduced hybridization and dissociation were used to switch scissor shaped DNA nanodevices reversibly between a closed state, which is locked by the duplex formation of *trans*-azobenzene DNA, and an open state after strand dissociation. [22, 25](Figure 3a). Modifying the closing strands of a DNA nanocapsule with azobenzene enabled the reversible photoresponsive opening of the nanocapsule after irradiation with UV light and closing after irradiation with visible light.[26] [23] Azobenzene-modified DNA could also be employed as intermolecular binding units between DNA origami for the design of photoswitchable supramolecular self-assemblies up to the micrometer scale (Figure 3b). [23] Introduction of structurally relative arylazopyrazole-modified DNA oligonucleotides as additional intermolecular binding strands enabled the control of two photoswitchable supramolecular self-assemblies with different irradiation wavelengths simultaneously.[27]

The modification of functional DNA nanostructures with chemical groups containing photolabile bonds opens up the possibility of a photocontrolled bond dissociation within a DNA nanodevice for applications such as drug delivery or the specific photo-uncaging of biomolecules. Nitrobenzyl is a photolabile group and can be incorporated into the DNA backbone for the synthesis of DNA strands for further cleaving by UV irradiation (Figure 1c). By using nitrobenzyl-modified strands for the binding of cargo molecules, DNA origami -based carrier systems for the light triggered release of bioactive molecules like proteins can be designed(Figure 3c).[4] Bioactive molecules may also be specifically caged in DNA nanostructures to suppress their biological activity. For example, trapping Cas9 protein with single guide RNA in a DNA origami by nitrobenzyl-modified binding strands enables photo-induced release and controlled activation of the Cas9 protein.[28] In another example, the hybridization activity of DNA strands was suppressed by protecting thymine bases with a 6-nitropiperonyloxymethyl (NPOM) caging groups preventing Watson Crick base pairing. The photocleavage of the NPOM groups from a caged trigger strand then opened a DNA nanotweezer.[29]

Beside the control of mechanical movement also mechanical properties *e.g.* stability can be controlled *via* light (Figure 3d). Using a photosensitizer embedded in a guanine-rich quadruplex, reactive oxygen species (ROS) is produced locally upon irradiation. Thus with spatiotemporal control, a dopamine polymerization was started using ROS.[24] Furthermore, modified DNA origami structures with photosensitizer offer a targeting carrier system for the delivery of ROS inside cells with spatiotemporal control and the possibility for photodynamic therapy.[30]

Glossary terms:

- Ohmic loss
- H-aggregate
- J-aggregates
- A-tract

1. Chen H, Li R, Li S, Andreasson J, Choi JH. Conformational Effects of UV Light on DNA Origami. *J Am Chem Soc* 2017, **139**(4)**:** 1380-1383.

2. Gerling T, Kube M, Kick B, Dietz H. Sequence-programmable covalent bonding of designed DNA assemblies. *Sci Adv* 2018, **4**(8)**:** eaau1157.

3. Brown TM, Fakih HH, Saliba D, Asohan J, Sleiman HF. Stabilization of Functional DNA Structures with Mild Photochemical Methods. *Journal of the American Chemical Society* 2023.

4. Kohman RE, Cha SS, Man H-Y, Han X. Light-Triggered Release of Bioactive Molecules from DNA Nanostructures. *Nano Letters* 2016, **16**(4)**:** 2781-2785.

5. Kuzyk A, Jungmann R, Acuna GP, Liu N. DNA Origami Route for Nanophotonics. *ACS Photonics* 2018, **5**(4)**:** 1151-1163.

6. Zijlstra P, Paulo PMR, Orrit M. Optical detection of single non-absorbing molecules using the surface plasmon resonance of a gold nanorod. *Nature Nanotechnology* 2012, **7**(6)**:** 379-382.

7. Mathur D, Samanta A, Ancona MG, Díaz SA, Kim Y, Melinger JS*, et al.* Understanding Förster Resonance Energy Transfer in the Sheet Regime with DNA Brick-Based Dye Networks. *ACS Nano* 2021, **15**(10)**:** 16452-16468.

8. Trofymchuk K, Glembockyte V, Grabenhorst L, Steiner F, Vietz C, Close C*, et al.* Addressable nanoantennas with cleared hotspots for single-molecule detection on a portable smartphone microscope. *Nat Commun* 2021, **12**(1)**:** 950.

9. Zhu F, Sanz-Paz M, Fernández-Domínguez AI, Zhuo X, Liz-Marzán LM, Stefani FD*, et al.* DNA-Templated Ultracompact Optical Antennas for Unidirectional Single-Molecule Emission. *Nano Letters* 2022, **22**(15)**:** 6402-6408.

10. Kuzyk A, Schreiber R, Fan Z, Pardatscher G, Roller E-M, Högele A*, et al.* DNA-based self-assembly of chiral plasmonic nanostructures with tailored optical response. *Nature* 2012, **483**(7389)**:** 311-314.

11. Heilemann M, Kasper R, Tinnefeld P, Sauer M. Dissecting and reducing the heterogeneity of excited-state energy transport in DNA-based photonic wires. *J Am Chem Soc* 2006, **128**(51)**:** 16864-16875.

12. Nicoli F, Barth A, Bae W, Neukirchinger F, Crevenna AH, Lamb DC*, et al.* Directional Photonic Wire Mediated by Homo-Förster Resonance Energy Transfer on a DNA Origami Platform. *ACS Nano* 2017, **11**(11)**:** 11264-11272.

13. Hemmig EA, Creatore C, Wunsch B, Hecker L, Mair P, Parker MA*, et al.* Programming Light-Harvesting Efficiency Using DNA Origami. *Nano letters* 2016, **16**(4)**:** 2369-2374.

14. Boulais É, Sawaya NPD, Veneziano R, Andreoni A, Banal JL, Kondo T*, et al.* Programmed coherent coupling in a synthetic DNA-based excitonic circuit. *Nature Materials* 2018, **17**(2)**:** 159-166.

15. Kaminska I, Bohlen J, Rocchetti S, Selbach F, Acuna GP, Tinnefeld P. Distance Dependence of Single-Molecule Energy Transfer to Graphene Measured with DNA Origami Nanopositioners. *Nano Letters*; 2019. pp. 4257-4262.

16. Yeşilyurt ATM, Huang J-S. Emission Manipulation by DNA Origami-Assisted Plasmonic Nanoantennas. *Advanced Optical Materials* 2021, **9**(21)**:** 2100848.

17. Tapio K, Mostafa A, Kanehira Y, Suma A, Dutta A, Bald I. A Versatile DNA Origami-Based Plasmonic Nanoantenna for Label-Free Single-Molecule Surface-Enhanced Raman Spectroscopy. *ACS Nano* 2021, **15**(4)**:** 7065-7077.

18. Glembockyte V, Grabenhorst L, Trofymchuk K, Tinnefeld P. DNA Origami Nanoantennas for Fluorescence Enhancement. *Acc Chem Res* 2021, **54**(17)**:** 3338-3348.

19. Hübner K, Pilo-Pais M, Selbach F, Liedl T, Tinnefeld P, Stefani FD*, et al.* Directing Single-Molecule Emission with DNA Origami-Assembled Optical Antennas. *Nano Letters* 2019, **19**(9)**:** 6629-6634.

20. Vogele K, List J, Pardatscher G, Holland NB, Simmel FC, Pirzer T. Self-Assembled Active Plasmonic Waveguide with a Peptide-Based Thermomechanical Switch. *ACS Nano* 2016, **10**(12)**:** 11377-11384.

21. Schreiber R, Luong N, Fan Z, Kuzyk A, Nickels PC, Zhang T*, et al.* Chiral plasmonic DNA nanostructures with switchable circular dichroism. *Nature Communications* 2013, **4**(1)**:** 2948.

22. Willner EM, Kamada Y, Suzuki Y, Emura T, Hidaka K, Dietz H*, et al.* Single-Molecule Observation of the Photoregulated Conformational Dynamics of DNA Origami Nanoscissors. *Angewandte Chemie International Edition* 2017, **56**(48)**:** 15324-15328.

23. Yang Y, Endo M, Hidaka K, Sugiyama H. Photo-Controllable DNA Origami Nanostructures Assembling into Predesigned Multiorientational Patterns. *Journal of the American Chemical Society* 2012, **134**(51)**:** 20645-20653.

24. Winterwerber P, Harvey S, Ng DYW, Weil T. Photocontrolled Dopamine Polymerization on DNA Origami with Nanometer Resolution. *Angewandte Chemie International Edition* 2020, **59**(15)**:** 6144-6149.

25. Kuzyk A, Yang Y, Duan X, Stoll S, Govorov AO, Sugiyama H*, et al.* A light-driven three-dimensional plasmonic nanosystem that translates molecular motion into reversible chiroptical function. *Nature Communications* 2016, **7**(1)**:** 10591.

26. Takenaka T, Endo M, Suzuki Y, Yang Y, Emura T, Hidaka K*, et al.* Photoresponsive DNA Nanocapsule Having an Open/Close System for Capture and Release of Nanomaterials. *Chemistry – A European Journal* 2014, **20**(46)**:** 14951-14954.

27. Mishra S, Park S, Emura T, Kumi H, Sugiyama H, Endo M. Photocontrolled DNA Origami Assembly by Using Two Photoswitches. *Chemistry – A European Journal* 2021, **27**(2)**:** 778-784.

28. Abe K, Sugiyama H, Endo M. Construction of an optically controllable CRISPR-Cas9 system using a DNA origami nanostructure. *Chemical Communications* 2021, **57**(45)**:** 5594-5596.

29. Liu M, Jiang S, Loza O, Fahmi NE, Šulc P, Stephanopoulos N. Rapid Photoactuation of a DNA Nanostructure using an Internal Photocaged Trigger Strand. *Angewandte Chemie International Edition* 2018, **57**(30)**:** 9341-9345.

30. Zhuang X, Ma X, Xue X, Jiang Q, Song L, Dai L*, et al.* A Photosensitizer-Loaded DNA Origami Nanosystem for Photodynamic Therapy. *ACS Nano* 2016, **10**(3)**:** 3486-3495.

7.3 Publication III: Pulsed interleaved MINFLUX

by

Luciano A. Masullo*, Florian Steiner*, Jonas Zähringer, Lucía F. Lopez, Johann Bohlen,

Lars Richter, Fiona Cole, Philip Tinnefeld, Fernando D. Stefani (* equal contribution)

published in

NanoLetters, 2021, 21, 840-846 (2021) DOI: 10.1021/acs.nanolett.0c04600

Author contributions:

The initial idea of pMINFLUX was proposed from our collaboration partner. I built the pMINFLUX setup together with Florian Steiner and Luciano Masullo. The control software was written by me on basis of an initial framework of Luciano Masullo. I designed the pointer experiments together with Johann Bohlen. The pointer measurements were performed together with Fiona Cole and me and I analyzed the data together with Luciano Masullo. All other experiments were designed, performed, and analyzed by me. I wrote parts of the manuscript.

NANO LETTERS

pubs.acs.org/NanoLett Letter

Pulsed Interleaved MINFLUX

Luciano A. Masullo,[▽] Florian Steiner,[▽] Jonas Zähringer, Lucía F. Lopez, Johann Bohlen, Lars Richter, Fiona Cole, Philip Tinnefeld,* and Fernando D. Stefani*

Cite This: https://dx.doi.org/10.1021/acs.nanolett.0c04600 Read Online

ACCESS | Metrics & More | Article Recommendations | Supporting Information

ABSTRACT: We introduce p-MINFLUX, a new implementation of the highly photon-efficient single-molecule localization method with a simplified experimental setup and additional fluorescence lifetime information. In contrast to the original MINFLUX implementation, p-MINFLUX uses interleaved laser pulses to deliver the doughnut-shaped excitation foci at a maximum repetition rate. Using both static and dynamic DNA origami model systems, we demonstrate the performance of p-MINFLUX for single-molecule localization nanoscopy and tracking, respectively. p-MINFLUX delivers 1−2 nm localization precision with 2000−1000 photon counts. In addition, p-MINFLUX gives access to the fluorescence lifetime enabling multiplexing and super-resolved lifetime imaging. p-MINFLUX should help to unlock the full potential of innovative single-molecule localization schemes.

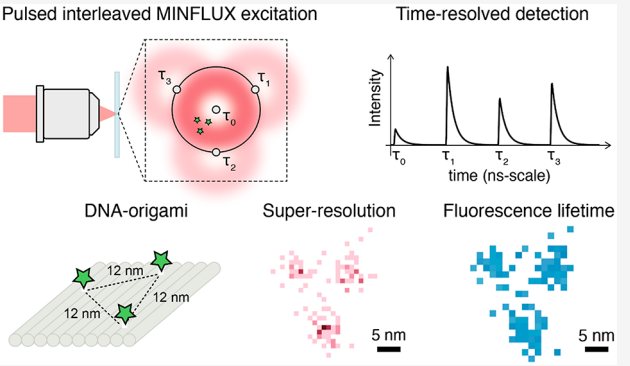

KEYWORDS: *fluorescence, super-resolution microscopy, DNA origami, single-molecule spectroscopy*

INTRODUCTION

Super-resolution fluorescence microscopy, also known as far-field fluorescence nanoscopy, has revolutionized biological imaging, because it keeps the advantages of fluorescence microscopy while delivering subdiffraction, theoretically unlimited, spatial resolution.[1−3] The first generation of super-resolution methods, which includes scanning methods, such as STED,[4,5] and wide-field single-molecule localization microscopy (SMLM) methods such as STORM[6] and PALM,[7,8] typically reaches lateral resolutions in the range of 20−50 nm, limited by fluorophore photostability. Axial resolution is normally 2-fold to 3-fold worse, in the range of 60−120 nm. More recently, this limitation was partly overcome by DNA-PAINT,[9,10] reaching lateral resolutions of <10 nm.[11,12] Imaging with this level of resolution is already enabling the characterization of subcellular structures and pathways in their natural environment with nanometric resolution, and the discovery of supramolecular protein structures.[13] Still, an extra push to the resolution limit was necessary to reach the ultimate resolution of a fluorescence microscope, namely, the molecular size of the fluorescent marker. This was achieved using a technique called MINFLUX (MINimal emission FLUXes),[14] which is a new strategy that combines structured illumination and single-molecule localization to extract maximum positional information of a single molecule using minimal photon counts. MINFLUX can routinely deliver a localization precision of ∼1 nm both in imaging and tracking of single molecules. It has been demonstrated in model systems (DNA origami structures),[14−16] fixed and living cells,[14,16,17] and it was recently extended to three dimensions.[16] While MINFLUX has represented a breakthrough, its widespread use has been slowed, because of the high technical complexity of its experimental implementation.

Here, we present pulsed interleaved MINFLUX (p-MINFLUX), which is a novel experimental realization of MINFLUX that is easier to implement in existing confocal microscopes equipped with a time-correlated single-photon counting (TCSPC) detection, only by modifying the excitation path of the microscope. No fast-scanning optics or field-programmable gate array (FPGA) electronics are required. Moreover, compared to the original MINFLUX, p-MINFLUX has the additional advantage of giving access to excited-state lifetime information, which is a relevant parameter in single-molecule spectroscopy, because it enables multiplexing of single-color measurements[18] and provides information about the environment of the fluorophore and its interactions with other molecules or materials.[19,20]

Received: November 19, 2020
Revised: December 14, 2020

https://dx.doi.org/10.1021/acs.nanolett.0c04600
Nano Lett. XXXX, XXX, XXX−XXX

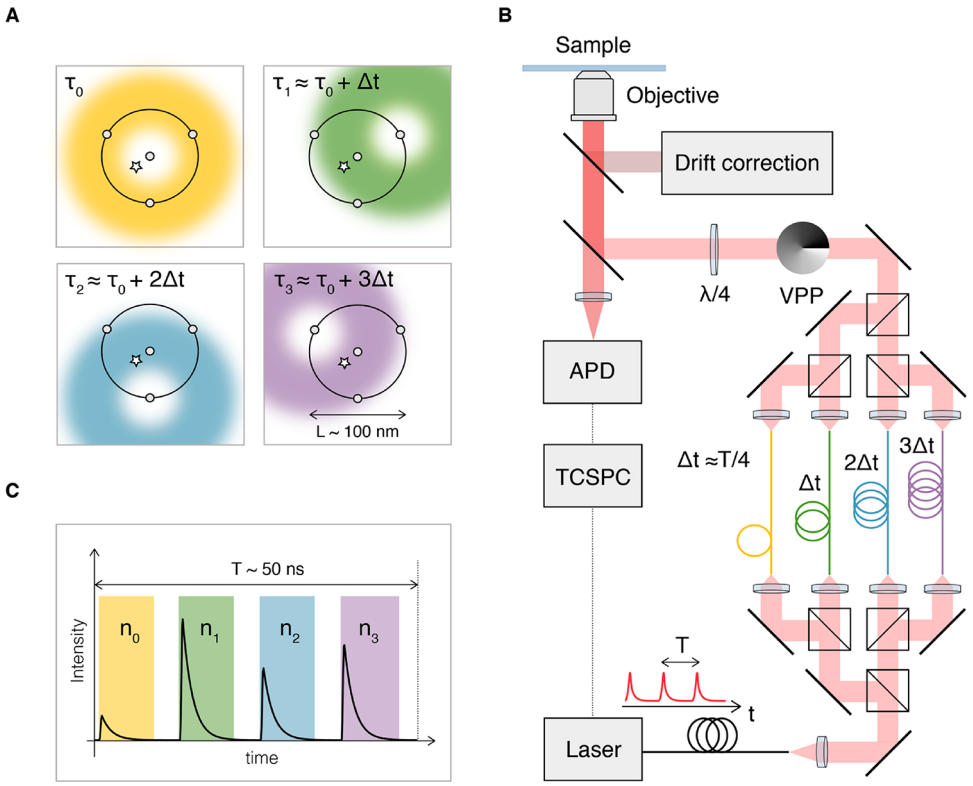

Figure 1. Description of the p-MINFLUX concept and the experimental system. (A) Four pulsed interleaved doughnut-shaped beams are focused on the sample arranged in a triangular pattern, with the fourth beam placed at the center of the triangle. The arrival time of each pulse is denoted as τ_i. The position of a single fluorescent molecule located between the laser spot positions is indicated by a star. (B) Schematic of the p-MINFLUX setup detailing the excitation pathway used to generate the pulsed interleaved doughnut foci delayed by Δt. (C) Schematic signal of detected photon counts within one period (T) of the original laser source.

WORKING PRINCIPLE AND EXPERIMENTAL SETUP

MINFLUX interrogates the position of single fluorescent molecules with a sequence of spatially displaced minima (ideally zeroes) of intensity. Figure 1A schematically shows the sequence and spatial distribution of the four doughnut-shaped foci used in this work for two-dimensional (2D) localization of single molecules. The four doughnut foci define an effective field of view of almost circular shape with a diameter L below the diffraction limit. Previous implementations of MINFLUX used the same excitation scheme, produced by shifting a continuous-wave beam between the four positions with an electro-optic scanner. By contrast, in p-MINFLUX, the excitation pattern is generated with interleaved laser pulses.[21] Figure 1B shows a schematic of the experimental setup, whose core is a confocal fluorescence microscope with modifications in the excitation path. The excitation beam is divided into four using beam splitters. Each beam is coupled into an optical fiber of different length, set to introduce time delays (Δt) of $T/4$ between the beams. The resulting arrival times of the four pulses are $\tau_i = \tau_0 + i\Delta t$, making the interleaved pulses evenly delayed within one period of the original pulse train T. For our laser source with a repetition rate of $f = 20$ MHz ($T = 50$ ns), the time delay between each one of the four excitation pulses is set to 12.5 ns ($T/4$). After outcoupling from the fibers, the four time-delayed beams are collimated. Each beam path has independent mirrors that allow the spatial alignment of the four doughnut-shaped foci into the MINFLUX excitation pattern. The four beams are recombined and passed through a $0-2\pi$ vortex phase plate (VPP) and polarization optics to create doughnut-shaped foci at the sample with a microscope objective. Further details of the setup and the control software are provided in Supplementary Section 1 in the Supporting Information.

The relative position between sample and objective is stabilized with an XYZ active drift correction by imaging fiducial nanoparticles with an independent camera. The position of the fiducial nanoparticles is recorded and eventually used for post-processing drift corrections (see Supplementary Section 2 and Figure S2A in the Supporting Information).

The detection path of the setup presents no differences from a time-resolved confocal microscope. Fluorescence from the sample is spectrally selected using conventional dichroic beam splitters and band-pass filters, and detected with an avalanche photodiode (APD). The photon counts from the APD are read out with a time-correlated single-photon counting (TCSPC) device synchronized with the laser source. In this way, detection time windows within the period T can be defined for each one of the excitation pulses (Figure 1C). Integrating the photon counts of the detection windows, an array of counts $\overline{n} = (n_0, n_1, n_2, n_3)$ is obtained, which, in turn, delivers the position of the emitter through a maximum likelihood estimation. Naturally, the excited-state lifetime information is also readily available as the photon arrival times from the four detection time windows can be combined. The setup is controlled with a dedicated open-source software written in Python, called PyFLUX (details in Supplementary Section 1 in the Supporting Information). A custom-written software was used to analyze the TCSPC data to obtain the MINFLUX position estimations of the emitter.

https://dx.doi.org/10.1021/acs.nanolett.0c04600
Nano Lett. XXXX, XXX, XXX−XXX

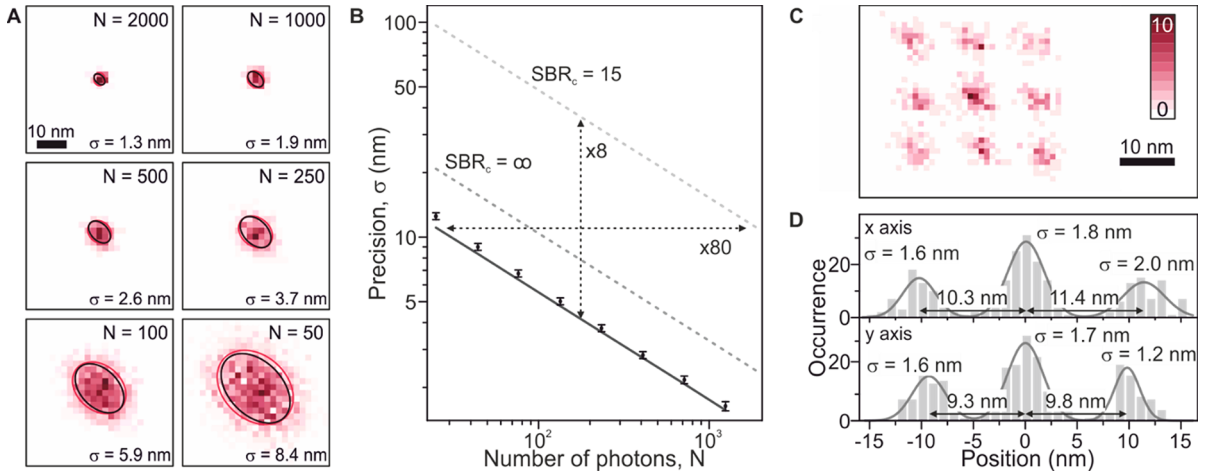

Figure 2. Evaluation of the localization performance of p-MINFLUX. (A) 2D localization histograms of a fixed single ATTO 532 dye for different number of photons, N, used to estimate the position. The red and black ellipses display the covariance of the experimental data and the Cramér-Rao bound, respectively. In this measurement, the SBR was ~15 and $L \approx 120$ nm. (B) Localization precision as a function of collected photons, N, and the Cramer-Rao-Bound (CRB) as a lower limit for the uncertainty of p-MINFLUX (black). The CRB for a camera-based localization technique for SBR = 15 and SBR = ∞ are shown in gray. (C) Localization histogram of a single GattaBead displaced by 10 nm steps in a 3 × 3 grid by using a piezo-positioner. Average $N = 2000$. (D) Cross-section along the central x-axis (top) and central y-axis (bottom) from the localization image shown in panel (C).

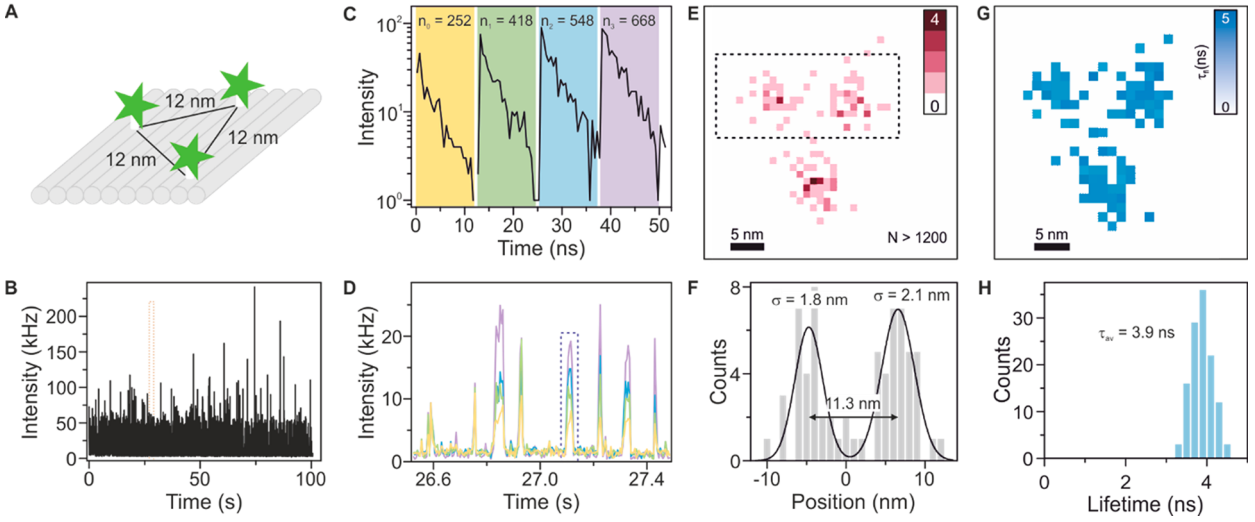

Figure 3. Super-resolution imaging with p-MINFLUX. (A) Schematic of the DNA origami structure with three ATTO 532 dyes in a triangular array. (B) 100 s trace of the total fluorescence intensity of a single DNA origami structure. In this measurement, the SBR was ~8. (C) Fluorescence decays and total integrated counts on the four detection channels for the single-molecule emission event marked in panel (D). (D) Expanded view of the time trace shown in panel (B). The intensity is split into the four detection time windows, corresponding to the four excitation beams (color-coded as in Figure 3C). (E) 2D localization image for one DNA origami structure. Single-molecule emission events with $N < 1200$ were discarded. (F) Average horizontal profile of localizations from the area marked in E. (G) p-MINFLUX fluorescence lifetime image. (H) Distribution of fluorescence lifetimes for all localizations in panel (E).

LOCALIZATION PRECISION, NANOSCOPY, AND TRACKING

The localization precision of p-MINFLUX as a function of the number of detected photons (N) was tested using single ATTO 532 molecules fixed to a DNA origami nanostructure (further details about DNA origami folding and the measurement protocol are described in Supplementary Sections 3–6, Supplementary Tables 1 and 2, in the Supporting Information). Figure 2A shows 2D histograms of position estimations using N ranging from 50 to 2000. As expected, MINFLUX is extremely photon efficient for localizing molecules. For example, the experimental standard deviation of localizations using $N = 50$ is $\sigma = 8.4$ nm, comparable to state-of-the-art PALM/STORM experiments, where $N = 5000$ photons are needed to achieve a precision of 8–10 nm (further details are given in Supplementary Section 7 in the Supporting Information).[22−24] With moderately high counts of $N = 1000$, the localization precision reaches $\sigma \approx 1$ nm. The experimental precision (covariance) is plotted as red ellipses and shows that the performance of p-MINFLUX closely follows the theoretically predicted Cramér-Rao bound (CRB, black ellipses) (details in Supplementary Section 7 in the Supporting Information). Figure 2B shows σ as a function of N. For comparison, curves of the experimental localization precision σ vs N for camera-based SMLM under infinite signal-to-background ratio (SBR = ∞) and under a realistic

https://dx.doi.org/10.1021/acs.nanolett.0c04600
Nano Lett. XXXX, XXX, XXX−XXX

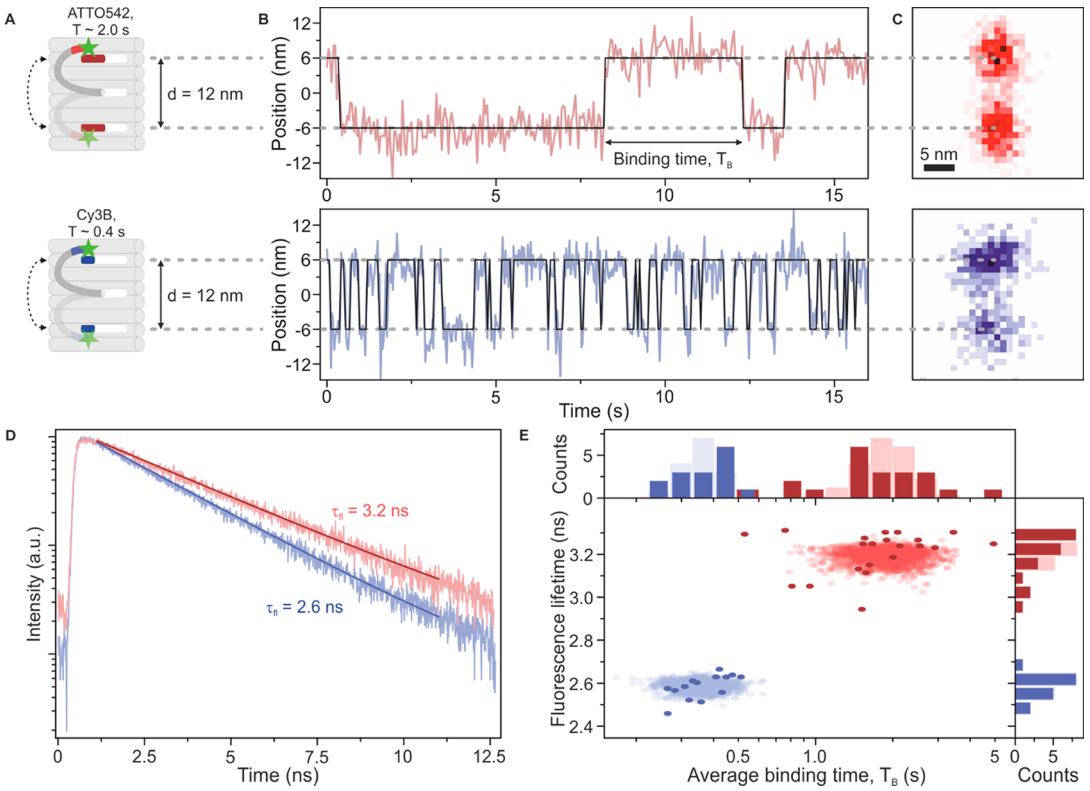

Figure 4. Molecular scale tracking of a DNA pointer on top of a DNA origami structure. (A) Schematics, (B) localization trace (binning time = 100 ms for the upper and 60 ms for the lower trace; SBR ≈ 8 for the upper trace and SBR ≈ 10 for the lower trace), and (C) 2D localization histograms of a DNA origami pointer labeled with a single ATTO 542 (upper row) and Cy3B (lower row) dye. (D) Exemplary single-molecule fluorescence decays for ATTO 542 (red) and Cy3B (blue) labeled structures. (E) Scatter plot of the average binding time T_B and fluorescence lifetime τ_{fl} obtained from the measurements on the DNA origami structures (dark red, dark blue) and from simulations (light red, light blue). The corresponding histograms for T_B and τ_{fl} are shown on top and on the right, respectively.

assumption of SBR = 15 are also depicted in Figure 2B. For the same number of detected photons, p-MINFLUX delivers almost 1 order of magnitude better localization precision than camera-based SMLM techniques. Conversely, almost 2 orders of magnitude fewer photons are needed in order to achieve the same precision as with camera-based SMLM techniques. In terms of localization precision, p-MINFLUX demonstrates an equivalent performance to the original MINFLUX microscope, given equivalent experimental conditions (L, N, SBR). This is expected because both methods work under the same principle of localization of single emitters.

The localization accuracy of p-MINFLUX was evaluated by localizing a single GattaBead (nanoparticle diameter of 23 nm, containing ATTO 542, fluorescence lifetime = 3.2 ns) as it was displaced using a piezo-positioner over a square grid with a step size of d = 10 nm. The 2D localization histogram at an average number of N = 2000 photons for each localization is shown in Figure 2C. Figure 2D shows the average profiles of the central row and the central column. The distance between the positions is $d \approx 10$ nm, which is in good agreement both with the set step size of the piezo-positioner and with the positions of the fiducial markers determined independently to correct for sample drift during the measurements (for details, see Figure S2B in the Supporting Information).

The working principle of p-MINFLUX was also evaluated through numerical simulations described in Supplementary Section 8 in the Supporting Information. The simulation results shown in Supplementary Section 9 in the Supporting Information show that the performance of p-MINFLUX is only weakly influenced by misalignments of the excitation beam pattern. For example, a lateral misalignment of any, or all four doughnut foci of up to15 nm deteriorates the localization precision by less than 1 nm (Figure S5 in the Supporting Information). We have also evaluated the effect on localization precision and accuracy of possible cross-talk between the detection time windows for different lifetimes (Supplementary Section 10 in the Supporting Information). Generally, this cross-talk may deteriorate the localization precision and/or introduce a localization bias. However, these effects are <1 nm for lifetimes smaller than 25% of the detection time windows (3 ns in our case), and are <2 nm for lifetimes up to 33% of the detection time windows (4 ns in our case; see Figure S6 in the Supporting Information).

Next, we applied p-MINFLUX to image a triangular arrangement of single-molecules separated by $d \approx 12$ nm in a DNA origami nanostructure, as depicted in Figure 3A. In this case, ATTO 532 was used because it shows appropriate blinking when inducing radical ion states in a reducing buffer for super-resolution blink microscopy (see the long blinking trace in Figure 3B).[25−27] Figure 3C shows the detected photons sorted according to their arrival times, relative to the laser sync signal, yielding four decays corresponding to the four excitation doughnuts. An expanded view of the fluorescence time trace in Figure 3B showing individual single-molecule emission events is depicted in Figure 3D. Each single-molecule event presents a different combination of intensity levels in the four detection channels, which encodes the fluorophore position. The integrated photon numbers in each detection

https://dx.doi.org/10.1021/acs.nanolett.0c04600
Nano Lett. XXXX, XXX, XXX−XXX

time window deliver the array of photon counts for each excitation doughnut $\overline{n}$ (as indicated by the colors in Figures 3C and 3D), which is then used to determine the molecular location.

Figure 3E shows the localization map obtained from the 100 s of measurement in Figure 3B. Single-molecule events with $N > 1200$ detected photons were considered. The threshold value of 1200 was chosen because it delivered a good compromise of localization precision (~2 nm) and frequency of events for this fluorophore and experimental conditions. The reconstructed image reveals three distinct populations in a triangular pattern that is in good agreement with the designed DNA origami structure. Suitable lower- and upper-intensity thresholds were used to discern single-molecule emission events from the background and multiple-molecule events, respectively (for details, see Supplementary Section 6 in the Supporting Information). The slice along the x-axis in Figure 3E is shown in Figure 3F, illustrating the achieved resolution. Two spots, separated by 11.3 nm, are clearly distinguishable (standard deviations of σ = 1.8 nm and σ = 2.1 nm). In addition, p-MINFLUX gives access to the fluorescence lifetime of each single-molecule detected, enabling the reconstruction of super-resolved fluorescence lifetime images, as shown in Figure 3G. For all localizations, the detected fluorescence lifetimes show a narrow distribution around an average value τ_{fl} = 3.9 ± 0.3 ns (Figure 3H).

Next, we tested the performance of p-MINFLUX for single-molecule tracking and multiplexing using fluorescence lifetime information. For this purpose, we used a dynamic DNA origami structure where three single-stranded DNAs protrude from the DNA origami platform with a separation distance of 6 nm between each strand, as indicated in the schemes of Figure 4A. The central protruding strand (also called pointer strand) can transiently hybridize to the other protruding strands (details in Supplementary Tables 3 and 4 in the Supporting Information). The end of the pointer strand is labeled with a single fluorophore, so that its position can be tracked via p-MINFLUX. Two DNA origami structures of this type were designed and fabricated. One was labeled with an ATTO 542 dye and had eight complementary nucleotides for transient binding (red, Figure 4A). The other was labeled with a Cy3B dye and had only seven complementary nucleotides for transient binding (blue, Figure 4A). As in any tracking experiment, temporal and spatial resolutions are linked and limited by the detected photon count rate. Being a single-photon counting technique, p-MINFLUX offers full flexibility to bin photons in time in order to optimize for time or spatial resolution, or a suitable compromise of both. In these experiments, we aimed to detect multiple transient bindings of the pointer strand, which imposes a requirement of minimum tracking time, different for each one of the two dynamic structures and limited by the fluorophore photostability. We ensured a localization precision of σ = 2−3 nm to clearly discern the two transient binding positions (x_0 = +6 nm, x_1 = −6 nm). This was achieved with a count rate of 20−60 kHz and time bins of 30−150 ms for ATTO 542, while for Cy3B we used a count rate of 20−110 kHz and time bins of 10−90 ms.

Figure 4B shows exemplary p-MINFLUX tracking traces for the two dynamic DNA origami structures. In both cases, the localizations of the fluorophores alternate between two positions separated by ~12 nm, as expected from the DNA origami design. Figure 4C shows the corresponding two-dimensional localization histograms. For the pointer labeled with ATTO 542, the two binding positions are found to be separated by 11.8 nm (σ = 2.2 nm), while for the pointer with Cy3B they are separated by 11.0 nm (σ = 2.5 nm).

By contrast, the transient binding times of the two structures differ significantly because of the different number of complementary nucleotides in the design. The pointer with eight complementary nucleotides (Figure 4B, top) presents binding times longer than the pointer with seven complementary nucleotides (Figure 4B bottom). Also, the two fluorophores used to label the pointers have distinct fluorescence lifetimes (Figure 4D).

Figure 4E shows a scatter plot of the average binding times versus fluorescence lifetimes of single DNA pointers labeled with ATTO 542 and Cy3B. The two structures are identifiable in this plot both by their distinct average binding times (T_B) of 1.92 and 0.37 s, and mean fluorescence lifetimes (τ_{fl}) of 3.2 and 2.6 ns, respectively. In Figure 4E, we also show simulations of the experiments (details in Supplementary Section 11 in the Supporting Information) in the background of the scatter plot. The simulations demonstrate that the experimentally observed variance in the binding times is dominated by the limited number of transitions detected for each structure before the fluorescent dye bleaches.

DISCUSSION AND CONCLUSIONS

We have presented p-MINFLUX, a new implementation of MINFLUX based on pulsed interleaved excitation and time-correlated single-photon counting. p-MINFLUX works under the same basic principle as the original MINFLUX and thus delivers equally photon-efficient single-molecule localizations, with its positive consequences for nanoscopy and tracking. We demonstrated localization precisions of $\sigma \approx 1-2$ nm with $N \approx 1000$ photons per localization, an improvement of ~10-fold compared to a typical camera-based localization. We demonstrated the performance of p-MINFLUX in the typical applications of molecular scale nanoscopy using blinking molecules as well as nanoscale tracking on DNA origami structures. In addition, p-MINFLUX is unique in providing access to excited-state lifetime information, enabling single-molecule identification (multiplexing) and FLIM nanoscopy with molecular-scale resolution; a 10−100 times improvement compared to previous works.[28,29] Fluorescence lifetime information may expand the field of application of p-MINFLUX, because it enables the specific detection of fluorescence in strongly scattering media.

In the first MINFLUX implementation, the subsequent excitations used to interrogate the position of single fluorophores were performed by shifting a laser focus with a scanner. To maximize scanning speed, an electro-optic scanner was used. By contrast, in p-MINFLUX, the excitation cycle is not limited by any optical scanner (~10−100 μs) but rather by the repetition rate of the pulsed laser, which corresponds to ~50 ns. Therefore, the time resolution is only limited by the detected emission rate, and ultimately by the decay lifetime of the emitter, holding potential for experiments exploring microsecond-scale dynamics. As an additional advantage, the setup can be regarded as a rather simple modification to a stage-scanning confocal microscope with pulsed excitation and TCSPC detection. Because of these advantages, we envision that p-MINFLUX will be more easily adopted and reproduced in other laboratories. To further facilitate this, all the instrumentation and data analysis Python code is available in

https://dx.doi.org/10.1021/acs.nanolett.0c04600
Nano Lett. XXXX, XXX, XXX−XXX

an open-source fashion. We note that a real-time adaptive arrangement of the excitation pattern, as demonstrated by Gwosch and co-workers,[16] can also be implemented in p-MINFLUX. This can be achieved, for example, by incorporating motorized mirror mounts. Also, photon efficiency can be maximized by the use of MINFLUX iterative approaches.[16]

In summary, p-MINFLUX constitutes a new analytical tool that combines molecular-scale spatial resolution with time-resolved lifetime measurements, which may be of use not only for ultraprecise single-molecule localization and nanoscopy, but also for new single-molecule energy transfer measurements such as FRET-, metal-, or graphene-induced energy transfer.

■ ASSOCIATED CONTENT

Supporting Information

The Supporting Information is available free of charge at https://pubs.acs.org/doi/10.1021/acs.nanolett.0c04600.

Details about the optical setups, the system for drift correction, the preparation of DNA origami samples, measurement of the excitation beam pattern and the point-spread functions, p-MINFLUX measurement protocol, position estimator and Cramér-Rao bound, p-MINFLUX simulations, effect of misalignment of the excitation beam pattern, crosstalk between detection time windows, and simulations of time traces of the pointer origami. Also, it contains a list of oligonucleotides used for each DNA origami used (PDF)

■ AUTHOR INFORMATION

Corresponding Authors

Philip Tinnefeld − *Department of Chemistry and Center for NanoScience, Ludwig-Maximilians-Universität München, 81377 München, Germany*; Email: philip.tinnefeld@cup.uni-muenchen.de

Fernando D. Stefani − *Centro de Investigaciones en Bionanociencias (CIBION), Consejo Nacional de Investigaciones Científicas y Técnicas (CONICET), C1425FQD Ciudad Autónoma de Buenos Aires, Argentina; Departamento de Física, Facultad de Ciencias Exactas y Naturales, Universidad de Buenos Aires, C1428EHA Ciudad Autónoma de Buenos Aires, Argentina;* orcid.org/0000-0002-3277-7215; Email: fernando.stefani@df.uba.ar

Authors

Luciano A. Masullo − *Centro de Investigaciones en Bionanociencias (CIBION), Consejo Nacional de Investigaciones Científicas y Técnicas (CONICET), C1425FQD Ciudad Autónoma de Buenos Aires, Argentina; Departamento de Física, Facultad de Ciencias Exactas y Naturales, Universidad de Buenos Aires, C1428EHA Ciudad Autónoma de Buenos Aires, Argentina*

Florian Steiner − *Department of Chemistry and Center for NanoScience, Ludwig-Maximilians-Universität München, 81377 München, Germany*

Jonas Zähringer − *Department of Chemistry and Center for NanoScience, Ludwig-Maximilians-Universität München, 81377 München, Germany*

Lucía F. Lopez − *Centro de Investigaciones en Bionanociencias (CIBION), Consejo Nacional de Investigaciones Científicas y Técnicas (CONICET), C1425FQD Ciudad Autónoma de Buenos Aires, Argentina*

Johann Bohlen − *Department of Chemistry and Center for NanoScience, Ludwig-Maximilians-Universität München, 81377 München, Germany*

Lars Richter − *Centro de Investigaciones en Bionanociencias (CIBION), Consejo Nacional de Investigaciones Científicas y Técnicas (CONICET), C1425FQD Ciudad Autónoma de Buenos Aires, Argentina; Department of Chemistry and Center for NanoScience, Ludwig-Maximilians-Universität München, 81377 München, Germany*

Fiona Cole − *Department of Chemistry and Center for NanoScience, Ludwig-Maximilians-Universität München, 81377 München, Germany*

Complete contact information is available at: https://pubs.acs.org/10.1021/acs.nanolett.0c04600

Author Contributions

[▽]These authors contributed equally to this work.

Author Contributions

The manuscript was prepared and written through the contributions of all authors. All authors have approved the final version of the manuscript.

Funding

This work has been supported by CONICET and ANPCYT Project Nos. PICT-2013-0792 and PICT-2014-0739. P.T. is grateful for support by the Deutsche Forschungsgemeinschaft (DFG, German Research Foundation) under Germany's Excellence Strategy − EXC 2089/1−390776260, and SFB1032. L.A.M. acknowledges a Ph.D. fellowship from CONICET and an exchange scholarship from the German Academic Exchange Service (DAAD). F.S. acknowledges support by the Boehringer Ingelheim Fonds. L.R. acknowledges funding from the German Academic Exchange Service (DAAD) and the German Academic Scholarship Foundation.

Notes

The authors declare no competing financial interest.

■ ACKNOWLEDGMENTS

F.D.S. acknowledges the support of the Max-Planck-Society and the Alexander von Humboldt Foundation.

■ REFERENCES

(1) Hell, S. W. Nanoscopy with Focused Light (Nobel Lecture). *Angew. Chem., Int. Ed.* **2015**, *54* (28), 8054−8066.

(2) Hell, S. W.; Sahl, S. J.; Bates, M.; Zhuang, X.; Heintzmann, R.; Booth, M. J.; Bewersdorf, J.; Shtengel, G.; Hess, H.; Tinnefeld, P.; et al. The 2015 Super-Resolution Microscopy Roadmap. *J. Phys. D: Appl. Phys.* **2015**, *48* (44), 443001.

(3) Sahl, S. J.; Hell, S. W.; Jakobs, S. Fluorescence Nanoscopy in Cell Biology. *Nat. Rev. Mol. Cell Biol.* **2017**, *18* (11), 685−701.

(4) Klar, T.; Hell, S. W. Subdiffraction Resolution in Far-Field Fluorescence Microscopy. *Opt. Lett.* **1999**, *24* (14), 954−956.

(5) Klar, T. A.; Jakobs, S.; Dyba, M.; Egner, A.; Hell, S. W. Fluorescence Microscopy with Diffraction Resolution Barrier Broken by Stimulated Emission. *Proc. Natl. Acad. Sci. U. S. A.* **2000**, *97* (15), 8206−8210.

(6) Rust, M. J.; Bates, M.; Zhuang, X. Sub-Diffraction-Limit Imaging by Stochastic Optical Reconstruction Microscopy (STORM). *Nat. Methods* **2006**, *3* (10), 793−796.

(7) Betzig, E.; Patterson, G. H.; Sougrat, R.; Lindwasser, O. W.; Olenych, S.; Bonifacino, J. S.; Davidson, M. W.; Lippincott-Schwartz, J.; Hess, H. F. Imaging Intracellular Fluorescent Proteins at Nanometer Resolution. *Science* **2006**, *313* (5793), 1642−1645.

(8) Hess, S. T.; Girirajan, T. P. K.; Mason, M. D. Ultra-High Resolution Imaging by Fluorescence Photoactivation Localization Microscopy. *Biophys. J.* **2006**, *91* (11), 4258−4272.
(9) Jungmann, R.; Steinhauer, C.; Scheible, M.; Kuzyk, A.; Tinnefeld, P.; Simmel, F. C. Single-Molecule Kinetics and Super-Resolution Microscopy by Fluorescence Imaging of Transient Binding on DNA Origami. *Nano Lett.* **2010**, *10* (11), 4756−4761.
(10) Schnitzbauer, J.; Strauss, M. T.; Schlichthaerle, T.; Schueder, F.; Jungmann, R. Super-Resolution Microscopy with DNA-PAINT. *Nat. Protoc.* **2017**, *12* (6), 1198−1228.
(11) Raab, M.; Schmied, J. J.; Jusuk, I.; Forthmann, C.; Tinnefeld, P. Fluorescence Microscopy with 6 Nm Resolution on DNA Origami. *ChemPhysChem* **2014**, *15* (12), 2431−2435.
(12) Strauss, S.; Nickels, P. C.; Strauss, M. T.; Jimenez Sabinina, V.; Ellenberg, J.; Carter, J. D.; Gupta, S.; Janjic, N.; Jungmann, R. Modified Aptamers Enable Quantitative Sub-10-Nm Cellular DNA-PAINT Imaging. *Nat. Methods* **2018**, *15* (9), 685−688.
(13) Xu, K.; Zhong, G.; Zhuang, X. Actin, Spectrin, and Associated Proteins Form a Periodic Cytoskeletal Structure in Axons. *Science* **2013**, *339* (6118), 452−456.
(14) Balzarotti, F.; Eilers, Y.; Gwosch, K. C.; GynnÅ, A. H.; Westphal, V.; Stefani, F. D.; Elf, J.; Hell, S. W. Nanometer Resolution Imaging and Tracking With Minimal Photon Fluxes. *Science* **2017**, *355* (6325), 606−612.
(15) Eilers, Y.; Ta, H.; Gwosch, K. C.; Balzarotti, F.; Hell, S. W. MINFLUX Monitors Rapid Molecular Jumps with Superior Spatiotemporal Resolution. *Proc. Natl. Acad. Sci. U. S. A.* **2018**, *115* (24), 6117−6122.
(16) Gwosch, K. C.; Pape, J. K.; Balzarotti, F.; Hoess, P.; Ellenberg, J.; Ries, J.; Hell, S. W. MINFLUX Nanoscopy Delivers 3D Multicolor Nanometer Resolution in Cells. *Nat. Methods* **2020**, *17* (2), 217−224.
(17) Pape, J. K.; Stephan, T.; Balzarotti, F.; Büchner, R.; Lange, F.; Riedel, D.; Jakobs, S.; Hell, S. W. Multicolor 3D MINFLUX Nanoscopy of Mitochondrial MICOS Proteins. *Proc. Natl. Acad. Sci. U. S. A.* **2020**, *117* (34), 20607−20614.
(18) Testa, I.; D'Este, E.; Urban, N. T.; Balzarotti, F.; Hell, S. W. Dual Channel RESOLFT Nanoscopy by Using Fluorescent State Kinetics. *Nano Lett.* **2015**, *15* (1), 103−106.
(19) Isbaner, S.; Karedla, N.; Kaminska, I.; Ruhlandt, D.; Raab, M.; Bohlen, J.; Chizhik, A.; Gregor, I.; Tinnefeld, P.; Enderlein, J.; et al. Axial Colocalization of Single Molecules with Nanometer Accuracy Using Metal-Induced Energy Transfer. *Nano Lett.* **2018**, *18* (4), 2616−2622.
(20) Kaminska, I.; Bohlen, J.; Rocchetti, S.; Selbach, F.; Acuna, G. P.; Tinnefeld, P. Distance Dependence of Single-Molecule Energy Transfer to Graphene Measured with DNA Origami Nanopositioners. *Nano Lett.* **2019**, *19* (7), 4257−4262.
(21) Müller, B. K.; Zaychikov, E.; Bräuchle, C.; Lamb, D. C. Pulsed Interleaved Excitation. *Biophys. J.* **2005**, *89* (5), 3508−3522.
(22) Thompson, R. E.; Larson, D. R.; Webb, W. W. Precise Nanometer Localization Analysis for Individual Fluorescent Probes. *Biophys. J.* **2002**, *82* (5), 2775−2783.
(23) Sigal, Y. M.; Zhou, R.; Zhuang, X. Visualizing and Discovering Cellular Structures with Super-Resolution Microscopy. *Science* **2018**, *361* (6405), 880−887.
(24) Dempsey, G. T. G. G. T.; Vaughan, J. C. J. J. C.; Chen, K. H. K.; Bates, M.; Zhuang, X. Evaluation of Fluorophores for Optimal Performance in Localization-Based Super-Resolution Imaging. *Nat. Methods* **2011**, *8* (12), 1027−1036.
(25) Vogelsang, J.; Kasper, R.; Steinhauer, C.; Person, B.; Heilemann, M.; Sauer, M.; Tinnefeld, P. A Reducing and Oxidizing System Minimizes Photobleaching and Blinking of Fluorescent Dyes. *Angew. Chem., Int. Ed.* **2008**, *47* (29), 5465−5469.
(26) Vogelsang, J.; Steinhauer, C.; Forthmann, C.; Stein, I. H.; Person-Skegro, B.; Cordes, T.; Tinnefeld, P. Make Them Blink: Probes for Super-Resolution Microscopy. *ChemPhysChem* **2010**, *11* (12), 2475−2490.
(27) van de Linde, S.; Krstić, I.; Prisner, T.; Doose, S.; Heilemann, M.; Sauer, M. Photoinduced Formation of Reversible Dye Radicals and Their Impact on Super-Resolution Imaging. *Photochem. Photobiol. Sci.* **2011**, *10* (4), 499−506.
(28) Thiele, J. C.; Helmerich, D. A.; Oleksiievets, N.; Tsukanov, R.; Butkevich, E.; Sauer, M.; Nevskyi, O.; Enderlein, J. Confocal Fluorescence-Lifetime Single-Molecule Localization Microscopy. *ACS Nano* **2020**, *14* (10), 14190−14200.
(29) Castello, M.; Tortarolo, G.; Buttafava, M.; Deguchi, T.; Villa, F.; Koho, S.; Pesce, L.; Oneto, M.; Pelicci, S.; Lanzanó, L.; et al. A Robust and Versatile Platform for Image Scanning Microscopy Enabling Super-Resolution FLIM. *Nat. Methods* **2019**, *16* (2), 175−178.

https://dx.doi.org/10.1021/acs.nanolett.0c04600
Nano Lett. XXXX, XXX, XXX−XXX

Supporting Information for

Pulsed interleaved MINFLUX

Luciano A. Masullo[1,2†], Florian Steiner[3†], Jonas Zähringer[3], Lucía F. Lopez[1], Johann Bohlen[3] Lars Richter[1,3], Fiona Cole[3], Philip Tinnefeld[3]*, Fernando D. Stefani[1,2]*

1 Centro de Investigaciones en Bionanociencias (CIBION), Consejo Nacional de Investigaciones Científicas y Técnicas (CONICET), Godoy Cruz 2390, C1425FQD, Ciudad Autónoma de Buenos Aires, Argentina

2 Departamento de Física, Facultad de Ciencias Exactas y Naturales, Universidad de Buenos Aires, Güiraldes 2620, C1428EHA, Ciudad Autónoma de Buenos Aires, Argentina

3 Department of Chemistry and Center for NanoScience, Ludwig-Maximilians-Universität München, Butenandtstr. 5-13 Haus E, 81377 München, Germany

Supplementary Information

Table of Contents

Supplementary Section 1. Optical set-ups

Two versions of the p-MINFLUX microscope were built and are fully functional. One in Prof. Fernando Stefani's laboratory at CIBION in Buenos Aires, Argentina, and the other in Prof. Philip Tinnefeld's laboratory at LMU in Munich, Germany.

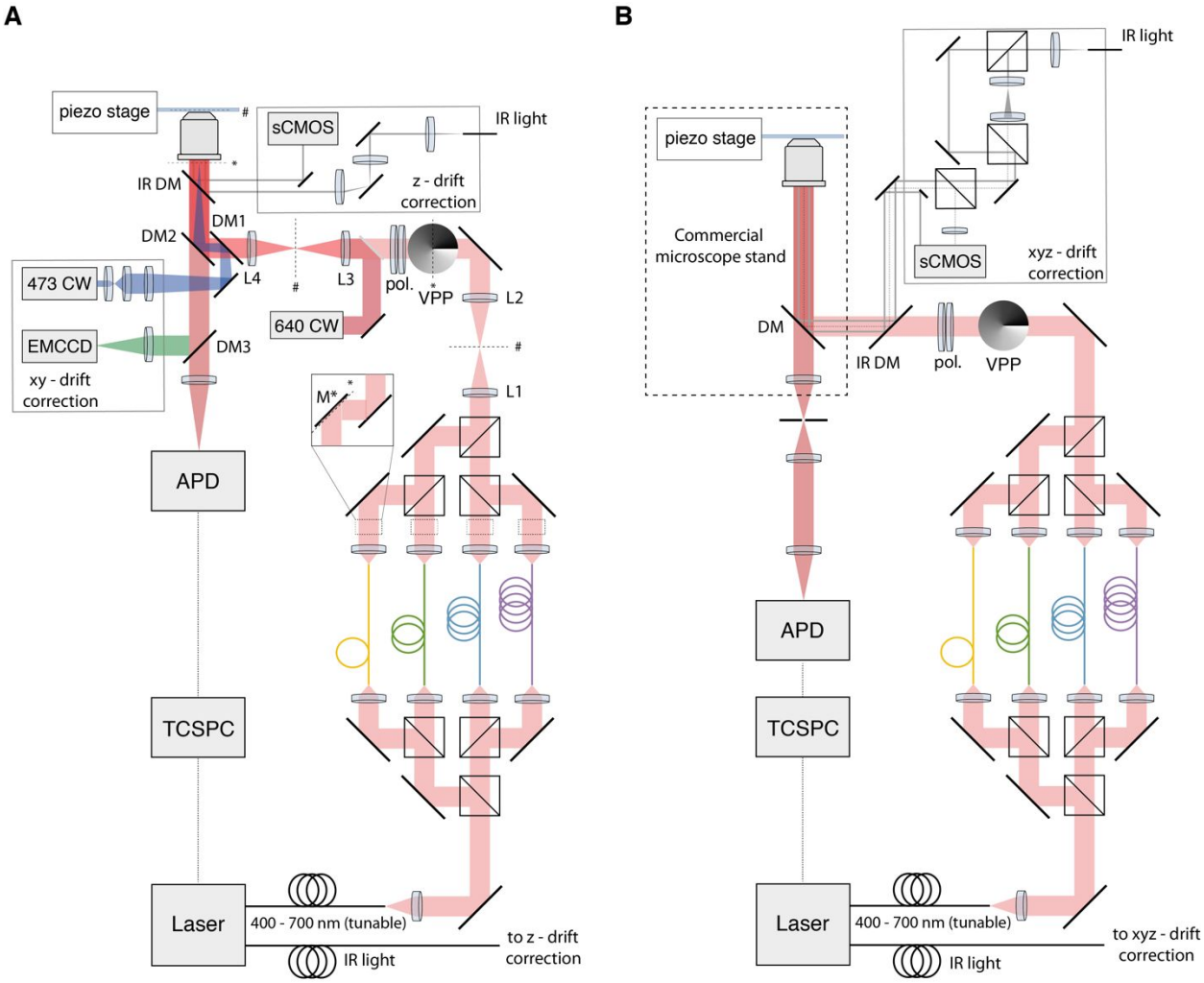

Supplementary Figure S1. A) p-MINFLUX setup built in Buenos Aires. Laser: Fianium SC 400-4 (NKT Photonics)**, 640 CW:** Lambda mini Evo, RGB Photonics GmbH, **473 CW:** GEM 473, Laser Quantum, **piezo stage:** NanoMax 300 with controller BPC303, Thorlabs Inc.), Lens 1 **(L1), L2, L3, L4:** AC254-300-A-ML (Thorlabs Inc.), **VPP:** V-633-10, Vortex Photonics, Polarizer (**pol.):** WPH05M-633 and WPQ05M-633, Thorlabs Inc.), Dichroic Mirror (**DM1):** ZT532/640RPC-UF, Chroma Technology Corporation, **DM2:** ZT532/640RPC, Chroma Technology Corporation, **IR DM:** T750SPXRXT-UF1, Chroma Technology Corporation, **DM3:**

ZT532RDC, Chroma Technology Corporation, **EMCCD:** iXon DV887 (Andor), **sCMOS:** ThorCam DCC1240C (Thorlabs Inc.), Avalanche Photodiode (**APD):** SPCM-AQR-13 (PerkinElmer Optoelectronics), time-correlated single-photon-counting (**TCSPC):** PicoHarp 300 (PicoQuant GmbH). **B) p-MINFLUX setup built in Munich. Laser:** SuperK Fianium FIU-15 (NKT Photonics GmbH)**, piezo stage:** P733.3CD (Physik Instrumente (PI) GmbH), **VPP:** V-532-20-1 (Vortex Photonics**) pol.:** WPQ05M-532 and WPH532M-532, Thorlabs GmbH**, IR DM:** ZT 785 SPXXR (Chroma Technology Corp.), **DM:** ZT532RDC – STED (Chroma Technology Corp.)**, sCMOS:** Zelux, (Thorlabs GmbH)**, APD:** SPCM-AQRH-16-TR (Excelitas Technologies GmbH & Co. KG), **TCSPC:** HydraHarp 400, PicoQuant GmbH).

Buenos Aires setup:

Excitation. A supercontinuum laser (Fianium SC 400-4, NKT Photonics) is used for excitation with pulses of $\sim 80\,ps$ width (FWHM) and a repetition rate of $1/T = 40\,MHz$. The emission spectrum ranges from $\lambda \sim 420\,nm$ to $\lambda \sim 2000\,nm$ and the output of the laser system is a collimated, unpolarized, beam. Infrared light with $\lambda > 1064\,nm$ is filtered out by a dichroic mirror (BLP01-1064R-25, Semrock Inc.). A small fraction of the IR light is sent to a custom-built, fast photodiode sensing the arrival of the laser pulses. The rest of the far-infrared light is dumped. Near-infrared light is split from the main beam (T750SPXRXT-UF1, Chroma Technology Corporation) and coupled into a multimode fiber to be used in the z-drift correction optics. From the remaining visible light, a ~20 nm band around 642 nm is selected for fluorescence excitation with an interference optical filter (ZET642/20x, Chroma Technology Corporation).

The light intensity is controlled using a flipper with a mounted ND filter (MFF101/M and NDK01, Thorlabs Inc.) and a continuous, ND filter NDC-50C-2. The excitation beam is then split by a polarizing beam splitter (PBS) (CCM1-PBS251/M, Thorlabs Inc.). The two beams have orthogonal polarization states. Each of the beams is sent to a non-polarizing 50:50 beam splitter (CCM1-BS013/M, Thorlabs Inc.). This beam splitting system generates two pairs of beams with each pair sharing the orthogonal linear polarization.

The four beams are coupled into polarization-maintaining fibers (PM630-HP, Thorlabs Inc.). Each of the fibers has a different optical path length, approx. $1.3\,m$, $2.6\,m$,$3.9\,m$, and $5.2\,m$ which generate the T/4 time delay between pulses. The light coupled out of the fibers carries linear polarization. It is reflected with dielectric mirrors (BB1-E02, Thorlabs Inc.) into the beam combining system. The four beams are combined by three non-polarizing 50:50 beam splitters (CCM1-BS013/M, Thorlabs Inc.) used as beam combiners. The axes of linear polarization are matched by turning the fiber out-couplers (60FC, Schäfter + Kirchhoff GmbH).

The recombined beams are focused by a lens L1, $f = 300\,mm$ (AC254-300-A-ML, Thorlabs Inc.) to a plane conjugated to the back focal plane of the microscope objective. Lens L1 is the first out of four identical lenses forming a double 4f-system. Between L2 and L3 a VPP (V-633-10, Vortex Photonics) is placed in the conjugated plane to the back focal plane (BFP) of the objective. Conjugated planes are indicated with * and # in Supplementary Figure S1. The VPP creates the doughnut-shaped focus in the focal plane of the oil-immersion objective (CFI Plan Fluor 100x,

NA = 1.4, Nikon Instruments Inc.). Circular polarization is needed to create the minima of intensity in the center of the doughnut-shaped foci and is achieved by the combination of $\lambda/2$ and $\lambda/4$ waveplates (WPH05M-633 and WPQ05M-633, Thorlabs Inc.) which are positioned close to L3.

The four temporally-separated pulses share the doughnut excitation pattern. To align the four doughnut centers to the desired EBP positions, the mirrors M* are employed. They are placed in the conjugate plane to VPP and BFP and allow to spatially shift the doughnut-shaped focus by changing their tilt angles without changing their lateral position relative to the VPP. This allows ensuring almost the same phase modulation in the Fourier plane for the four beams. Additionally, a pinhole can be placed into the conjugated plane of the sample before the VPP to clean-up the beams for possible distortions at the beam splitters used for recombination.

An auxiliary confocal system consisting of a CW diode laser (Lambda mini Evo, RGB Photonics GmbH) emitting at $\lambda = 640\ nm$ was added to the setup to provide an excitation with a gaussian beam profile. Using a pellicle 92:8 beam splitter (BP108, Thorlabs Inc.), the collimated laser light is coupled into the excitation optical path.

Detection. The light emitted by the sample is collected by the objective. It passes a dichroic mirror (ZT532/640RPC, Chroma Technology Corporation) which reflects the excitation beams. Notch filters block the excitation light from the red excitation beams (ZET642NF, Chroma Technology Corporation), from the blue widefield excitation (ZET473NF, Chroma Technology Corporation), and the reflected infrared beam (NF808-34, AHF Analysentechnik AG).

The fluorescence emission is focused by a tube lens (AC254-50-A-ML, Thorlabs Inc.) onto an avalanche photodiode (APD) (SPCM-AQR-13, PerkinElmer Optoelectronics). The APD detects photons with 90% quantum efficiency at $\lambda = 650\ nm$. It provides a single photon timing resolution of $350\ ps$ (FWHM) and typically exhibits 150 dark counts per second. The digital signal from the fluorescence photons is sent from the APD to a TCSPC unit (PicoHarp 300, PicoQuant). The internal timer of the TCSPC unit correlates the photon detection signal from the APD to the signal from the photodiode which senses the arrival of the excitation laser pulse. For every counted photon, it returns an absolute time from the beginning of the measurement and the time elapsed since the last laser pulse. The temporal resolution of the TCSPC unit is $8\ ps$ and the dead time after a photon detection is reported by the manufacturer to be $< 95\ ns$.

Drift correction. The optical system providing z-stabilization employs the near-infrared light coupled into a multimode fiber. After attenuation and clean-up (ET705/72M and T750SPXRXT-UF1, Chroma Technology Corporation), the IR light is guided to the objective. The collimated beam enters the objective at the edge of the back focal aperture. After reflection from the sample-coverslip interface, the IR light leaves the objective parallel to the incident IR beam. The reflected light passes a tube lens (AC254-150-A-ML, Thorlabs Inc.) and is focused on a CMOS camera (ThorCam DCC1240C, Thorlabs Inc.). Through a calibration with the piezo stage, we determined that the z position of the slide can be tracked with a precision better than $10\ nm$ and actively corrected with a feedback loop.

The lateral stabilization of the sample is realized tracking bright green fluorescent beads (FluoSpheres, $0{,}2\ \mu m$, Nile Red, Thermo Fisher Scientific). As displayed in Supplementary Figure

S1, a widefield configuration is employed for illuminating the beads at (GEM 473, Laser Quantum). The fluorescence emission is reflected by a dichroic mirror (ZT647RDC, Chroma Technology Corporation) and filtered (ZET473NF, Chroma Technology Corporation). The light is focused by a tube lens (AC254-300-A-ML, Thorlabs Inc.) and imaged by an EMCCD camera (iXon DV887, Andor). The processing of the data for the xy-stabilization is explained in Supplementary Section S2.

Setup control. The core of the instrument control system is a data acquisition board (DAQ board) (ADwin Gold II, Jäger GmbH) which serves as an analog-digital and digital-analog converter. The *ADwin* allows programming its output channels for the direct control of the connected devices from a computer. The *ADwin* receives and processes the raw photon count data from the APD which are used for creating an image from the confocal scan. Additionally, it connects to the piezo controller and the electromechanical shutters (MediaLas STP 8xl, spectrabeam.de) closing/opening the different beam paths. The piezo stage (NanoMax 300 with controller BPC303, Thorlabs Inc.) translates the sample in all three dimensions with a resolution of 5 nm when running in closed-loop mode.

The setup control software constitutes an open-source instrumentation project called PyFLUX, freely available at https://github.com/lumasullo/pyflux and https://github.com/cibion-conicet/pyflux. Further details on specific Python instrumentation and updated versions of the code are available at this repository.

Munich setup:

Excitation. A supercontinuum laser (SuperK Fianium FIU-15, NKT Photonics GmbH, Germany) is used at 19.5 MHz repetition rate as a light source in combination with a tunable bandpass filter (SuperK VARIA, NKT Photonics GmbH, Germany) to select the desired wavelength range (527 – 537 nm) in the visible light spectrum followed by an additional clean-up filter (520/35 Brightline HC, Semrock Inc., USA). The unpolarized light from the laser source is split by a polarizing beam splitter cube (PBS251, Thorlabs GmbH, Germany) into two beams of orthogonal polarizations. Each of the beams is further split by a non-polarizing 50:50 beam splitter cube (BS013, Thorlabs GmbH, Germany). This beam splitting system generates two pairs of beams with each pair sharing the orthogonal linear polarization. The resulting four laser beams are coupled into polarization-maintaining single-mode fibers (PM-S405-XP, Thorlabs GmbH, Germany) of lengths $2.0\ m$, $4.6\ m$, $7.1\ m$ and $9.7\ m$ such that the time delay between the beams after the fiber is ~12.5 ns (= T/4). The four beams are collimated after the fibers with an achromatic lens (AC254-035-A, Thorlabs GmbH, Germany) and recombined by using three 50:50 beam splitter cubes (BS013, Thorlabs GmbH, Germany). The overlay of the beams can be adjusted to obtain the required arrangement of laser foci in the object plane. The axes of linear polarization are matched by turning the fiber out-couplers (Thorlabs GmbH, Germany). Subsequently, the linearly polarized laser beams pass a combination of a quarter- and a half-wave plate (WPQ05M-532 and WPH532M-532, Thorlabs GmbH, Germany) to make them circularly polarized. A vortex phase plate (V-532-20-1, Vortex Photonics, Germany) is then used to introduce the phase modulation necessary to

generate the donut-shaped foci. The beams are guided into the back entrance of the microscope body (IX83, Olympus Deutschland GmbH, Germany), reflected on a dichroic mirror (ZT532RDC – STED, Chroma Technology Corp., USA) and focused with an objective (UPLSAPO100XO/1.4, Olympus Deutschland GmbH, Germany) onto the sample plane.

Detection. The fluorescence light is collected with the same objective and transmitted through the dichroic mirror, focused via an Olympus tube lens onto a pinhole (120 µm, Owis, Germany), collimated with an achromatic lens (AC254-150-A, Thorlabs GmbH, Germany) and focused with a second achromatic lens (AC127-025-A, Thorlabs GmbH, Germany) to the chip of an avalanche photodiode (SPCM-AQRH-16-TR, Excelitas Technologies GmbH & Co. KG, Germany) after filtering the remaining scattered light from the laser with suitable interference optical filters (785 SP EdgeBasic, Semrock Inc., USA, 2x 582/75 Brightline HC, Semrock Inc. USA). The digital signal from the APD is sent to a TCSPC unit (HydraHarp 400, PicoQuant GmbH, Germany).

Drift correction. To measure and correct for sample drift during the measurements, the IR output of the variable bandpass filter is used. A beam of wavelength between 850 and 900 nm is selected with optical filters (875/50 bandpass, Edmund Optics GmbH), coupled into a single-mode fiber (780HP, Thorlabs GmbH, Germany), outcoupled and collimated. This beam is then split with a 50:50 beam splitter cube (BS014, Thorlabs GmbH, Germany) and combined again after inserting a lens system (ACN254-040-B, AC254-150-B, Thorlabs GmbH, Germany) into one of the two paths that focuses the beam to the back focal plane of the objective (dotted line) to create a wide-field illumination at the sample plane. This beam is used for xy drift correction where the position of fiducial markers is localized during the measurement. The collimated IR beam is focused onto the sample plane at an oblique angle to achieve a z position-dependent spot at the detector and use this for z drift correction. Both IR beams are coupled to the main beam path via a dichroic mirror (ZT 785 SPXXR, Chroma Technology Corp., USA) and fed into the microscope to illuminate a region close, but not overlapping with the field of view used for MINFLUX. The reflected and backscattered light is split with an additional 50:50 beam splitter cube (BS014, Thorlabs GmbH, Germany) from the excitation IR beam and detected on a single CMOS camera (Zelux, Thorlabs GmbH, Germany) at different positions of the chip.

Setup control. . The piezo stage (P733.3CD, Physik Instrumente (PI) GmbH &Co. KG, Germany) translates the sample in all three dimensions with a resolution of 0.3 nm when running in closed-loop mode. All components of the setup including the piezo stage are controlled digitally and integrated via a custom version of the PyFLUX project. Further details and source-code of this control software version are available at https://github.com/zaehringer-Jonas/pyflux

Supplementary Section 2. Drift correction

Both the xy position using fiducial markers and the z position using the reflected IR beam are recorded in every experiment. The achieved fiducial tracking precision in xy is better than 1 nm and the z precision is better than 10 nm which is sufficient for our expected p-MINFLUX localization precision. An active drift correction is typically applied during the measurements by means of a feedback loop between the xyz signal and the piezo stage (Supplementary Figure S2A). Typically, the active drift correction achieves a stabilization better than 5 nm in xy and better than 10 nm in z (standard deviation). Any residual xyz drift can be corrected via post-processing using the tracking information. The xyz stabilization system can also be used to scan an emitter over the field of view. Fiducial tracking data from Figure 2C is shown in Supplementary Figure S2B

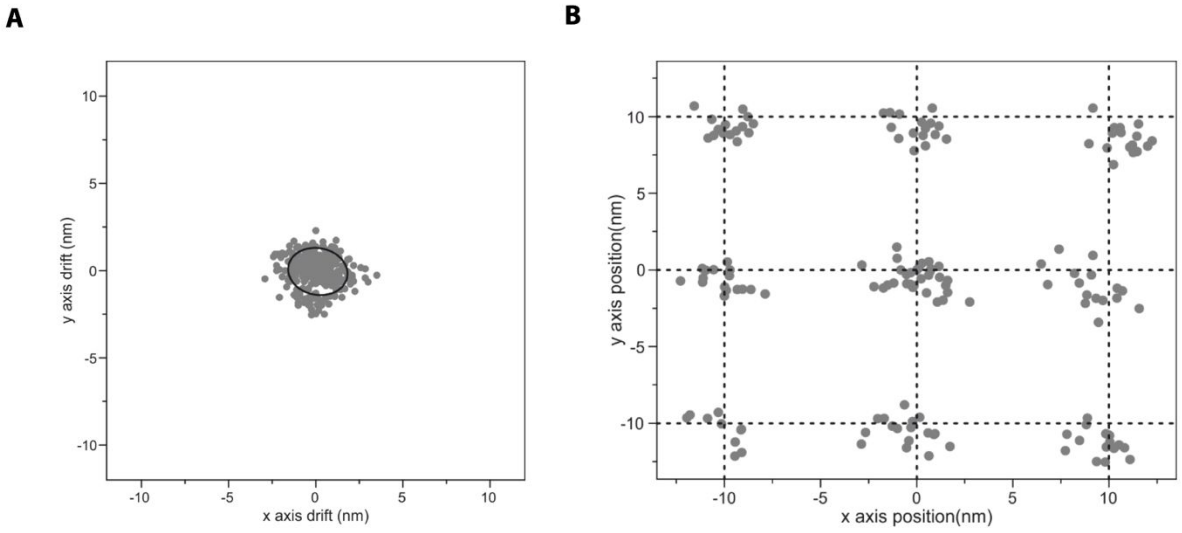

Supplementary Figure S2. A) Camera-based localization of fiducial markers during a 30 s point measurement and the covariance ellipse (black) showing a precision of $\sigma = 1.5$ nm. B) Camera-based localization of fiducial markers during the measurement from Figure 2C. The piezo positioner is moved in a grid with a spacing of 10.0 nm in average, and an average precision of $\sigma = 1.7$ nm.

Supplementary Section 3. DNA-origami structure folding

The DNA origami structures were folded with a 10-fold excess of staples to the scaffold in folding buffer (20 mM $MgCl_2 \times 6H_2O$, 40 mM Tris base, 20 mM acetic acid, 1 mM EDTA-$Na_2 \times 2H_2O$) with a 16 h nonlinear folding ramp[1].

Gel electrophoresis was used for purification. The 50 mL gel contains 1.5% agarose, 2 µL peqGreen DNA stain and gel buffer (12 mM $MgCl_2 \times 6H_2O$, 40 mM Tris base, 20 mM acetic acid, 1 mM EDTA-$Na_2 \times 2H_2O$). After adding 1 x BlueJuice gel loading buffer to the DNA origami solution, the cooled gel runs for 2 h at 60 V. Afterwards, the gel was cut, and the DNA origami solution was extracted via squeezing. The DNA origami concentration was measured with a NanoDrop 2000/2000c Spectrophotometer (ThermoFisher Scientific).

Supplementary Section 4. Sample preparation

The coverslips were first washed using ultrapure water, then cleaned using an ozone cleaner (PSD-UV4, Novascan Technologies, Inc., USA) and washed again using ultrapure water. For sample immobilization, the flow chamber was coated using biotin-labeled bovine serum albumin (1 mg/mL Sigma-Aldrich Chemie GmbH) and NeutrAvidin (1 mg/mL, Sigma-Aldrich Chemie GmbH). In the flow chamber, the DNA origami structures (100 pM in 1x gel buffer) were immobilized due to the biotin-NeutrAvidin binding.

To suppress blinking and photobleaching, an oxidizing and reducing buffer system[2] (1x TAE, 12 mM MgCl2, 2 mM trolox/troloxquinone, 1% (w/v) D-(+) glucose) was used in combination with an oxygen scavenging system with a final concentration of 100 u/ml glucose oxidase and 2500 u/ml catalase. To induce blinking for super-resolution imaging, 50 mM beta-mercaptoethanol was added to the buffer (1x TAE, 12 mM $MgCl_2$, 2 mM trolox/troloxquinone, 1% (w/v) D-(+) glucose). 2 mM cyclooctatetraene was added to increase the stability of the dye.

Supplementary Section 5. Determination of the excitation beam pattern and the point-spread functions

To measure the exact center and shape of the four excitation beams (point-spread functions) an area of 400x400 nm^2 (pixel size: 2 nm) around a fixed fluorescent nanoparticle (GATTAbead labeled with ATTO 542) was scanned with all the four excitation beams simultaneously. After separating the detected photons according to their arrival times (see Figure 1C in the main text) via the commercial software SymPhoTime64 (PicoQuant GmbH, Berlin, Germany), four images can be extracted (see Supplementary Figure S3, upper row) and fitted to a 4^{th} order polynomial in two dimensions. This fit result (Supplementary Figure S3, bottom row) is the basis for the position estimators as described in Supplementary Section 7.

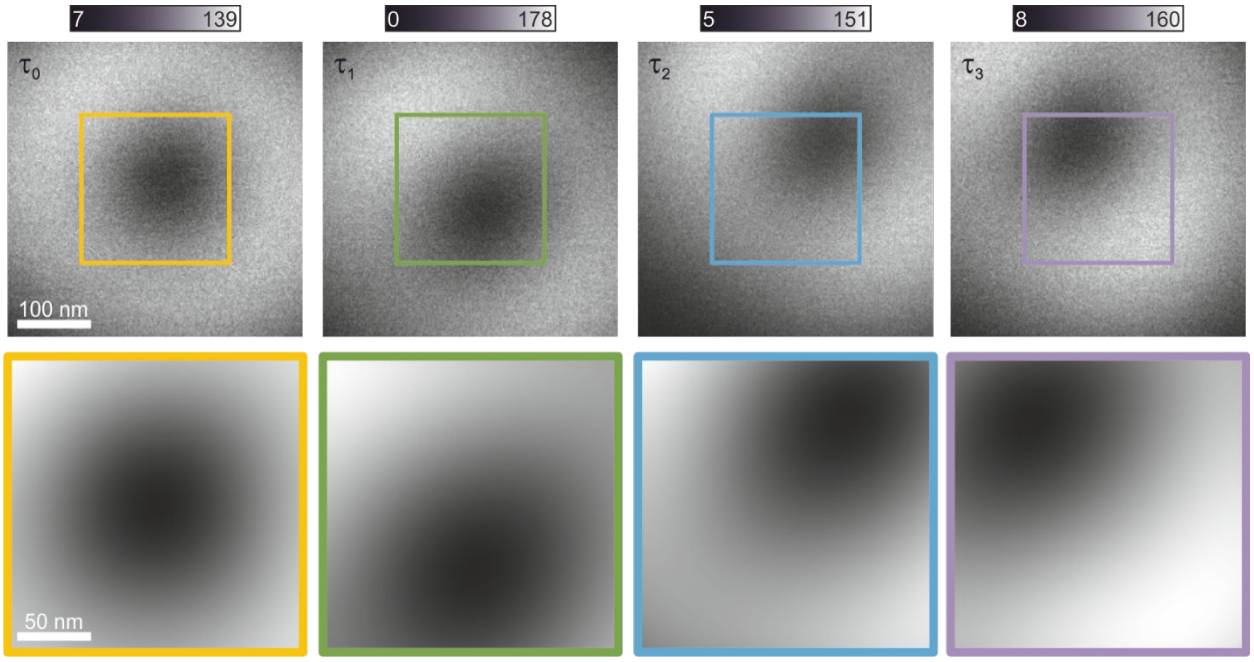

Supplementary Figure S3. Upper row: Simultaneous scan of one fluorescent ATTO542 GATTAbead with the four excitation beams; bottom row: Multi-polynomial fit of the central part

Supplementary Section 6. p-MINFLUX measurement

At first, a large area (10x10 μm^2) was scanned with the central donut of the excitation beam pattern (Figure S5). In this case, the sample consisted of a mixture of the structures described in Figure 4 of the main text. In the fluorescence lifetime image, the lifetimes of ATTO 542 ($\tau = 3.2$ ns) and Cy3B ($\tau = 2.6$ ns) dyes are easily distinguished.

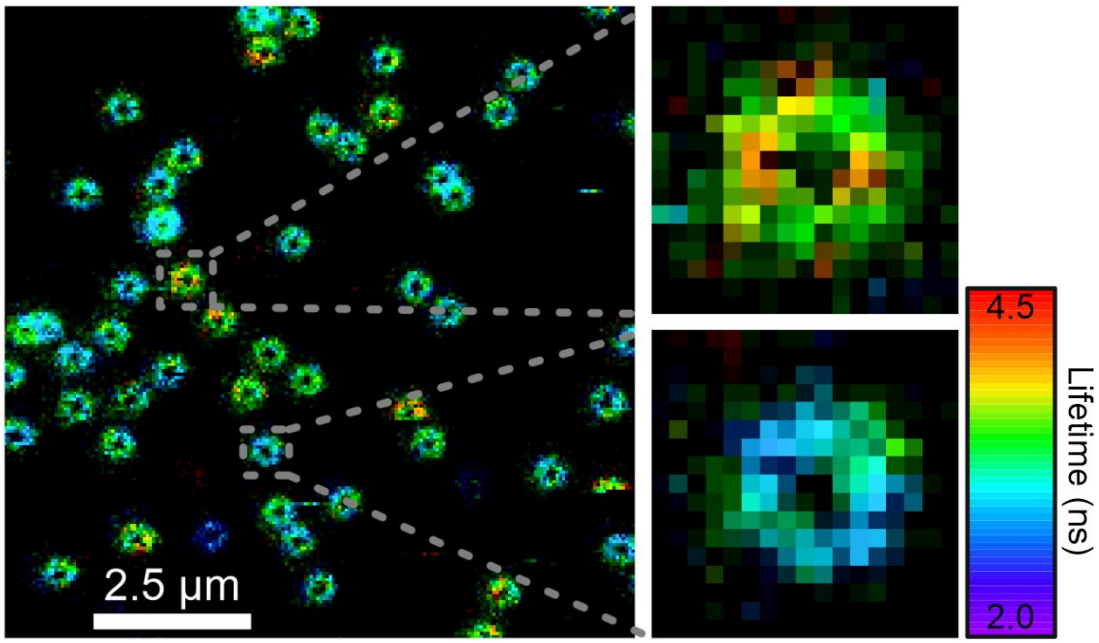

Supplementary Figure S4. 10x10 μm fluorescence lifetime scan image and zoom-in to two individual DNA-origami structures of a sample with a mixture of DNA origamis carrying ATTO 542 or Cy3b as described in Figure 4 of the main text.

Subsequently, the sample was moved in order to place a given DNA-origami at the center of the central donut. Then, the TCSPC measurement is started and the four laser foci were enabled. The measurements run until the molecule photobleaches. The TCSPC data contains the information about the emission intensity at each excitation beam and therefore can be used to obtain the position of the emitter as explained in the following section.

For the superresolution imaging experiments (Figure 3) molecular ON and OFF states have to be discerned. We used a time-binned trace and a suitable threshold to separate ON events from background signal (OFF events). The threshold was chosen well above the noise of the background signal to make sure no OFF states were considered as ON events (false positive) even at the expense of discarding possible low-count rate ON states (false negatives). We also discarded events with a very high photon count rate since they are likely to come from an event in which two

molecules in the ON state are emitting at the same time. The trace displayed in Figure 3 is representative of the measurements. It was time-binned at 0.5 ms, it had a background level of ~10.2 kHz with a noise of ~2.4 kHz, and an average single-molecule ON state count rate of ~80 kHz. A lower threshold of 25 counts, an upper threshold 80 counts, and a minimal ON-time length of 3 ms were used as threshold parameters. Then, every single-molecule emission event is analyzed separately and an (x, y) position estimation is obtained as explained in Supplementary Section 7.

Supplementary Section 7. Position estimator and Cramér-Rao bound

To compute the position estimators and to evaluate the theoretical maximum localization precision we followed the work by Balzarotti et al.[3] We outline here the most important results used in this work.

Position estimator

The likelihood function of the (p-)MINFLUX experiment for a given position of the single emitter $\vec{r} = (x, y)$ and K expositions can be written as

$$\mathcal{L}(\vec{r} \mid \overline{n}) = \frac{N!}{\prod_{i=0}^{K-1} n_i!} \prod_{i=0}^{K-1} p_i(\vec{r})^{n_i} \tag{S1}$$

For all our experiments $K = 4$. The multinomial parameters p_i depend on the spatial coordinates and are defined as

$$p_i(\vec{r}) = \frac{SBR}{SBR+1} \frac{I_i(\vec{r})}{\sum_{j=0}^{K-1} I_j(\vec{r})} + \frac{1}{SBR+1} \frac{1}{K} \tag{S2}$$

where $I_i(\vec{r})$ are the intensity profiles of the excitation foci and SBR is the signal-to-background ratio of the experiment. To estimate the spatial position of the single emitter from the detected photons we used a Maximum Likelihood Estimator (MLE). Since $\mathcal{L}$ and $l = \ln(\mathcal{L}) + const$ share the position of its maximum, we compute the log-likelihood function as

$$l(\vec{r} \mid \overline{n}) = \sum_{i=0}^{K-1} n_i \ln p_i(\vec{r}) \tag{S3}$$

We note that in p-MINFLUX n_i are the number of photons detected for each time window of detection, and that p_i are calculated according to (S2) based on the experimental measurements of the arrangement of foci. The maximum of l is found numerically and thus the MLE for $\vec{r}$ is

$$\hat{r}^{MLE} = \arg\max\ (l) \tag{S4}$$

All functions used to analyze the data arrays containing the arrival time of the photons, to construct l and to find the MLE are fully implemented in Python and are open-source and available at https://github.com/lumasullo/p-minflux/blob/main/tools/tools_analysis.py and https://github.com/cibion-conicet/p-minflux/blob/main/tools/tools_analysis.py

Custom scripts using those functions were written to analyze every experiment. Those scripts are available upon request.

Cramér-Rao bound

To evaluate the theoretical lower bound in uncertainty we computed the Cramér-Rao bound for our experimental arrangement of excitation foci and also for a camera-based single-molecule localization approach. The Cramér-Rao bound expression for an arrangement of four beam expositions can be derived[3] as the inverse of the Fisher information matrix which can, in turn, be derived from the Likelihood function of the experiment. For a two-dimensional (p-)MINFLUX experiment the Fisher information matrix is

$$\mathcal{I} = N \sum_{i=0}^{K-1} \frac{1}{p_i} \begin{bmatrix} \left(\frac{\partial p_i}{\partial x}\right)^2 & \frac{\partial p_i \partial p_i}{\partial x\, \partial y} \\ \frac{\partial p_i \partial p_i}{\partial y\, \partial x} & \left(\frac{\partial p_i}{\partial y}\right)^2 \end{bmatrix} \tag{S5}$$

and hence the CRB matrix is defined as the inverse of $\mathcal{I}$ and poses a lower bound for the covariance of the estimator of the position

$$\Sigma_{cov}(\vec{r}) \geq \Sigma_{CRB}(\vec{r}) = \mathcal{I}^{-1}. \tag{S6}$$

The eigenvalues of Σ_{cov} and Σ_{CRB} are denoted as ${\sigma_x}^2$ and ${\sigma_y}^2$. It is common practice to represent Σ_{cov} and Σ_{CRB} as ellipses with the principal axes directions given by the eigenvectors of the matrices and the length of the axes given by $2\sigma_x$ and $2\sigma_y$ respectively. This representation is used

in Figure 2 of the main text and Supplementary Figure S2, and is useful to illustrate the anisotropies in the MLE precision due to the geometry of the excitation beam pattern.

In order to evaluate the 2-D precision of the localizations with a scalar value, we use the same expression as used by Balzarotti et al.[3], namely

$$\sigma_{CRB} = \sqrt{\frac{1}{2} tr(\Sigma_{CRB})}. \tag{S7}$$

Consequently, we chose to evaluate our experimental precision with an analog expression given by

$$\sigma_{exp} = \sqrt{\frac{1}{2} tr(\Sigma_{cov})}. \tag{S8}$$

This definition of σ is used for the calibration measurements in Figure 2 of the main text. For the σ values reported in Figures 3 and 4, we used the σ parameter of the Gaussian function that resulted from the fit of the 1D projections.

For the comparison with camera-based single-molecule localization techniques, we used the same expression for σ_{CRB} but using the $p_i(x, y)$ given by

$$p_i(x,y) = \frac{1}{K + SBR_C} + \frac{SBR_C}{K + SBR_C} \cdot \frac{1}{4} \cdot \left(\text{erf}\left(\frac{x_i + a/2 - x}{\sqrt{2}\,\sigma_{PSF}} \right) - \text{erf}\left(\frac{x_i - a/2 - x}{\sqrt{2}\,\sigma_{PSF}} \right) \right) \cdot \left(\text{erf}\left(\frac{y_i + a/2 - y}{\sqrt{2}\,\sigma_{PSF}} \right) - \text{erf}\left(\frac{y_i - a/2 - y}{\sqrt{2}\,\sigma_{PSF}} \right) \right) \tag{S9}$$

Where a is the pixel size of the simulated camera and σ_{PSF} the σ of the simulated emission gaussian PSF (not to be confused with localization precision) and K the number of pixels taken into account around the single-molecule image. The index i indicates the pixel, while (x, y) indicate the coordinate of the position of the emitter. For the simulations in Figure 2, we used $a = 100$ nm, $K = 81$ (9 x 9 pixels), and $\sigma_{PSF} = 100$ nm

All the Python functions that we wrote to compute the CRB of both p-MINFLUX and camera-based SMLM to compare with our experimental data are open-source and can be found at

https://github.com/lumasullo/p-minflux/blob/main/tools/tools_simulations.py and https://github.com/cibion-conicet/p-minflux/blob/main/tools/tools_simulations.py

Supplementary Section 8. p-MINFLUX simulations

To estimate the overall performance of p-MINFLUX, as well as the influence of the different experimental parameters, we developed a software package with functions that simulate a complete p-MINFLUX experiment, including pulsed excitation with different beam patterns, fluorescence emission, TCSPC detection, and the position estimation of the emitter from the photon arrival times.

Briefly, in a first step doughnut-shaped foci (or foci with any other geometry) are created. Next, given a certain position of the emitter within the foci arrangement, an array of $\overline{n} = [n_0, n_1, n_2, n_3]$ photons is extracted from a multinomial distribution. Photon arrival times are generated based on predefined emission statistics; we used a single exponential distribution in agreement with the observed behavior of the fluorophores. The simulated photon arrival times are registered in both the fluorescence lifetime scale (i.e. from the laser excitation pulse; micro time) and in the absolute time scale of the simulation (i.e. from the beginning of the simulated experiment; macro time). Background photons with a uniform distribution of both macro and micro time are added in order to simulate different SBR situations.

At this point, the analysis is performed exactly in the same way as with the real data by calculating the MLE of the position of the emitter as explained in Supplementary Section 7. For each desired set of experimental parameters typically $M = 1000$ simulations of p-MINFLUX were performed obtaining the full probability distribution of the estimator in a Monte-Carlo fashion. Typically, the mean error of the distribution was used as the localization quality metric.

$$\varepsilon = \sqrt{\frac{1}{2M}\sum_{i=1}^{M}\left((x_i - x)^2 + (y_i - y)^2\right)} \tag{S10}$$

where M are the number of simulated results, (x, y) indicate the ground truth position of the emitter and (x_i, y_i) are the result of the i-th simulation. It should be noted that (S10) is very similar to equation (S7) but uses the ground truth position instead of the mean estimated position for the calculation of the trace of the covariance matrix thus accounting for the error due to any possible bias.

Functions used to simulate the experiments are open-source and can be found at https://github.com/lumasullo/p-minflux/blob/main/tools/tools_simulations.py and https://github.com/cibion-conicet/p-minflux/blob/main/tools/tools_simulations.py

Supplementary Section 9. Effect of misalignment of the excitation beam pattern

Unlike the MINFLUX implementation by Balzarotti *et al*.[3], the excitation beam pattern (EBP) in p-MINFLUX is neither scanned during the measurement nor positioned with any active control or feedback loop. The alignment of the beams into the desired arrangement (usually an equilateral triangle with one beam in its center) is achieved by operating the kinematic mirrors mounts. In the experiments presented this was done manually and controlled through measurements as described in Supplementary Section 5. We were able to routinely align the EBP with $5-10$ nm accuracy, in both set-ups (Supplementary Section 1).

We performed Monte-Carlo simulations to quantitatively analyze the influence of EBP misalignments on the attainable localization precision. Different emitter positions within the EPB were simulated and the resulting localization precisions were visualized in 2D maps. The EBP centers were displaced from their ideal positions by a radial offset *r*. During one simulation run, all four-excitation point spread functions (PSFs) constituting the EBP were off-set by the same value *r*.

For each emitter position and radial offset, we performed 1000 simulation runs. The angular direction of each PSF's displacement was randomly chosen and changed after 100 runs. This procedure of analyzing 10 random EBP for the same *r* allowed us to find an averaged result which does not overestimate a particularly good or bad EBP. The simulations were carried out for $N = 1000$ detected photons, $SBR = 20$, and $L = 100$ nm. In Supplementary Figure S5A, we show the exemplary simulation results for one random EBP with offsets of $r = 0, 10$ and 20 nm, respectively.

To facilitate the evaluation of the simulation results, we computed $\sigma(0,0)$, the localization precision of an emitter placed at the center of the ideal EBP and $\langle\sigma\rangle_{FOV}$, the mean localization precision within the emitter position space of each 2D map. Figure S5B shows that the localization precision for an emitter at the EBP center decreases significantly for radial offsets $r > 20$ nm. The mean localization precision, $\langle\sigma\rangle_{FOV}$, deteriorates by less than 0.5 nm for radial offsets smaller than 15 nm.

Appreciating the experimental and computational findings, we conclude that the attainable localization precision in p-MINFLUX is robust against moderate misalignments of the EBP. Displacements of the PSFs' from their target positions by less than 15 nm do not lead to a significant decrease in localization precision. It must be emphasized that our analyses assumed PSFs which are measured and fitted with high precision and accuracy, as described in Supplementary Section 5.

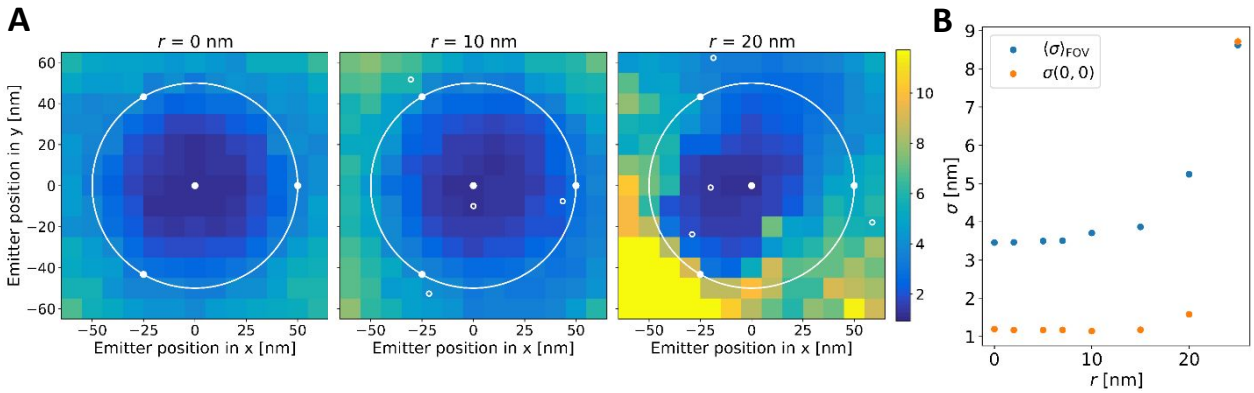

Supplementary Figure S5. Analysis of misalignments of the p-MINFLUX excitation beam pattern (EBP). A) Example 2D maps of the attainable localization precision for different emitter positions and radial EBP offsets $r = 0, 10$ and 20 nm. The solid dots indicate the PSFs' center position of the ideal EBP whereas the small circles correspond to the misaligned EBP. B) The localization precision at the EBP center, $\sigma(0,0)$, and the mean over the emitter position space, $\langle\sigma\rangle_{FOV}$, is plotted for different radial offset values. The simulations were performed for $N = 1000$ detected photons, $SBR = 20$ and 10 randomly misaligned EBP for each r.

Supplementary Section 10. Photon arrival times and crosstalk between detection time windows

As any other pulsed-interleaved technique, p-MINFLUX relies on the fact that minimal cross-talk exists between the arrival time-windows corresponding to each of the pulsed laser excitations. The probability of cross-talk can be calculated analytically taking into account the fluorescence lifetime of the molecule and the size of the detection time-windows.

The expected influence of the photon crosstalk on the p-MINFLUX localization precision and accuracy is however not straightforward. Thus we simulated p-MINFLUX experiments at different degrees of crosstalk. In Supplementary Figure S6A, we show simulated localization precision and accuracy for typical values of $N = 1200$, $SBR = 15$, $L = 100$ nm and fluorescence lifetimes ranging from 1.0 to 4.0 ns for detection time windows of 12.5 ns. From our simulations, we conclude that effects on precision and accuracy are < 1 nm for fluorescence lifetimes up to 3.0 ns , which corresponds to roughly ¼ of the detection time window and $\sim 1\%$ crosstalk. Measurements above this limit are still acceptable although a ~ 2 nm bias is present and precision decreases slightly compared to the 1.0 ns (showing almost no crosstalk effect). In particular, we simulate the experimental situation of our super-resolution imaging experiments (Figure 3 of main text) and we found that despite the $\sim 5\%$ crosstalk, p-MINFLUX is expected to fully resolve the DNA-origami structure (Supplementary Figure S6B).

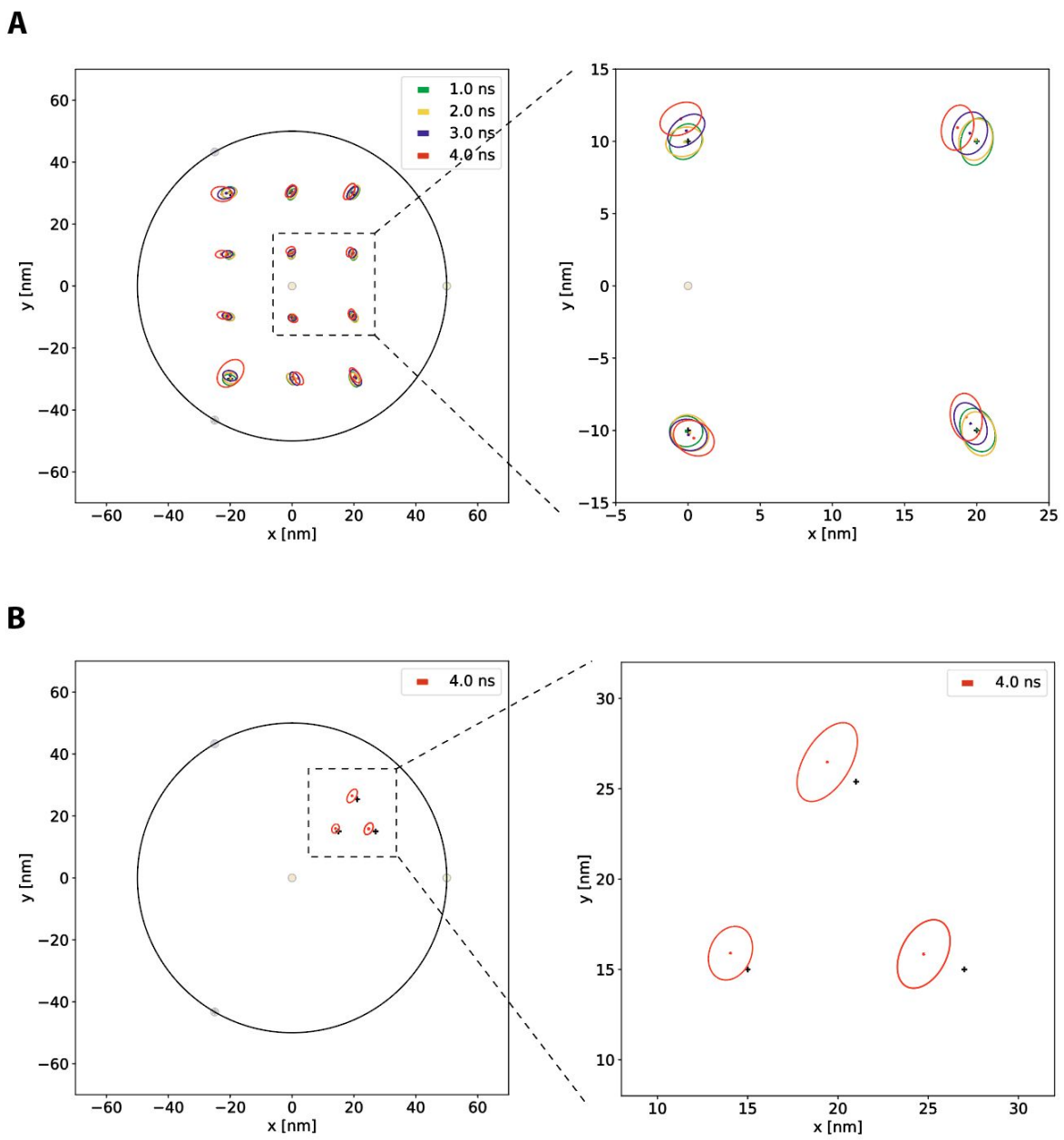

Supplementary Figure S6. A) Precision and accuracy of p-MINFLUX at different positions within the field of view for different fluorescence lifetimes. B) Simulation of a representative imaging experiment with a DNA-origami labeled with fluorophores with a fluorescence lifetime of ~ 4.0 ns in analogy to the data presented in Figure 3 of the main text. Black crosses indicate the ground truth of the simulations.

We note that although in the Likelihood function (Equation S1) of the experiment we neglect crosstalk, the arrival times of the photons could be directly modeled, and hence the analysis

optimized and very likely extend the scope of p-MINFLUX for larger crosstalk provided good SNR.

Finally, we note that since the crosstalk probability scales with the repetition rate of the laser, a lower repetition rate would solve the crosstalk and extend the range of possible fluorescence lifetimes. In particular, we demonstrated p-MINFLUX with a $20\ \mathrm{MHz}$ pulsed laser, hence allowing to use of fluorophores and other single emitters with fluorescence (luminescence) lifetimes up to $\sim 4\ \mathrm{ns}$. A setup with a repetition rate of $10\ \mathrm{MHz}$ would imply minimal changes to our current setup and extend the range of suitable fluorescence lifetimes up to $\sim 8\ \mathrm{ns}$ which cover most of the organic fluorophores typically used in fluorescence microscopy and spectroscopy.

Supplementary Section 11. Localization time traces simulation

To estimate the expected distribution of binding times measured from finite, photon-limited localization traces we simulated the p-MINFLUX tracking experiment assuming the switching between positions of the DNA pointers (Figure 4) is stochastic and memory-less, and hence the transient binding times are distributed exponentially. We thus generated simulated p-MINFLUX localization traces with transient binding times at the two positions in the DNA-origami structure. We simulated the localizations to have a precision of $\sigma = 3$ nm and the distance between the two positions was set to $d = 12$ nm. We generated traces with parameters (fluorescent lifetime, approximate binding time, number of transitions between positions) taken from our experimental data for both DNA-origami designs. Traces were then analyzed, and average binding times and fluorescent lifetimes were extracted using the same algorithms that we used to analyze the experimental data.

Supplementary Table S1: Unmodified staples from the 5' to the 3' end for the DNA-origami structure used for the superresolution imaging experiments (Figure 3).

Sequence (5' to 3')	**Length [nt]**
TAAGAGCAAATGTTTAGACTGGATAGGAAGCC	32
AATAGTAAACACTATCATAACCCTCATTGTGA	32
TCAAATATAACCTCCGGCTTAGGTAACAATTT	32
GTACCGCAATTCTAAGAACGCGAGTATTATTT	32
ATTATCATTCAATATAATCCTGACAATTAC	30
AAATTAAGTTGACCATTAGATACTTTTGCG	30
ATACATACCGAGGAAACGCAATAAGAAGCGCATTAGACGG	40
AAAGTCACAAAATAAACAGCCAGCGTTTTA	30
AAAGGCCGGAGACAGCTAGCTGATAAATTAATTTTTGT	38
ACAAACGGAAAAGCCCCAAAAACACTGGAGCA	32
TCTTCGCTGCACCGCTTCTGGTGCGGCCTTCC	32
GACAAAAGGTAAAGTAATCGCCATATTTAACAAAACTTTT	40
GATTTAGTCAATAAAGCCTCAGAGAACCCTCA	32
TATATTTTGTCATTGCCTGAGAGTGGAAGATTGTATAAGC	40
GCTTTCCGATTACGCCAGCTGGCGGCTGTTTC	32
CACCAGAAAGGTTGAGGCAGGTCATGAAAG	30
CGCGCAGATTACCTTTTTTAATGGGAGAGACT	32
ACAACATGCCAACGCTCAACAGTCTTCTGA	30
GTTTATCAATATGCGTTATACAAACCGACCGTGTGATAAA	40
AACGCAAAGATAGCCGAACAAACCCTGAAC	30
CTTTTACAAAATCGTCGCTATTAGCGATAG	30
CAACTGTTGCGCCATTCGCCATTCAAACATCA	32
CAGCGAAACTTGCTTTCGAGGTGTTGCTAA	30
AAGGCCGCTGATACCGATAGTTGCGACGTTAG	32

AGGCTCCAGAGGCTTTGAGGACACGGGTAA	30
TTAGGATTGGCTGAGACTCCTCAATAACCGAT	32
GATGGCTTATCAAAAAGATTAAGAGCGTCC	30
TAAATCGGGATTCCCAATTCTGCGATATAATG	32
AGGCAAAGGGAAGGGCGATCGGCAATTCCA	30
TTTCGGAAGTGCCGTCGAGAGGGTGAGTTTCG	32
TCACCAGTACAAACTACAACGCCTAGTACCAG	32
AACAAGAGGGATAAAAATTTTTAGCATAAAGC	32
AAATCACCTTCCAGTAAGCGTCAGTAATAA	30
CAGCAAAAGGAAACGTCACCAATGAGCCGC	30
TGTAGCCATTAAAATTCGCATTAAATGCCGGA	32
TATTAAGAAGCGGGGTTTTGCTCGTAGCAT	30
TACGTTAAAGTAATCTTGACAAGAACCGAACT	32
GCAAGGCCTCACCAGTAGCACCATGGGCTTGA	32
TGCATCTTTCCCAGTCACGACGGCCTGCAG	30
AATTGAGAATTCTGTCCAGACGACTAAACCAA	32
GCCATCAAGCTCATTTTTTAACCACAAATCCA	32
TAAATGAATTTTCTGTATGGGATTAATTTCTT	32
ATGCAGATACATAACGGGAATCGTCATAAATAAAGCAAAG	40
AATACGTTTGAAAGAGGACAGACTGACCTT	30
TTATACCACCAAATCAACGTAACGAACGAG	30
CATGTAATAGAATATAAAGTACCAAGCCGT	30
TATAACTAACAAAGAACGCGAGAACGCCAA	30
ATCGCAAGTATGTAAATGCTGATGATAGGAAC	32
CATAAATCTTTGAATACCAAGTGTTAGAAC	30
GCGAAAAATCCCTTATAAATCAAGCCGGCG	30
TAAATCATATAACCTGTTTAGCTAACCTTTAA	32
CTTTAGGGCCTGCAACAGTGCCAATACGTG	30

CGAAAGACTTTGATAAGAGGTCATATTTCGCA	32
AGCAAGCGTAGGGTTGAGTGTTGTAGGGAGCC	32
TCAAGTTTCATTAAAGGTGAATATAAAAGA	30
TCATTCAGATGCGATTTTAAGAACAGGCATAG	32
CTACCATAGTTTGAGTAACATTTAAAATAT	30
ATCCCAATGAGAATTAACTGAACAGTTACCAG	32
ACCTTGCTTGGTCAGTTGGCAAAGAGCGGA	30
CTGTGTGATTGCGTTGCGCTCACTAGAGTTGC	32
GCCGTCAAAAAACAGAGGTGAGGCCTATTAGT	32
GTATAGCAAACAGTTAATGCCCAATCCTCA	30
AGACGACAAAGAAGTTTTGCCATAATTCGAGCTTCAA	37
ACCCTTCTGACCTGAAAGCGTAAGACGCTGAG	32
ATATTTTGGCTTTCATCAACATTATCCAGCCA	32
ATATTCGGAACCATCGCCCACGCAGAGAAGGA	32
TTCCAGTCGTAATCATGGTCATAAAAGGGG	30
CGGATTGCAGAGCTTAATTGCTGAAACGAGTA	32
AAAGCACTAAATCGGAACCCTAATCCAGTT	30
GACCTGCTCTTTGACCCCCAGCGAGGGAGTTA	32
GTTTATTTTGTCACAATCTTACCGAAGCCCTTTAATATCA	40
TAATCAGCGGATTGACCGTAATCGTAACCG	30
GCGAGTAAAAATATTTAAATTGTTACAAAG	30
CTTAGATTTAAGGCGTTAAATAAAGCCTGT	30
CCAGGGTTGCCAGTTTGAGGGGACCCGTGGGA	32
TAGGTAAACTATTTTTGAGAGATCAAACGTTA	32
CGATAGCATTGAGCCATTTGGGAACGTAGAAA	32
GCGCAGACAAGAGGCAAAAGAATCCCTCAG	30
CCTGATTGCAATATATGTGAGTGATCAATAGT	32
GCCCGAGAGTCCACGCTGGTTTGCAGCTAACT	32

TCATCGCCAACAAAGTACAACGGACGCCAGCA	32
CTGTAGCTTGACTATTATAGTCAGTTCATTGA	32
GAATTTATTTAATGGTTTGAAATATTCTTACC	32
CCTAAATCAAAATCATAGGTCTAAACAGTA	30
AGCGCGATGATAAATTGTGTCGTGACGAGA	30
GATGTGCTTCAGGAAGATCGCACAATGTGA	30
GCCTCCCTCAGAATGGAAAGCGCAGTAACAGT	32
TTTATCAGGACAGCATCGGAACGACACCAACCTAAAACGA	40
CACAACAGGTGCCTAATGAGTGCCCAGCAG	30
CTGAGCAAAAATTAATTACATTTTGGGTTA	30
TGACAACTCGCTGAGGCTTGCATTATACCA	30
GCGAACCTCCAAGAACGGGTATGACAATAA	30
TGAAAGGAGCAAATGAAAAATCTAGAGATAGA	32
GCACAGACAATATTTTTGAATGGGGTCAGTA	31
TCACCGACGCACCGTAATCAGTAGCAGAACCG	32
GCCCTTCAGAGTCCACTATTAAAGGGTGCCGT	32
CCACCCTCTATTCACAAACAAATACCTGCCTA	32
ATTTTAAAATCAAAATTATTTGCACGGATTCG	32
GTAATAAGTTAGGCAGAGGCATTTATGATATT	32
TTAACACCAGCACTAACAACTAATCGTTATTA	32
TTTTATTTAAGCAAATCAGATATTTTTTGT	30
AACACCAAATTTCAACTTTAATCGTTTACC	30
GATGGTTTGAACGAGTAGTAAATTTACCATTA	32
CTCGTATTAGAAATTGCGTAGATACAGTAC	30
ATCCCCCTATACCACATTCAACTAGAAAAATC	32
CTTATCATTCCCGACTTGCGGGAGCCTAATTT	32
GCGGAACATCTGAATAATGGAAGGTACAAAAT	32
GACCAACTAATGCCACTACGAAGGGGGTAGCA	32

ACGGCTACAAAAGGAGCCTTTAATGTGAGAAT	32
TGGAACAACCGCCTGGCCCTGAGGCCCGCT	30
GCGGATAACCTATTATTCTGAAACAGACGATT	32
CCCGATTTAGAGCTTGACGGGGAAAAAGAATA	32
TTAAAGCCAGAGCCGCCACCCTCGACAGAA	30
CAGAAGATTAGATAATACATTTGTCGACAA	30
AGAAAACAAAGAAGATGATGAAACAGGCTGCG	32
CGTAAAACAGAAATAAAAATCCTTTGCCCGAAAGATTAGA	40
ACCGATTGTCGGCATTTTCGGTCATAATCA	30
AATAGCTATCAATAGAAAATTCAACATTCA	30
AAACAGCTTTTTGCGGGATCGTCAACACTAAA	32
ATTATACTAAGAAACCACCAGAAGTCAACAGT	32
TTGACAGGCCACCACCAGAGCCGCGATTTGTA	32
TACCGAGCTCGAATTCGGGAAACCTGTCGTGCAGCTGATT	40
GCCAGTTAGAGGGTAATTGAGCGCTTTAAGAA	32
AGCCAGCAATTGAGGAAGGTTATCATCATTTT	32
CATTTGAAGGCGAATTATTCATTTTTGTTTGG	32
ACACTCATCCATGTTACTTAGCCGAAAGCTGC	32
ACCTTTTTATTTTAGTTAATTTCATAGGGCTT	32
GCTATCAGAAATGCAATGCCTGAATTAGCA	30
AAGTAAGCAGACACCACGGAATAATATTGACG	32
CAGGAGGTGGGGTCAGTGCCTTGAGTCTCTGAATTTACCG	40
TTAATGAACTAGAGGATCCCCGGGGGGTAACG	32
AAGGAAACATAAAGGTGGCAACATTATCACCG	32
CATCAAGTAAAACGAACTAACGAGTTGAGA	30
AATGGTCAACAGGCAAGGCAAAGAGTAATGTG	32
CAACCGTTTCAAATCACCATCAATTCGAGCCA	32
GGCCTTGAAGAGCCACCACCCTCAGAAACCAT	32

TAAATCAAAATAATTCGCGTCTCGGAAACC	30
GAGGGTAGGATTCAAAAGGGTGAGACATCCAA	32
TTATTACGAAGAACTGGCATGATTGCGAGAGG	32
ATACCCAACAGTATGTTAGCAAATTAGAGC	30
TTAACGTCTAACATAAAAACAGGTAACGGA	30
AGTATAAAGTTCAGCTAATGCAGATGTCTTTC	32
CACATTAAAATTGTTATCCGCTCATGCGGGCC	32
CTTTAATGCGCGAACTGATAGCCCCACCAG	30
GAAATTATTGCCTTTAGCGTCAGACCGGAACC	32
AACGCAAAATCGATGAACGGTACCGGTTGA	30
ACAACTTTCAACAGTTTCAGCGGATGTATCGG	32
GCCTTAAACCAATCAATAATCGGCACGCGCCT	32
TCCACAGACAGCCCTCATAGTTAGCGTAACGA	32
GCCCGTATCCGGAATAGGTGTATCAGCCCAAT	32
TCAATATCGAACCTCAAATATCAATTCCGAAA	32
GTCGACTTCGGCCAACGCGCGGGGTTTTTC	30
GCAATTCACATATTCCTGATTATCAAAGTGTA	32
CTCCAACGCAGTGAGACGGGCAACCAGCTGCA	32
TGTAGAAATCAAGATTAGTTGCTCTTACCA	30
TTCTACTACGCGAGCTGAAAAGGTTACCGCGC	32
CAAATCAAGTTTTTTGGGGTCGAAACGTGGA	31
CCAATAGCTCATCGTAGGAATCATGGCATCAA	32
TTAGTATCACAATAGATAAGTCCACGAGCA	30
AGGAACCCATGTACCGTAACACTTGATATAA	31
GAGAGATAGAGCGTCTTTCCAGAGGTTTTGAA	32
TCGGCAAATCCTGTTTGATGGTGGACCCTCAA	32
AAGCCTGGTACGAGCCGGAAGCATAGATGATG	32
AGAAAGGAACAACTAAAGGAATTCAAAAAAA	31

ACGCTAACACCCACAAGAATTGAAAATAGC	30
CCACCCTCATTTTCAGGGATAGCAACCGTACT	32
TTTAGGACAAATGCTTTAAACAATCAGGTC	30
AGAGAGAAAAAAATGAAAATAGCAAGCAAACT	32
AACGTGGCGAGAAAGGAAGGGAAACCAGTAA	31
CCAACAGGAGCGAACCAGACCGGAGCCTTTAC	32
AACAGTTTTGTACCAAAAACATTTTATTTC	30
TTTACCCCAACATGTTTTAAATTTCCATAT	30
TAAAAGGGACATTCTGGCCAACAAAGCATC	30
TTTTCACTCAAAGGGCGAAAAACCATCACC	30
TCTAAAGTTTTGTCGTCTTTCCAGCCGACAA	31
GTTTTAACTTAGTACCGCCACCCAGAGCCA	30

Supplementary Table S2. Modified and extended staples from the 5' to the 3' end for the DNA-origami structure used for the superresolution imaging experiments (Figure 3).

Sequence (5' to 3')	**Length [nt]**	**Function**
Biotin- GAGAAGAGATAACCTTGCTTCTGTTCGGGAGAAACAATAA	40	Biotin for immobilization
Biotin- ATAAGGGAACCGGATATTCATTACGTCAGGACGTTGGGAA	40	Biotin for immobilization
Biotin- AGCCACCACTGTAGCGCGTTTTCAAGGGAGGGAAGGTAAA	40	Biotin for immobilization
Biotin- CGGATTCTGACGACAGTATCGGCCGCAAGGCGATTAAGTT	40	Biotin for immobilization
Biotin- GAAACGATAGAAGGCTTATCCGGTCTCATCGAGAACAAGC	40	Biotin for immobilization
Biotin- TAGAGAGTTATTTTCATTTGGGGATAGTAGTAGCATTA	40	Biotin for immobilization
TTCCTCTACCACCTACATCACAA ATTACCTTTGAATAAGGCTTGCCCAAATCCGC	56	External labeling site of Atto 532 for super resolution imaging
TTCCTCTACCACCTACATCACAA TTGCTCCTTTCAAATATCGCGTTTGAGGGGGT	56	External labeling site of Atto 532 for super resolution imaging
TTCCTCTACCACCTACATCACAA AATACTGCCCAAAAGGAATTACGTGGCTCA	54	External labeling site of Atto 532 for super resolution imaging
TTCCTCTACCACCTACATCACAA CTTTTGCAGATAAAAACCAAAATAAAGACTCC	56	External labeling site of Atto 532 for super resolution imaging
Atto532-TTTGTGATGTAGGTGGTAGAGGAA	25	Atto 532 external labeling strand for super resolution imaging
GATGGCTTATCAAAA-**Atto532**-GATTAAGAGCGTCC	30	Internal Atto 532 for evaluation of the localization performance

Supplementary Table S3: Unmodified staples from the 5' to the 3' end for the DNA-origami structure used for the tracking experiments (Figure 4).

Sequence (5' to 3')	**Length [nt]**
CAATTCATATAGATAATAAATCCTTTGCCCG	31
ATGAGTGACCTGTGCAGTTTCTGCCAGCACG	31
GGAACCCAAAACTACAAACAGTTTCAGCG	29
GTTTTCCCGTAGATGGCAGGAAGATCGCACT	31
TTTTTTAATGCACGTACAAGTTACCCATTCAG	32
CCCGCCGCGCTTAATGAAAGCCGGCGAACGTG	32
AAATCCCGTAAAAAAACGTTTTTTGGACTTGT	32
AGGAAACCGAGGACGTAGAAAAAGTACCG	29
TATCATTTTGCGGAACATCCTGATATAAAGAA	32
CTTAATTGAGACCGGAAACAGGTCAGGATTAGAGGTGGCA	40
TTTTTTTTTTTTAAAACTAG	20
GCCGATTAAGGAAGGGCGCGTAACCACCACA	31
ATGGCTACAATCAACTGAGAGCCAGCAGCAAATGAAAAACGAACCTAATGCGCTTGGCAGA	61
GTCCACTAAACGCGCGGACGGGCAACAGCTG	31
TGCGGCCAGAATGCGGTTTT	20
TTTTATTGGGCTTGAGATGGCCAGAACGATT	31
ATTGCCCTTCACCGCCCCAGCTGCTTGCGTTG	32
TGATGTTACTTAGCCGGAAAAGACAGCACTACGAA	35
TTTTCTTTACAAACAATTCG	20
TATTTTGTTAAAATTCGGGTATATATCAAAAC	32
TAATAGTATTCTCCGTGCATTAAATTTTTGTT	32
TGTTGCCCTGCGGCTGATCAGATGCAGTGTCA	32
TTTTTTGCATCAAAAGCCTGAGTAATTTT	29
TTTTTTGAGGGGACGACGAC	20

TGATTGCTTTGAATACAAACAGAATGTTTGGA	32
ACATAGCGATAGCTTATTTT	20
TTTTCCCTTACACTGGTTGC	20
CGGCCTCGTTAGAATCTTTT	20
TTACCCATAACCCTCGAAATACAATGTTTAAACAGGG	37
TTTTTTAGGAATACCACAGTAGTAATTTT	29
TGTAATCTTGACAAGAACCGAAC	23
CTTCTGACCTAAATTTGCAGAGGCCAGAACGCAATTTACG	40
AGATGAAGGGTAAAGTTTTT	20
CACAGACATTTCAGGGATCTCCAAAAAAAAGGTTCTTAAAGCCGCTTT	48
TCTTTAGGCTGAATAATGCTCATTAGTAACAT	32
CAAAGGGCCTGTCGTGTGGCCCTGAGAGAGTT	32
GCAGAGGCGAATTATTTTTCATTTGCTATTAA	32
TTTCGACTTGATCGAGAGGGTTGATATAAGTATTTT	36
TTTTCATATAAAAGAAAGCCGAACATTTT	29
TTTTAAACATCAAGAAAAAA	20
CAAAAGAATAAAATACCCAGCGATTATACCAAGCGCGAA	39
GAGCCGATATAACAACAACCATCGCCCTTTTTTT	34
TTTTTTCCTGATTATCACGT	20
CCGAATCTAAAGCATCTTTT	20
TTTTGCTAATATCAGAGAGATAACCCCGCCACCGCG	36
TGTACTGGTAATAAGTTCAGTGCC	24
TTTTCGCAAATGGTCAATAAACCATTAGATGC	32
ATCAAAAAGTCATAAAACGGAACAACATTATCAACTTTAGTAGAT	45
GGCTTAGGTTGGGTTAAGCTAATGATTTTCGA	32
AACGTTATTAATTTTACAACTAATCAGTTGGC	32
TGCGAATAATAATCGACAATGTTCGGTCG	29
CTGCAACAGTGCCACGTATCTGGTAGATTAGA	32

CCAGCCAGCTTTCCGGGTAATGGGGTAACAAC	32
CCGTGCATCTGCCAGTTTTT	20
TTTTCCCGACTTACAAAATAAACAGTTTT	29
GAAAGGAGCGGGCGCTAGGTTTT	23
CATTGCCTGAGAGTCTTTATGACCATAAATCATTTCATTT	40
TTTTGGCGCATAGGCTGGCTAACGGTGTTAAATTGT	36
CTCCAATCGTCTGAAATTTT	20
CCCCCTGCGCCCGCTTTAGCTGTTTCCTGTGT	32
GGAGCCTTCACCCTCAGAGCCACC	24
TTTTTTGTTCCAGTTTGGAACAAGA	25
TTAATTAAACCATACATACATAAAGGTGGCAATTTT	36
TTTTTATCATCGCCTGAACAGACCATTTT	29
TCTTACCATAAAGCCATAATTTAGAATGGTTTAGGGTAGC	40
TTTTATTGCTGAATATAATACATTTTTTT	29
AAATCAACACGTGGCATCAGTATTCTCAATCC	32
AGAACGTTAACGGCGTAATGGGTAAAGGTTTCTTTGCGTCGGTGGTGCTGGTCTTGCCGTT	61
GCCTAATTATCATATGATAAGAGATTTAGTTAATTTCAT	39
TTTTCCATATTATTTATCCCAATCCAAAGTCAGAGA	36
ACCCTCATGCCCTCATTTTCTGTATGGGATTTAGTTAAAGCAGCTTGA	48
GTCGAAATCCGCGACCTGCTCCACCAACTTTTAGCATTC	39
CCGGAACCGCAAGAAAGCAATAGCTATCTTACTCACAATCCGATTGAG	48
AACGTCAATAGACGGGGAATACCCAAAAGAACAAGACTCCGTTTTTAT	48
GCAGTTGGGCGGTTGTCCAGTTATGGAAGGAG	32
CCGTCGGAGTAGCATTCAAAAACAGGAAGATT	32
TTTTTTATCACCGTCACAGCGTCAGTTTT	29
CCAACATGACGCTCAATGCCGGAGGAAATACC	32
TACAGGCATTAAATTAACCAATAGGAACGCCATCAAAGTCAATCAGAATTAGCCTAAATCG	61
AGTTGATTAGCTGAAAAGAGTACCTTTAATTGTTAATTCGGACCATAA	48

AGCGAACCAGAAGCCTGGAGAATCACAAAGGCTATCAGGT	40
TTTTGAACAACTAAAGGAACACTGATTTT	29
CGGGAAACGAAAAACCTGATGGTGGTTCCGAA	32
CGTTGAAAATAGCAAGCCCAATA	23
GACAGATGGACCTTCATCAAGAGCCCTGAC	30
GCGAGAAAAGGGATGACGAGCACGTATAACGTGCTTTTCACGCTGAAGAAAGC	53
TCGATAGCAGCACCGTAAAATCACGTTTTGCT	32
TTTTCCCTCAGAGCCACCACCCTCAGAAAGCGCTTA	36
ATCGGCAAAATCCCTTACGTGGACTCCAACGT	32
TTCAAATTTTTAGAAAAAACAGGAGCAAACAAGAGAATCGATGAAGGGTGAGATATTTTA	60
TTTTTAGCCCGGAATAGCCTATTTCTTTT	29
TACCGATAGTTGCGCTTTTTCA	22
TTTTCAGGGTGGTTTTTCTT	20
AAAGACAAATTAGCAAGTCACCAATGAAACCA	32
CCAGAATGGAGCCGCCAATCAAGTTTGCC	29
TTTTTGGATTATTTACAGAA	20
ATTATAGCGTCGTAATAGTAAAATGTTTTTT	31
TAGTCAGAAGCAAAGCGGATTTT	23
AGGCGAAAATCCTGTTGTCTATCACCCCCGAT	32
GGGGCGCGCCCAATTCACTAAAGTACGGTGTCACGAGAATAGCTTCAA	48
GCCGTCACAATATAAAAGAAACCACCAGAAGGAGCGGACTCGTATTACATTTGTCAAATAT	61
GAAATTGTTATCCGCTCACATTAAATTAATGA	32
TTTTTCCAAGAACGGGTGCGAACCTTTTT	29
TGCTCATTCTTATGCGTTAATAAAACGAACTATATTCATTGGCTTTTG	48
TTTTTAGACTGGCATCAGTTGAGATTTTTT	30
AAACGGGGTTTTGCTACATAACGCCAAAAAAGGCT	35
ACAAAGTATGAGGAAGCTTTGAGGACTAAAGATTTT	36
TCATCAACAAGGCAAATATGTACCCCGGTTG	31

ACAAGAAATAGGAATCCCAATAGCAAGCAAATATAGCAGCATCCTGAA	48
AGGAGGTGGCGGATAAGTATTAAGAGGCTAAATCCTCTACAGGAG	45
TTCCGGAATCATAATTTTTT	20
TTTTGAATGCCAACGGCAGC	20
TCGAAGATGATGAAACTTTT	20
TGCCATTCAACAATAGAAAATTCATATGGT	30
TTTTACTGTAGCCTCAGAACCGCCATTTT	29
CTGCGCGGCTAACTCACAATTCCACACAACATACGAGTACCGGGGCTCTGTGGGTGTTCAG	61
AAGCGCATAAATGAAACAGATATAGAAGGCTTAGCAAGCCTTATTACG	48
CACTCATGAAACCACCTTAAATCAAGATTGAGCGTCTTTTTGTTT	45
TATTTTTGAGAGATCTGCCATATTTCCTCTACTCAATTGA	40
GTACTATGGTTGCTTTTTTAGACACGCAAATT	32
AATGCAATAGATTAAGGGCTTAGAGCTTATTTT	33
GTATAAGCAAATATTTTAGATAAGTAACAACG	32
AAGGGAACCGGATATTCACTCATCTTTGACCCGTAATGCCATCGGAAC	48
TGTAGCTCAACATTTACCCTCGAAAGAC	28
TTTTGTGTAGGTAAAGATTC	20
TTTTGCCTCAGAGCATAAAGAAAATTAAGCAATAAATTTT	40
CATAGGTCTGAGAGACAAATCGTCGAATTACC	32
AGCATGTACGAGAACAATCCGGTATTCTAAGAACGATTTTCCAGA	45
GAGAAACATTTAATTTTACAGGTAGAAAG	29
TTTTAGAGCGGGAGCTAGAT	20
GTAAGAATAGTTGAAACTTTCGCAAACACCGC	32
ACCTCGTCATAAACATTTTT	20
TTCGTAATCATGGTCATCCATCAGTTATAAGT	32
TTTTGTGTAAAGCCTGGCGG	20
CCTGCAGCCATAACGGGGTGTCCAGCATCAGC	32
TTTGCGTATTGGGCGCTTTT	20

TTTTCGGGCCGTTTTCACGG	20
GCCGGGCGCGGTTGCGCCGCTGACCCCTTGTG	32
TTATACTTAGCACTAAAAAGTTTGTGCCGCCA	32
GGCACCAAAACCAAAAGTAAGAGCAACACTATAGCAACGTAAATCGCC	48
CTAGCTGATAAATTAACAGTAGGG	24
ATACGCAAAGAAAATTATTCATTAAAGGTGAATTTT	36
AGAGCAAATCCTGTCCAGATACCGACAAAAGGTAATTTT	39
GCCAGTACGTTATAAGGCGTTAAATAAGAATAAACACAAAT	41
TTTTTAAACGATGCTGATGG	20
CCTCAGAGCACAAGAAGAAAAGTAAGCAG	29
ACAGTTGAGGATCCCCAGATAGAACTGAAAGC	32
ATAATCAGAAAAGCCCAACATCCACTGTAATA	32
AAATTATTTGGAAACAGCCATTCGAAAATCGC	32
ACATTCTGAAGAGTCTCCGCCAGCAGCTCGAA	32
TTTCATCGAATAATATCCAGCTACAATACTCCAGCAATTTCTTTACAG	48
TGAATTACCAGTGAATGGAATTACGAGGCATATAGCGAGAGAATCCCC	48
CGTGCCTGTTCTTCGCATCCAGCGCCGGGTTA	32
TTAGAGCTATCCTGAGGCTGGTTTCAGGGCGC	32
TAGTAATAACATCACTTTTT	20
TAATAAGAAGAGCCACCCTTATTAGCGTT	29
ATCCAGAACAATATTAGTCCATCAGGAACGGT	32
TTTTATCGCCATTAAAAATA	20
TTTTGATTAAGACGCTGAGA	20
GGAATTAGGTAAATTTTCGGTCATAGCCCCACCGGAACCACCACC	45
TTTTAGAACGCGAGAAAACTTT	22
GGGCCTCTTCGCTATTACGTTGTACCTCACCG	32
TTTTTGCCTGAGTAGAAGAA	20
GCCAGTGCGATTGACCCACCGCTTCTGGTGCC	32

TAAAGTTTAGAACCGCTAATTGTATCGCGGGGTTTAAGTTTGGCCTTG	48
TTTTATTAAGTTGGGTACGC	20
ATATATATAAAGCGACGACATCGGCTGTCTTTCCTTATCATTTTT	45
CAGATGAATATACAGTTTTT	20
GACCGTGTGATAAATACAAATTCT	24
CATAATAATTCGCGTCTTTT	20
ACAAATTATCATCATATTTT	20
TCACCGGAAGCATAAATTTT	20
ATCAAACTTAAATTTCTGGAAGGGCCATATCA	32
TTCATAGGGTTGAGTGTTTT	20
GCCCCCTGGTGTATCACCGTACTC	24
TTCTGAAACATGAAAGTGCCGGCCATTTG	29
TTTTGGAACCTAAGTCTCTGAATTTTTTTTTT	32
TTTTCTTTTTCACAACGGAGATTTGTTTT	29
GTTGTACCACCCTCATAAAGGCCGGAGACAG	31
CCGAGTAAGCCAACAGGGGTACCGCATTGCAA	32
AGTGTGCTGCAAGGCGTTTT	20
CCCTGAACAAATAAGAAACGCGAGGCGTT	29
CATTATACCAGTGATTTGGCATCAGGACGTTGTAACATAAACCAGACG	48
CAACTAATGCAGACAGAGGGGCAATACTG	29
CGTTGGTAGTCACGACGCCAGCTGGCGAAAGGGGGATATCGGCCTGCGCATCGGCCAGCTT	61
AAACGGCGCAAGCTTTGAAGGGCGATCGGTGC	32
TTTTGTTTCGTCACCAGTACTGTACCGTAAT	31
CAGTATGTTTATTTTGCGAAGCCCTTTTTAATTGAGTTCTGAACA	45
TCAAATCACCATCAATACGCAAGG	24
CGCTGGCACCACGGGAGACGCAGAAACAGCGG	32
GAAACAACGCGGTCGCCGCACAGGCGGCCTTTAGTGACTTTCTCCACGTACAGACGCCAGG	61
TGCTTTCGAGGTGAATCTCCAAAA	24

TAGTTGCCAGTTGCGGGAGGTTTTGAAGATCAATAA	36
AATTACATAGATTTTCAATAACGGATTCGCC	31
TTTTACCGTTCCAGTAAGCGTCATACATGGCTTCAGTTAAT	41
TTTTAACAGTACCTTTTACA	20
CTTTTGCGTTATTTCAATGATATTCAACCGTT	32
TTTTCATCGGCATATTGACGGCACCACGG	29
CTCTCACGGAAAAAGAACGGATAAAAACGACG	32
CGGAATCTCAGGTCTGTTTTAAATATGCATGCGAACGAATCATTG	45
TGCGGGATAGCAGCGACGAGGCGCAGAGAAACGGCCGCGGTAACGATC	48
ATTGCGTTTAACAACATTTCAATTACCTGAGCAAAAGGGAGAAACAGGTTTAAGATGATGG	61
TTCACCAGGTAGCAATGGCCTTGCTGGTAAT	31
GCCTGTTTGCTTCTGTTACCTTTTAACGTTAA	32
CCATTACCAAGGGCGACATCTTTTCATAGGCAGAAAGAATAGGTTGAG	48
TCAGCAGCAACCGCAATTTT	20
CAAATCGTCAGCGTGGTGCCATCCCACGCAA	31
TTGAGTAAGCCACCCTCAGAACCG	24
GGAGGGAAGAGCCAGCAATCAGTAGCGACAGACCAGAACCGCCTC	45
ATAAACAATCCCTTAGTGAATTTATCAAAAT	31
CACATCCTCAGCGGTGGTATGAGCCGGGTCAC	32
GCTGCGCAACTGTTGGCAGACCTATTAGAAGG	32
AAATCAGCTCATTTTTGTGAGCGAATAGGTCA	32
TTTTAGTAATTCAATCGCAAGACAATTTT	29
GGAAACCAGGCAAAGCGTACATAAGTGAGTGA	32
CAAACCCTTTAGTCTTACCAGCAGAAGATAA	31
CAGTACCATTAGTACCCAGTGCCCGTATAAATTGATGAATTAAAG	45
AACAGAGGTGAGGCGGCAGACAATTAAAAGGG	32
TTTTAAGTTACCAGGGTAATTGAGCTTTT	29
ATTTAGAAGTATTAGATTTT	20

CTGATAGCCCTAAAACTTTT	20
CCGGCAAATCGGCGAAGTGGTGAAGGGATAG	31
TTTTACCTTGCTGAACCAGG	20
GGGGTCATTGCAGGCGGGAATTGACTAAAATA	32
CGCTCACTATCAGACGGTCCGTGAGCCTCCTC	32
GCAGCAAGCGGTCCACAAGTGTTTTGAGGCCA	32
CCACCCTCTGTTAGGAAGGATCGTCTTTCCAGCAGACGATTATCAGCT	48
CTCAAATGTTCAGAAATGGAAGTTTCACGCGCATTACTTCAACTGGCT	48
ATAACCTTATCAACAAAAATTGTATAACCTCC	32
ATCGGCCTTAAAGAATAAATCAAAAGAATAGCCCGAGACCAGTGAGGGAGAGGGGTGCCTA	61
CCAGCTTACGGCTGGAAACGTGCCCGTCTCGT	32
CTGAGGCCAACGGCTACAGAGGTTTCCATT	30
AAAACGGTAATCGTTTTTTT	20
TGGAGCCGGCCTCCGGGTACATCGACATAAAA	32
ACGCCAGATGACGGGGCGCCGCTAGCCCCAGC	32
TTTTACGCATAATGAGAATAGAAAGTTTT	29
CATGTTTACCAGTCCCTTTT	20
TTAATTTCATGTTCTATAACTATATGTAAATGCTGATGTCAATAGAATCCTTGACAAAATT	61
TTTTACTAGAAAAAGCCTGTT	21
TTAGTTTGCCTGTTTAGGTCATTTTTGCGGATAGGAAGCCGACTATTA	48
AATAAGTTAGCAAAAACGCAATAATAACGAGAATTAAAAGCCCAA	45
TTTTTGGCCTTCCTGTATAA	20
CAGGAAAAACGCTCATACCAGTAAATTTTTGA	32
ATATTCACCGCCAGCATTGACAGGCAAAATCA	32
AACCGTTTCACACGGGAAATACCTACATTTTGACGCTAAACTATCACTTCTTTAACAGGAG	61
TTTTGCGCTGGCAAGTGTAG	20
TTTTGGAATTTGTGAGAGAT	20

Supplementary Table S4. Modified and extended staples from the 5' to the 3' end for the DNA-origami structure used for the tracking experiments (Figure 4).

Sequence (5' to 3')	**Length [nt]**	**Function**
Biotin-AGAGCCGCAAACAAATGAGACTCCTCAAGA GATTAGCGGGCAGTAGCA	48	Biotin for immobilization
Biotin-GAGGGTAGTTGCAGGGTGCTAAACAACTTTCA CGCCTGGAAAGAG	45	Biotin for immobilization
Biotin-TACCAGTAACGCTAACAGTTGCTATTTTGCAC CCCATCCT	40	Biotin for immobilization
Biotin-ATAAAAATATCGCGTTCTCCTTTTGATAAGAG CTATAT	38	Biotin for immobilization
AGAAACAGCTTTAGAAGGAAGAAAAATCTACGATTTT AAGCATATAACTTTTAAATGC	58	Catching site 1 for Cy3B Pointer
GCACCCTCCGTCAGGTACGTTAGTAAATGAATAGTTA GCGTCAATCATTTTTAAATGC	58	Catching site 2 for Cy3B Pointer
ACGATAAACCTAAAACAAAGAATACACTAAAACATTA CCCAACAAAGCTTTTTTTTTCGGGCATTTA-**CY3B**	67	Pointer – Cy3B
AGAAACAGCTTTAGAAGGAAGAAAAATCTACGATTTT AAGCATATAACTTTTAAATGCC	58	Catching site 1 for Atto542 Pointer
GCACCCTCCGTCAGGTACGTTAGTAAATGAATAGTTA GCGTCAATCATTTTTAAATGCC	58	Catching site 2 for Atto 542 Pointer
ACGATAAACCTAAAACAAAGAATACACTAAAACATTA CCCAACAAAGCTTTTTTTTTCGGGCATTTA-**ATTO542**	67	Pointer – Atto542

References

(1) Nickels, P. C.; Wünsch, B.; Holzmeister, P.; Bae, W.; Kneer, L. M.; Grohmann, D.; Tinnefeld, P.; Liedl, T. Molecular Force Spectroscopy with a DNA Origami – Based Nanoscopic Force Clamp. *Science* **2016**, *354* (6310), 305–307.

(2) Vogelsang, J.; Kasper, R.; Steinhauer, C.; Person, B.; Heilemann, M.; Sauer, M.; Tinnefeld, P. A Reducing and Oxidizing System Minimizes Photobleaching and Blinking of Fluorescent Dyes. *Angew. Chemie* **2008**, *47* (29), 5465–5469. https://doi.org/10.1002/anie.200801518.

(3) Balzarotti, F.; Eilers, Y.; Gwosch, K. C.; Gynnå, A. H.; Westphal, V.; Stefani, F. D.; Elf, J.; Hell, S. W. Nanometer Resolution Imaging and Tracking With Minimal Photon Fluxes. *Science* **2017**, *355* (December), 606–612.

7.4 Publication IV: Combining pMINFLUX, Graphene Energy Transfer and DNA-PAINT for Nanometer Precise 3D Super-Resolution Microscopy

by

Jonas Zähringer, Fiona Cole, Johann Bohlen, Florian Steiner, Izabela Kamińska, and Philip Tinnefeld

published in

Light: Science and Applications, 70 (2023) DOI: 10.1038/s41377-023-01111-8

Author contributions:

I adjusted the pMINFLUX setup with Fiona Cole for dual-color measurements in green and red. The samples were designed with help of Johann Bohlen. Together with Johann Bohlen I prepared the sample of the L-PAINT measurements. I performed and analysed all experiments and wrote parts of the manuscript.

Official journal of the CIOMP 2047-7538
www.nature.com/lsa

ARTICLE Open Access

Combining pMINFLUX, graphene energy transfer and DNA-PAINT for nanometer precise 3D super-resolution microscopy

Jonas Zähringer[1], Fiona Cole[1], Johann Bohlen[1], Florian Steiner[1,3], Izabela Kamińska[1,2] and Philip Tinnefeld[1]✉

Abstract

3D super-resolution microscopy with nanometric resolution is a key to fully complement ultrastructural techniques with fluorescence imaging. Here, we achieve 3D super-resolution by combining the 2D localization of pMINFLUX with the axial information of graphene energy transfer (GET) and the single-molecule switching by DNA-PAINT. We demonstrate <2 nm localization precision in all 3 dimension with axial precision reaching below 0.3 nm. In 3D DNA-PAINT measurements, structural features, i.e., individual docking strands at distances of 3 nm, are directly resolved on DNA origami structures. pMINFLUX and GET represent a particular synergetic combination for super-resolution imaging near the surface such as for cell adhesion and membrane complexes as the information of each photon is used for both 2D and axial localization information. Furthermore, we introduce local PAINT (L-PAINT), in which DNA-PAINT imager strands are equipped with an additional binding sequence for local upconcentration improving signal-to-background ratio and imaging speed of local clusters. L-PAINT is demonstrated by imaging a triangular structure with 6 nm side lengths within seconds.

Introduction

3D super-resolution with nanometer precision opens exciting new insights in nanostructures and biological systems by achieving molecular or even submolecular resolution. There is a multitude of techniques extending single-molecule localization microscopy (SMLM) to the third dimension, including PSF manipulation[1,2], 4-Pi microscopy[3], total internal reflection fluorescence (TIRF) microscopy[4], repetitive optical selective exposure (ROSE-Z)[5] or Supercritical Angle Localization Microscopy (SALM)[6] and many more. However, in these techniques, the precision is mostly limited to the emission information, and hence the camera localization does not reach precisions of about the size of a fluorophore of 1–2 nm of all three dimensions. The coordinate-targeted approach of 3D stimulated emission depletion microscopy (STED)[7] has similar limitations in precision. To this end MINFLUX nanoscopy[8] and later MINSTED nanoscopy[9] were introduced. By interrogating the emitter location with a series of targeted illuminations, localization precisions of <2 nm are reached with moderate photon budgets. It later was extended to 3D by superimposing vortex beams to generate a tophat[10]. However, the instrumental and engineering requirements increase with dimensionality and the photon budget is divided between the axial and lateral dimensions. Each photon only contributes to either the lateral or the axial localization depending on the kind of vortex mask of the respective illumination event.

Alternative to optical approaches, the axial position of a fluorescent dye can be determined from near-field interactions with a modified coverslip. To this end, energy transfer between a dye and a metal- or graphene-layer is read out from fluorescence intensity or fluorescence lifetime and is converted to an axial information

Correspondence: Philip Tinnefeld (philip.tinnefeld@cup.uni-muenchen.de)
[1]Department of Chemistry and Center for NanoScience, Ludwig-Maximilians-Universität München, Butenandtstr. 5-13 Haus E, 81377 München, Germany
[2]Institute of Physical Chemistry Polish Academy of Sciences, Kasprzaka 44/52, 01-224, Warsaw, Poland
Full list of author information is available at the end of the article

in approaches termed metal-induced energy transfer (MIET)[11–13] or graphene energy transfer (GET)[14–16]. GET with graphene-on-glass coverslips has the advantage of high optical substrate transparency (>97%)[17], lack of autofluorescence and steep d^{-4} distance dependence yielding the highest localization precision within its dynamic range[14,18].

In this work, we combine GET and pulsed-interleaved MINFLUX nanoscopy (pMINFLUX) with DNA-PAINT to enable nanometer precise 3D super-resolution imaging. pMINFLUX was introduced as simpler MINFLUX realization that additionally provides the fluorescence lifetime[19]. In combination with GET, axial position determination from the intensive property fluorescence lifetime is advantageous as it is intensity independent and does not require internal referencing. In the GET-pMINFLUX combination, each photon is synergetically used for both, xy- as well as z-localization optimally exploiting the available information[20]. Using DNA origami nanopositioners, fluorescent molecules and DNA point accumulation for imaging in nanoscale topography (DNA-PAINT), binding sites are placed precisely in 3D[21]. These nanopositioners are then used to evaluate the GET-pMINFLUX DNA-PAINT combination for 3D localization and 3D super-resolution imaging at different distances to graphene[14]. To overcome the comparatively small field of view of pMINFLUX and the limited binding kinetics of DNA-PAINT, we also introduce local PAINT (L-PAINT) in which a DNA imager strand binds for longer times locally and quickly probes ("PAINT") neighboring binding sites.

Results

In GET-pMINFLUX nanoscopy, the xy position of a single fluorescent molecule placed on a graphene-on-glass coverslip using a DNA origami nanopositioner (Fig. 1a, top) is localized using pMINFLUX nanoscopy, while the axial position is determined by GET. To determine the 2D position of the dye it is excited by four spatially displaced and pulsed interleaved vortex beams[19]. By binning the fluorescent intensity trace (Fig. 1a, bottom), the number of photons corresponding to each of the four pulsed vortex beams is extracted via time-correlated single-photon-counting (TCSPC) (Fig. 1b). The position of the fluorophore is determined by a maximum likelihood estimator as described in earlier works[8,19] for the fluorescence intensities and the known excitation profile and positions of all beams. By dividing the fluorescence intensity trace into time or photon bins, the same molecule is localized many times yielding 2D histograms of localizations (Fig. 1c).

For the axial dimension, the pulsed interleaved approach entails the fluorescence lifetime of the molecule, which is extracted for each localization from the TCSPC histogram (Fig. 1d and Supplementary Information 2.1). In the case of a designed 16 nm distance to graphene, the resulting fluorescence lifetime is 1.3 ns. With an unquenched fluorescence lifetime of ATTO647N of

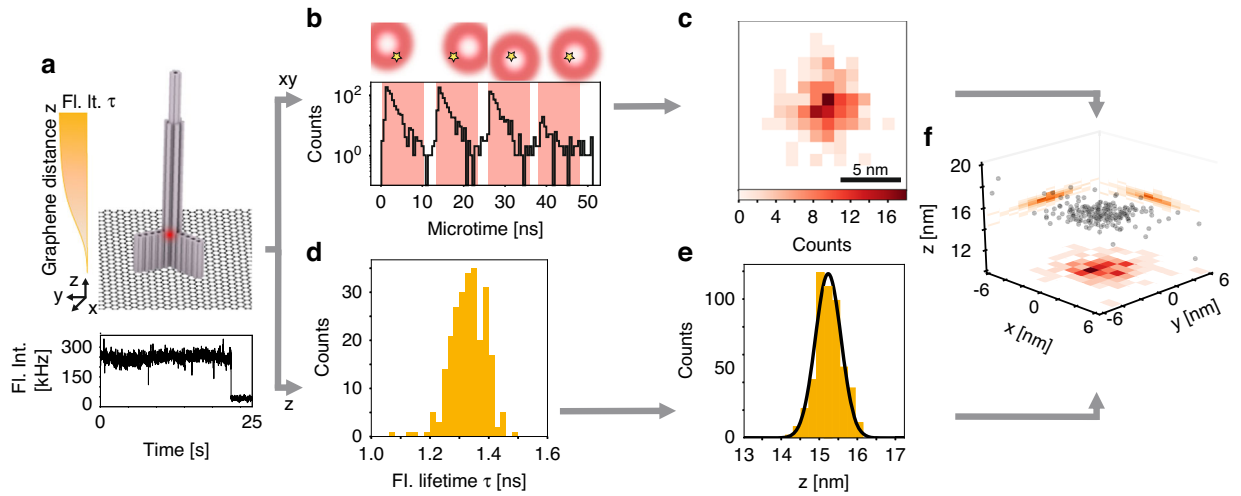

Fig. 1 Combining pMINFLUX with graphene energy transfer for precise 3D localizations. a Top: Schematic of a DNA origami structure with a single dye positioned at a height of 16 nm above a graphene-on-glass coverslip. Bottom: Fluorescence intensity trace of the total fluorescence intensity of a single dye molecule in a single DNA origami structure. **b** Fluorescence decays for each of the four pulsed interleaved vortex-shaped beams which are focused on the sample arranged in a triangular pattern with the fourth beam placed at the center of the triangular structure. The star indicates the xy position of the dye molecule. **c** xy localization histogram of time bins. **d** Distribution of fluorescence lifetimes obtained from the time bins. **e** Distribution of the distances to graphene z calculated from the fluorescence lifetimes of d). **f** 3D localizations of the full fluorescence intensity trace using the 2D information of pMINFLUX and the z distances from the fluorescence lifetimes. The individual localizations are shown in black and on the sides the corresponding projections with a binning of 1 nm for xy and 0.2 nm for z

4.2 ns, a GET efficiency of 69% is measured. With the known d^{-4} fluorescence lifetime – distance to graphene relation[14,18], the distance to graphene z is calculated for each localization (Fig. 1e). The resulting distance to graphene z of 15.3 nm is obtained using the 50% energy transfer distance d_0 of 18.5 nm for ATTO647N[14]. By combining both, the 2D position and the distance to graphene z, a single fluorophore is localized in 3D with a precision of 1.9 nm in lateral and 0.3 nm in axial dimensions with moderate photon count rates of 1000 photons (Fig. 1f). Notably in contrast to the xy localization, where a nanometer precise drift correction is needed, the z localization is not impeded by drift, as the distance to graphene is measured. This is another reason for the remarkable precision in z-direction.

The precision in z is, on the one hand, determined by the precision of the fluorescence lifetime estimation, on the other hand, dependent on the slope of the graphene energy transfer relation hence on the absolute distance to graphene z (Supplementary Information 2.3).

To evaluate the dependency of the absolute distance to graphene z on the precision, fluorophores were placed at different heights using DNA origami nanopositioners (Fig. 2a). Close to the 50% quenching distance d_0, GET reaches axial precisions of <0.3 nm at moderate photon number of 2000 photons per localization outperforming the xy precision of pMINFLUX nanoscopy which is at 1–2 nm. At higher distances to graphene of around 30 nm, the axial GET precision matches the lateral precision of pMINFLUX.

As also the axial precision is a function of the number of detected photons (N), the fluorescence intensity trace of a fixed ATTO 647 N fluorophore is binned using different bin widths, hence different photon numbers N ranging from 100 to 2000 photons (Fig. 2b). For a 16 nm distance to graphene and N ranging from 100 to 1000, the resulting axial precision is estimated between 1 and 0.3 nm, respectively. The comparison of the axial precision for different heights in dependence of the photon number is depicted in Fig. 2c and compared to the photon number dependent precision of the xy determination by MINFLUX. Both the axial as well as the lateral precision show the expected dependence. The theory of the axial precision agrees well within the error of the experimental data (Supplementary Information 2.3). A suitable range for precisions of GET and pMINFLUX is between 8 and 35 nm (Supplementary Information Fig. S4). At higher distances to graphene, the slope of the energy transfer relation decreases and the axial precision drops. Due to the excitation with vortex shaped laser beams, a challenge of MINFLUX is the Signal to Background Ratio (SBR)[10]. Hence below ~8 nm distance to graphene, the signal is so strongly quenched that the SBR drops and MINFLUX localizations are less precise.

For MINFLUX nanoscopy, redox blinking or thiol induced switching was used to enable successive localization of single molecules as a background signal from diffusing molecules required in PAINT approaches is avoided[8,10]. This, however, limits the choice of dyes, the

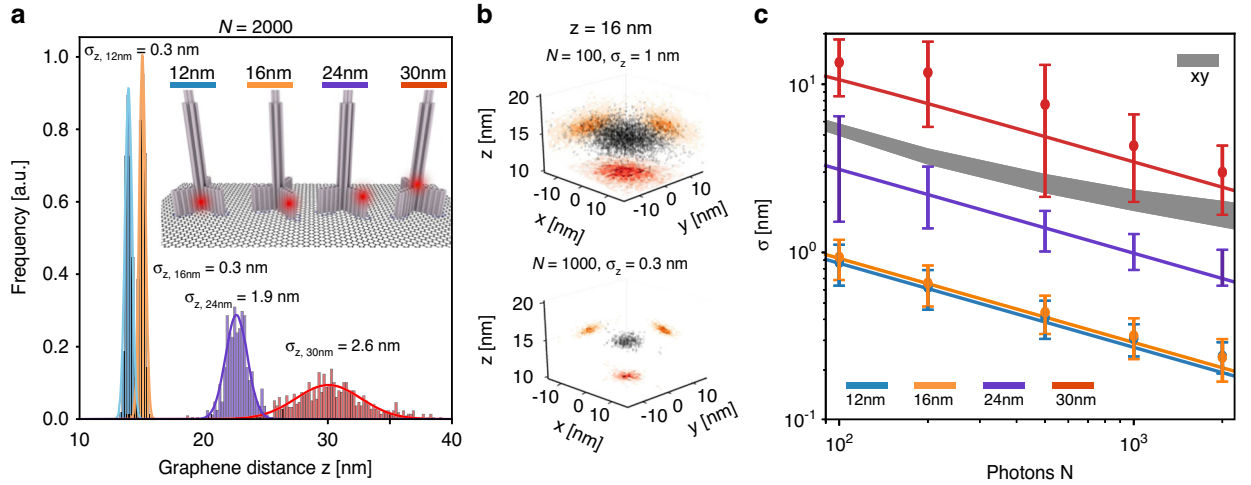

Fig. 2 Localization performance of the GET p-MINFLUX combination. a Distributions of the distance z from graphene for exemplary molecules with a different dye position ranging from 12 to 30 nm analyzed with a fixed number of photons of $N = 2000$. **b** Exemplary 3D localization plots of a single fixed dye at a distance to graphene z of 16 nm with different number of photons, N, used to evaluate the precision. In this measurement, the SBR was 7. The individual localizations are shown in black and on the sides the corresponding projections. The red histogram is projection to xy. The orange histograms are the projection to xz and yz. The individual localizations are shown in black and on the sides the corresponding projections have a binning of 1 nm for xy and 0.2 nm for z. **c** Localization precision in xy and z as a function of the number of photons N for fixed dye molecules placed at different height. The gray stripe indicates the xy precision of MINFLUX in the corresponding experiments, the lines indicate the theoretical lower limit of precision

duty cycle and the available photon budget. To apply GET-pMINFLUX in combination with photon optimized DNA-PAINT[22], we increase the binding kinetics by a concatenated and periodic DNA motif[23] such that a DNA-PAINT imager has multiple binding options.

Using a 7-nucleotides long ATTO542 labeled DNA-PAINT imager strand, a 3D docking site pattern on a DNA origami nanopillar was imaged, of which the central motif is depicted in Fig. 3a and the full structure is shown in Fig. S5. Out of the 300 s of the GET-pMINFLUX measurement, a 3D localization map was generated (Fig. 3b). To evaluate the performance of GET-pMINFLUX with DNA-PAINT, a projection of the localizations representing the four docking sites in the center of the structure (as depicted in Fig. 3a) on the z-axis is shown in Fig. 3c. A multi-Gaussian fit reveals the well-resolved 3 nm distances between the docking sites with axial precisions between 0.4 and 1.3 nm. With xy precisions of the individual docking sites between 1.6 and 2.3 nm, we show nanometer precise 3D super-resolution resolving a 3D structure with 3-nm features. Beside enabling 3D super-resolution, the efficient energy transfer to graphene eliminates background localization events as unspecific bound imagers are fully quenched close to graphene. This is especially important for MINFLUX nanoscopy, which is prone to background influences from unspecific binding events in the vicinity of the vortex beams.

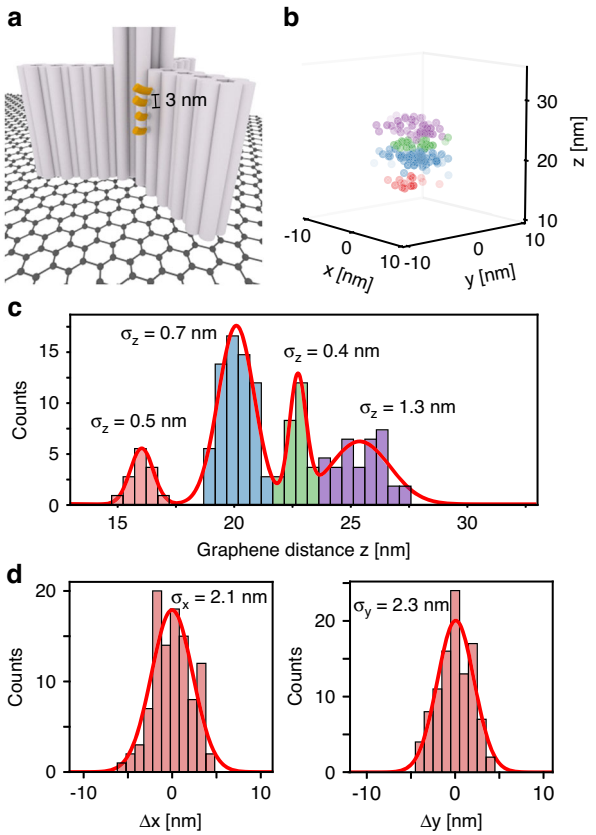

Fig. 3 Super-resolution DNA-PAINT imaging with pMINFLUX and GET. a Schematic illustration of the imaged structure with protruding docking sites. **b** 3D localizations of the DNA-PAINT trace with corresponding projections on the side. Binning along the *x* and *y* axis is 1.5 nm and along the *z* axis 0.5 nm. **c** Histogram of the distance to graphene z of the selected xy localizations. **d** Histograms of xy localizations relative to the mean molecule position

In DNA-PAINT, imaging speed requires higher imager concentration[23–25]. However, a higher imager concentration reduces the SBR as diffusing molecules are excited by the comparable large excitation volumes of MINFLUX. The situation is aggravated by the serial nature of MINFLUX, which calls for fast binding kinetics to speed up imaging and to reduce the requirements for drift corrections.

We address this challenge by local PAINT (L-PAINT), in which a locally high imager concentration is achieved by a hierarchy of binding interactions without creating higher background. In L-PAINT, the imager strand has two binding sequences (Fig. 4a). One binding site is comparatively strong (in the extreme, it can be thermally stable) and keeps the imager strand bound to the structure of interest creating a locally high concentration (therefore referred to as concentrator sequence). The labeled imager sequence on the other end of the L-PAINT imager creates the short binding events with docking strands typical for DNA-PAINT. The size of the docking site cluster that can be sampled with one imager strand binding event depends on the length of the linker between concentrator sequence and imager sequence.

For L-PAINT demonstration, we design a L-PAINT imager whose concentrator sequence binds stably to a DNA origami structure from which the imager sequence protrudes. In this limiting case of thermally stable binding of the imager strand over the time scale of the experiment, the local concentration of the imager strand is always high and no imager strand is required in the imaging buffer. The resulting imager concentration in solution thus corresponds to 0 nM. After a linker of 12 nucleotides, a Cy3B dye is attached at the end of the 7 nucleotides imager sequence (Fig. 4b). With GET-pMINFLUX, we visualize the imager sequence transiently binding to a triangular structure of docking strands protruding from the DNA origami structure displayed in Fig. 4c. Within only 2 s of the trace (Fig. 4d) and an integration time of 50 ms per localization, the triangular structure with 6 nm side length is resolved (Fig. 4e). After 30 sec, a highly sampled 3D localization map is obtained (Fig. 4f and extended data movie). Smaller integration times per localization show that the 6 nm jumps between

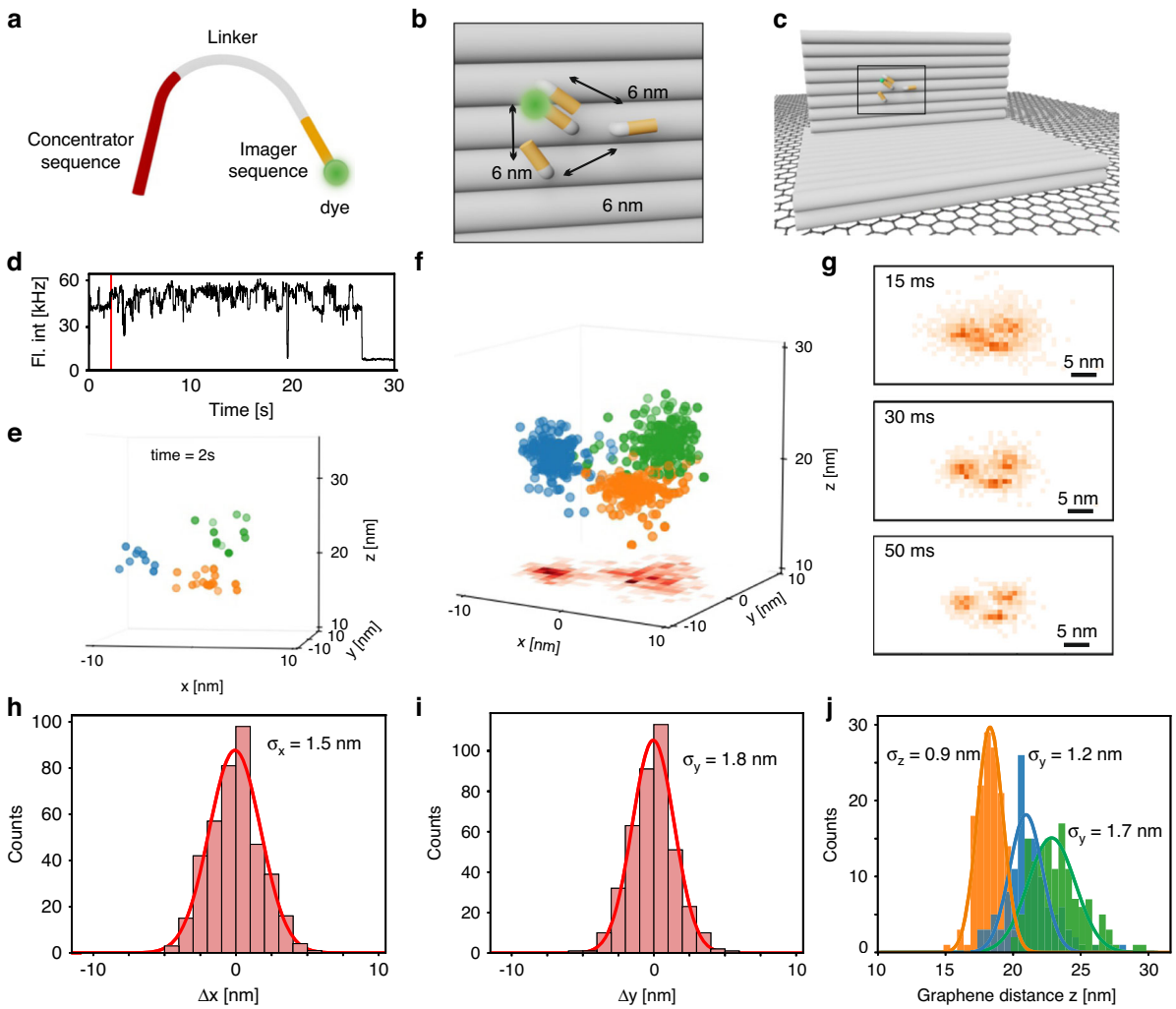

Fig. 4 L-PAINT imaging with pMINFLUX and GET. a Schematic of a L-PAINT imager strand. **b** A DNA origami structure with 3 protruding strands to which a Cy3b dye-labeled imager sequence can transiently bind. The L-PAINT imager is bound to the DNA origami structure by the concentrator sequence. **c** Zoom out of the DNA origami structure on graphene. **d** Fluorescence intensity trace with a red line at 2 s. **e** 3D localizations of the L-PAINT trace after 2 s. **f** 3D localizations of the 30 s L-PAINT trace with the xy projection on the bottom with a binning of 1 nm. **g** 2D histogram of the xz projection with a binning of 1 nm with time bins for localization varying from 15 to 50 ms. **h** Histogram of distances to each mean binding position in x. **i** Histogram of distances to each mean binding position in y. **j** Histogram of the distances to graphene z

the binding sites are already resolved at 15 ms integration time (Fig. 4g). Higher integration times show the trade-off between time resolution and localization precision (Fig. 4g).

To evaluate the performance, the localizations of the 30 s trace with 50 ms integration time were assigned to binding site clusters (Fig. 4f) in the xz projection, showing xy precisions of 1.5 and 1.8 nm (Fig. 4h, i) and axial precisions between 0.9 nm and 1.7 nm (Fig. 4j), respectively. In contrast to other super-resolution techniques, the dye is tracked at different binding sites; hence the trace is continuous resulting in a high number of localizations per unit time while avoiding high imager concentrations and double-binding events.

Discussion

We present the combination of graphene energy transfer, pMINFLUX and DNA-PAINT. MINFLUX yields ultra-high localization precision in xy, in synergy GET provides outstanding z-localization close to the coverslip surface (8–35 nm) enabled by the fluorescence lifetime information of pulsed-interleaved MINFLUX, and DNA-PAINT provides the switching mechanism to proceed from super-localization to super-resolution. These three complementary and orthogonal components for super-resolution fully utilize the information of each detected photon and each component is realized fairly easily especially in light of recent progress[26,27]. Precisions better than 2 nm are shown in different

experiments in all dimensions and structural details of 3 nm are resolved.

In order to increase binding kinetics and to reduce the background, we introduce L-PAINT with GET-pMINFLUX. The longer concentrator sequence keeps the imager strand connected to the region of interest while the scanning of the imager sequence quickly creates localizations in the proximity. With L-PAINT the imaging of docking sites with distances of 6 nm in 3D within less than 2 s and additionally, the tracking of the binding trajectory with 15 ms time resolution was demonstrated.

L-PAINT is not limited to DNA nanostructures and could also be applied to cell imaging with identical docking sites that are differently occupied by the concentrator and imager sequences. As fast imaging of the local environment circumvents drift problems L-PAINT is especially advantageous for dense molecular clusters. The limitation that the photon budget of the dye is distributed over different binding sites, which is less of a problem for MINFLUX than for less photon efficient camera based localization schemes could be compensated by slowly exchanging the imager strands with weakened concentrator sequences or by adding an additional binding hierarchy with a slowly exchanging dye labeled sequence for self-regenerating L-PAINT[28,29].

In itself, GET-pMINFLUX is an extremely precise tool within a range of 8 to 35 nm above the coverslip. Here, the axial information is achieved by only adding a graphene layer on top of a coverslip. Furthermore, GET-pMINFLUX can be easily extended using spectral multiplexing[30]. In the future, GET-pMINFLUX nanoscopy will be used to investigate artificial bilayers[31], cellular membranes and adhesion complexes as well as macromolecular complexes with nanometer 3D precision.

Materials and methods

Buffer

To stabilize all dyes, a combination of ROXS and oxygen scavenging system is used. Details of the buffers can be found in Table 1. For ATTO647N and Cy3B for the data in Figs. 1, 2, and 4, the buffer contains aqueous solution of aged Trolox[32] with PCA (PCA/Trolox) and the second a 50× PCD (for measurements both buffers were mixed in a 1:50 ratio (50× PCD: Trolox/PCA).

For DNA-PAINT experiments, the imaging buffer consists of an aqueous solution of aged Trolox with PCA (PAINT PCA/Trolox) and one of PCD. Both buffers were mixed in a 1(PCD):50(Trolox/PCA) ratio.

All chemicals were purchased from Sigma Aldrich.

Table 1 List of buffers with recipes

Buffer name	Recipe
PCA/Trolox	2 mM Trolox (6-hydroxy-2,5,7,8-tetramethylchroman-2-carboxylic acid) 12 mM PCA (protocatechuic acid) 12.5 mM $MgCl_2 \cdot 6H_2O$ 40 mM Tris base 20 mM acetic acid 1 mM EDTA-$Na_2 \cdot 2H_2O$
PAINT PCA/Trolox	2 mM Trolox (6-hydroxy-2,5,7,8-tetramethylchroman-2-carboxylic acid) 2.4 mM PCA (protocatechuic acid) 6 mM $MgCl_2 \cdot 6H_2O$ 40 mM Tris base 20 mM acetic acid 1 mM EDTA-$Na_2 \cdot 2H_2O$
50 × PCD	2.8 mM PCD (protocatechuate 3,4-dioxygenase from pseudomonas sp.) 50% glycerol 50 mM KCl 100 mM Tris HCl 1 mM EDTA-Na2·$2H_2O$
FOB	12.5 mM $MgCl_2 \cdot 6H_2O$ 20 mM Tris base 20 mM acetic acid 1 mM EDTA-$Na_2 \cdot 2$ H_2O

Preparation of DNA origami structures

The DNA origami structures were folded with 10-fold excess of oligonucleotide strands and a 100-fold excess of pyrene-modified oligonucleotides in comparison to the scaffold in 1× FOB buffer. Details of the folding program are found in ref. [33] After folding, 1× Blue Juice gel loading buffer was added to the folded DNA origami which was then purified via agarose-gel electrophoresis with 1.5% agarose gel in 50 mL of FOB buffer at 80 V for 1.5 h with 2 µL peqGREEN (ordered from VWR) per 100 µL buffer. The specific band for the nanostructure was extracted from the gel. Before putting the purified DNA origami solution onto graphene, the concentration was adjusted with FOB buffer to 75 pM.

Graphene coverslips

In order to prepare graphene coverslips, a wet-transfer approach was used to transfer the CVD-grown graphene onto glass coverslips[14,16,27]. First, glass coverslips were cleaned with 1% Hellmanex and then subsequently washed twice in milliQ water, each step for 15 min in ultrasonication bath. Pieces of roughly 0.25 cm^2 were cut from PMMA/graphene/copper foil and let to float on 0.2 M ammonium persulfate for copper etching. After ~3–4 h (when the copper foil was fully etched), PMMA/graphene was scooped gently with a clean coverslip and transferred to milliQ water to wash out the

residues of ammonium persulfate. The washing step with the fresh milliQ water was repeated twice. Next, PMMA/graphene was scooped with a glass coverslip and carefully dried with a nitrogen stream. Samples were left for drying overnight. Next, ~10 µl of PMMA ($M_w = 15{,}000$ g/mol) in chlorobenzene (50 mg/mL) was drop-casted to cure the protection layer of PMMA on graphene. After ~30 min, when the solvent evaporated, the graphene-on-glass coverslip was placed in acetone for 7 min (×2) and in toluene for 7 min. After each step, the sample was dried with a nitrogen stream, and at last placed on active coal, heated on the heating plate to 230 C, for 30 min. Finally, the graphene-on-glass coverslip was removed from the active coal, and the incubation chamber (Grace Bio-Labs®) was placed on a glass coverslip so that the graphene piece was in the middle of the chamber.

Sample preparation

The DNA origami solution was immobilized on graphene-on-glass coverslips for 2 min and then the sample was washed 3x using FOB. Next, gold nanorods for drift correction were immobilized on the surface via electrostatic interaction by incubating the gold nanorods for 2 min in FOB and afterward the sample was washed 3x with FOB. For DNA-PAINT measurements, surface passivation with ssDNA staples strands with 1 µM concentration in FOB was performed. The staples were incubated for 10 min and the sample was washed with FOB. Last, the buffer was exchanged for the experiment specific imaging buffer. The chamber was then sealed.

pMINFLUX setup

The pMINFLUX setup is described in the original pMINFLUX publication[19]. For detailed information see the supporting information.

Acknowledgements

P.T. is grateful for support by the Deutsche Forschungsgemeinschaft (DFG, German Research Foundation) under Germany's Excellence Strategy – EXC 089/1 – 390776260, and 201269156-SFB1032. Funded by the Federal Ministry of Education and Research (BMBF) and the Free State of Bavaria under the Excellence Strategy of the Federal Government and the Länder through the ONE MUNICH Project Munich Multiscale Biofabrication. IK acknowledges support by DFG (KA 5449/2-1) and National Science Center (Sonata 2019/35/D/ST5/00958).

Author details

[1]Department of Chemistry and Center for NanoScience, Ludwig-Maximilians-Universität München, Butenandtstr. 5-13 Haus E, 81377 München, Germany. [2]Institute of Physical Chemistry Polish Academy of Sciences, Kasprzaka 44/52, 01-224, Warsaw, Poland. [3]Present address: Department of Physics, Ludwig-Maximilians-Universität München, Schellingstraße 4, 80799 München, Germany

Author contributions

The manuscript was written through contributions of all authors. All authors have given approval to the final version of the manuscript. J.Z., J.B., F.S., and P.T. conceived the experiment. J.Z. performed the experiment with help from F.C., J.B., and I.K. who helped with the sample preparation. J.Z. and F.C. are responsible for the pMINFLUX and analyzed the data.

Funding

Open Access funding enabled and organized by Projekt DEAL.

Conflict of interest

Parts of this manuscript are subject of a patent application.

Supplementary information The online version contains supplementary material available at https://doi.org/10.1038/s41377-023-01111-8.

Received: 10 October 2022 Revised: 7 February 2023 Accepted: 16 February 2023
Published online: 10 March 2023

References

1. Huang, B. et al. Three-dimensional super-resolution imaging by stochastic optical reconstruction microscopy. *Science* **319**, 810–813 (2008).
2. Pavani, S. R. et al. Three-dimensional, single-molecule fluorescence imaging beyond the diffraction limit by using a double-helix point spread function. *Proc. Natl Acad. Sci. USA* **106**, 2995–2999 (2009).
3. Huang, F. et al. Ultra-high resolution 3D imaging of whole cells. *Cell* **166**, 1028–1040 (2016).
4. Szalai, A. M. et al. Three-dimensional total-internal reflection fluorescence nanoscopy with nanometric axial resolution by photometric localization of single molecules. *Nat. Commun.* **12**, 517 (2021).
5. Gu, L. S. et al. Molecular-scale axial localization by repetitive optical selective exposure. *Nat. Methods* **18**, 369–373 (2021).
6. Dasgupta, A. et al. Direct supercritical angle localization microscopy for nanometer 3D superresolution. *Nat. Commun.* **12**, 1180 (2021).
7. Klar, T. A. et al. Fluorescence microscopy with diffraction resolution barrier broken by stimulated emission. *Proc. Natl Acad. Sci. USA* **97**, 8206–8210 (2000).
8. Balzarotti, F. et al. Nanometer resolution imaging and tracking of fluorescent molecules with minimal photon fluxes. *Science* **355**, 606–612 (2017).
9. Weber, M. et al. MINSTED fluorescence localization and nanoscopy. *Nat. Photonics* **15**, 361–366 (2021).
10. Gwosch, K. C. et al. MINFLUX nanoscopy delivers 3D multicolor nanometer resolution in cells. *Nat. Methods* **17**, 217–224 (2020).
11. Berndt, M. et al. Axial nanometer distances measured by fluorescence lifetime imaging microscopy. *Nano Lett.* **10**, 1497–1500 (2010).
12. Thiele, J. C. et al. Isotropic three-dimensional dual-color super-resolution microscopy with metal-induced energy transfer. *Sci. Adv.* **8**, eabo2506 (2022).
13. Isbaner, S. et al. Axial colocalization of single molecules with nanometer accuracy using metal-induced energy transfer. *Nano Lett.* **18**, 2616–2622 (2018).
14. Kaminska, I. et al. Distance dependence of single-molecule energy transfer to graphene measured with DNA origami nanopositioners. *Nano Lett.* **19**, 4257–4262 (2019).
15. Ghosh, A. et al. Graphene-based metal-induced energy transfer for sub-nanometre optical localization. *Nat. Photonics* **13**, 860–865 (2019).
16. Kamińska, I. et al. Graphene energy transfer for single-molecule biophysics, biosensing, and super-resolution microscopy. *Adv. Mater.* **33**, 2101099 (2021).
17. Nair, R. R. et al. Fine structure constant defines visual transparency of graphene. *Science* **320**, 1308 (2008).
18. Swathi, R. S. & Sebastian, K. L. Resonance energy transfer from a dye molecule to graphene. *J. Chem. Phys.* **129**, 054703 (2008).
19. Masullo, L. A. et al. Pulsed interleaved MINFLUX. *Nano Lett.* **21**, 840–846 (2021).
20. Barroso, M. M. Graphene boost. *Nat. Photonics* **13**, 825–826 (2019).
21. Rothemund, P. W. K. Folding DNA to create nanoscale shapes and patterns. *Nature* **440**, 297–302 (2006).
22. Jungmann, R. et al. Single-molecule kinetics and super-resolution microscopy by fluorescence imaging of transient binding on DNA origami. *Nano Lett.* **10**, 4756–4761 (2010).
23. Strauss, S. & Jungmann, R. Up to 100-fold speed-up and multiplexing in optimized DNA-PAINT. *Nat. Methods* **17**, 789–791 (2020).

24. Chung, K. K. H. et al. Fluorogenic DNA-PAINT for faster, low-background super-resolution imaging. *Nat. Methods* **19**, 554–559 (2022).
25. Schueder, F. et al. An order of magnitude faster DNA-PAINT imaging by optimized sequence design and buffer conditions. *Nat. Methods* **16**, 1101–1104 (2019).
26. Masullo, L. A. et al. An alternative to MINFLUX that enables nanometer resolution in a confocal microscope. *Light Sci. Appl.* **11**, 199 (2022).
27. Krause, S. et al. Graphene-on-glass preparation and cleaning methods characterized by single-molecule DNA origami fluorescent probes and raman spectroscopy. *ACS Nano* **15**, 6430–6438 (2021).
28. Scheckenbach, M. et al. Self-regeneration and self-healing in DNA origami nanostructures. *Angew. Chem. Int. Ed.* **60**, 4931–4938 (2021).
29. Stehr, F. et al. Tracking single particles for hours via continuous DNA-mediated fluorophore exchange. *Nat. Commun.* **12**, 4432 (2021).
30. Zhang, Z. Y. et al. Ultrahigh-throughput single-molecule spectroscopy and spectrally resolved super-resolution microscopy. *Nat. Methods* **12**, 935–938 (2015).
31. Fullbrunn, N. et al. Nanoscopic anatomy of dynamic multi-protein complexes at membranes resolved by graphene-induced energy transfer. *eLife* **10**, e62501 (2021).
32. Cordes, T., Vogelsang, J. & Tinnefeld, P. On the mechanism of Trolox as antiblinking and antibleaching reagent. *J. Am. Chem. Soc.* **131**, 5018–5019 (2009).
33. Nickels, P. C. et al. Molecular force spectroscopy with a DNA origami-based nanoscopic force clamp. *Science* **354**, 305–307 (2016).

Supporting information

Combining pMINFLUX, Graphene Energy Transfer and DNA-PAINT for Nanometer Precise 3D Super-Resolution Microscopy

Jonas Zähringer[1], Fiona Cole[1], Johann Bohlen[1], Florian Steiner[1,3], Izabela Kamińska[1,2], Philip Tinnefeld[1]

[1] Department of Chemistry and Center for NanoScience, Ludwig-Maximilians-Universität München, Butenandtstr. 5-13 Haus E, 81377 München, Germany

[2] Institute of Physical Chemistry Polish Academy of Sciences, Kasprzaka 44/52, 01-224 Warsaw, Poland

[3] current address: Department of Physics, Ludwig-Maximilians-Universität München, Schellingstraße 4, 80799 München, Germany

Corresponding Author: philip.tinnefeld@cup.uni-muenchen.de

Supplementary Section 1: Materials

1.1 Gold Nanorods

Gold nanorods were used as fiducial markers for drift correction. The 900 nm long gold nanorods were fabricated following the protocol for long GNRs.[1] After purification, transmission electron microscopy images were taken for characterization (Figure S1).

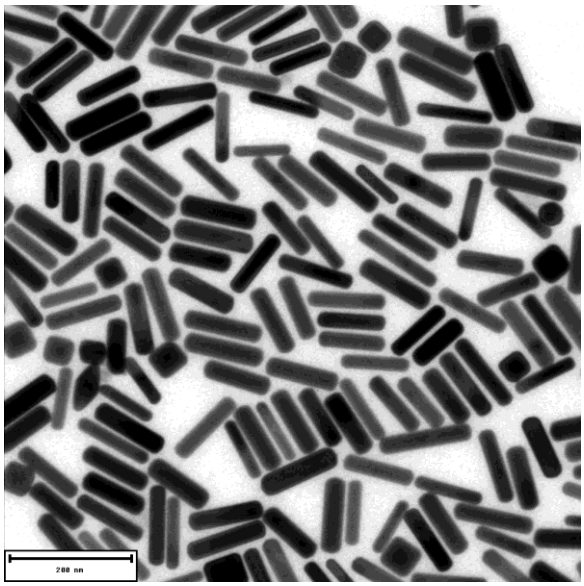

Figure S1. TEM image of 900 nm long gold nanorods

1.2 pMINFLUX Setup

The pMINFLUX setup is described in the original pMINFLUX publication.[2] Depending on the excitation color, different optical elements such as filters, the vortex phase plate or polarization optics are used, however the beam path remains unchanged (Figure S2).

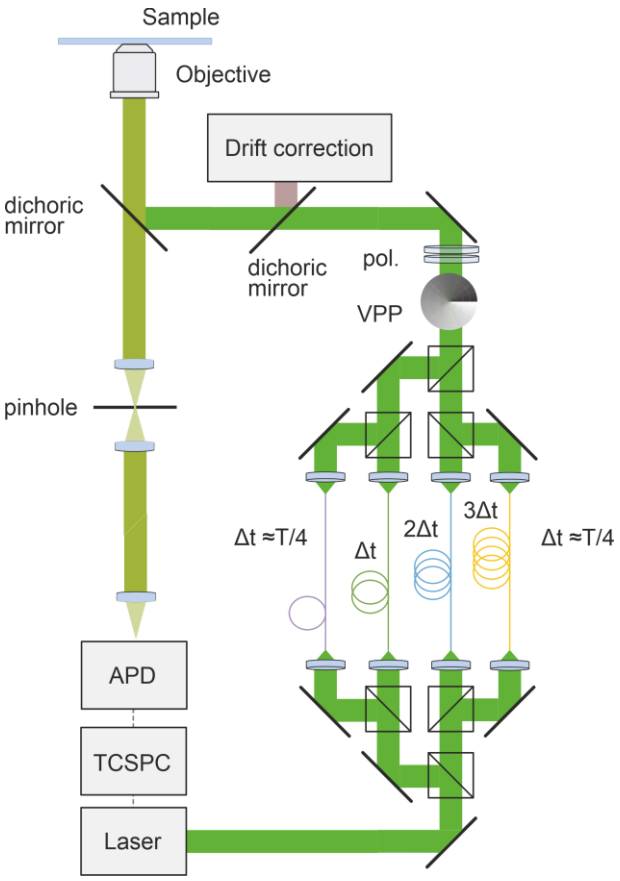

Figure S2. pMINFLUX setup. The pulsed laser is split into four beams and coupled to optical fibers, delaying the laserpulses as a function of the length of the fiber. The beams are recombined and doughnut shaped beams are created with a vortex phase plate and polarization optics. The beams are focused on the sample arranged in a triangular pattern with the fourth beam placed at the center of the triangle. For detection an APD is used together with a TCSPC unit.

Excitation. A supercontinuum laser (SuperK Fianium FIU-15, NKT Photonics GmbH, Germany) is used at 19.5 MHz repetition rate (*T*) as light source in combination with a tunable bandpass filter (SuperK VARIA, NKT Photonics GmbH, Germany) to select the desired wavelength range in the visible light spectrum. An additional clean-up filter (green: FLH532-10, Thorlabs GmbH, Germany, red: ZET 635/10, Chroma, USA) is used to further spectrally clean the excitation beam. Using a polarizing beam splitter cube (PBS251, Thorlabs GmbH, Germany) the light is split into two beams of orthogonal polarizations.

Each of the beams is further split by a non-polarizing 50:50 beam splitter cube (BS013, Thorlabs GmbH, Germany). This beam splitting system generates two pairs of beams with each pair sharing the orthogonal linear polarization. The resulting four laser beams are coupled into

polarization maintaining single-mode fibers (PM-S405-XP, Thorlabs GmbH, Germany) of lengths 2.0 m, 4.6 m, 7.1 m and 9.7 m such that the time delay between the beams after the fiber is ~12.5 ns (= *T*/4). The four beams are collimated after the fibers with an achromatic lens (AC254-035-A, Thorlabs GmbH, Germany) and recombined by using three 50:50 beam splitter cubes (BS013, Thorlabs GmbH, Germany). The overlay of the beams can be adjusted to obtain the required arrangement of laser foci in the object plane. The axes of linear polarization are matched by turning the fiber out-couplers (Thorlabs GmbH, Germany). Subsequently, the linearly polarized laser beams pass a combination of a quarter- and a half-wave plate (WPQ05M-532 and WPH532M532, Thorlabs GmbH, Germany; for red: additional linear polarisator: LPVISC100-MP2, Thorlabs GmbH, Germany, RAC 5.2.10, B. Halle, Germany, WPQ05M-633, Thorlabs GmbH, Germany) to make them circularly polarized. A vortex phase plate (green: VPP, V-532-20-1, Vortex Photonics, Germany; red: VPP, V-633-20-1, Vortex Photonics, Germany) is then used to introduce the phase modulation necessary to generate the donut-shaped foci. The beams are guided into the back entrance of the microscope body (IX83, Olympus Deutschland GmbH, Germany), reflected on a dichroic mirror (ZT532/640rpc flat–STED, Chroma Technology Corp., USA) and focused with an objective (UPLSAPO100XO/1.4, Olympus Deutschland GmbH, Germany) onto the sample plane.

Detection. The fluorescence light is collected with the same objective and transmitted through the dichroic mirror, focused via an Olympus tube lens onto a pinhole (120 µm, Owis, Germany), collimated with an achromatic lens (AC254-150-A, Thorlabs GmbH, Germany). The beam is focused with a second achromatic lens (AC127-025-A, Thorlabs GmbH, Germany) to the chip of an avalanche photodiode (SPCM-AQRH-16-TR, Excelitas Technologies GmbH & Co. KG, Germany) after filtering the remaining scattered light from the laser with suitable interference optical filters (785 SP EdgeBasic, Semrock Inc., USA, green: 582/75 Brightline HC, Semrock Inc. USA, red: 700/75 ET Bandpass, Chroma, USA). The digital signal from the APD is sent to a TCSPC unit (HydraHarp 400, PicoQuant GmbH, Germany).

Drift correction. To measure and correct for sample drift during the measurement, the IR output of the variable bandpass filter is used. A beam of wavelength between 850 and 900 nm is selected with optical filters (875/50 bandpass, Edmund Optics GmbH), coupled into a single-mode fiber (780HP, Thorlabs GmbH, Germany), outcoupled and collimated. This beam is then split with a 50:50 beam splitter cube (BS014, Thorlabs GmbH, Germany) and combined again

after inserting a lens system (ACN254-040-B, AC254-150-B, Thorlabs GmbH, Germany) into one of the two paths that focuses the beam to the back focal plane of the objective (dotted line) to create a widefield illumination at the sample plane. This beam is used for xy drift correction where the position of fiducial markers is localized during the measurement. The collimated IR beam is focused onto the sample plane at an oblique angle to achieve a z position-dependent spot at the detector and use this for z drift correction. Both IR beams are coupled to the main beam path via a dichroic mirror (ZT 785 SPXXR, Chroma Technology Corp., USA) and fed into the microscope to illuminate a region close, but not overlapping with the field of view used for MINFLUX. The reflected and backscattered light is split with an additional 50:50 beam splitter cube (BS014, Thorlabs GmbH, Germany) from the excitation IR beam and detected on a single CMOS camera (Zelux, Thorlabs GmbH, Germany) at different positions of the chip.

Setup control. The piezo stage (P733.3CD, Physik Instrumente (PI) GmbH &Co. KG, Germany) translates the sample in all three dimensions with a resolution of 0.3 nm when running in closed loop mode. All components of the setup including the piezo stage are controlled digitally and integrated via a custom version of the PyFLUX project. Further details and source-code of this control software version are available at https://github.com/zaehringer-Jonas/pyflux

Alignment. For MINFLUX measurements, the 4 vortex beams were aligned in a fixed triangular excitation beam pattern (EBP), with a $L \approx 100$ nm.

Supplementary Section 2: Experiments

2.1 Reconvoluted Fluorescence Lifetime Fit

For the fluorescence lifetime fit, the microtime histogram (also known as TCSPC histogram) was extracted for each localization so each time bin of the fluorescence trace (Figure S3 a). The microtime histogram was then rebinned such that the four decays overlay (Figure S3 b and c). The resulting single decay was then fitted with an IRF reconvoluted exponential fit using a least square minimization. To include background contributions, the fit has an additional background component. The background was determined after bleaching (Figure 1, 2 and 4) or for DNA-PAINT as no binding event was detected.

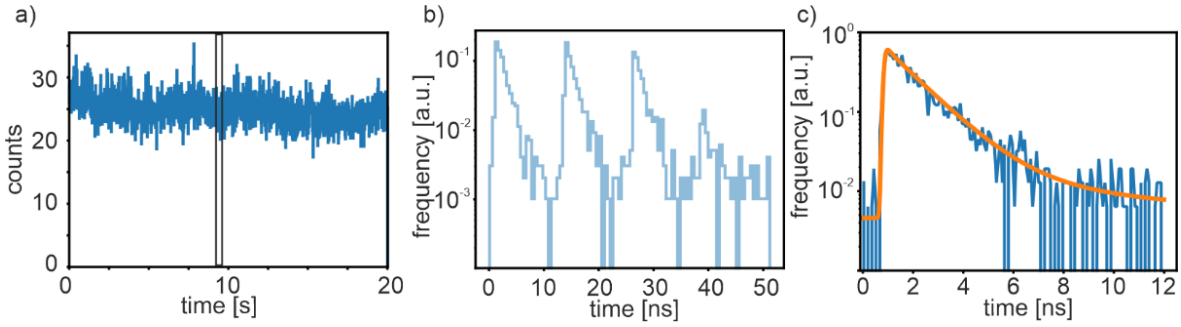

Figure S3. Fitting of the fluorescence lifetime. a) In the fluorescence intensity trace a time bin is selected. b) The microtime histogram of this time bin shows four peaks, corresponding to the four vortex beam excitations. c) The microtime histogram is rebinned such that it results in single decay. This is fitted using a IRF reconvoluted exponential fit (yellow line).

2.2 Graphene MINFLUX Theory:

The energy transfer efficiency from a dye molecule to graphene can be calculated from the equation:

$$\eta = 1 - \frac{\tau}{\tau_0}$$

where τ and τ_0 stand for the fluorescence lifetime of a dye molecule immobilized on graphene or glass, respectively. At the same time, the energy transfer efficiency from an emitter to graphene scales with d^{-4}, where d is the distance between the dye and graphene, and d_0 is the distance of 50% energy transfer efficiency to graphene:

$$\eta = \frac{1}{1 + \left(\frac{d}{d_0}\right)^4}$$

Based on both equations for the energy transfer efficiency, the distance *d* between the dye molecule and graphene is calculated: [3]

$$d = \ d_0 * \sqrt[4]{\frac{1}{\frac{\tau_0}{\tau} - 1}}$$

with parameters for ATTO 647N: unquenched lifetime $\tau_0 = 4.2\,ns$, and the 50% quenching height $d_0 = 18.5\,nm$ and for ATTO 542 $\tau_0 = 3.4\,ns$, and the 50% quenching height $d_0 = 17.7\,nm$ and for Cy3b $\tau_0 = 2.6\,ns$, and the 50% quenching height $d_0 = 17.7\,nm$.[3]

In this article, instead of using *d* for the calculated distance values, we define the distance as *z*, to stay consistent with the three-axis *x, y, z* in a Cartesian coordinate system.

2.3 Axial Precision

For the theoretical errors of the *z* precision, first the error of fluorescence lifetime at a certain number of photons was calculated for a mono-exponential decay with constant background.[4] Here, parameters were estimated according to the experiments with *N* ranging from 100 to 2000 photons, reconvoluted lifetimes τ from 1.0 to 3.8 ns, time window from 5 to 12 ns, 100 bins and SBRs from 2 – 16. The resulting variance of the fluorescence lifetime was then used to estimate the variance according to Gaussian error propagation:

$$\sigma_z^2 = \frac{1}{4}\, d_0\, \left(\frac{\tau}{\tau_0 - \tau}\right)^{-\frac{3}{4}}\, \left(\frac{\tau_0}{\tau_0 - \tau}\right)^2 * \sigma_\tau^2$$

The precision of *z* in dependence of the absolute value of *z* using quenched lifetimes and quenched SBR is plotted in Figure S4 with a fixed number of 1000 photons.

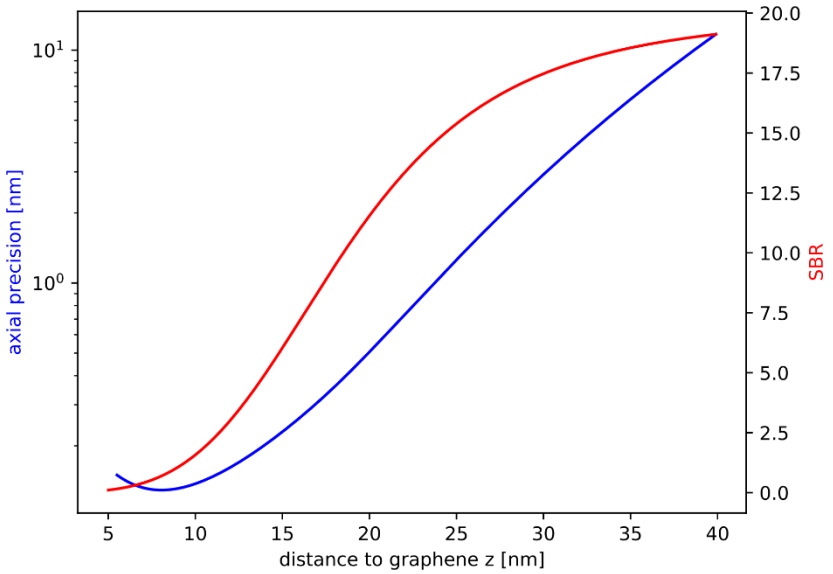

Figure S4. Dynamic range of GET-pMINFLUX. The theoretical value of SBR in red and the theoretical axial precision blue is plotted against the graphene distance.

On the one hand, with the condition of a SBR > 1, the lower end of GET-pMINFLUX will be limited to $z > 8$ nm. On the other hand, for isotropic precision, the axial precision should be similar to that of pMINFLUX. With 1000 photons this is reached at around 30-35 nm graphene distances. Hence for isotropic nanometer precise precision of GET-pMINFLUX, the graphene distance range is between 8 – 35 nm.

2.4 DNA-PAINT measurement

For DNA-PAINT measurements, a DNA origami structure (Figure S5 a) with in total 8 binding sites on its three faces were incorporated. The faces are labeled in Figure S4 b and their respective heights can be found in Table S2. On face A, 2 binding sites are spaced roughly 3 nm horizontally, on another face 2 binding sites are spaced 6 nm horizontally and on the third face there are 4 binding sites with 3 nm distance (Figure S5 b). Additionally, an internal dye (ATTO542) was incorporated to check correct orientation on graphene and graphene quality as well as to facilitate correct centering in the excitation beam pattern. For the DNA-PAINT measurements the sequence of $T(TCC)_9T$ was used as docking site sequence to increase the binding kinetics.[5] The DNA-PAINT imager strand has the following sequence: AGGAGGA-ATTO542.

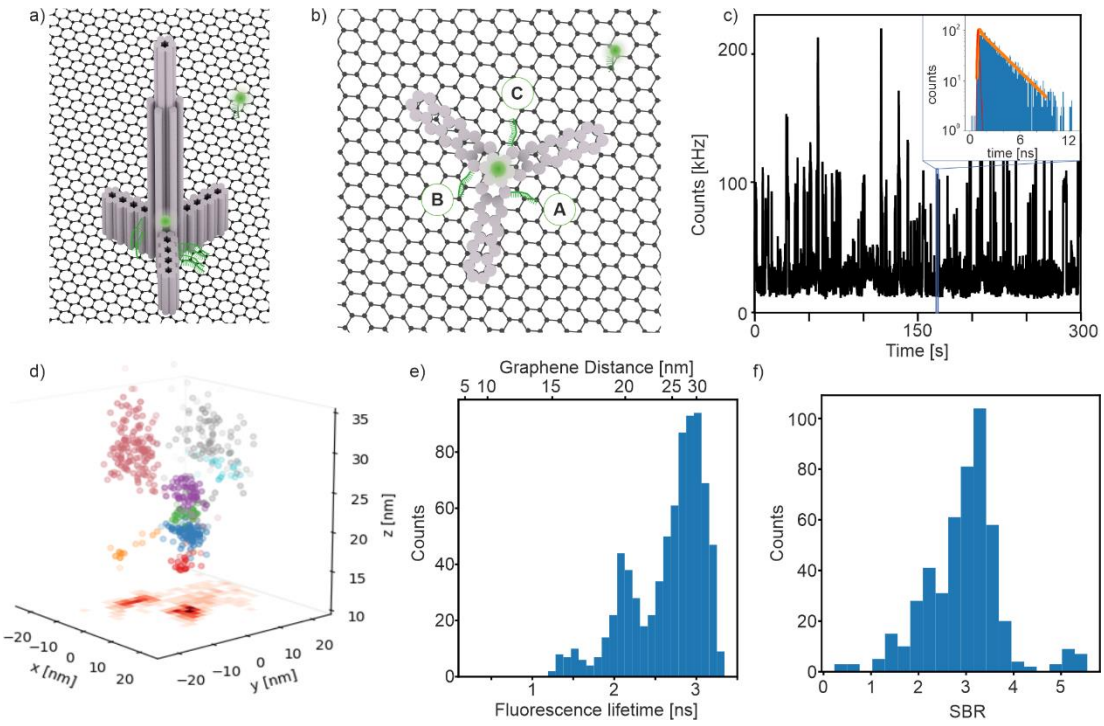

Figure S5. GET pMINFLUX with DNA-PAINT. a) Sketch of the DNA origami structure with indicated positions of permanent dye and docking strands. b) Top view with label for each face. Face A has 4 binding sites, face B and C have 2 binding sites each. The heights are indicated in Table S2. c) Trace of the fluorescence intensity showing binding events of the DNA-PAINT measurement. The inset shows the fitted fluorescence decay of such a segment together with the IRF. d) 3D localization plot of the trace. e) Histogram of the fluorescence lifetimes and the corresponding graphene distances. f) Histogram of the SBRs.

In the 300 s measurements (see intensity trace in Figure S5c), events were found using a fluorescence intensity threshold of 230 photons per 10 ms and a minimal event duration of 30 ms. To exclude double binding events, a maximum threshold of 1500 photons/10 ms was set. The extracted events were then binned into segments of 3500 photons. On the one hand, the segments were analyzed using a maximum likelihood estimator for xy localization. On the other hand, the fluorescence lifetime was extracted using a reconvoluted fit. The histogram of the fluorescence lifetimes is shown in Figure S5e, displaying several distinct peaks.

All events in the EBP are shown in figure S5d. Here, the two faces in front can be easily identified as face A and B and have xy distance of around 11 nm. Face A with its four docking sites is highlighted in Figure 3c by extracting all data points at the four binding sites in a diameter of 11 nm (radius = 5.5 nm). As the binding sites are different in their graphene

distance also the quenching and the SBR is different. The histogram of the SBR (Figure S5f) shows distinct peaks in analogy to the histogram of fluorescence lifetimes.

Table S2. Designed Distances oft the DNA-PAINT docking sites to Graphene

Face	Designed graphene distance of the docking site [nm]
A	16.7 20 23 27.7
B	17.7 24.7
C	19 22.3

2.5 Experimental DNA-PAINT precision

As the DNA-PAINT binding sites are repetitive, rather long and furthermore are pointing parallel to the graphene surface. Assuming rapid molecular dynamics of the docking and imager strand within the integration time for one localization, the movement of the long binding sites average out for the axial orientation, but it has a potentially decreasing effect on the precision for xy localizations. Especially, as the docking strand has several binding positions, the localizations might be slightly broadened.

To estimate the effect of the length of the sequence the freely jointed chain model was used. The most extreme case of imager attaching at the different ends of the docking strand corresponds to a length of 21 nt ssDNA. With a Kuhn length of a chain segment of 1.5 nm for ssDNA[6] results in an average end to end distance of the binding sites furthest apart of

$$\sqrt{\langle R^2 \rangle} = \sqrt{\frac{21}{2}} * 1.5\ nm = 4.9\ nm$$

With the expectation of equal accessibility of all 8 binding sites, the resulting standard deviation is $\sigma_x = 1.7\ nm$.

In a DNA-PAINT experiment, the binding strands are protruding from the origami on the side. Due to steric hindrance of the tripod base of the DNA-origami the DNA-PAINT strand can only access about 120°. This is modeled with a simplified density function on 120° of a circle: $f(\alpha) = \frac{\cos(\alpha)}{\sqrt{3}}$ for $\alpha \in [-\frac{\pi}{3}, \frac{\pi}{3}]$ and $x = \sigma_x \cos(\alpha)$ we get:

$$< \sigma_x > = \int_{-\frac{\pi}{3}}^{\frac{\pi}{3}} x\, f(\alpha) d\alpha = \int_{-\frac{\pi}{3}}^{\frac{\pi}{3}} \frac{\sigma_x * \cos(\alpha)^2}{\sqrt{3}} d\alpha = \sigma_x \left(\frac{1}{4} + \frac{\pi}{3 * \sqrt{3}}\right) = 1.4\, nm$$

The experimental precision is a convolution of the distribution of the spot and the MINFLUX precision. In the case of a MINFLUX precision of 1.5 nm an experimental precision of 2.1 nm would follow. This rough estimation agrees with the experimental DNA-PAINT MINFLUX data and indicates that the xy-precision of the pMINFLUX method itself is rather slightly better than the reported values.

3. DNA origami sequences

Table S3. Core staples from the 5’ to the 3’ end for the pillar-shaped DNA origami structure.

Staple ID	Sequence (5’ to 3’)
P1	GAGAAGGCATCTGCAATGGGATAGGTCAAAAC
P2	AACCGTGTCATTGCAACGGTAATATATTTTAAATGAAAGGGT
P3	ATCGGTCAGATGATATTCACAAACCAAAAGA
P4	GCTGGCATAGCCACATTATTC
P5	CTGTATGGGATTACCGTTAGTATCA
P6	CCATAATGCCAGGCTATCAAGGCCGGAGACATCTA
P7	CTCATCGGGATTGAGTGAGCGAGTAACAACCCGTC
P8	TAGCCAGCTTTCATCCAAAAATAAACGT
P9	TAGCCTCAGAGCATACCCTGT
P10	AATACCCCAACATTCATCAAAAATAATTCGCGTCT
P11	GGCTAAAACTTCAGAAAAGTTTTGCGGGAGATAGAACC
P12	CCCGGTTGATAAAGCATGTCAATC
P13	ATCGATGCTGAGAGTCTACAAGGAGAGGGAACGCCAAAAGGA
P14	GACAATTACGCAGAGGCATTTTCGAG
P15	TAAGTTGGCATGATTAAAGAA
P16	CCAATGTTTAAGTACGGTGTCCAAC
P17	CGGAATAGAAAGGAATGCCTTGCTAAACAACTTTCAAC
P18	GAGTTAAAAGGGTAATTGAGCGCTAATATCAGAGGAACTGAACACC
P19	TTTAGCGATACCAACGCGTTA
P20	TTTTTGCGGATGCTCCTAAAATGTTTAGATGAATTTTGCAAAAGAAGTT
P21	AATAAAACGAACTATGACCCCACCAAGC
P22	AATATCGTTAAGAGAGCAAAGCGGATTGTGAAAAATCAGGTCTTT
P23	ATTACGAGATAAATGCCAGCTTTGAGGGGACGACGACAG
P24	ACAACGCCTGTAGCATTTACCGTATAGGAAG
P25	TTACCATTAGCAAGGCCTTGAATTAGAGCCAGCCCGACTTGAGC
P26	CAGCAGCGCCGCTTGTTTATCAGCTTCACGAAAAA
P27	CTTACGGAACAGTCAGGACGTTGGGAAGAAA
P28	AGCTCTTACCGAAGCCCAATA
P29	TATTACGAATAATAAACAAATCAGATATGCGT
P30	CACGGCAACAATCCTGATATACTT
P31	CATCGAGATAACGTCAAACATAAAAGAGCAAAAGAATT
P32	CAAGCCCAATAGGAACCACCCTCACCCGGAA
P33	CATTTCGCAAATGTCATCTGCGAACGAGAGATTCACAATGCC
P34	GGCGCAGACGGTCAATCATCGAGACCTGCTCCATGTGGT
P35	CAAACGGAATAGGAAACCGAGGAATAAGAAATTACAAG
P36	ACCAACAAACCAAAATTAACAATTTCATTTGAATTACCGAGG
P37	CATTTGAGATAACCCACGAAACAATG
P38	AGGACAGATGAACGGTGTAACATAAGGGAACCGAAGAAT
P39	TGGCTTTTTACCGTAGAATGGAAAGCG
P40	GTTAAAGGAAAGACAGCATCTGCCTATTTAAGAGGCAGGAGGTTTA
P41	AGTAGGTATATGCGTTATACA
P42	CGAACACCAAATAAAATAGCAGCCAAGTTTGCCTTTAGCGTCAGA
P43	GCGAAACAAAGTGTAAAACACATGGCCTCGATTGAACCA
P44	AAGAAAGCTTGATACCGCCACGCATACAGACCAGGCGCTGAC
P45	CTGAATATAGAACCAAATTATTTGCACGTAAAACAACGT
P46	AGACAGCAGAAACGAAAGAGGAAATAAATCGAGGTGACAGTTAAAT
P47	CGAGGGTACTTTTTCATGAACGGGGTCATAATGCCGAGCCACCACC
P48	TAAAGCCTCCAGTACCTCATAGTTAGCG
P49	AATATGCAACTACCATCATAGACCGGAACCGC
P50	AGAAATCGTTAGACTACCTTTTTAAGGCGTTCTGACCTTTTTGCA
P51	CTAAATCGGTCAGAATTAGCAAAATTAAGCAATAAAATAATA
P52	AAATCAGCTCATTTTTTAACCATTTTGTTAAAATTCGCATTA
P53	ATAGCGAGAGGCTATCATAACCAAATCCCAAAGAAAATTTCATCCTCAT

P54	GAACTGGCTCATTACAACTTTAATCATTCTTGAGATTACTTA
P55	ACGCGAGAGAAGGCCATGTAATTTAGGCCAGGCTTAATTGAGAATCGC
P56	TAATATCAAAGGCACCGCTTCTGGCACT
P57	TTTCCATGGCACCAACCTACGTCATACA
P58	AAGACAAATCAGCTGCTCATTCAGTCTGACCA
P59	CCGTAATCAGTAGCGACAGAATCTAATTATTCATTAAAAAGG
P60	CTGGCATTAGGAGAATAAAATGAAGAAACGATTTTTTGAGTA
P61	CGCGCCGCCACCAGAACAGAGCCATAAAGGTGGAA
P62	TAGCCCGGAATAGGTGTAAGGATAAGTGCCGTCGA
P63	AAGGCTCCAAAAGGAGCCTTTATATTTTTTCACGTGCTACAGTCACCCT
P64	CAAAATCACCGGAACCAGAGCCAGATTTTGTCACAATCACAC
P65	AATTGTGTCGAAATCCGCGGCACACAACGGAGATTTGTATCA
P66	CCTCGTCTTTCCACCACCGGAACCGCCTCCCTCA
P67	CCGTGTGATAAATAACCTCCGGCTGATG
P68	CCCAGCTACAATGACAGCATTTGAGGCAAGTTGAGAAATGAA
P69	TATTTAAATTGCAGGAAGATTG
P70	AAGGGATATTCATTACCGTAATCTATAGGCT
P71	ACCAGACCGGATTAATTCGAGC
P72	AAGGCCTGTTTAGTATCATGTTAGCTACCTC
P73	AGCAACAAAGTCAGAAATAATATCCAATAATCGGCTCAGGGA
P74	TGAGTAAAGGATAAGTTTAGCTATATCATAGACCATTAGATA
P75	GAGTCTGGATTTGTTATAATTACTACATACACCAC
P76	TTCGGTCCCATCGCATAGTTGCGCCGACATGCTTTCGAGGTG
P77	CGTGTCAAATCACCATCTAGGTAATAGATTT
P78	GGAACCATACAGGCAAGGCAAATCAAAAAGACGTAGTAGCAT
P79	ATTTGGAAGTTTCATGCCTCAACATGTTTTA
P80	AATTTCTTAAACCCGCTTAATTGTATCGTTGCGGGCGATATA
P81	GAGCATTTATCCTGAATCAAACGTGACTCCT
P82	TTATAAGGGTATGGAATAATTCATCAATATA
P83	TAACGACATTTTTACCAGCGCCAAAGAAAGTTACCAGAACCCAAA
P84	AAAGATTACAGAACGGGAGAAGGAAACGTCACCAATGAAACCA
P85	GCTGTAGTTAGAGCTTAATTG
P86	AGTTTCCAACATTATTACATTATAC
P87	GGGATATTGACGTAGCAATAGCTAAGATAGC
P88	AACAAGAGCCTAATGCAGAACGCGC
P89	AGTTTATTGTCCATATAACAGTTGATTC
P90	TATTGAAAGGAATTGAGGTAG
P91	AATAGAAAAAAATAAACGTCTGAGAGGAATATAAGAGCAACACTATGAT
P92	TCGTGCCGGAGTCAATAGTGAATTTGCAGAT
P93	TTAGTTTGAGTGCCCGAGAAATAAAGAAATTGCGTAGAGATA
P94	TTGGTAGAACATTTAATTAAGCAAC
P95	TAACATCCAATAAATGCAAAGGTGGCATCAACATTATGAAAG
P96	TAAGTTTACACTGAGTTTCGT
P97	AGAACTTAGCCTAATTATCCCAAGCCCCCTTATTAGCGTTTGCCA
P98	ACCGCCACCCTCAGAACCCGTACTCTAGGGA
P99	TTAGCCCTGACGAGAAACACCAGAAATTGGGGTGAATTATTTTAA
P100	ATAAAGTCTTTCCTTATCACT
P101	ATTTCCTGATTATCAGATGATGGCTTTAAAAAGACGCTAAAA
P102	ACATAAGTAGAAAAATCAAGAAGCAAAAGAAGATGTCAT
P103	TTCATCGGCATTTTCGGTCATATCAAAA
P104	GAACCGCCACCCTCCATATCATACC
P105	ACTAATGCCACTACGAATAAA
P106	CAAGCCGCCCAATAGCAAGTAAACAGCCATATTATTTTGCCATAAC
P107	TGAAAATCCGGTCAATAACCTAAATTTTAGCCTTT
P108	CCTCGTTTACCAGAAACCAAA
P109	CAAATTATTCATTTCAATTACCTGAGTA
P110	ATTTCAACCAAAAATTCTACTAATAGTTAGTTTCATTTGGGGCGCGAGC
P111	AGGCTTGCGAGACTCCTCAAGAGAAAAGTATTCGGAAC

P112	AATATTCATTGAATCCATGCTGGATAGCGTCCAAT
P113	CTAGTCAGTTGGCAAATCAACAGTCTTTAGGTAGATAACAAA
P114	TATGACTTTATACATTTTTTTTTAATGGAAACAGTACACCGT
P115	ACTAAAGAGCAACGTGAAAATCTCCACCCACAACTAAAGGAA
P116	TTGCGAATAATATTTACAGCGGAGTGAGGTAAAATTTTGAGG
P117	CCGACTTGTTGCTAAAATTTATTTAGTTCGCGAGAGTCGTCTTTCCAGA
P118	ATTGTTATCTGAGAAGAAACCAGGCAAAGCGCCATTCGTAGA
P119	AGTACCGCATTCCACAACATGTTCAGCCTTAAGGTAAAGTAATTC
P120	AAACTCACAGGAACGGTACGCCAGTAAAGGGGGTGAGGAACC
P121	CGCTTTCCAGTTAGCTGTTTAAAGAACGT
P122	GGCGAAGCACCGTAATAACGCCAGGGTTTTCCCAGTCATGGG
P123	TTTACCAGTCCCGGCCTGCAGCCCACTACGGGCGCACCAGCT
P124	GGCAACACCAGGGTCTAATGAGTGAGCTCACAACAATAGGGT
P125	GAAGGAGCGGAATTATCATCATATATCATTTACATAGCACAA
P126	CGCGCTACAGAGTAATAAAAGGGACATTCTGATAGAACTTAG
P127	GTAATTAATTTAGAATCTGGGAAGGGCGATCGGTGCGGCAAA
P128	GGATGTGGTTTGCCCCAGCAG
P129	GCCAGCAGTTGGGCGCAAATCAGGTTTCTTGCCCTGCGTGGT
P130	TATCAGCAACCGCAAGAATGCCAATGAGCCTGAGGATCTATC
P131	GAGAACAATATACAAAATCGCGCAGAGGCGATTCGACAAATCCTTTAAC
P132	GTAAAACGACGGCCCATCACCCAAATCAGCGC
P133	ACGGGCCGATAATCCTGAGAAGTGTTTTTATGGAGCTAACCG
P134	TGCTAAATCGGGGAGCCCCCGATTTAGAGCTAGCAGAACATT
P135	ACGCGGTCCGTTTTTGGGTAAGTGA
P136	GCGTCCACTATTCCTGTGTGAAATGCTCACTGCC
P137	CGTACTATGGTAACCACTAGTCTTTAATGCGCGAACTGAATC
P138	AGAATTTTAGAGGAAAACAATATTACCGCCAGCTGCTCATTT
P139	TTGGGCGGCTGATTTCGGCAAAATCCCT
P140	TGGTGGTTGTTCCAGTTTGGAACA
P141	AGTCGCCTGATACTTGCATAACAGAATACGTGGCACAGCTGA
P142	TGCTGATTGCCGTTGTCATAAACATCGGGCGG
P143	TGAGTGTTCCGAAAGCCCTTCACCGCCTAGGCGGTATTA
P144	TGAGCAAATTTATACAGGAATAACATCACTTGCCTGAGTCTT
P145	CCTGCGCTGGGTGGCGAGAAAGGAAGGGAAGGAGCGGGGCCG
P146	CGTACAGGCCCCCTAACCGTCCCCGGGTACCGAGCGTTC
P147	TTTAGATTCACCAGTCACACGACCGGCGCGTGCTTTCCCAGA
P148	CCCCGCTAGGGCAACAGCTGGCGAAAGGGGGATGTGCTTATT
P149	TCACAGCGTACTCCGTGGTGAAGGGATAGCTAAGAGACGAGG
P150	TGCGTGTTCAGGTTGTGTACATCG
P151	AGGGAGCCGCCACGGGAACGGATAGGCGAAAGCATCAGCACTCTG
P152	AAGAAAGCGCTGAACCTCAAATATTCTAAAGGAAAGCGTTCA
P153	AGCGCAGCTCCAACCGTAATCATGGTCACGGGAAACCT
P154	CCTCATCACCCCAGCAGGCCTCTTCGCTATTACGCCAGTGCC
P155	GTCGCGTGCCTTCGAATTGTCAAAG
P156	TTCGGGGTTTCTGCCAGGCCTGTGACGATCC
P157	AGAGAAAATCCAGAGAGTTGCAGCAAATC
P158	TGCCATCCCACGCAGGCAGTTCCTCATTGCCGTTTTAAACGA
P159	GCCCGAGTACGAGCCGGAAGC
P160	GAGGCCAAGCTTTGAATACCAAGTACGGATTACCTTTTCAAA
P161	ACGTAAGAATTCGTTCTTAGAAGAACTCAAACTATCGGATAA
P162	TAAAACCGTTAAAGAGTCTGTCCATCCAGAAACCACACAATC
P163	ACGAGCGGCGCGGTCAGGCAAGGCGATTAAGTTGGGTAAAAC
P164	TTTTCCAGCATCAGCGGGGCTAAAGAACCTCGTAGCACGCCA
P165	CAAAGCACTAGATAGCTCCATTCAGGCTGCGCAACTGTCTTG
P166	ATTGCGTTGCTGTTATCCGCTCACAATTCCAAACTCACTTGCGTA
P167	GAGAGATAGACTTTACGGCATCAGA
P168	TGACCGCGCCTTAATTTACAATATTTTTGAATGGCTATCACA
P169	CCTAATTTAACAAACCCTCAATCAATATCTGATTCGCTAATC

P170	TTAACTCGGAATTAGAGTAAATCAATATATGTGAGTGATTCT
P171	ATGAAGGGTAAAGTTCACGGTGCGGCCATGCCGGTCGCCATG
P172	ACATAAAGCCCTTACACTGGTCGGGTTAAATTTGT
P173	AAATGCGGAAACATCGGTTTTCAGGTTTAACGTCAGATTAAC
P174	GTCGCAGAAAAACTTAAATTTGCC
P175	GAATTCGTCTCGTCGCTGGGTCTGCAATCCATTGCAACACGG
P176	GCGAAAATCCCGTAAAAAAAGCCGTGGTGCTCATACCGGCGTCCG
P177	CTTGTAGAACGTCAGCGGCTGATTGCAGAGTTTTTCGACGTT
P178	TCATACATTTAATACCGATAGCCCTAAAACATCGAACGTAAC
P179	TACGGCTGGAGGTGCGCACTCGTCACTGTTTGCTCCCGGCAA
P180	AAATGACGCTAAATGGATTATTTACATTGGCGAATACCTGGA
P181	AACAACAGGAAGCACGTCCTTGCTGGTAATATCCAGAAACGC
P182	TGCATTAATGAGCGGTCCACGCTCACTGCGCCACGTGCCAGC
P183	ACCTGACGGGGAAAGCCGGCGAACCAAGTGTCTGCGCGTTGC
P184	CCAGCCTCCGATCCTCATGCCGGA
P185	GCTGGTCTGGTCAGGAGCCGGAATCCGCCGTGAACAGTGCCA
P186	GCGAATCAGTGAGGCCACCGAGTAGTAGCAACTGAGAGTTGA
P187	GGCCAACGCGCGGGGAGGGCCCTGTGTTTGA
P188	AGCTTTCAGAGGTGGCGATGGCCAGCGGGAAT
P189	ATTAGCGGGGTTTTGCTCAGTACCAGGCTGACAACAAGCTG
P190	TGCCCGTATAAACAGTGTGCCTTCTGGTAA
P191	AGAAAACGAGAATGACCATAAATCTACGCCCCTCAAATGCTTTA
P192	ATAACTATATGTAAATGCTTAGGATATAAT
P193	AGGAATCATTACCGCGTTTTTATAAGTACC
P194	GATTAGAGAGTACCTTAACTCCAACAGG
P195	CCTTAAATCAAGATTAGCGGGAGGCTCAAC
P196	GCATGTAGAAACCAATCCATCCTAGTCCT

Table S4. Staples from the 5’ to the 3’ end for the pillar-shaped DNA origami structure with extensions for pyrene-modified staples binding.

Sequence (5’ to 3’)	Function	Replace
ATATTTCCTCTACCACCTACATCACTAATTAGCGGGGT TTTGCTCAGTACCAGGCTGACAACAAGCTG	External labeling with pyrene	P189
ATATTTCCTCTACCACCTACATCACTAAGAAAACGAG AATGACCATAAATCTACGCCCCTCAAATGCTTTA	External labeling with pyrene	P190
ATATTTCCTCTACCACCTACATCACTAATAACTATATG TAAATGCTTAGGATATAAT	External labeling with pyrene	P191
ATATTTCCTCTACCACCTACATCACTAGCATGTAGAAA CCAATCCATCCTAGTCCTG	External labeling with pyrene	P192
ATATTTCCTCTACCACCTACATCACTATGCCCGTATAA ACAGTGTGCCTTCTGGTAA	External labeling with pyrene	P193
ATATTTCCTCTACCACCTACATCACTAAGGAATCATTA CCGCGTTTTTATAAGTACC	External labeling with pyrene	P194
ATATTTCCTCTACCACCTACATCACTAGATTAGAGAGT ACCTTAACTCCAACAGG	External labeling with pyrene	P195
ATATTTCCTCTACCACCTACATCACTACCTTAAATCAA GATTAGCGGGAGGCTCAAC	External labeling with pyrene	P196
GTGATGTAGGTGGTAGAGGAAATAT-**pyrene**	Pyrene at 3’	-

Table S5. Staples from the 5’ to the 3’ end for the pillar-shaped DNA origami structure for Distance determination from fluorescence lifetimes.

Sequence (5’ to 3’)	Function	Replace
AGACAGCAGAAACGAAAGAGGAAATAAATCGAGGTG ACAGTTAAAT- **ATTO647N**	Dye ATTO647N at 3’ (11.6 nm)	P46
CATTTGAGATAACCCACGAAACAATG-**ATTO647N**	Dye ATTO647N at 3’ (15.9 nm)	P37

AAGGGATATTCATTACCGTAATCTATAGGCT-ATTO647N	Dye ATTO647N at 3' (23.4 nm)	P70
ATTGTTATCTGAGAAGAAACCAGGCAAAGCGCCATTC GTAGA-ATTO647N	Dye ATTO647N at 3' (30 nm)	P118

For the Experiment the staples of pillar-shaped DNA origami structure: 3, 4, 6, 13, 15, 23, 30, 43, 45, 49, 50, 61, 64, 66, 68, 75, 79, 82, 90, 91, 92, 102, 105, 157, 157, 167 were replaced with the following:

Table S6. Staples from the 5' to the 3' end for the pillar-shaped DNA origami structure for DNA-PAINT experiments

CCAGAACAGAGCCATAAAGGTGGAATAAGTTGGCATGATTAAAGAAAATA GAAA T TCCTCCTCCTCCTCCTCCTCCTCCTCCT	DNA-PAINT binding site
AACTACCATCATAGACCGGAATCTGGATTTGTTATAA T TCCTCCTCCTCCTCCTCCTCCTCCTCCT	DNA-PAINT binding site
TTATAAGGGTATGGAATAATTCATCAATATAATCCT T TCCTCCTCCTCCTCCTCCTCCTCCTCCT	DNA-PAINT binding site
CGCCACATAAGTAGAAAAATCAAGAAGCAAAAGAAGATGATGGC T TCCTCCTCCTCCTCCTCCTCCTCCTCCT	DNA-PAINT binding site
ACAATGACAGCATTTGAGGCAGGTCAGATGATATTC T TCCTCCTCCTCCTCCTCCTCCTCCTCCT	DNA-PAINT binding site
AGAAATCGTTAGGAATATAAGAGCA T TCCTCCTCCTCCTCCTCCTCCTCCTCCT	DNA-PAINT binding site
CCATAATGCCAGGCTATCAAGGCCGGAGACATCTAGCTGG T TCCTCCTCCTCCTCCTCCTCCTCCTCAT	DNA-PAINT binding site
TCGTGCCGGAGTCAATAGTGAATTTGCAGATAAAAGGAAT T TCCTCCTCCTCCTCCTCCTCCTCCTCCT	DNA-PAINT binding site
TATTGAAAGGAATTGAGGAA T TCCTCCTCCTCCTCCTCCTCCTCCTCCT	DNA-PAINT binding site
AAAATAAACGTCTGAGAGACTACCTTTTTAAGGC	Exchange staple
TTACTACATACACCACCCTCGTCTTTCCACCACCGGAACCGCCTCCCTCA	Exchange staple

CGCAAAGACACCACGGCAACA	Exchange staple
CAAAATCACCGGAACCAGAGCCAGATTTTGTCA	Exchange staple
GATATACTTCTGAATATAGAACCAAATTAT	Exchange staple
ATAGCGAGAGGCTATCATAACCAAATCCCAAAGAAAATTTCATCCTCAT	Exchange staple
CTCGATTGAACCAGAGCCGCCGCGCCGCCA	Exchange staple
GCGAAACAAAGTGTAAAACACTCAT	Exchange staple
AGTTTCCAACATTATTACATT	Exchange staple
TTGCACGTAAAACAACGT	Exchange staple
ACAAACCAAAAGAATACACTAATGCCACTACGAATAAA	Exchange staple
GTTCTGACCTTTTTGCACCCAGCT	Exchange staple
AGCCACATTATTCATCAGTTGAGAAATGAA	Exchange staple
TTCATGCCTCAACATGTTTTAAATATGC	Exchange staple
TACGAGATAAATGCCAGCTTTGAGGGGACGACGACAG	Exchange staple
CAAGAGAATCGATGCTGAGAGTCTACAAGGAGAGG	Exchange staple
ACACTATGATATTTGGAAGT	Exchange staple
ACCGGAATCTGGATTTGTTATAA	Exchange staple
TTCATGCCTCAACATGTTTTAAATATGCAACTACCATCATAGT - ATTO542	Internal Dye

Table S7. **Core staples from the 5’ to the 3’ end for the L-shaped DNA origami structure for LPAINT L197-L252 were left out in the experiments with the L-shaped DNA origami structure labeled with 42 pyrene molecules.**

staple ID	Sequence (5’ to 3’)
L1	ATCCAGAACAATATTAGTCCATCAGGAACGGT
L2	CGTGCCTGTTCTTCGCATCCAGCGCCGGGTTA
L3	ATAATCAGAAAAGCCCAACATCCACTGTAATA
L4	CATAGGTCTGAGAGACAAATCGTCGAATTACC
L5	ATTGCCCTTCACCGCCCCAGCTGCTTGCGTTG
L6	TTCGTAATCATGGTCATCCATCAGTTATAAGT
L7	CCCGCCGCGCTTAATGAAAGCCGGCGAACGTG
L8	AGGCGAAAATCCTGTTGTCTATCACCCCCGAT
L9	GCTGCGCAACTGTTGGCAGACCTATTAGAAGG
L10	CTGCAACAGTGCCACGTATCTGGTAGATTAGA
L11	AACAGAGGTGAGGCGGCAGACAATTAAAAGGG
L12	AAATCCCGTAAAAAAACGTTTTTTGGACTTGT

L13	GGCTTAGGTTGGGTTAAGCTAATGATTTTCGA
L14	TATTTTGTTAAAATTCGGGTATATATCAAAAC
L15	GTATAAGCAAATATTTTAGATAAGTAACAACG
L16	CCAGCCAGCTTTCCGGGTAATGGGGTAACAAC
L17	GGGGTCATTGCAGGCGGGAATTGACTAAAATA
L18	TGTTGCCCTGCGGCTGATCAGATGCAGTGTCA
L19	GGAAACCAGGCAAAGCGTACATAAGTGAGTGA
L20	CTCTCACGGAAAAAGAACGGATAAAAACGACG
L21	ATCGGCAAAATCCCTTACGTGGACTCCAACGT
L22	TCAAATCACCATCAATACGCAAGG
L23	GCAGTTGGGCGGTTGTCCAGTTATGGAAGGAG
L24	CTTCTGACCTAAATTTGCAGAGGCCAGAACGCAATTTACG
L25	ATCAAACTTAAATTTCTGGAAGGGCCATATCA
L26	TATCATTTTGCGGAACATCCTGATATAAAGAA
L27	GACCGTGTGATAAATACAAATTCT
L28	TGATTGCTTTGAATACAAACAGAATGTTTGGA
L29	GCCGGGCGCGGTTGCGCCGCTGACCCCTTGTG
L30	GTACTATGGTTGCTTTTTTAGACACGCAAATT
L31	GGGCCTCTTCGCTATTACGTTGTACCTCACCG
L32	GCAGCAAGCGGTCCACAAGTGTTTTGAGGCCA
L33	AACGTTATTAATTTTACAACTAATCAGTTGGC
L34	GAAATTGTTATCCGCTCACATTAAATTAATGA
L35	CCAGCTTACGGCTGGAAACGTGCCCGTCTCGT
L36	GCAGAGGCGAATTATTTTTCATTTGCTATTAA
L37	CATTGCCTGAGAGTCTTTATGACCATAAATCATTTCATTT
L38	CTAGCTGATAAATTAACAGTAGGG
L39	AAATCAGCTCATTTTTGTGAGCGAATAGGTCA
L40	TATTTTTGAGAGATCTGCCATATTTCCTCTACTCAATTGA
L41	CAGGAAAAACGCTCATACCAGTAAATTTTTGA
L42	ACAGTTGAGGATCCCCAGATAGAACTGAAAGC
L44	AGAAACAGCTTTAGAAGGAAGAAAAATCTACGATTTTAAGCATATAAC
L45	GCACCCTCCGTCAGGTACGTTAGTAAATGAATAGTTAGCGTCAATCAT
L46	AGTTGATTAGCTGAAAAGAGTACCTTTAATTGTTAATTCGGACCATAA
L47	CTCAAATGTTCAGAAATGGAAGTTTCACGCGCATTACTTCAACTGGCT
L48	TTTCATCGAATAATATCCAGCTACAATACTCCAGCAATTTCTTTACAG
L49	TGCTCATTCTTATGCGTTAATAAAACGAACTATATTCATTGGCTTTTG
L50	GGCACCAAAACCAAAAGTAAGAGCAACACTATAGCAACGTAAATCGCC
L51	AAGGGAACCGGATATTCACTCATCTTTGACCCGTAATGCCATCGGAAC
L52	ATATTCACCGCCAGCATTGACAGGCAAAATCA
L53	CGGAATCTCAGGTCTGTTTTAAATATGCATGCGAACGAATCATTG
L54	AAAGACAAATTAGCAAGTCACCAATGAAACCA
L55	TCGATAGCAGCACCGTAAAATCACGTTTTGCT
L56	TGAATTACCAGTGAATGGAATTACGAGGCATATAGCGAGAGAATCCCC
L57	TAGTTGCCAGTTGCGGGAGGTTTTGAAGATCAATAA
L58	GCCCCCTGGTGTATCACCGTACTC
L59	AATAAGTTAGCAAAAACGCAATAATAACGAGAATTAAAAGCCCAA
L60	CAAAAGAATAAAATACCCAGCGATTATACCAAGCGCGAA
L61	TTTTCATCGGCATATTGACGGCACCACGG
L62	GGGGCGCGCCCAATTCACTAAAGTACGGTGTCACGAGAATAGCTTCAA
L63	CCGGCAAATCGGCGAAGTGGTGAAGGGATAG
L64	ATCAAAAAGTCATAAAACGGAACAACATTATCAACTTTAGTAGAT
L65	TTAGTTTGCCTGTTTAGGTCATTTTTGCGGATAGGAAGCCGACTATTA
L66	GCGAGAAAAGGGATGACGAGCACGTATAACGTGCTTTTCACGCTGAAGAAAGC
L67	CCCTGAACAAATAAGAAACGCGAGGCGTT
L68	CTGAGGCCAACGGCTACAGAGGTTTCCATT
L69	ACATTCTGAAGAGTCTCCGCCAGCAGCTCGAA
L70	AAATCAACACGTGGCATCAGTATTCTCAATCC
L71	TTATACTTAGCACTAAAAAGTTTGTGCCGCCA

L72	CCAACATGACGCTCAATGCCGGAGGAAATACC
L73	CCGGAACCGCAAGAAAGCAATAGCTATCTTACTCACAATCCGATTGAG
L74	GTAAGAATAGTTGAAACTTTCGCAAACACCGC
L75	GCCAGTGCGATTGACCCACCGCTTCTGGTGCC
L76	AGGAAACCGAGGACGTAGAAAAAGTACCG
L77	CTGCGCGGCTAACTCACAATTCCACACAACATACGAGTACCGGGGCTCTGTGGGTGTTCAG
L78	AATTACATAGATTTTCAATAACGGATTCGCC
L79	ATAACCTTATCAACAAAAATTGTATAACCTCC
L80	CCAGAATGGAGCCGCCAATCAAGTTTGCC
L81	TTTTTTAATGCACGTACAAGTTACCCATTCAG
L82	CATTATACGGTTTACCCATAACCCTCGAAATACAATGTTTAAACAGGG
L83	CTTTTGCGTTATTTCAATGATATTCAACCGTT
L84	GACAGATGGACCTTCATCAAGAGCCCTGAC
L85	ACAAGAAATAGGAATCCCAATAGCAAGCAAATATAGCAGCATCCTGAA
L86	AAATTATTTGGAAACAGCCATTCGAAAATCGC
L87	CACTCATGAAACCACCTTAAATCAAGATTGAGCGTCTTTTTGTTT
L88	GCCTAATTATCATATGATAAGAGATTTAGTTAATTTCAT
L89	GAGGGTAGTTGCAGGGTGCTAAACAACTTTCACGCCTGGAAAGAG
L90	AGAGCCGCAAACAAATGAGACTCCTCAAGAGATTAGCGGGCAGTAGCA
L91	ATTGCGTTTAACAACATTTCAATTACCTGAGCAAAAGGGAGAAACAGGTTTAAGATGATGG
L92	CCACCCTCTGTTAGGAAGGATCGTCTTTCCAGCAGACGATTATCAGCT
L93	GCCAGTACGTTATAAGGCGTTAAATAAGAATAAACACAAAT
L94	CAATTCATATAGATAATAAATCCTTTGCCCG
L95	GCCGTCACAATATAAAAGAAACCACCAGAAGGAGCGGACTCGTATTACATTTGTCAAATAT
L96	TACCAGTAACGCTAACAGTTGCTATTTTGCACCCCATCCT
L97	GTCGAAATCCGCGACCTGCTCCACCAACTTTTAGCATTC
L98	GTCCACTAAACGCGCGGACGGGCAACAGCTG
L99	AACCGTTTCACACGGGAAATACCTACATTTTGACGCTAAACTATCACTTCTTTAACAGGAG
L100	CGCTGGCACCACGGGAGACGCAGAAACAGCGG
L101	CAAATCGTCAGCGTGGTGCCATCCCACGCAA
L102	GCCGATTAAGGAAGGGCGCGTAACCACCACA
L103	TGTAGCTCAACATTTACCCTCGAAAGAC
L104	GAGAAACATTTAATTTTACAGGTAGAAAG
L105	TTGAGTAAGCCACCCTCAGAACCG
L106	TTAGAGCTATCCTGAGGCTGGTTTCAGGGCGC
L107	TTCACCAGGTAGCAATGGCCTTGCTGGTAAT
L108	CGCTCACTATCAGACGGTCCGTGAGCCTCCTC
L109	ATTCATATCAGTGATTTGGCATCAGGACGTTGTAACATAAACCAGACG
L110	GGAGGGAAGAGCCAGCAATCAGTAGCGACAGACCAGAACCGCCTC
L111	AACGTCAATAGACGGGGAATACCCAAAAGAACAAGACTCCGTTTTTAT
L112	TGTACTGGTAATAAGTTCAGTGCC
L113	TTCAAATTTTTAGAAAAAACAGGAGCAAACAAGAGAATCGATGAAGGGTGAGATATTTTA
L114	TAATAAGAAGAGCCACCCTTATTAGCGTTTGCCATTCAACAATAGAAA
L115	TTCTGAAACATGAAAGTGCCGGCCATTTG
L116	CAAACCCTTTAGTCTTACCAGCAGAAGATAA
L117	AAACGGGGTTTTGCTACATAACGCCAAAAAAGGCTTGTAATCTTG
L118	TGGAGCCGGCCTCCGGGTACATCGACATAAAA
L119	CCGAGTAAGCCAACAGGGGTACCGCATTGCAA
L120	ACAAGAACCGAACTGATGTTACTTAGCCGGAAAAGACAGCACTACGAA
L121	AGAACGTTAACGGCGTAATGGGTAAAGGTTTCTTTGCGTCGGTGGTGCTGGTCTTGCCGTT
L122	GGAGCCTTCACCCTCAGAGCCACC
L123	CCCCCTGCGCCCGCTTTAGCTGTTTCCTGTGT

L124	TGCGGGATAGCAGCGACGAGGCGCAGAGAAACGGCCGCGGTAACGATC
L125	TAATAGTATTCTCCGTGCATTAAATTTTTGTT
L126	CACATCCTCAGCGGTGGTATGAGCCGGGTCAC
L127	CACAGACATTTCAGGGATCTCCAAAAAAAAGGTTCTTAAAGCCGCTTT
L128	CCATTACCAAGGGCGACATCTTTTCATAGGCAGAAAGAATAGGTTGAG
L129	ATGAGTGACCTGTGCAGTTTCTGCCAGCACG
L130	AAGCGCATAAATGAAACAGATATAGAAGGCTTAGCAAGCCTTATTACG
L131	ATAAAAATATCGCGTTCTCCTTTTGATAAGAGCTATAT
L132	ATCGGCCTTAAAGAATAAATCAAAAGAATAGCCCGAGACCAGTGAGGGAGAGGGGTG CCTA
L133	CCTGCAGCCATAACGGGGTGTCCAGCATCAGC
L134	ATGGCTACAATCAACTGAGAGCCAGCAGCAAATGAAAAACGAACCTAATGCGCTTGGC AGA
L135	TACAGGCATTAAATTAACCAATAGGAACGCCATCAAAGTCAATCAGAATTAGCCTAAAT CG
L136	CCGTCGGAGTAGCATTCAAAAACAGGAAGATT
L137	GTTTTCCCGTAGATGGCAGGAAGATCGCACT
L138	GCCTGTTTGCTTCTGTTACCTTTTAACGTTAA
L139	AAACGGCGCAAGCTTTGAAGGGCGATCGGTGC
L140	TACCGATAGTTGCGCTTTTTCA
L141	CAGTACCATTAGTACCCAGTGCCCGTATAAATTGATGAATTAAAG
L142	CAACTAATGCAGACAGAGGGGCAATACTG
L143	ACCCTCATGCCCTCATTTTCTGTATGGGATTTAGTTAAAGCAGCTTGA
L144	ATAAACAATCCCTTAGTGAATTTATCAAAAT
L145	CCTCAGAGCACAAGAAGAAAAGTAAGCAG
L146	CAGTATGTTTATTTTGCGAAGCCCTTTTTAATTGAGTTCTGAACA
L147	CGGGAAACGAAAAACCTGATGGTGGTTCCGAA
L148	CTTAATTGAGACCGGAAACAGGTCAGGATTAGAGGTGGCA
L149	TCATCAACAAGGCAAATATGTACCCCGGTTG
L150	TGCTTTCGAGGTGAATCTCCAAAA
L151	AGCATGTACGAGAACAATCCGGTATTCTAAGAACGATTTTCCAGA
L152	TCTTACCATAAAGCCATAATTTAGAATGGTTTAGGGTAGC
L153	CGTTGAAAATAGCAAGCCCAATA
L154	GTTGTACCACCCTCATAAAGGCCGGAGACAG
L155	GAAACAACGCGGTCGCCGCACAGGCGGCCTTTAGTGACTTTCTCCACGTACAGACGC CAGG
L156	CAAAGGGCCTGTCGTGTGGCCCTGAGAGAGTT
L157	TTAATTTCATGTTCTATAACTATATGTAAATGCTGATGTCAATAGAATCCTTGACAAAATT
L158	AGCGAACCAGAAGCCTGGAGAATCACAAAGGCTATCAGGT
L159	CGTTGGTAGTCACGACGCCAGCTGGCGAAAGGGGGATATCGGCCTGCGCATCGGCCA GCTT
L160	GGAACCCAAAACTACAAACAGTTTCAGCG
L161	AGGAGGTGGCGGATAAGTATTAAGAGGCTAAATCCTCTACAGGAG
L162	GGAATTAGGTAAATTTTCGGTCATAGCCCCACCGGAACCACCACC
L163	TCTTTAGGCTGAATAATGCTCATTAGTAACAT
L164	TGCGAATAATAATCGACAATGTTCGGTCG
L165	ACGCCAGATGACGGGGCGCCGCTAGCCCCAGC
L166	TAAAGTTTAGAACCGCTAATTGTATCGCGGGGTTTAAGTTTGGCCTTG
L167	ATTATAGCGTCGTAATAGTAAAATGTTTTTT
L168	TTTTTTTTTTTTAAAACTAG
L169	TTTTTGCCTGAGTAGAAGAA
L170	TTTTGATTAAGACGCTGAGA
L171	TTTTGGCGCATAGGCTGGCTAACGGTGTTAAATTGT
L172	TTTGCGTATTGGGCGCTTTT
L173	TAGTCAGAAGCAAAGCGGATTTT
L174	TTTTCGCAAATGGTCAATAAACCATTAGATGC
L175	TTTTTTGCATCAAAAGCCTGAGTAATTTT
L176	TTTTCCATATTATTTATCCCAATCCAAAGTCAGAGA

L177	GAAAGGAGCGGGCGCTAGGTTTT
L178	ATATATATAAAGCGACGACATCGGCTGTCTTTCCTTATCATTTTT
L179	TCAGCAGCAACCGCAATTTT
L180	TTTTGTTTCGTCACCAGTACTGTACCGTAAT
L181	TTTTCTTTACAAACAATTCG
L182	TTTTACCGTTCCAGTAAGCGTCATACATGGCTTCAGTTAAT
L183	TTTTGGAATTTGTGAGAGAT
L184	AGAGCAAATCCTGTCCAGATACCGACAAAAGGTAATTTT
L185	ATACGCAAAGAAAATTATTCATTAAAGGTGAATTTT
L186	TTAATTAAACCATACATACATAAAGGTGGCAATTTT
L187	CTGATAGCCCTAAAACTTTT
L188	TTTTATTGGGCTTGAGATGGCCAGAACGATT
L189	CAGATGAATATACAGTTTTT
L190	TTTTCGGGCCGTTTTCACGG
L191	CCGTGCATCTGCCAGTTTTT
L192	TTTTGCTAATATCAGAGAGATAACCCCGCCACCGCG
L193	ACAAAGTATGAGGAAGCTTTGAGGACTAAAGATTTT
L194	TTTCGACTTGATCGAGAGGGTTGATATAAGTATTTT
L195	TTTTCCCTCAGAGCCACCACCCTCAGAAAGCGCTTA
L196	GAGCCGATATAACAACAACCATCGCCCTTTTTTT

Table S8. **Staples from the 5’ to the 3’ end for the L-shaped DNA origami structure with extensions for pyrene-modified staple binding.**

Sequence (5’ to 3’)	Function	Replace
ATATTTCCTCTACCACCTACATCACTAATCCAGAACAA TATTAGTCCATCAGGAACGGT	External labeling with pyrene	L1
ATATTTCCTCTACCACCTACATCACTACGTGCCTGTTC TTCGCATCCAGCGCCGGGTTA	External labeling with pyrene	L2
ATATTTCCTCTACCACCTACATCACTAATAATCAGAAA AGCCCAACATCCACTGTAATA	External labeling with pyrene	L3
ATATTTCCTCTACCACCTACATCACTACATAGGTCTGA GAGACAAATCGTCGAATTACC	External labeling with pyrene	L4
ATATTTCCTCTACCACCTACATCACTAATTGCCCTTCA CCGCCCCAGCTGCTTGCGTTG	External labeling with pyrene	L5
ATATTTCCTCTACCACCTACATCACTATTCGTAATCAT GGTCATCCATCAGTTATAAGT	External labeling with pyrene	L6
ATATTTCCTCTACCACCTACATCACTACCCGCCGCGCT TAATGAAAGCCGGCGAACGTG	External labeling with pyrene	L7
ATATTTCCTCTACCACCTACATCACTAAGGCGAAAATC CTGTTGTCTATCACCCCCGAT	External labeling with pyrene	L8

ATATTTCCTCTACCACCTACATCACTAGCTGCGCAACT GTTGGCAGACCTATTAGAAGG	External labeling with pyrene	L9
ATATTTCCTCTACCACCTACATCACTACTGCAACAGTG CCACGTATCTGGTAGATTAGA	External labeling with pyrene	L10
ATATTTCCTCTACCACCTACATCACTAAACAGAGGTGA GGCGGCAGACAATTAAAAGGG	External labeling with pyrene	L11
ATATTTCCTCTACCACCTACATCACTAAAATCCCGTAA AAAAACGTTTTTTGGACTTGT	External labeling with pyrene	L12
ATATTTCCTCTACCACCTACATCACTAGGCTTAGGTTG GGTTAAGCTAATGATTTTCGA	External labeling with pyrene	L13
ATATTTCCTCTACCACCTACATCACTATATTTTGTTAA AATTCGGGTATATATCAAAAC	External labeling with pyrene	L14
ATATTTCCTCTACCACCTACATCACTAGTATAAGCAAA TATTTTAGATAAGTAACAACG	External labeling with pyrene	L15
ATATTTCCTCTACCACCTACATCACTACCAGCCAGCTT TCCGGGTAATGGGGTAACAAC	External labeling with pyrene	L16
ATATTTCCTCTACCACCTACATCACTAGGGGTCATTGC AGGCGGGAATTGACTAAAATA	External labeling with pyrene	L17
ATATTTCCTCTACCACCTACATCACTATGTTGCCCTGC GGCTGATCAGATGCAGTGTCA	External labeling with pyrene	L18
ATATTTCCTCTACCACCTACATCACTAGGAAACCAGGC AAAGCGTACATAAGTGAGTGA	External labeling with pyrene	L19
ATATTTCCTCTACCACCTACATCACTACTCTCACGGAA AAAGAACGGATAAAAACGACG	External labeling with pyrene	L20
ATATTTCCTCTACCACCTACATCACTAATCGGCAAAAT CCCTTACGTGGACTCCAACGT	External labeling with pyrene	L21
ATATTTCCTCTACCACCTACATCACTATCAAATCACCA TCAATACGCAAGG	External labeling with pyrene	L22
ATATTTCCTCTACCACCTACATCACTAGCAGTTGGGCG GTTGTCCAGTTATGGAAGGAG	External labeling with pyrene	L23
ATATTTCCTCTACCACCTACATCACTACTTCTGACCTA AATTTGCAGAGGCCAGAACGCAATTTACG	External labeling with pyrene	L24
ATATTTCCTCTACCACCTACATCACTAATCAAACTTAA ATTTCTGGAAGGGCCATATCA	External labeling with pyrene	L25

ATATTTCCTCTACCACCTACATCACTATATCATTTTGC GGAACATCCTGATATAAAGAA	External labeling with pyrene	L26
ATATTTCCTCTACCACCTACATCACTAGACCGTGTGAT AAATACAAATTCT	External labeling with pyrene	L27
ATATTTCCTCTACCACCTACATCACTATGATTGCTTTG AATACAAACAGAATGTTTGGA	External labeling with pyrene	L28
ATATTTCCTCTACCACCTACATCACTAGCCGGGCGCGG TTGCGCCGCTGACCCCTTGTG	External labeling with pyrene	L29
ATATTTCCTCTACCACCTACATCACTAGTACTATGGTT GCTTTTTTAGACACGCAAATT	External labeling with pyrene	L30
ATATTTCCTCTACCACCTACATCACTAGGGCCTCTTCG CTATTACGTTGTACCTCACCG	External labeling with pyrene	L31
ATATTTCCTCTACCACCTACATCACTAGCAGCAAGCGG TCCACAAGTGTTTTGAGGCCA	External labeling with pyrene	L32
ATATTTCCTCTACCACCTACATCACTAAACGTTATTAA TTTTACAACTAATCAGTTGGC	External labeling with pyrene	L33
ATATTTCCTCTACCACCTACATCACTAGAAATTGTTAT CCGCTCACATTAAATTAATGA	External labeling with pyrene	L34
ATATTTCCTCTACCACCTACATCACTACCAGCTTACGG CTGGAAACGTGCCCGTCTCGT	External labeling with pyrene	L35
ATATTTCCTCTACCACCTACATCACTAGCAGAGGCGAA TTATTTTTCATTTGCTATTAA	External labeling with pyrene	L36
ATATTTCCTCTACCACCTACATCACTACATTGCCTGAG AGTCTTTATGACCATAAATCATTTCATTT	External labeling with pyrene	L37
ATATTTCCTCTACCACCTACATCACTACTAGCTGATAA ATTAACAGTAGGG	External labeling with pyrene	L38
ATATTTCCTCTACCACCTACATCACTAAAATCAGCTCA TTTTTGTGAGCGAATAGGTCA	External labeling with pyrene	L39
ATATTTCCTCTACCACCTACATCACTATATTTTTGAGA GATCTGCCATATTTCCTCTACTCAATTGA	External labeling with pyrene	L40
ATATTTCCTCTACCACCTACATCACTACAGGAAAAACG CTCATACCAGTAAATTTTTGA	External labeling with pyrene	L41
ATATTTCCTCTACCACCTACATCACTAACAGTTGAGGA TCCCCAGATAGAACTGAAAGC	External labeling with pyrene	L42
GTGATGTAGGTGGTAGAGGAAATAT-pyrene	Pyrene at 3’	-

Table S9. Staples from the 5' to the 3' end for the L-shaped DNA origami structure for L-PAINT

Sequence (5' to 3')	Function	Replace
GGCACCAAAACCAAAAGTAAGAGCAACACTATAGCA ACGTAAATCGCCTTTTTTTTTCGGGCATTTA-Cy3B	Pointer-Cy3B at 3'	L43
AACGAATCATTGTGAATTACCTTTTTTAAATGCC	Lower binding site	L49
GGCACCAAAACCAAAAGTAAGAGCAACACTATAGCA ACTTTTAAATGC	Middle binding site	L50
AGCGTCAATCATAAGGGAACCGGTTTTAAATGCC	Upper binding site	L51
GCACCCTCCGTCAGGTACGTTAGTAAATGAATAGTT	Exchange staple	L45
TGCTCATTCAGTGAATGGAATTACGAGGCATATAGCG AGAGAATCCCC	Exchange staple	L49
ATATTCACTCATCTTTGACCCGTAATGCCATCGGAAC	Exchange staple	L51
ATATTCACCGCCAGCATCGATAGCAGCACCGTAAAAT CACGTTTTGCT	Exchange staple	L52
CGGAATCTCAGGTCTGTTTTAAATATGCATGCG	Exchange staple	L53
GTAAATCGCCAAAGACAAATTA	Exchange staple	L54
GCAAGTCACCAATGAAACCATTGACAGGCAAAATCA	Exchange staple	L55
ATGCGTTAATAAAACGAACTATATTCATTGGCTTTTG	Exchange staple	L56

REFERENCES

1. Wang S, Xi W, Cai F, Zhao X, Xu Z, Qian J*, et al.* Three-photon luminescence of gold nanorods and its applications for high contrast tissue and deep in vivo brain imaging. *Theranostics* 2015, **5**(3)**:** 251-266.

2. Masullo LA, Steiner F, Zahringer J, Lopez LF, Bohlen J, Richter L*, et al.* Pulsed Interleaved MINFLUX. *Nano Lett* 2021, **21**(1)**:** 840-846.

3. Kaminska I, Bohlen J, Rocchetti S, Selbach F, Acuna GP, Tinnefeld P. Distance Dependence of Single-Molecule Energy Transfer to Graphene Measured with DNA Origami Nanopositioners. *Nano Letters*; 2019. pp. 4257-4262.

4. Thiele JC, Nevskyi O, Helmerich DA, Sauer M, Enderlein J. Advanced Data Analysis for Fluorescence-Lifetime Single-Molecule Localization Microscopy. *Front Bioinform* 2021, **1:** 740281.

5. Strauss S, Jungmann R. Up to 100-fold speed-up and multiplexing in optimized DNA-PAINT. *Nat Methods* 2020, **17**(8)**:** 789-791.

6. Nickels PC, Wunsch B, Holzmeister P, Bae W, Kneer LM, Grohmann D*, et al.* Molecular force spectroscopy with a DNA origami-based nanoscopic force clamp. *Science* 2016, **354**(6310)**:** 305-307.

7.5 Publication V: Super-Resolved FRET and Co-Tracking in pMINFLUX

by

Fiona Cole*, Jonas Zähringer*, Johann Bohlen, Tim Schröder, Florian Steiner,

Fernando Stefan and Philip Tinnefeld (* equal contribution)

published in

bioRxiv 2023.03.24.534096; DOI: https://doi.org/10.1101/2023.03.24.534096

in revisions

Author contribution:

Fiona Cole and I developed and conceptualized the project. I designed, performed and analyzed the FRET-MINFLUX experiments and helped with the design and analysis of the pMINFLUX multiplexing experiments. I wrote parts of the manuscript.

Super-Resolved FRET and Co-Tracking in pMINFLUX

Fiona Cole[1,4], Jonas Zähringer[1,4], Johann Bohlen[1], Tim Schröder[1], Florian Steiner[1], Fernando D. Stefani[2,3] and Philip Tinnefeld[1]*

[1] Department of Chemistry and Center for NanoScience, Ludwig-Maximilians-Universität München, Butenandtstr. 5-13, 81377 München, Germany

[2] Centro de Investigaciones en Bionanociencias (CIBION), Consejo Nacional de Investigaciones Científicas y Técnicas (CONICET), Godoy Cruz 2390, C1425FQD, Ciudad Autónoma de Buenos Aires, Argentina

[3] Departamento de Física, Facultad de Ciencias Exactas y Naturales, Universidad de Buenos Aires, Güiraldes 2620, C1428EHA, Ciudad Autónoma de Buenos Aires, Argentina

[4] These authors contributed equally

* Correspondence: philip.tinnefeld@cup.uni-muenchen.de

Graphical Abstract

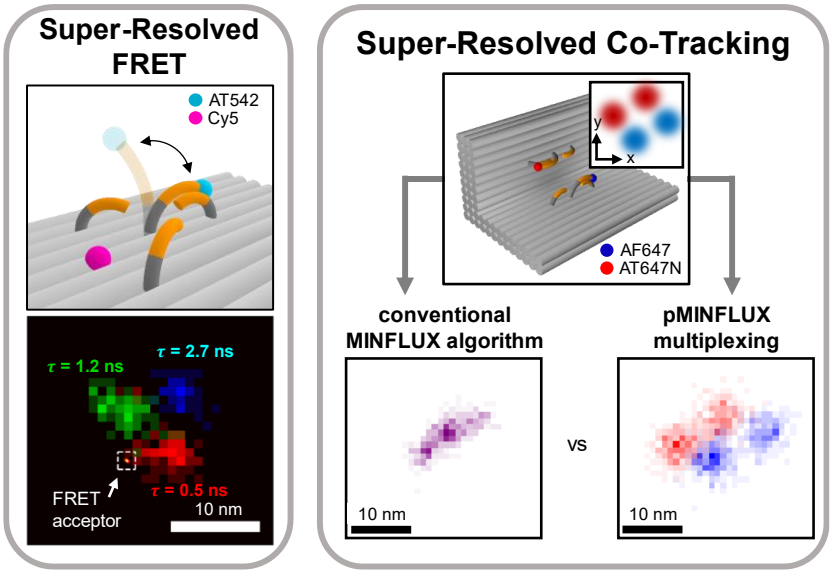

Super-Resolved FRET and Co-Tracking in pMINFLUX

Summary

Single-molecule FRET (smFRET) is widely used to investigate dynamic (bio) molecular interactions taking place over distances of up to 10 nm. With the advent of recent super-resolution methods such as MINFLUX, MINSTED or RASTMIN, the spatiotemporal resolution of these techniques advanced towards the smFRET regime. While these methods do not suffer from the spatial restriction of FRET, they only visualize one emitter at a time, thus rendering fast dynamics of interactions out of reach. Here, we describe two approaches to overcome this limitation in pMINFLUX using its intrinsic fluorescence lifetime information. First, we combined pMINFLUX with smFRET. This enabled us to track a FRET donor fluorophore and simultaneously co-localize its FRET acceptor with nanometer precision. To extend co-localized tracking beyond the FRET range, we developed pMINFLUX lifetime multiplexing, a method to simultaneously track two fluorophores with similar spectral properties but distinct fluorescence lifetimes. We demonstrated its application on both static and dynamic DNA origami systems with a precision better than 2 nm. Within the FRET range, pMINFLUX lifetime multiplexing additionally uses a novel combined phasor-microtime-gating approach. This paves the way for nanometer precise co-localized tracking for inter-dye distances between 4 nm and 100 nm, closing the resolution gap between smFRET and co-tracking.

Introduction

Molecular interactions and changes of conformational states are beautifully revealed with single-molecule FRET (smFRET).[1] With its high sensitivity for small distance changes, smFRET has provided unique insight into the molecular mechanisms of life, including DNA replication[2,3], transcription[2,4], translation[5,6] and repair[3], protein folding[7,8] and various enzymatic functions[9,10]. However, its working range limited to distances smaller than 10 nm leaves many other relevant biological dynamics occurring at larger distances, such as protein-protein interactions in dimerization, oligomerization and in multicomponent molecular machineries, out of reach for smFRET. Here, the co-tracking of multiple molecules of interest with nanometer precision may offer an alternative. However, experimental limitations such as chromatic aberrations in multicolor experiments and photon-inefficient single-molecule localizations by camera-based systems have so far restricted widespread applications. Combined single-molecule tracking and FRET visualizations have therefore been rare (see e.g. refs [11–14]).

In recent years, new conceptual and technological advances including MINFLUX[15–17] and later MINSTED[18] and RASTMIN[19] have demonstrated the routine localization of single-molecules with nanometer precision, thus reaching the working range of FRET. In MINFLUX, emitters are localized by sequentially interrogating their position with spatially displaced, vortex shaped excitation beams. By comparing the number of photons emitted upon excitation with the different beams with their known beam profiles, the absolute position of emitters is estimated. Furthermore, MINFLUX can reach sub-millisecond temporal resolution ideal for tracking applications with strikingly optimized photon budgets.[20,21] However, while multiplexing with MINFLUX was achieved in imaging by spectral splitting[17] and Exchange DNA-PAINT[22], fast simultaneous tracking below the diffraction limit with nanometer precision remained restricted to single emitters. As soon as two or more fluorescent emitters are present, neither of them could be localized correctly, making multiplexed tracking experiments so far unfeasible with these techniques.

Here, using pulsed interleaved MINFLUX (pMINFLUX)[16,23] in a series of experiments on DNA origami model nanostructures, we demonstrate multiplexed single-molecule tracking spanning from the FRET range to the range of super-resolved tracking. pMINFLUX provides fast localization rates by performing the excitation sequence at the repetition rate of the laser, typically in MHz and direct access to the fluorescence lifetime.[16] The fluorescence lifetime information both enables additional FRET efficiency determination within the FRET range and serves as a distinguishable characteristic to separate the photons from different molecules as previously demonstrated in FLIM and STED microscopy.[24–26]

In a first experiment, we tracked a FRET donor labelled DNA sequence which transitions between the vertices of a triangular structure with 6 nm side length. Tracking with pMINFLUX provides the donor position and at the same time detects the proximity of a FRET acceptor by the shortened fluorescence lifetime of the donor. Calculation of the FRET efficiency enables the estimation of the inter-dye distance at the different donor positions. This, in turn, enables determining the position of the acceptor relative

to the triangular structure. Next, we introduce a concept to localize two dye molecules with similar spectra but distinct fluorescence lifetimes in distances beyond the FRET range without photoswitching. We simultaneously localize an ATTO647N molecule and an Alexa Fluor 647 molecule separated by 15 nm with a precision only slightly reduced compared to individual localizations. We then continue to use this concept to simultaneously track the position of two dye molecules that independently jump between different sites on a DNA origami, demonstrating its applicability in super-resolved co-tracking beyond the FRET range. With a combined phasor-microtime gating approach, we extend the concept to dye molecules positioned at distances within the FRET range and thus close the resolution gap between single-molecule FRET and co-tracking. Altogether, these experiments exemplify how MINFLUX in combination with the fluorescence lifetime information can provide new insights into molecular interactions and dynamics occurring in the FRET range and beyond.

Results

Super-Resolved FRET in pMINFLUX

We used a DNA origami molecular balance[27] as a platform to carry out simultaneous p-MINFLUX and FRET tracking experiments (Fig. 1A). The molecular balance features a 19 nucleotides (nt) long single-stranded DNA pointer labelled at the tip with an ATTO542 molecule (FRET donor). The position of the donor was tracked via pMINFLUX using green excitation (Supplementary Fig. 1). The pointer can transiently hybridize to three single-stranded protrusions placed in a nearly equilateral triangle of ~6 nm side length, via an 8 nt complementary sequence. An additional Cy5 molecule (FRET acceptor) was placed at a fixed position in proximity to the protrusions on the DNA origami structure, (details in Supplementary Tables 2-4).

To monitor FRET, the detection was spectrally split in two channels for donor and acceptor emission. The fluorescence transients recorded for ATTO542 and Cy5 show anticorrelated fluctuations between three intensity levels which are correlated with fluctuations of the fluorescence lifetime of ATTO542 (Fig. 1B), as expected for the DNA pointer transitioning between the three positions. Calculation of the FRET efficiency from the fluorescence lifetime of ATTO542 (Fig. 1C) reveals that the donor-acceptor distances for the three pointer positions are 5.3 nm, 6.7 nm and 9.5 nm (Fig. 1D, R_0 = 7.1 nm, Supplementary Note 2).

Localization analysis of the same pMINFLUX transient shown in Fig. 1B delivers the binding positions of the donor with ~1-2 nm precision at 100 ms temporal resolution. The two-dimensional localization histogram shown in Fig. 1E confirms that the DNA pointer visited the three positions separated ~6 nm from each other, in agreement with the DNA origami design.

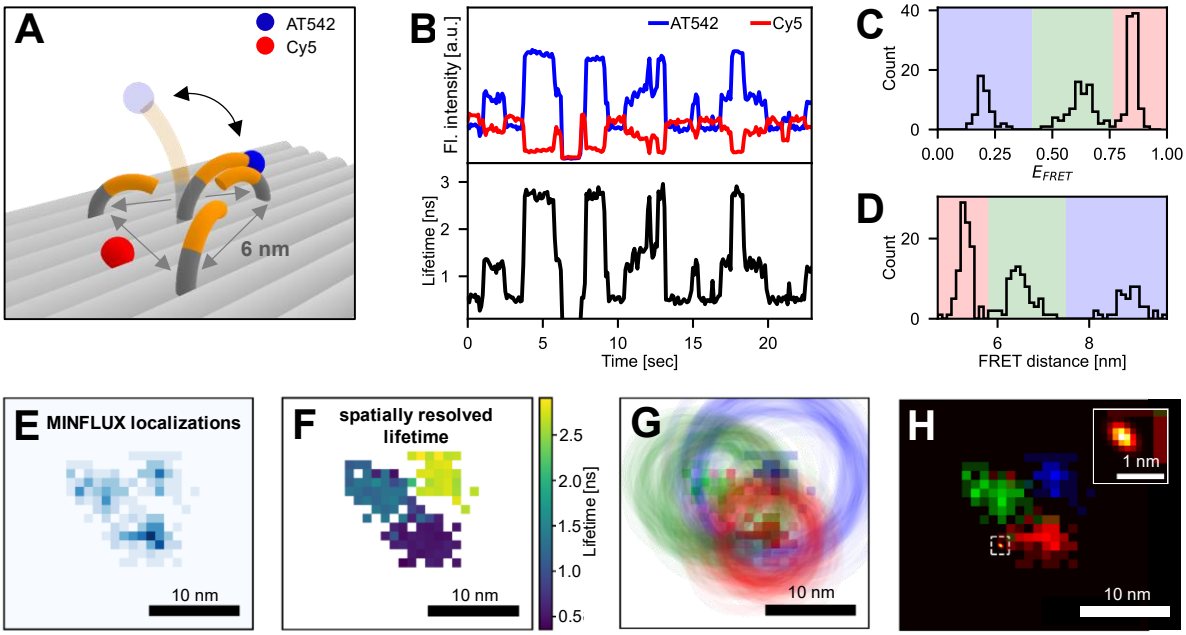

Figure 1. Super-resolved FRET in pMINFLUX. (A) Schematic of the dynamic DNA origami with three protruding strands in distances of 6 nm to each other to which an ATTO542 labelled DNA pointer transiently hybridizes. (B) Anticorrelated fluctuations in ATTO542 (blue) and Cy5 (red) fluorescence between three intensity levels which are correlated to fluctuations in the fluorescence lifetime of ATTO542, indicating transitions of the DNA pointer between three positions. (C, D) FRET efficiency and FRET distance distributions calculated from the fluorescence lifetimes of ATTO542, featuring three distinct populations highlighted in blue, green and red. (E) 2D histogram of the pMINFLUX localizations of the DNA pointer. (F) Spatially resolved fluorescence lifetimes of the ATTO542 dye on the DNA pointer. (G,H) Multilateration of the position of the Cy5 dye. By combining each MINFLUX localization of the DNA pointer (square) with a FRET distance (circle) (G), a multiplicative probability density map of the position of the Cy5 molecule is constructed (H). The inset shows a zoom-in around the area of the multilaterated Cy5 position highlighted by the dashed white box. The corresponding maximum in the probability density map has a full-width at half-maximum of only FWHM = 0.17 nm.

For synergistically combining MINFLUX with FRET, each MINFLUX localization was assigned to its corresponding fluorescence lifetime. The resulting super-resolved fluorescence lifetime image in Fig. 1F shows that the ATTO542 molecule decays with different lifetimes depending on the pointer position, confirming that both FRET and MINFLUX data describe the DNA pointer dynamics well.

Next, both methods were combined to maximize their information output. From each pMINFLUX localization, both the position of ATTO542 and its separation distance to Cy5 were determined (the latter using the fluorescence lifetime information). Then, a circle centered at the ATTO542 position with a radius of the assigned FRET distance was defined. Doing this repeatedly as the DNA pointer explores the three positions delivered three sets of circles (Fig. 1G, Supplementary Video 1). From these circles, a multiplicative probability density map for the location of Cy5 was created (Fig. 1H, Supplementary Fig. 2). This density map featured a single, very narrow peak with a full-width at half-maximum of FWHM = 0.17 nm, determining the position of the Cy5 molecule in close proximity to two of the three DNA pointer locations by multilateration.[28–31]

As such, we demonstrated the combination of pMINFLUX localizations with their intrinsic FRET information. Besides applications in multilateration approaches, this combination can generally be used to track the absolute position of a molecule with pMINFLUX while simultaneously tracking the position of a second molecule relative to the first molecule using FRET. Due to the simplicity of its experimental implementation on pMINFLUX setups, we believe that this combination has the potential to become a powerful tool when studying biological interactions. However, due to the use of FRET as an information source, the approach probes interactions occurring in distances of below ~12 nm. If molecular interactions occur with the dyes being further apart, structural information is lost. Thus, other methods that exploit the optical distinguishability of different emitters either spectrally or in the fluorescence lifetime domain are required for MINFLUX.

Fluorescence Lifetime-Multiplexing for Co-Tracking in pMINFLUX

To this end, we developed a fluorescence lifetime based multiplexing of pMINFLUX to localize more than one emitter simultaneously without photoswitching.

pMINFLUX lifetime multiplexing is based on obtaining the fluorescence intensities necessary for the position estimation from fits to the fluorescence decays corresponding to each one of the four excitation beams rather than from the conventional counting of the absolute number of photons emitted upon excitation with the four different beams (Supplementary Section 3). A first test of the suitability of this approach was done by comparing pMINFLUX localizations of single AlexaFluor647 (AF647) molecules obtained from intensity counts and from monoexponential fits. Localizations with both approaches exhibit negligible differences in AF647 position and localization precision (Supplementary Fig. 3).

Next, we set out to localize two emitters simultaneously using lifetime multiplexing. For these experiments, we designed a static DNA origami with two fluorophores, an AF647 and an ATTO647N molecule, placed in fixed positions with a nominal separation distance of 14.6 nm (Fig. 2A). AF647 and ATTO647N have similar spectral properties (see Supplementary Fig. 4), but distinct fluorescence lifetimes of 1.1 ns and 4.3 ns, respectively. Figure 2B shows a fluorescence intensity transient with two photobleaching steps recorded for a single DNA origami structure in a pMINFLUX measurement. The fluorescence lifetime decay before the first bleaching step exhibits a biexponential behavior, indicating the presence of both dyes (time window I in Fig. 2B). After the first photobleaching event, the decay shows a monoexponential profile with a fluorescence lifetime of 4.3 ns corresponding to ATTO647N (time window II in Fig. 2B).

Measurement time window I where both fluorophores were in their emissive state (Supplementary Fig. 5) was analyzed using a biexponential fit. From the fit, the fluorescence decays of AF647 and ATTO647N were extracted (Fig. 2C), to obtain their fluorescence intensities upon excitation with each one of the four beams (blue and red overlays in Fig. 2C,D). The resulting two-dimensional localization histogram features

two distinct populations describing the positions of AF647 and ATTO647N, with a separation distance of 15.0 nm in agreement with the DNA origami design (Fig. 2E).

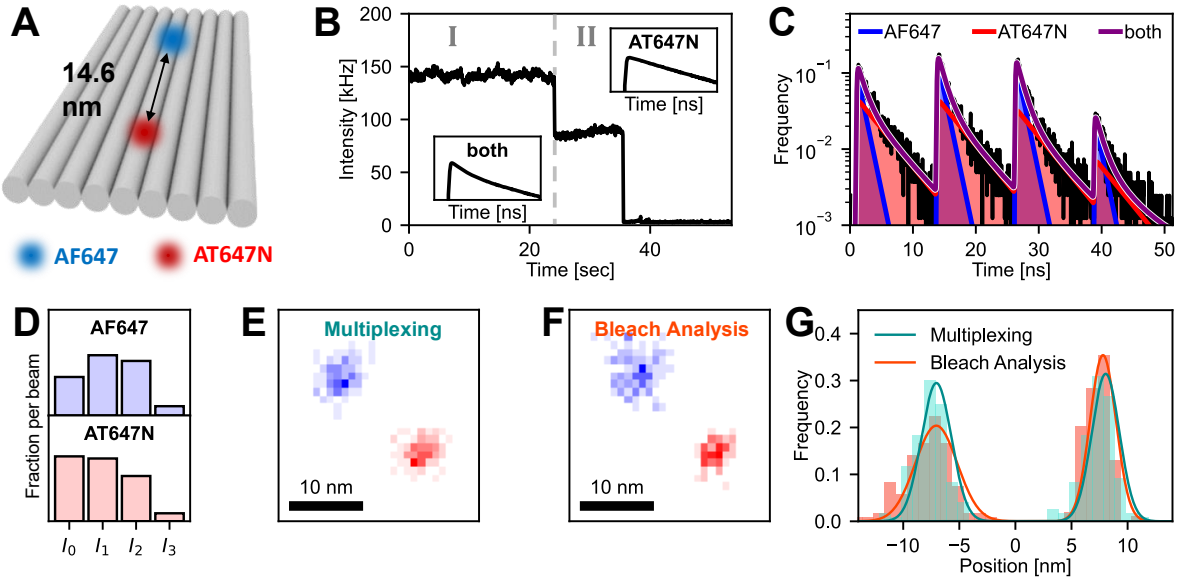

Figure 2. pMINFLUX lifetime multiplexing principle and accuracy. (A) Schematic of a static DNA origami with AF647 and ATTO647N placed in a fixed distance of ~14.6 nm from each other. (B) Fluorescence intensity transient recorded for a single DNA origami structure shown in panel A during a pMINFLUX measurement. Insets show the fluorescence lifetime decays before and after photobleaching of AF647 (dashed gray line). (C) Fluorescence microtime decays for time window I in panel B. Biexponential fitting (purple) reveals the fluorescence decay profiles of AF647 (blue) and ATTO647N (red) separately. (D) Relative fluorescence intensities recorded upon excitation from the four pulsed-interleaved beams for both dyes. The intensity values were extracted from the biexponential fit model shown in Panel C. (E) 2D histogram of the lifetime multiplexed pMINFLUX localizations recorded while both dyes simultaneously were in their fluorescent state. Localizations of AF647 and ATTO647N are shown in blue and red, respectively. (F) 2D histogram of pMINFLUX localizations of the same trace obtained by bleach analysis (see Supplementary Fig. 6). (G) Line profiles of the localizations shown in Panel E,F projected along the axis of both localizations. The two maxima found with both approaches correspond to the localizations of AF647 (left) and ATTO647N (right).

We tested the accuracy of the lifetime multiplexing by comparing its results to localizations obtained using the so-called bleach analysis. Analogous to similar approaches used in wide-field super-resolution imaging,[32–34] we performed measurements until both molecules photobleached. Then, we first localized the lasting molecule (ATTO647N) after the first photobleaching event, as shown in Fig. 2B, using the data in time window II. The position of the other molecule (AF647) was estimated by subtracting the average fluorescence intensity of ATTO647N from the fluorescence of both dyes in time window I (Fig. 2F, Supplementary Fig. 6). The resulting positions of both dyes match the positions obtained by lifetime multiplexing (Fig. 2G). In contrast to lifetime multiplexing, the bleach analysis can only be applied to static systems.

Next, we evaluated the localization precision achievable in lifetime multiplexed pMINFLUX. Using the same measurement shown in Figure 2, we varied the number of photons used for each localization. Figures 3A-F depict two-dimensional histograms of lifetime multiplexed localizations of AF647 and ATTO647N performed with photon

counts between 100 and 4000. The localization precision of both molecules follows the expected inverse dependency with $\sqrt{N}$, and with moderate photon counts of 2000 photons per emitter, both emitters were simultaneously localized with precisions better than 3 nm.

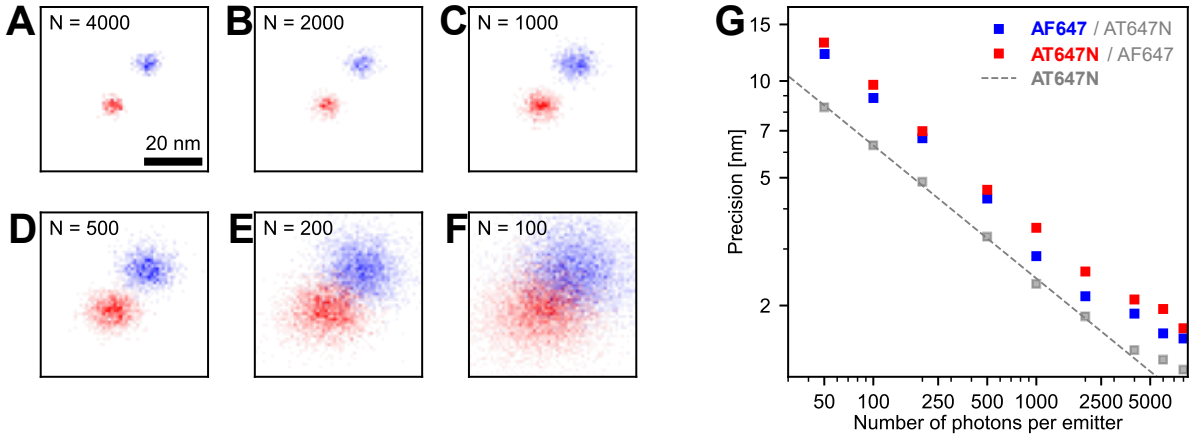

Figure 3. Evaluation of the localization precision in pMINFLUX lifetime multiplexing. (A-F) 2D histograms of the lifetime multiplexed pMINFLUX localizations of an AF647 (blue) and an ATTO647N (red) dye in a fixed distance of 14.6 nm for different number of photons per emitter, N, used to estimate their positions. (G) localization precision as a function of collected photons per emitter for both AF647 (blue) and ATTO647N (red) localized simultaneously in pMINFLUX lifetime multiplexing. The localization precision of a single ATTO647N dye at the same position as in the multiplexing localized after photobleaching of AF647 is shown in gray.

Interestingly, the multiplexed simultaneous localizations have precisions about 40% worse compared to the localization precision attained for the individual ATTO647N molecule (time window II in Fig. 2B), (Fig. 3G). These lower precisions can be attributed to uncertainties of photon assignment. To investigate this, we performed numerical simulations (Supplementary Section 8) varying the relative intensity and lifetime contrast of the two target fluorophores. We found that the brightness ratio of the emitters does not have a systematic influence on the attainable localization precision. By contrast, the localization precision reduces with lifetime contrast (Supplementary Fig. 7), which explains the reduction in localization precision observed in the experiments for the pair AF647-ATTO647N. Using the simulation framework, other suitable dye pairs for lifetime multiplexed pMINFLUX can be identified. As example, we identified and experimentally demonstrated the suitability of ATTO542 and Alexa Fluor 555 to expand the range of multiplexed pMINFLUX to the green range (Supplementary Fig. 8).

In contrast to conventional MINFLUX nanoscopy, lifetime multiplexed pMINFLUX offers the possibility to track multiple emitters simultaneously on the nanoscale. To demonstrate its potential in tracking applications, we designed a dynamic DNA origami, similar to the FRET pointer system shown Figure 1A, but in this case the structure features two DNA pointers, one labelled with AF647 and the other with ATTO647N (Fig. 4A). Each DNA pointer can transiently hybridize to two single-stranded protrusions on the DNA origami distanced ~12 nm from each other. By choosing

different lengths for the sequences complementary to the DNA pointer on the protrusions, differing kinetics for each DNA pointer system were achieved.[27]

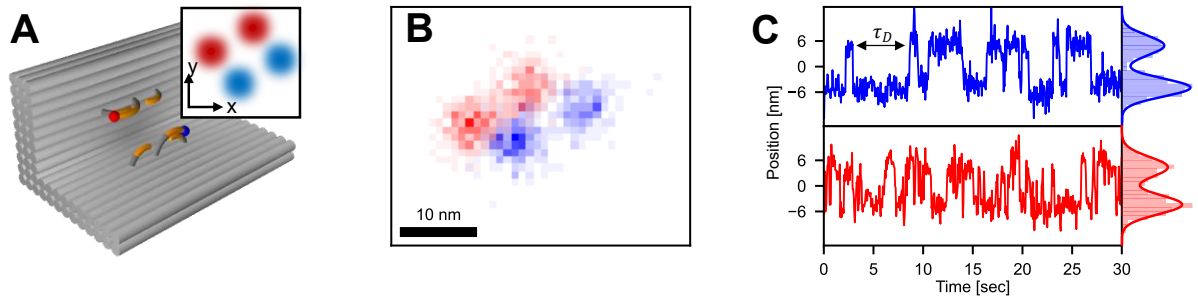

Figure 4. Simultaneous tracking using lifetime multiplexed pMINFLUX. (A) Schematic of the dynamic DNA origami with both an AF647 labelled DNA pointer (blue) and an ATTO647N labelled DNA pointer (red) which can each transiently hybridize to two protruding strands distanced ~12 nm from each other. The pointer strands have complementary sequences of 8 nt and 7 nt to the protruding strands for the AF647 and the ATTO647N pointer, respectively. The inset shows the xy-projection of the protruding strands to which AF647 (blue) and ATTO647N (red) can bind. (B) 2D histogram of the lifetime multiplexed pMINFLUX localizations of AF647 and ATTO647N, featuring each two distinct positions. (C) Localization trajectory of the AF647 (blue) and ATTO647N DNA pointer (red), revealing uncorrelated fluctuations between two positions with different kinetics for both DNA pointers. The double-headed arrow indicates one dwell time τ_D the AF647 pointer spends bound to one protruding strand.

Lifetime multiplexed pMINFLUX enabled the simultaneous tracking of both fluorophores as they jump between the two binding positions (Fig. 4B,C, Supplementary Video 2). The two-dimensional localization histogram (Fig. 4B) shows that each fluorophore explores two positions in agreement with the designed geometrical arrangement. Kinetics of the transitions between the different protrusions were extracted from spatial trajectories of the DNA pointers, separately for each dye. The AF647 DNA pointer system with complementary sequence of 8 nt with the docking site shows a mean dwell time of τ_D = 1.5 s at each protrusion, whereas the ATTO647N system with a shorter complementary sequence of 7 nt exhibited a dwell time of τ_D = 0.5 s. Due to the differing kinetics, the measurement data was re-analyzed with different temporal resolutions individually for both DNA pointers to achieve the best trade-off between temporal resolution and localization precision, separately for both systems (Supplementary Fig. 9). The flexibility of optimizing spatio-temporal resolution in post-processing is another advantage of pMINFLUX lifetime multiplexing.

pMINFLUX Lifetime Multiplexing within the FRET Range

At distances compatible with FRET, fluorophores with similar spectra such as AF647 and ATTO647N interact and cannot be considered independent from each other. Due to the mutual overlap of excitation and emission spectra of both fluorophores, FRET occurs both from AF647 to ATTO647N and vice versa. As a consequence, a detected photon cannot accurately be assigned to the excitation of a specific fluorophore, as needed for MINFLUX localizations (Fig. 5A). Instead, as the distance shortens and FRET becomes stronger, the fluorescence decay shows an increasingly

monoexponential profile (see Fig. 5B, Supplementary Fig. 10). Naturally, this affects the accuracy of the lifetime multiplexing. Monte Carlo simulations for AF647 and ATTO647N at different distances to each other show deviations from the estimated distances to the ground truth at inter-dye distances smaller than ~10 nm (see Fig. 5C).

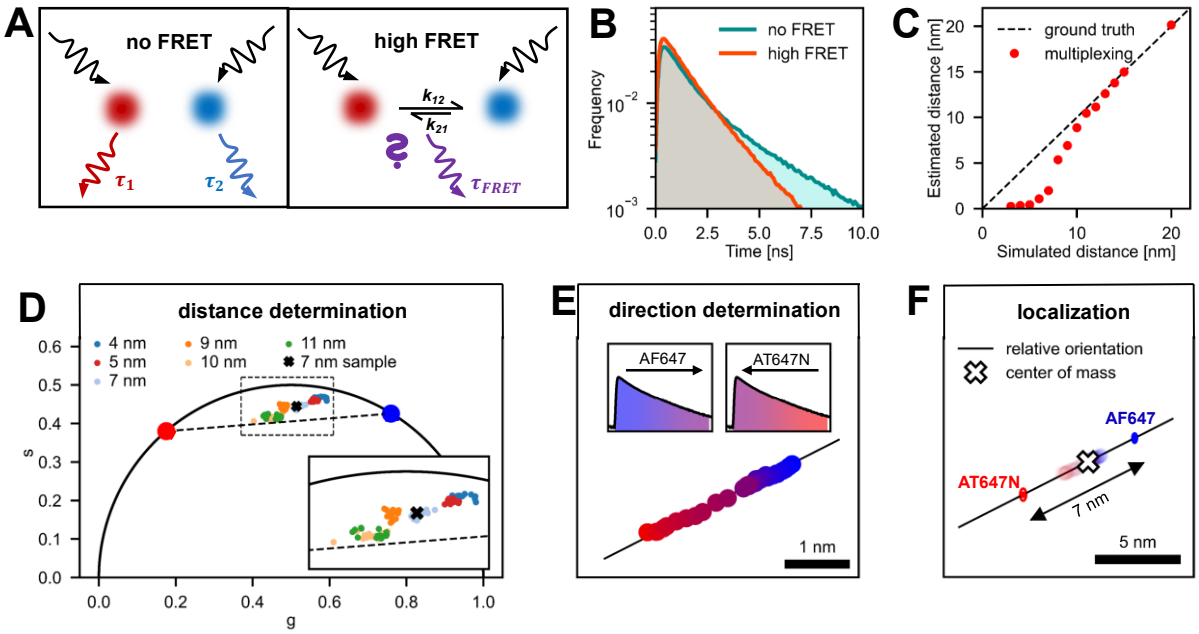

Figure 5. pMINFLUX lifetime multiplexing within the FRET range. (A) At large distances when no FRET occurs, the fluorescence of two emitters can be considered to be independent of each other. Photon absorption and emission take place at the same emitter. At small distances, the fluorescence of two emitters with similar spectral properties becomes coupled. Due to FRET in both directions (k_{12}, k_{21}), photons are not necessarily emitted from the emitter that absorbed the photon. (B) Experimental fluorescence lifetime decays measured for the combination of AF647 and ATTO647N at a distance of 14 nm (no FRET) and a distance of 4 nm (high FRET). (C) Accuracy of pMINFLUX lifetime multiplexing in the FRET range according to Monte-Carlo simulations. The dashed black line has a slope of one and indicates perfect accuracy. (D) Phasor plot of DNA origami structures with AF647 and ATTO647N placed at different distances. The red and blue dots correspond to the fluorescence of pure ATTO647N and AF647, respectively. Datapoints on the dashed black line between them indicate structures containing both dyes in distances without interactions. The inset shows a zoom-in of the area highlighted by the dashed box. The black cross corresponds to the measurement used to demonstrate the phasor/ microtime gating based localization approach in (E,F). (E) pMINFLUX microtime gating in the FRET range. By analyzing only a subset of photons selected in microtime gate windows, the direction defined by the positions of AF647 and AT647N can be determined. Increasing the size of the microtime gate from early (blue) to late detected photons (purple) after pulsed laser excitation (left inset) and from late (red) to early detected photons (right inset) yields a line of localizations along the line defined by the positions of the two target molecules (black line). The corresponding localizations are shown with a color gradient from blue to purple for microtime gates of increasing size for the early photons and from red to purple for microtime gates of increasing size for the late photons. The color code corresponds to the color gradient used to visualize the gradual expansion of the microtime gates in the insets. (F) pMINFLUX position estimation in the FRET range. Combining the distance information from the phasor plot (black arrow) with the found distance from the microtime gating (black line) and the center of mass localization of the coupled system (white cross) yields an estimation on the absolute position of AF647 and ATTO647N (blue and red ellipses).

To achieve accurate simultaneous localizations with pMINFLUX in the FRET range, we complemented the lifetime multiplexing with phasor analysis[35] and microtime-gated detection[27,36]. The idea is that, although the positions of the fluorophores cannot be determined directly, they can be deduced from their separation distance, the direction of the connecting vector and the center of mass of the two positions.

The separation distance can be obtained using the phasor approach.[35] Under this framework, emitting species with a pure monoexponential decay have a phasor lying along a so-called universal circle. As the coordinates of the phasor plot are additive, the phasor of systems of two fluorophores in which no FRET occurs lie on the line joining the individual phasors, in our case the ones of the AF647 and the ATTO647N phasor (Fig. 5D). In such systems, lifetime multiplexed pMINFLUX works well as described above. By contrast, if FRET occurs, the resulting phasor deviates from this line. In our case of mutual FRET, as the separation shortens, the coupling between the two fluorophores increases and eventually they display an increasingly monoexponential decay similar to a single emitter. In the phasor analysis this shows as a deviation from the AF647-ATTO647N lines towards the universal circle (Fig. 5D, Supplementary Section 11). Using a calibration with DNA origami structures containing AF647 and ATTO647N at different fixed distances, this deviation can be calibrated to estimate the separation distance between AF647 and ATTO647N in the FRET range (see Fig. 5D, Supplementary Fig. 11).

The direction defined by the actual positions of AF647 and ATTO647N is then determined by combining the standard pMINFLUX localization algorithm with microtime gated detection[27,36] (Fig. 5E). Due to the different fluorescence lifetimes of AF647 and ATTO647N, photons arriving shortly after each excitation pulse are predominantly due to AF647 emission, whereas photons with late microtimes are mainly emitted from ATTO647N. Thus, performing pMINFLUX using microtime gates at the beginning and at the end of each excitation window leads to inaccurate localizations at intermediate positions between the two molecules. Gradually increasing the size of the microtime gates gives a sequence of localizations along the line defined by the positions of the two target molecules.

Finally, performing a localization using all detected photons (no microtime gating) delivers the center of mass of the coupled system of both fluorophores. Combining this center of mass with the separation distance between both fluorophores as determined by phasor analysis and the direction defined by their positions extracted from the microtime gating approach yields two absolute positions for AF647 and ATTO647N (Fig. 5F), extending the applicability of our pMINFLUX lifetime multiplexing approach to the FRET range.

We additionally validated the accuracy of the phasor/microtime-gating based localization approach in the FRET range by performing Monte-Carlo simulations for systems with AF647 and ATTO647N placed at different distances. At distances above ~ 4 nm, the approach localizes both fluorophores accurately. At lower distances, high FRET values reduce the distinguishability of both fluorophores, resulting in a lower colocalization bound of about 4-5 nm (see Supplementary Fig. 10-12).

In analogy to the pMINFLUX lifetime multiplexing approach in the fluorescence lifetime domain, we propose a multiplexing approach based on differing spectral properties of emitters. By exploiting small shifts in the emission spectra of different emitters, their fluorescence responses are also separated without photoswitching, resulting in their simultaneous localization (see Supplementary Fig. 13). This alternative approach can also be applied to continuous-wave MINFLUX. With the emitter pair ATTO542-Cy3B which exhibits good photostability ideal for co-tracking, it yields localization precisions only two-fold worse compared to single emitters in simulations. While this is slightly worse than the decrease in localization precision by a factor of 1.4 experimentally observed in pMINFLUX multiplexing in the lifetime domain, it still suffices for photo-efficient tracking. In future, a redundancy achieved by combining both approaches can be used to robustly apply simultaneous multiplexing in more complex environments such as cells.

Conclusion

In conclusion, we demonstrated how the fluorescence lifetime information intrinsic to pMINFLUX measurements is synergistically used to combine MINFLUX localizations with FRET. The combination allows tracking single emitters on the nanoscale while simultaneously scanning their immediate environment for the presence of acceptor molecules, the distance to which can also be determined. Next, we established an approach to track multiple emitters simultaneously in pMINFLUX using only one excitation color by separating them based on their fluorescence lifetimes. At distances above 10 nm, the position of two emitters is estimated with nanometer precision by implementing a biexponential fluorescence lifetime fit in the pMINFLUX localization algorithm. At lower distances, a combined phasor-microtime gating approach allows their simultaneous localization.

Both the combination of pMINFLUX and FRET as well as the pMINFLUX lifetime multiplexing approach are not limited to pMINFLUX. As all developed algorithms are based solely on the microtime information of the emitters, no further instrumental effort is required. As such, both approaches have great potential to become generalized techniques for the simultaneous super-resolved tracking of two or more emitters. Their implementation should in principle be possible in any stochastic super-resolution technique with fluorescence lifetime information, such as RASTMIN,[19] confocal fluorescence-lifetime single-molecule localization microscopy[37] and wide-field fluorescence lifetime imaging.[38] Also, the principal findings are not limited to two-dimensional imaging as shown here but should be extendable to 3D super-resolution microscopy.

We additionally developed a multiplexing approach in the spectral domain which also allows the simultaneous localization of two emitters for setups operating with continuous-wave lasers. Here, the same spatial limitations as for the pMINFLUX lifetime multiplexing approach hold: FRET sets a lower limit for the resolution at ~4 nm below which photons originating from emitters become indistinguishable. An upper limit is given by the limited field of view of MINFLUX. Depending on the spatial arrangement of the excitation beams, molecules in distances of up to 100 nm can be tracked

simultaneously. Similar to all MINFLUX experiments, this field of view could be further extended by the use of single-photon avalanche detector arrays,[39] yielding the simultaneous nanometer precise localizations of multiple emitters over a large range of distances. Overall, we envision that further developing these approaches will pave the way for nanometer precise multi-color tracking experiments in living cells. The approaches could directly visualize dynamic process such as the stepping mechanism of kinesin motor proteins[20,40] or diffusion processes through nuclear pore complexes on the nanoscale,[41] giving more direct insights into dynamic processes in interplay with their environment in cell biology.

Resource availability

Lead contact

Philip Tinnefeld: Department of Chemistry and Center for NanoScience, Ludwig-Maximilians-Universität München, Butenandtstr. 5-13, 81377 München, Germany. Philip.tinnefeld@cup.uni-muenchen.de

Experimental methods and analysis

Preparation of DNA origami structures

DNA origami structures were designed using the open-source software caDNAno2[42] and assembled and purified using published protocols.[43] Positions and distances of dyes in DNA origami structures were estimated assuming a distance of 0.34 nm between the nucleotides along the DNA double helix and 2.7 nm between the centers of adjacent helices.[44,45] For the exact sequences of all unmodified and modified DNA staple strands used to fold the DNA origami structures see Supplementary Tables 2-7. DNA staple strands were purchased from Eurofins Genomics GmbH (Germany) and Integrated DNA Technologies (USA). p8064 scaffold used for the dynamic pointer origamis and p7049 used for the static two-color origamis (both derived from M13mp18 bacteriophages) were produced in house.

For DNA origami folding, 10 nM scaffold in 1xTAE (40 mM Tris, 20 mM acetic acid, 1 mM EDTA; pH 8) containing 12.5 mM/ 20 mM $MgCl_2$ (static/ dynamic origami) was mixed with a 10-fold excess of all unmodified and a 30-fold excess of all modified oligonucleotides, respectively. The mixture was heated to 65 °C and kept at this temperature for 15 min before being cooled down to 25 °C either with a temperature gradient of -1 °C min^{-1} (static origami) or with a non-linear thermal annealing ramp over 16 h[46] (dynamic origami). Folded DNA origami were purified from excessive staple strands by gel electrophoresis. All gels were ran using a 1.5% agarose gel, 1xTAE containing 12.5 mM $MgCl_2$ for 2 hours at 6 V/cm. The target band containing DNA origami was cut from the gel and DNA origami solution extracted from the band via squeezing. Samples were stored at -20 °C until further use.

Surface sample preparation for pMINFLUX measurements

As sample chambers, flow chambers consisting of a glass coverslip glued onto an objective slide with double-sided scotch tape were used. Prior to chamber assembly, coverslips were cleaned by incubation with 1% Hellmanex for 20 min followed by two 15 min washing steps with MilliQ water. After surface passivation by incubation with BSA-Biotin (0.5 mg/mL, Sigma Aldrich, USA) for 10 min, the surface was washed with 200 µL 1×PBS buffer (137 mM NaCl, 2.7 mM KCl, 10 mM Na_2HPO_4, 1.8 mM KH_2PO_4; pH 8). 150 µL neutrAvidin (0.25 mg/mL, Thermo Fisher, USA) was incubated for 10 min and then washed with 200 µL 1×PBS buffer. DNA origami solution was diluted in 1×TE buffer (10 mM Tris, 1 mM EDTA) containing 750 mM NaCl to a concentration of ~100 pM and then immobilized on the biotin-neutrAvidin surface via biotin-neutrAvidin interactions. For this, 100 µL of the DNA origami sample solution was added and incubated for 5 min. Residual unbound DNA origami was removed by washing the chambers with 150 µL 1xTE buffer containing 750 mM NaCl. Next, gold nanorods with a longitudinal LSPR peak at 900 nm (fabricated following established protocols)[47] were immobilized on the surface as fiducial markers for drift correction. Chambers were incubated with a diluted gold nanorod solution in 1xTAE containing 12.5 mM $MgCl_2$ for 2 min and flushed with 150 µL 1xTAE (12.5 mM $MgCl_2$). Directly prior to MINFLUX measurements, an oxidizing and reducing buffer system (1xTAE, 12.5 mM $MgCl_2$, 2 mM Trolox/ Troloxquinone)[48] was added in combination with an oxygen scavenging system (12 mM protocatechuic acid, 56 µM protocatechuate 3,4-dioxygenase from pseudomonas sp., 1% glycerol, 1 mM KCl, 2 mM Tris, 20 µM EDTA) to suppress blinking and photobleaching. After photostabilization chambers were sealed with picodent twinsil and measured.

pMINFLUX setup

A description of the pMINFLUX setup is given in the first pMINFLUX implementation.[16] For detailed information see Supplementary Section 1.

Data analysis

Data processing and analysis of the MINFLUX experiments was realized using custom-written Python scripts. A description of the used algorithms is given in the Supplementary Information. All Python scripts used for data analysis are available from the authors upon request.

Acknowledgments

P.T. gratefully acknowledges financial support from the Deutsche Forschungsgemeinschaft (DFG, German Research Foundation) – Project-ID 201269156 – SFB 1032 (A13), Ti329/15-1 (project number 470075523), from the Federal Ministry of Education and Research (BMBF) and the Free State of Bavaria under the Excellence Strategy of the Federal Government and the Länder through the

ONE MUNICH Project Munich Multiscale Biofabrication and by Germany's Excellence Strategy − EXC 2089/1-390776260. We thank Luna, Xaverl and Charly for their support with the measurements and data analysis and Angelika, Hildegard, Frau Steger and Herr Ehrl for lab upkeep.

Author contributions

F.C., J.Z., T.S., F.S., Fe. S. and P.T developed the concept. F.C., J.Z. and J.B. designed and prepared samples. F.C. and J.Z. performed and analyzed measurements. P.T. supervised the project. All authors have written, read and approved the final manuscript.

Declaration of interests

The authors declare no competing interests.

References

(1) Lerner, E.; Cordes, T.; Ingargiola, A.; Alhadid, Y.; Chung, S.; Michalet, X.; Weiss, S. Toward dynamic structural biology: Two decades of single-molecule Förster resonance energy transfer. *Science (New York, N.Y.)* **2018**, *359* (6373). DOI: 10.1126/science.aan1133.

(2) Robinson, A.; van Oijen, A. M. Bacterial replication, transcription and translation: mechanistic insights from single-molecule biochemical studies. *Nat Rev Microbiol* **2013**, *11* (5), 303–315. DOI: 10.1038/nrmicro2994. Published Online: Apr. 3, 2013.

(3) Stracy, M.; Uphoff, S.; Garza de Leon, F.; Kapanidis, A. N. In vivo single-molecule imaging of bacterial DNA replication, transcription, and repair. *FEBS letters* **2014**, *588* (19), 3585–3594. DOI: 10.1016/j.febslet.2014.05.026. Published Online: May. 23, 2014.

(4) Alhadid, Y.; Chung, S.; Lerner, E.; Taatjes, D. J.; Borukhov, S.; Weiss, S. Studying transcription initiation by RNA polymerase with diffusion-based single-molecule fluorescence. *Protein Science* **2017**, *26* (7), 1278–1290. DOI: 10.1002/pro.3160. Published Online: Apr. 2, 2017.

(5) Blanchard, S. C. Single-molecule observations of ribosome function. *Current Opinion in Structural Biology* **2009**, *19* (1), 103–109. DOI: 10.1016/j.sbi.2009.01.002. Published Online: Feb. 14, 2009.

(6) Munro, J. B.; Vaiana, A.; Sanbonmatsu, K. Y.; Blanchard, S. C. A new view of protein synthesis: mapping the free energy landscape of the ribosome using single-molecule FRET. *Biopolymers* **2008**, *89* (7), 565–577. DOI: 10.1002/bip.20961.

(7) Gambin, Y.; Deniz, A. A. Multicolor single-molecule FRET to explore protein folding and binding. *Molecular BioSystems* **2010**, *6* (9), 1540–1547. DOI: 10.1039/C003024D. Published Online: Jul. 2, 2010.

(8) Schuler, B.; Eaton, W. A. Protein folding studied by single-molecule FRET. *Current Opinion in Structural Biology* **2008**, *18* (1), 16–26. DOI: 10.1016/j.sbi.2007.12.003. Published Online: Jan. 24, 2008.
(9) Sasmal, D. K.; Pulido, L. E.; Kasal, S.; Huang, J. Single-molecule fluorescence resonance energy transfer in molecular biology. *Nanoscale* **2016**, *8* (48), 19928–19944. DOI: 10.1039/C6NR06794H.
(10) Weikl, T. R.; Paul, F. Conformational selection in protein binding and function. *Protein Science* **2014**, *23* (11), 1508–1518. DOI: 10.1002/pro.2539. Published Online: Sep. 6, 2014.
(11) Sako, Y.; Minoghchi, S.; Yanagida, T. Single-molecule imaging of EGFR signalling on the surface of living cells. *Nat Cell Biol* **2000**, *2* (3), 168–172. DOI: 10.1038/35004044.
(12) Winckler, P.; Lartigue, L.; Giannone, G.; Giorgi, F. de; Ichas, F.; Sibarita, J.-B.; Lounis, B.; Cognet, L. Identification and super-resolution imaging of ligand-activated receptor dimers in live cells. *Sci Rep* **2013**, *3* (1), 2387. DOI: 10.1038/srep02387.
(13) Asher, W. B.; Geggier, P.; Holsey, M. D.; Gilmore, G. T.; Pati, A. K.; Meszaros, J.; Terry, D. S.; Mathiasen, S.; Kaliszewski, M. J.; McCauley, M. D.; Govindaraju, A.; Zhou, Z.; Harikumar, K. G.; Jaqaman, K.; Miller, L. J.; Smith, A. W.; Blanchard, S. C.; Javitch, J. A. Single-molecule FRET imaging of GPCR dimers in living cells. *Nat Methods* **2021**, *18* (4), 397–405. DOI: 10.1038/s41592-021-01081-y. Published Online: Mar. 8, 2021.
(14) Mieskes, F.; Ploetz, E.; Wehnekamp, F.; Rat, V.; Lamb, D. C. Multicolor 3D Orbital Tracking. *Small* **2023**, e2204726. DOI: 10.1002/smll.202204726. Published Online: Jan. 29, 2023.
(15) Balzarotti, F.; Eilers, Y.; Gwosch, K. C.; Gynnå, A. H.; Westphal, V.; Stefani, F. D.; Elf, J.; Hell, S. W. Nanometer resolution imaging and tracking of fluorescent molecules with minimal photon fluxes. *Science (New York, N.Y.)* **2017**, *355* (6325), 606–612. DOI: 10.1126/science.aak9913. Published Online: Dec. 22, 2016.
(16) Masullo, L. A.; Steiner, F.; Zähringer, J.; Lopez, L. F.; Bohlen, J.; Richter, L.; Cole, F.; Tinnefeld, P.; Stefani, F. D. Pulsed Interleaved MINFLUX. *Nano letters* **2021**, *21* (1), 840–846. DOI: 10.1021/acs.nanolett.0c04600. Published Online: Dec. 18, 2020.
(17) Gwosch, K. C.; Pape, J. K.; Balzarotti, F.; Hoess, P.; Ellenberg, J.; Ries, J.; Hell, S. W. MINFLUX nanoscopy delivers 3D multicolor nanometer resolution in cells. *Nat Methods* **2020**, *17* (2), 217–224. DOI: 10.1038/s41592-019-0688-0. Published Online: Jan. 13, 2020.
(18) Weber, M.; Leutenegger, M.; Stoldt, S.; Jakobs, S.; Mihaila, T. S.; Butkevich, A. N.; Hell, S. W. MINSTED fluorescence localization and nanoscopy. *Nat. Photonics* **2021**, *15* (5), 361–366. DOI: 10.1038/s41566-021-00774-2. Published Online: Mar. 15, 2021.
(19) Masullo, L. A.; Szalai, A. M.; Lopez, L. F.; Pilo-Pais, M.; Acuna, G. P.; Stefani, F. D. An alternative to MINFLUX that enables nanometer resolution in a confocal microscope. *Light Sci Appl* **2022**, *11* (1), 199. DOI: 10.1038/s41377-022-00896-4. Published Online: Jun. 30, 2022.
(20) Deguchi, T.; Iwanski, M. K.; Schentarra, E.-M.; Heidebrecht, C.; Schmidt, L.; Heck, J.; Weihs, T.; Schnorrenberg, S.; Hoess, P.; Liu, S.; Chevyreva, V.; Noh, K.-M.; Kapitein, L. C.; Ries, J. *Direct observation of motor protein stepping in living cells using MINFLUX*, 2022. DOI: 10.1101/2022.07.25.500391.

(21) Eilers, Y.; Ta, H.; Gwosch, K. C.; Balzarotti, F.; Hell, S. W. MINFLUX monitors rapid molecular jumps with superior spatiotemporal resolution. *Proceedings of the National Academy of Sciences of the United States of America* **2018**, *115* (24), 6117–6122. DOI: 10.1073/pnas.1801672115. Published Online: May. 29, 2018.
(22) Ostersehlt, L. M.; Jans, D. C.; Wittek, A.; Keller-Findeisen, J.; Inamdar, K.; Sahl, S. J.; Hell, S. W.; Jakobs, S. DNA-PAINT MINFLUX nanoscopy. *Nat Methods* **2022**, *19* (9), 1072–1075. DOI: 10.1038/s41592-022-01577-1. Published Online: Sep. 1, 2022.
(23) Jonas Zähringer, Fiona Cole, Johann Bohlen, Florian Steiner, Izabela Kamińska, Philip Tinnefeld. Combining pMINFLUX, Graphene Energy Transfer and DNA-PAINT for Nanometer Precise 3D Super-Resolution Microscopy. *Light Sci Appl* **2023**, *Accepted*.
(24) Betzig, E. Proposed method for molecular optical imaging. *Opt. Lett., OL* **1995**, *20* (3), 237–239. DOI: 10.1364/OL.20.000237.
(25) Heilemann, M.; Herten, D. P.; Heintzmann, R.; Cremer, C.; Muller, C.; Tinnefeld, P.; Weston, K. D.; Wolfrum, J.; Sauer, M. High-resolution colocalization of single dye molecules by fluorescence lifetime imaging microscopy. *Analytical chemistry* **2002**, *74* (14), 3511–3517. DOI: 10.1021/ac025576g.
(26) Bückers, J.; Wildanger, D.; Vicidomini, G.; Kastrup, L.; Hell, S. W. Simultaneous multi-lifetime multi-color STED imaging for colocalization analyses. *Opt. Express, OE* **2011**, *19* (4), 3130–3143. DOI: 10.1364/OE.19.003130.
(27) Schröder, T.; Bohlen, J.; Ochmann, S. E.; Schüler, P.; Krause, S.; Lamb, D. C.; Tinnefeld, P. Shrinking gate fluorescence correlation spectroscopy yields equilibrium constants and separates photophysics from structural dynamics. *Proceedings of the National Academy of Sciences of the United States of America* **2023**, *120* (4), e2211896120. DOI: 10.1073/pnas.2211896120. Published Online: Jan. 18, 2023.
(28) Mahalingam, M.; Girgenrath, T.; Svensson, B.; Thomas, D. D.; Cornea, R. L.; Fessenden, J. D. Structural mapping of divergent regions in the type 1 ryanodine receptor using fluorescence resonance energy transfer. *Structure* **2014**, *22* (9), 1322–1332. DOI: 10.1016/j.str.2014.07.003. Published Online: Aug. 14, 2014.
(29) Svensson, B.; Oda, T.; Nitu, F. R.; Yang, Y.; Cornea, I.; Chen-Izu, Y.; Fessenden, J. D.; Bers, D. M.; Thomas, D. D.; Cornea, R. L. FRET-Based Trilateration of Probes Bound within Functional Ryanodine Receptors. *Biophysical Journal* **2014**, *107* (9), 2037–2048. DOI: 10.1016/j.bpj.2014.09.029.
(30) Muschielok, A.; Andrecka, J.; Jawhari, A.; Brückner, F.; Cramer, P.; Michaelis, J. A nano-positioning system for macromolecular structural analysis. *Nat Methods* **2008**, *5* (11), 965–971. DOI: 10.1038/nmeth.1259. Published Online: Oct. 12, 2008.
(31) Muschielok, A.; Michaelis, J. Application of the nano-positioning system to the analysis of fluorescence resonance energy transfer networks. *The journal of physical chemistry. B* **2011**, *115* (41), 11927–11937. DOI: 10.1021/jp2060377. Published Online: Sep. 23, 2011.
(32) Qu, X.; Wu, D.; Mets, L.; Scherer, N. F. Nanometer-localized multiple single-molecule fluorescence microscopy. *Proceedings of the National Academy of Sciences of the United States of America* **2004**, *101* (31), 11298–11303. DOI: 10.1073/pnas.0402155101. Published Online: Jul. 26, 2004.
(33) Ram, S.; Ward, E. S.; Ober, R. J. Beyond Rayleigh's criterion: a resolution measure with application to single-molecule microscopy. *Proceedings of the National*

Academy of Sciences of the United States of America **2006**, *103* (12), 4457–4462. DOI: 10.1073/pnas.0508047103. Published Online: Mar. 1, 2006.
(34) Gordon, M. P.; Ha, T.; Selvin, P. R. Single-molecule high-resolution imaging with photobleaching. *Proceedings of the National Academy of Sciences of the United States of America* **2004**, *101* (17), 6462–6465. DOI: 10.1073/pnas.0401638101. Published Online: Apr. 19, 2004.
(35) Digman, M. A.; Caiolfa, V. R.; Zamai, M.; Gratton, E. The phasor approach to fluorescence lifetime imaging analysis. *Biophysical Journal* **2008**, *94* (2), L14-6. DOI: 10.1529/biophysj.107.120154. Published Online: Nov. 2, 2007.
(36) Hedley, G. J.; Schröder, T.; Steiner, F.; Eder, T.; Hofmann, F. J.; Bange, S.; Laux, D.; Höger, S.; Tinnefeld, P.; Lupton, J. M.; Vogelsang, J. Picosecond time-resolved photon antibunching measures nanoscale exciton motion and the true number of chromophores. *Nat Commun* **2021**, *12* (1), 1327. DOI: 10.1038/s41467-021-21474-z. Published Online: Feb. 26, 2021.
(37) Thiele, J. C.; Helmerich, D. A.; Oleksiievets, N.; Tsukanov, R.; Butkevich, E.; Sauer, M.; Nevskyi, O.; Enderlein, J. Confocal Fluorescence-Lifetime Single-Molecule Localization Microscopy. *ACS Nano* **2020**, *14* (10), 14190–14200. DOI: 10.1021/acsnano.0c07322. Published Online: Oct. 9, 2020.
(38) Oleksiievets, N.; Thiele, J. C.; Weber, A.; Gregor, I.; Nevskyi, O.; Isbaner, S.; Tsukanov, R.; Enderlein, J. Wide-Field Fluorescence Lifetime Imaging of Single Molecules. *The journal of physical chemistry. A* **2020**, *124* (17), 3494–3500. DOI: 10.1021/acs.jpca.0c01513. Published Online: Apr. 17, 2020.
(39) Slenders, E.; Vicidomini, G. ISM-FLUX: MINFLUX with an array detector*. *bioRxiv* **2022**, 2022.04.19.488747. DOI: 10.1101/2022.04.19.488747.
(40) Carter, N. J.; Cross, R. A. Mechanics of the kinesin step. *Nature* **2005**, *435* (7040), 308–312. DOI: 10.1038/nature03528.
(41) Timney, B. L.; Raveh, B.; Mironska, R.; Trivedi, J. M.; Kim, S. J.; Russel, D.; Wente, S. R.; Sali, A.; Rout, M. P. Simple rules for passive diffusion through the nuclear pore complex. *J Cell Biol* **2016**, *215* (1), 57–76. DOI: 10.1083/jcb.201601004. Published Online: Oct. 3, 2016.
(42) Douglas, S. M.; Marblestone, A. H.; Teerapittayanon, S.; Vazquez, A.; Church, G. M.; Shih, W. M. Rapid prototyping of 3D DNA-origami shapes with caDNAno. *Nucleic acids research* **2009**, *37* (15), 5001–5006. DOI: 10.1093/nar/gkp436. Published Online: Jun. 16, 2009.
(43) Wagenbauer, K. F.; Engelhardt, F. A. S.; Stahl, E.; Hechtl, V. K.; Stömmer, P.; Seebacher, F.; Meregalli, L.; Ketterer, P.; Gerling, T.; Dietz, H. How We Make DNA Origami. *ChemBioChem* **2017**, *18* (19), 1873–1885. DOI: 10.1002/cbic.201700377. Published Online: Aug. 10, 2017.
(44) Fischer, S.; Hartl, C.; Frank, K.; Rädler, J. O.; Liedl, T.; Nickel, B. Shape and Interhelical Spacing of DNA Origami Nanostructures Studied by Small-Angle X-ray Scattering. *Nano letters* **2016**, *16* (7), 4282–4287. DOI: 10.1021/acs.nanolett.6b01335. Published Online: Jun. 8, 2016.
(45) Ke, Y.; Douglas, S. M.; Liu, M.; Sharma, J.; Cheng, A.; Leung, A.; Liu, Y.; Shih, W. M.; Yan, H. Multilayer DNA origami packed on a square lattice. *Journal of the American Chemical Society* **2009**, *131* (43), 15903–15908. DOI: 10.1021/ja906381y.
(46) Nickels, P. C.; Wünsch, B.; Holzmeister, P.; Bae, W.; Kneer, L. M.; Grohmann, D.; Tinnefeld, P.; Liedl, T. Molecular force spectroscopy with a DNA origami–based

nanoscopic force clamp. *Science (New York, N.Y.)* **2016**, *354* (6310), 305–307. DOI: 10.1126/science.aah5974.
(47) Wang, S.; Xi, W.; Cai, F.; Zhao, X.; Xu, Z.; Qian, J.; He, S. Three-photon luminescence of gold nanorods and its applications for high contrast tissue and deep in vivo brain imaging. *Theranostics* **2015**, *5* (3), 251–266. DOI: 10.7150/thno.10396. Published Online: Jan. 1, 2015.
(48) Cordes, T.; Vogelsang, J.; Tinnefeld, P. On the mechanism of Trolox as antiblinking and antibleaching reagent. *Journal of the American Chemical Society* **2009**, *131* (14), 5018–5019. DOI: 10.1021/ja809117z.

Supporting Information

Super-Resolved FRET and Co-Tracking in pMINFLUX

Fiona Cole[1,4], Jonas Zähringer[1,4], Johann Bohlen[1], Tim Schröder[1], Florian Steiner[1], Fernando Stefani[2,3] and Philip Tinnefeld[1]*

[1] Department of Chemistry and Center for NanoScience, Ludwig-Maximilians-Universität München, Butenandtstr. 5-13, 81377 München, Germany

[2] Centro de Investigaciones en Bionanociencias (CIBION), Consejo Nacional de Investigaciones Científicas y Técnicas (CONICET), Godoy Cruz 2390, C1425FQD, Ciudad Autónoma de Buenos Aires, Argentina

[3] Departamento de Física, Facultad de Ciencias Exactas y Naturales, Universidad de Buenos Aires, Güiraldes 2620, C1428EHA, Ciudad Autónoma de Buenos Aires, Argentina

[4] These authors contributed equally

* Correspondence: philip.tinnefeld@cup.uni-muenchen.de

Supplementary Section 1. pMINFLUX setup.

The pMINFLUX setup is described in the original pMINFLUX publication.[1] Depending on the excitation color, different optical elements such as filters, the vortex phase plate or polarization optics are used, however the beam path remains unchanged (see Supplementary Figure 1).

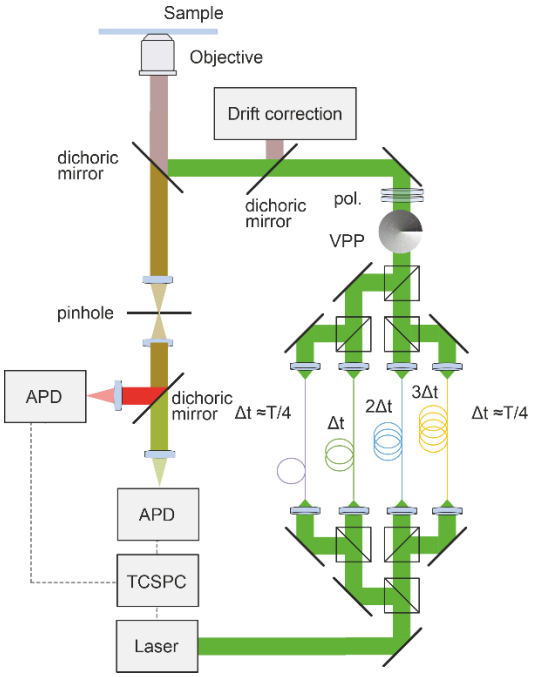

Supplementary Figure 1: pMINFLUX setup. A pulsed laser is split into four beams using beam splitters and coupled into optical fibers which delay the laser pulses as a function of the length of the fiber. The beams are recombined and doughnut-shaped beams are created with a vortex phase plate and polarization optics. The beams are focused onto the sample arranged in a triangular pattern with the fourth beam placed at the center of the triangle. For detection, APDs are used in combination with a TCSPC unit.

Excitation. A supercontinuum laser (SuperK Fianium FIU-15, NKT Photonics GmbH, Germany) is used at 19.5 MHz repetition rate as light source in combination with a tunable bandpass filter (SuperK VARIA, NKT Photonics GmbH, Germany) to select the desired wavelength range in the visible light spectrum. An additional clean-up filter (green: FLH532-10, Thorlabs GmbH, Germany, red: ZET 635/10, Chroma, USA) is used to further spectrally clean the excitation beam. Using a polarizing beam splitter cube (PBS251, Thorlabs GmbH, Germany), the light is split into two beams of orthogonal polarizations. Each of the beams is further split by a non-polarizing 50:50 beam splitter cube (BS013, Thorlabs GmbH, Germany). This beam splitting system generates two pairs of beams with each pair sharing the orthogonal linear polarization. The resulting four laser beams are coupled into polarization maintaining single-mode fibers (PM-S405-XP, Thorlabs GmbH, Germany) of lengths 2.0 m, 4.6 m, 7.1 m and 9.7 m such that the time delay between the beams after the fiber is ~12.5 ns (= T/4). The four beams are collimated after the fibers with an achromatic lens (AC254-035-A, Thorlabs GmbH, Germany) and recombined by using three 50:50 beam splitter cubes (BS013, Thorlabs GmbH, Germany). The overlay of the beams can be adjusted to

obtain the required arrangement of laser foci in the object plane. The axes of linear polarization are matched by turning the fiber out-couplers (Thorlabs GmbH, Germany). Subsequently, the linearly polarized laser beams pass a combination of a quarter- and a half-wave plate (green: WPQ05M-532 and WPH532M532, Thorlabs GmbH, Germany; red: additional linear polarizer: LPVISC100-MP2, Thorlabs GmbH, Germany, RAC 5.2.10, B. Halle, Germany, WPQ05M-633, Thorlabs GmbH, Germany) to make them circularly polarized. A vortex phase plate (green: VPP, V-532-20-1, Vortex Photonics, Germany; red: VPP, V-633-20-1, Vortex Photonics, Germany) is then used to introduce the phase modulation necessary to generate the doughnut-shaped foci. The beams are guided into the back entrance of the microscope body (IX83, Olympus Deutschland GmbH, Germany), reflected on a dichroic mirror (ZT532/640rpc flat– STED, Chroma Technology Corp., USA) and focused with an objective (UPLSAPO100XO/1.4, Olympus Deutschland GmbH, Germany) onto the sample plane.

Detection. The fluorescence light is collected with the same objective and transmitted through the dichroic mirror, focused via an Olympus tube lens onto a pinhole (120 µm, Owis, Germany), collimated with an achromatic lens (AC254-150-A, Thorlabs GmbH, Germany) and spectrally split with a dichroic mirror (640 RDC dichroic mirror, Chroma, USA). The beams then are focused with a second achromatic lens (AC127-025-A, Thorlabs GmbH, Germany) to the chip of an avalanche photodiode (SPCM-AQRH-16-TR, Excelitas Technologies GmbH & Co. KG, Germany) after filtering the remaining scattered light from the laser with suitable interference optical filters (785 SP EdgeBasic, Semrock Inc., USA, green: 582/75 Brightline HC, Semrock Inc. USA, red: 700/75 ET Bandpass, Chroma, USA). The digital signal from the APD is sent to a TCSPC unit (HydraHarp 400, PicoQuant GmbH, Germany).

Drift correction. To measure and correct for sample drift during the measurement, the IR output of the variable bandpass filter is used. A beam of wavelength between 850 and 900 nm is selected with optical filters (875/50 bandpass, Edmund Optics GmbH), coupled into a single-mode fiber (780HP, Thorlabs GmbH, Germany), outcoupled and collimated. This beam is then split with a 50:50 beam splitter cube (BS014, Thorlabs GmbH, Germany) and combined again after inserting a lens system (ACN254-040-B, AC254-150-B, Thorlabs GmbH, Germany) into one of the two paths that focuses the beam to the back focal plane of the objective (dotted line) to create a widefield illumination at the sample plane. This beam is used for xy drift correction where the position of fiducial markers is localized during the measurement. The collimated IR beam is focused onto the sample plane at an oblique angle to achieve a z position-dependent spot at the detector and use this for z drift correction. Both IR beams are coupled to the main beam path via a dichroic mirror (ZT 785 SPXXR, Chroma Technology Corp., USA) and fed into the microscope to illuminate a region close, but not overlapping with the field of view used for MINFLUX. The reflected and backscattered light is split with an additional 50:50 beam splitter cube (BS014,

Thorlabs GmbH, Germany) from the excitation IR beam and detected on a single CMOS camera (Zelux, Thorlabs GmbH, Germany) at different positions of the chip.

Setup control. The piezo stage (P733.3CD, Physik Instrumente (PI) GmbH &Co. KG, Germany) translates the sample in all three dimensions with a resolution of 0.3 nm when running in closed loop mode. All components of the setup including the piezo stage are controlled digitally and integrated via a custom version of the PyFLUX project. Further details and source-code of this control software version are available at https://github.com/zaehringer-Jonas/pyflux

Alignment. For measurement the four vortex beams were aligned in a fixed triangular excitation beam pattern (EBP), with L ≈ 100-150 nm.

Supplementary Section 2. FRET multilateration algorithm

Determination of FRET distances

The fluorescence lifetime of ATTO542 was determined via a fluorescence lifetime fit on the photons arriving at the green detection channel. The microtimes of these photons were extracted for each of the four excitation windows. They were then rebinned according to their maximal microtime bin in each excitation window and the resulting single histogram fitted with an IRF re-convoluted exponential fit. The fit model included an additional background component the weight of which was determined by a separate background measurement. By fitting each 'localization bin' in the time trace, the fluorescence lifetime of ATTO542 was extracted separately for each localization.

The FRET efficiency E_{FRET} between two molecules was then calculated from the following equation:

$$E_{FRET} = 1 - \frac{\tau_{FRET}}{\tau_0}$$

where τ_{FRET} and τ_0 are the fluorescence lifetimes of the FRET donor in presence and absence of the FRET acceptor, respectively. In the FRET pointer system, a fluorescence lifetime of τ_0 = 3.3 ns was measured for ATTO542 in absence of the Cy5 acceptor.

As the FRET efficiency between two dye molecules depends on the distance r between them with an inverse 6th-power law, it can also be described as a function of this distance.

$$E_{FRET} = \frac{1}{1 + \left(\frac{r}{R_0}\right)^6}$$

where R_0, the so-called Förster distance, defines the inter-dye distance at which 50% energy transfer occurs. For the donor-acceptor pair ATTO542/ Cy5 in the FRET pointer system, we assumed a Förster distance of R_0 = 7.06 nm.

By combining both equations, the distance between ATTO542 and Cy5 was calculated for each MINFLUX localization using the corresponding measured fluorescence lifetime τ_{FRET}.

$$r = R_0 \sqrt[6]{\frac{1}{\frac{\tau_0}{\tau_{FRET}} - 1}}$$

Multilateration of FRET acceptor position

The position of the red acceptor fluorophore in the FRET pointer measurement was multilaterated by combining each pMINFLUX localization with its respective FRET radius. For each localization of the ATTO542 donor fluorophore, a circle centered

around the localization with a radius corresponding to the FRET radius of the localization was drawn. These circles were convoluted with a Gaussian distribution with a standard deviation corresponding to the uncertainties in position and radius of the circle. The uncertainty in position of the circle center was estimated by the precision of the ATTO542 localizations. The uncertainty in radius was calculated in an error propagation of the error of the fluorescence lifetime fit. The resulting density maps describe the probability of the FRET acceptor to be found at different positions, individually for each localization.

To multilaterally localize the FRET acceptor, multiple of these density maps were combined in a multiplicative fashion. The Gauss-convoluted FRET circles of all localizations were multiplied, resulting in the multiplicative density map shown in Fig, 1H.

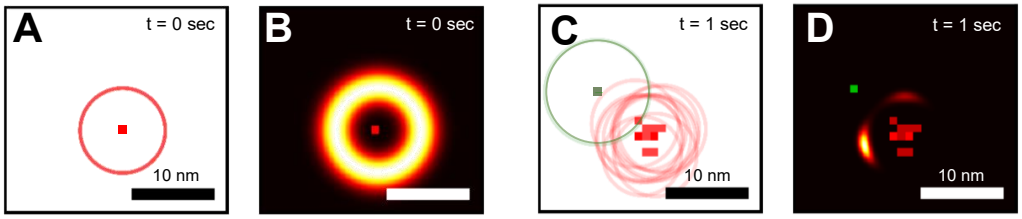

Supplementary Figure 2: Multilateration of a FRET acceptor position by pMINFLUX. By combining FRET donor (ATTO542) localizations (squares) with FRET distances (calculated through the corresponding fluorescence lifetimes of the FRET donor, circles), a probability density map for the location of the FRET acceptor (Cy5) was created. (A, C) FRET donor location and FRET distance combinations for (A) the first measurement point and (C) after 1 sec of measurement. (B,D) corresponding multiplicative probability density maps for the location of the FRET acceptor.

Supplementary Section 3. pMINFLUX lifetime multiplexing algorithm and validation with single molecules

Model fit function

The fluorescence decay of a single emitter $F(t)$ can be described by the probability density function (PDF) of an exponential distribution.

$$F(t) = \tau^{-1} \exp\left(-\frac{t}{\tau}\right) u(t)$$

where t is the emission time of a photon with respect to the preceding laser pulse, τ denotes the fluorescence lifetime of the corresponding emitter and $u(t)$ is the unit step function of t.

To correct for the instrument response function (IRF) and temporal crosstalk due to the finite repetition period T of pulsed lasers, the fluorescence decay is convolved with the IRF, and the fluorescence signal of the preceding excitation pulse added to the recorded fluorescence intensity.

$$I(t) = \sum_{i=0}^{1} F(t + iT, \tau) \star \mathrm{irf}$$

where $I(t)$ is the PDF of the measured fluorescence intensity, irf the normalized IRF and $\star$ the convolution operator.

In pMINFLUX, emitters are excited by four different, temporally delayed beam pulses per repetition period. The fit model thus is expanded to account for four beam pulses with the IRFs $\mathrm{irf_j}$.

$$I(t) = \sum_{j=0}^{3} a_j \sum_{i=0}^{1} F(t + iT, \tau) \star \mathrm{irf}_j$$

Here, a_j describes the integrated fluorescence intensity upon excitation by beam *j*. To maintain normalization of the PDF, a_j must be normalized to the accumulated integrated fluorescence intensity caused by all beams such that $\sum_j a_j = 1$.

To account for the fluorescence of multiple emitters, the fit model is expanded further to include the fluorescence decay of K emitters of different lifetimes τ_k.

$$\sum_{j=0}^{3} a_j \sum_{k=0}^{K} b_{jk} \sum_{i=0}^{1} F(t + iT, \tau_k) \star \mathrm{irf}_j$$

where b_{jk} describes the integrated fluorescence intensity of emitter k upon excitation with beam j. Similar to a_j, the ratios of b_{jk} must be normalized to the accumulated

integrated fluorescence intensity of all emitters excited by beam k such that $\sum_k b_{jk} = 1$.

Contributions from background photons are included by adding a fraction γ of background signal $\mathrm{bg}(t)$ added to the model fit function. The final model fit function thus is described by the following equation.

$$I(t) = (1-\gamma)\left[\sum_{j=0}^{3} a_j \sum_{k=0}^{K} b_{jk} \sum_{i=0}^{1} F(t+iT, \tau_k) \star \mathrm{irf}_j\right] + \gamma \cdot \mathrm{bg}(t)$$

Both $\mathrm{bg}(t)$ and the fraction γ of $\mathrm{bg}(t)$ scatter as well as the fluorescence lifetimes τ_k were determined in separate background and calibration measurements. As a result, the fit function only depends on the parameter sets a_j and b_{jk}. Due to the normalization constraints placed on the parameter sets, only a total number of $(4 \cdot K - 1)$ parameters must be fitted when describing the fluorescence of K emitters in pMINFLUX measurements.

Parameter sets a_j and b_{jk}. are retrieved separately for each localization by fitting the model fit function to the corresponding pMINFLUX TCSPC data using maximum likelihood estimation.

Multiplying the parameter sets a_j and b_{jk} then gives a set of four parameters for each emitter k which describe the relative integrated fluorescence intensities of emitter k upon excitation with laser beam pulses j. These integrated fluorescence intensities correspond to the photon counts calculated for emitter k for the four beam pulses. They thus can be used as input parameters for the MINFLUX localisation algorithm, making the simultaneous localisation of multiple emitters possible.

Supplementary Section 4. Performance of the fluorescence fitting approach for the localization of single emitters

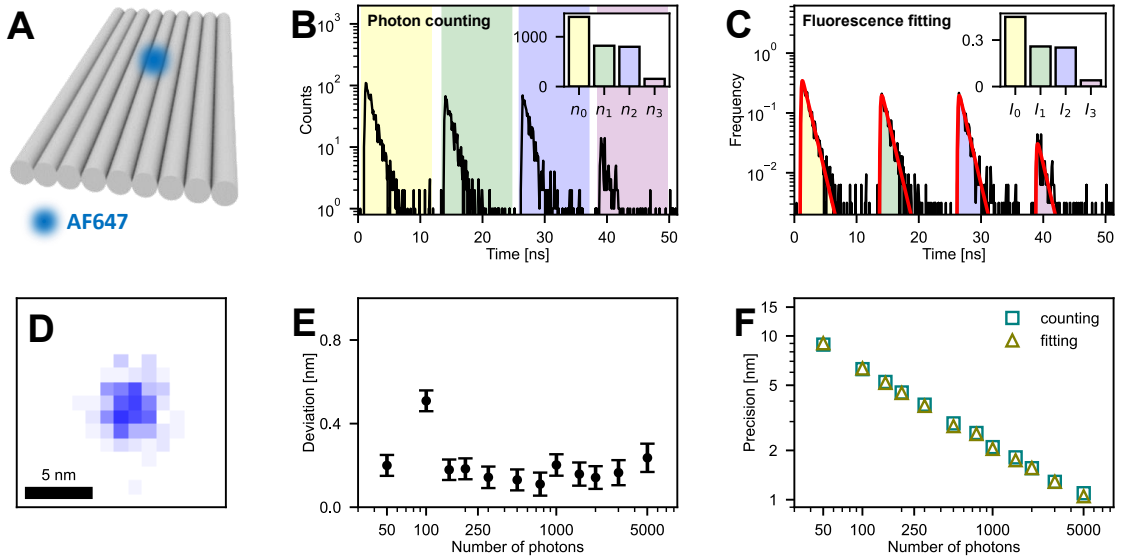

Supplementary Figure 3: Comparison of the localization of a single emitter via fluorescence fitting and photon counting. (A) Schematic of the static DNA origami carrying a single AF647 dye (τ = 1.1 ns) used in the pMINFLUX measurement to compare localizations obtained with the different approaches. (B, C) Fluorescence microtime decay of a pMINFLUX measurement of a single DNA origami as shown in (A). Colored areas mark (B) the detection microtime windows of the four different excitation beams and (C) the corresponding integrated fluorescence intensities extracted from the fitted fluorescence decay (red) used in the photon counting and the fluorescence fitting approach, respectively. The insets show (B) the photon numbers and (C) the relative fluorescence intensities upon excitation with the four different beams extracted from the pMINFLUX TCSPC data for both approaches. (D) 2D histogram of the pMINFLUX localizations of AF647 obtained by fluorescence fitting. (E) Deviation in position of localizations obtained by photon counting and fluorescence fitting as a function of the number of photons used for each localization. Deviations were calculated for the mean positions obtained from 2D Gaussian fits to 2D localization histograms as exemplarily shown in (D). (F) Localization precisions when using the fluorescence fitting and the photon counting approach as a function of the number of photons used for each localization.

Supplementary Section 5. Excitation and emission spectra of AF647 and ATTO647N

The absorption and emission spectra of AF647 and ATTO647N attached to DNA are shown in Supplementary Fig. 4. The absorption spectra of both dyes are similar, whereas the emission spectrum of ATTO647N features a small red shift compared to AF647. Both the absorption spectrum of AF647 and the emission spectrum of ATTO647N as well as the absorption spectrum of ATTO647N and the emission spectrum of AF647 have a substantial overlap.

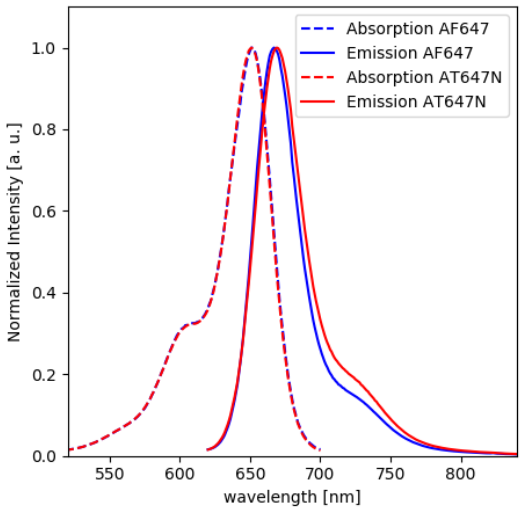

Supplementary Figure 4: Normalized absorption and emission spectra of AF647 and ATTO647N covalently bound to DNA.

Supplementary Section 6. Performance of pMINFLUX lifetime multiplexing in presence of two, one and zero emitters.

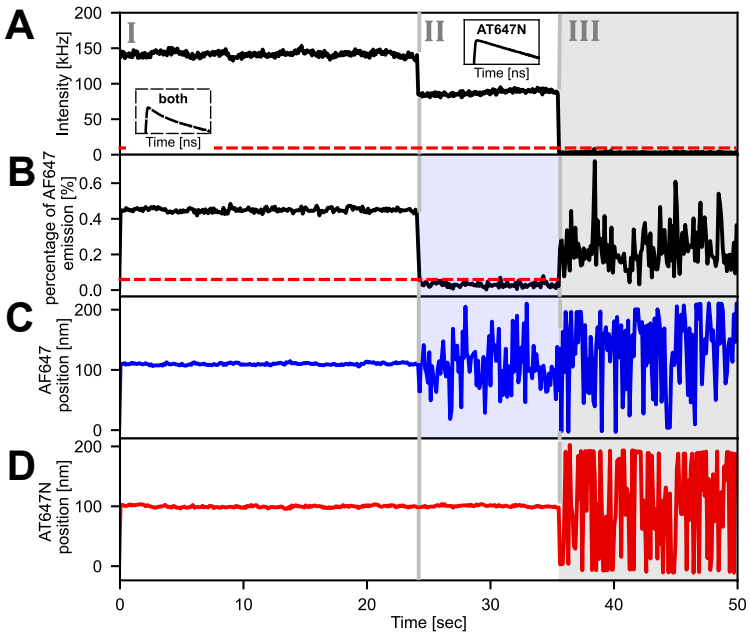

Supplementary Figure 5: pMINFLUX lifetime multiplexing in presence of two, one and zero emitters. Data analysis in this figure is based on the same measurement as in Fig. 2. (A) Fluorescence intensity transient recorded for a single DNA origami structure with AF647 and ATTO647N at a distance of 14.6 nm during a pMINFLUX measurement. Insets show the fluorescence lifetime decays before and after photobleaching of the first emitter, AF647 (first dashed gray line). Photobleaching of the second emitter, AT647N, and the subsequent drop of the fluorescence intensity to the background level is indicated by the second dashed gray line. The red line indicates a background threshold. Measurement points with a fluorescence intensity below this threshold are discarded (gray areas). (B) Percentage of AF647 emission of the total emission of both fluorophores as determined by the pMINFLUX lifetime multiplexing algorithm. In presence of both emitters, ~45% of the emitted photons are attributed to AF647 whereas the percentage drops close to zero after photobleaching of AF647. The red line indicates a percentage threshold for AF647. For measurement points with an AF647 emission percentage below this threshold, the localizations of AF647 are discarded as photobleaching of this emitter is assumed (blue areas). For AT647N, a threshold is defined analogously. (C) Position of AF647 as determined by pMINFLUX lifetime multiplexing. In presence of both emitters, AF647 is localized at a constant position. After photobleaching of AF647, its apparent localizations are distributed over the whole field of view (0-200 nm). However due to the priorly set thresholds, these false localizations are discarded. (D) Position of AT647N as determined by pMINFLUX lifetime multiplexing. Both in presence of both emitters and after photobleaching of AF647, the biexponential fitting approach of pMINFLUX lifetime multiplexing localizes AT647N at a constant position. Only after the second photobleaching step, the apparent localizations scatter. These false localizations however are discarded due to the priorly set background threshold.

Supplementary Section 7. Bleach analysis in pMINFLUX

The bleach analysis approach is based on similar concepts applied in wide-field super-resolution imaging.[2–4] Here, multiple emitters located within in a diffraction limited area are localized without photoswitching by imaging the same area multiple times. Ideally, during the imaging period the sequential photobleaching of all emitters occurs such that towards the end of the imaging period only one emitter is in its fluorescent state. This emitter can then be localized using standard procedures. For all images recorded prior to this, the fluorescence of the last emitter is then subtracted. This allows the localization of the emitter bleaching second-to-last. By again subtracting its fluorescence from all priorly recorded images, the next emitter can be localized. Repetition of this procedure eventually results in the full reconstruction of all emitter locations.

For its application in pMINFLUX, we adapted this concept to use the photon microtime information instead of recorded images. In the following, this adaption is described using the pMINFLUX measurement of AF647 and ATTO647N at a distance of 14.6 nm shown in Fig. 2 during which photobleaching of both emitters occurred (Supplementary Fig. 6A) as an example.

In a first step, we localized the emitter which photobleached last – in our case ATTO647N. For this, we applied the fluorescence fitting approach to the photon microtimes of photons detected after photobleaching of AF647 (time window II in Supplementary Fig. 6A) to extract the relative fluorescence intensities of ATTO647N upon excitation with the four different excitation beams (Supplementary Fig. 6B). We subsequently used these relative fluorescence intensities to determine the location of ATTO647N (red localization density map in Supplementary Fig. 6E) and calculated the number of photons emitted from ATTO647N by excitation with the different beams by multiplying the relative fluorescence intensities with the total number used for each localization.

We then applied the photon counting approach to the photon microtimes of photons detected while both AF647 and ATTO647N were in their fluorescent state (time window I in Supplementary Fig. 6A). The values extracted from this correspond to the number of photons emitted from both emitters upon excitation with the four different beams. To calculate the number of photons emitted from AF647 upon excitation with the different beams, we subtracted the number of photons emitted from ATTO647N as determined from time window II from the number of photons emitted from both emitters (see visualization in Supplementary Fig. 6C, Supplementary Fig. 6D). In a final step, the resulting photon numbers were used to determine the location of AF647 (blue localization density map in Supplementary Fig. 6E).

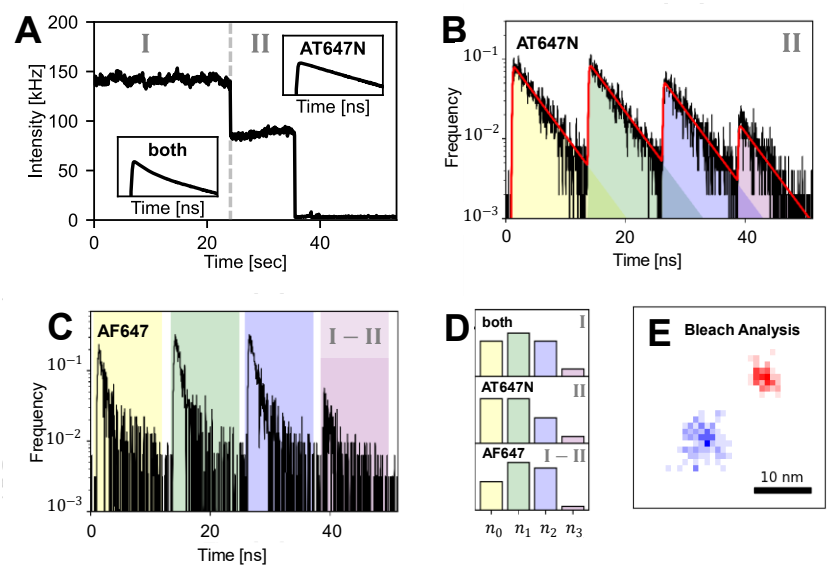

Supplementary Figure 6: Bleach analysis for the sequential localization of multiple emitters in pMINFLUX without photoswitching. The figure describes the bleach analysis used in Fig. 2 to validate the accuracy of the pMINFLUX multiplexing approach. Data analysis is based on the same measurement as in Fig. 2. (A) Fluorescence intensity transient recorded for a single DNA origami structure with AF647 and ATTO647N at a distance of 14.6 nm during a pMINFLUX measurement. Insets show the fluorescence lifetime decays before and after photobleaching of AF647 (dashed gray line). (B) Fluorescence microtime decay for ATTO647N in time window II in panel A. Colored areas mark the integrated fluorescence intensities for the different excitation beams extracted from the fluorescence fit (red line). The relative integrated fluorescence intensities then are used to localize ATTO647N. (C) Difference in the fluorescence microtime decays of time windows I and II, illustrating the sequential localization of AF647. Colored areas mark the detection microtime windows of the four different excitation beams in which the arriving photons are counted. (D) Retrieved normalized ratios of photon numbers/ fluorescence intensities of the four excitation beams for time window I (upper panel, fluorescence of both AF647 and ATTO647N), for time window II (middle panel, fluorescence of ATTO647N; used for the localization of ATTO647N) and for the difference between time windows I and II (lower panel, effective fluorescence of AF647; used for the localization of AF647). (E) 2D histogram of MINFLUX localizations obtained by bleach analysis. The localization of AF647 (blue) is less precise than the localization of ATTO647N (red) as it was not obtained directly.

Supplementary Section 8. Effect of the fluorescent properties of the emitters on the performance of the pMINFLUX lifetime multiplexing approach

To estimate the effect of the fluorescent properties of the emitters on the overall performance of the pMINFLUX lifetime multiplexing approach, we performed different numerical simulations. Here, we compared the effects both different fluorescence lifetime contrasts as well as different brightness ratios have on the attainable localization precision.

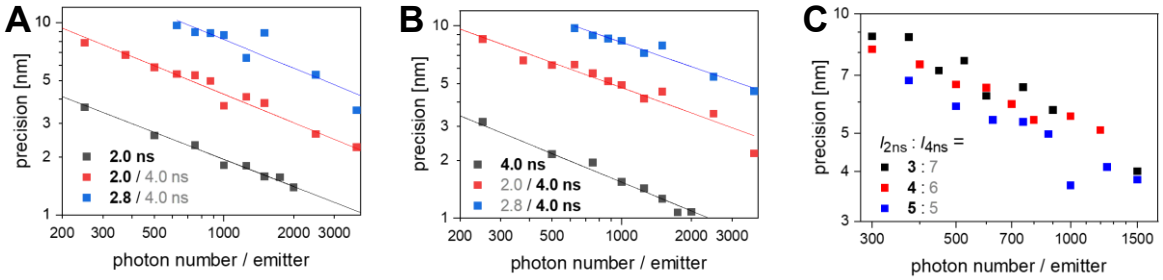

Supplementary Figure 7: Effect of fluorescence lifetime contrasts and brightness ratios of two emitters on the performance of the pMINFLUX lifetimemultiplexing approach in numerical simulations. (A,B) Localization precision as a function of the number of photons detected for the characterized emitter when simultaneously localizing two equally bright emitters of different fluorescence lifetimes by pMINFLUX lifetime multiplexing. The fluorescence lifetime of the characterized emitter is highlighted in black. For comparison, the localization precision when localizing a single emitter with the photon counting approach is given as reference. (C) localization precision of the emitter with a lifetime of τ_0 = 2.0 ns as a function of the number of detected for the emitter when simultaneously localizing two emitters (τ_1 = 4.0 ns) with different brightness ratios with pMINFLUX lifetime multiplexing. Numerical simulations were performed with a SBR of 10 and assuming a uniform background distribution.

Supplementary Section 9. pMINFLUX lifetime multiplexing in the green spectral range

In the green spectral range, we identified ATTO542 and Alexa Fluor 555 (AF555) as a suitable emitter pair for pMINFLUX lifetime multiplexing. On reference DNA origami systems, ATTO542 exhibited a fluorescence lifetime of 3.3 ns whereas AF555 showed a biexponential decay profile with fluorescence lifetimes of 0.8 ns (85%) and 2.4 ns (15%), resulting in a high overall contrast in fluorescence lifetime of the emitter pair ideal for pMINFLUX lifetime multiplexing.

To account for the biexponential nature of the fluorescence of AF555, the model fit function of the multiplexing approach (see Supplementary Section 3) was extended to incorporate the biexponential decay of AF555 with fixed relative intensities.

We evaluated the performance of the pMINFLUX lifetime multiplexing approach when using AF555 and ATTO542 as an emitter pair by placing both emitters in a distance of ~18.7 nm from each other on a static DNA origami (Supplementary Fig. 8A) and performing a pMINFLUX measurement. The recorded fluorescence intensity/ fluorescence lifetime transient of the measurement (Supplementary Fig. 8B) featured time windows in which both fluorophores were in their fluorescent state (I), only AF555 was in its fluorescent state while ATTO542 was in a non-fluorescent state (II) and only ATTO542 was in its fluorescent state while AF555 was in a non-fluorescent state (III). This allowed localizing both AF555 and ATTO542 from time windows II and III using the standard photon counting approach (Supplementary Fig. 8C).

By applying the standard photon counting approach to photons arriving in time window I during which both fluorophores were in their fluorescent state, only the intensity-weighted average localization of both fluorophores was obtained (purple localizations in Supplementary Fig. 8C). In contrast, application of the pMINFLUX lifetime multiplexing approach to photons arriving in time window I revealed two separate locations for AF555 and ATTO542 (blue and red localizations in Supplementary Fig. 8D) which coincide with the positions for both fluorophores located via photon counting in Supplementary Fig. 8C, indicating a good accuracy of the pMINFLUX lifetime multiplexing approach when using AF555 and ATTO542 as an emitter pair.

When comparing the localization precisions achieved when simultaneously localizing both emitters using pMINFLUX lifetime multiplexing to those achieved when localizing single emitters using photon counting, localizations performed using pMINFLUX lifetime multiplexing are only less than two times less precise when using AF555 and ATTO542 as an emitter pair (Supplementary Fig. 8E,F).

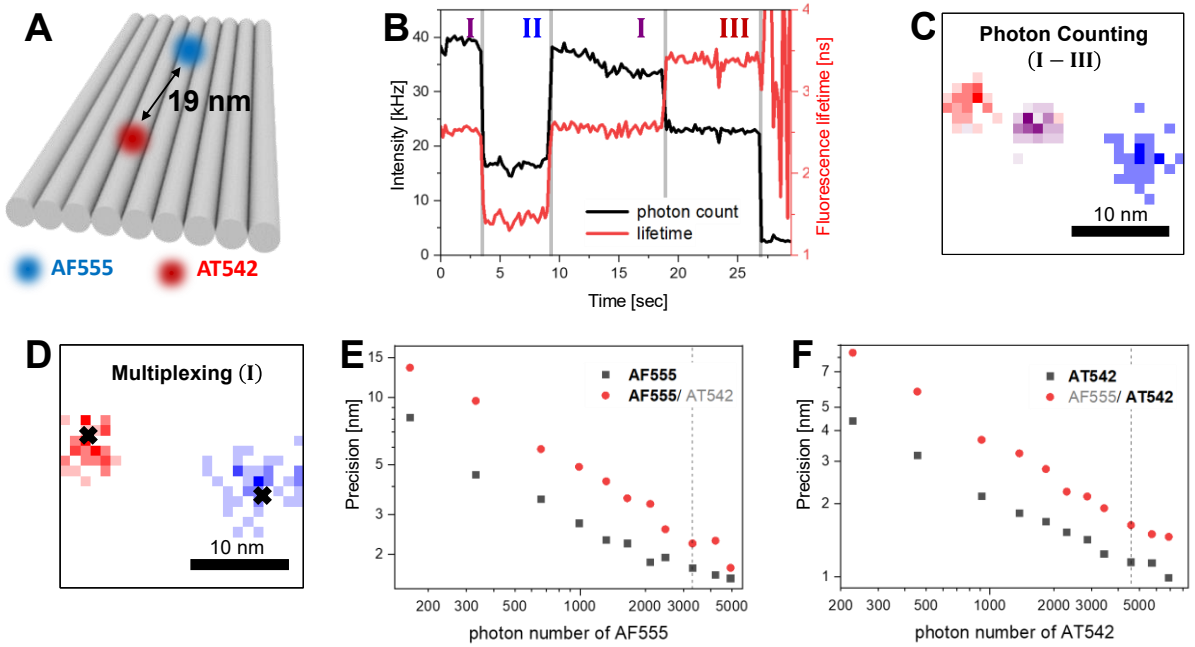

Supplementary Figure 8: pMINFLUX lifetime multiplexing in the green spectral range using AF555 and ATTO542 as an emitter pair. (A) Schematic of a static DNA origami on which both an AF555 dye and an ATTO542 dye are placed in a fixed distance of ~18.7 nm from each other. (B) Fluorescence intensity transient (black) recorded for a single DNA origami structure shown in panel A during a pMINFLUX measurement. The corresponding fluorescence lifetime transient as determined by a monoexponential fit model is shown in red. The dashed gray lines separate the transient into time windows during which both emitters (I) were in their fluorescent state and time windows during which only AF555 (II) or ATTO542 (III) were in their fluorescent state while the other emitter was in a non-fluorescent state. (C) 2D histogram of the pMINFLUX localizations in time windows I-III obtained by photon counting. Localizations of time window I corresponding to the combined fluorescence of both emitters are shown in purple, localizations of time window II corresponding to AF555 in blue and localizations of time window III corresponding to ATTO542 in red. (D) 2D histogram of the lifetime multiplexed pMINFLUX localizations in time window I. Localizations of AF555 are shown in blue, localizations of ATTO542 in red. The positions of the two emitters as determined by photon counting in panel C are indicated by black crosses. (E,F) Localization precision as a function of collected photons per emitter for both AF555 (E) and ATTO542 (F) localized simultaneously in time window I with pMINFLUX lifetime multiplexing (red). For comparison, the localization precision of the emitters localized during time windows II (E) and III (F) during which only the localized emitter was in its fluorescent state using the photon counting approach are shown in black. The dashed lines indicate the number of photons used per localization in the 2D histograms shown in panels C,D.

Supplementary Section 10. Adjustment of the temporal resolution of the separate emitters in pMINFLUX lifetime multiplexing

In pMINFLUX lifetime multiplexing, different temporal resolutions can be chosen for tracking the different emitters. If two processes with differing kinetics are studied, this allows separately optimizing the spatiotemporal resolution of both processes in a single, multiplexed measurement as demonstrated in Supplementary Fig. 9.

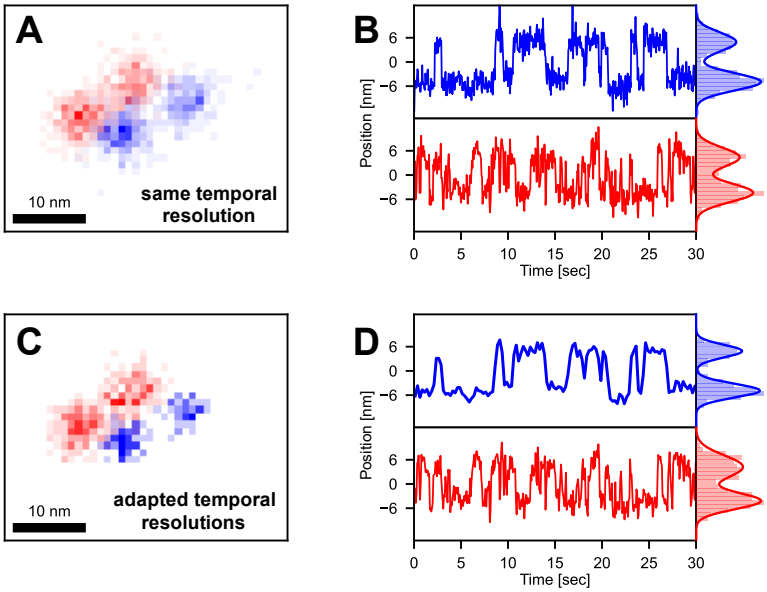

Supplementary Figure 9: Dual-color molecular scale tracking of the double pointer system using pMINFLUX lifetime multiplexing with individually adaptable temporal resolutions. (A,C) 2D histogram of the lifetime multiplexed pMINFLUX localizations of AF647 (blue) and ATTO647N (red), featuring each two distinct positions. (B,D) Localization trajectory of the AF647 (blue) and ATTO647N DNA pointer (red). In panels A and b, the temporal resolution is set to 60 ms for both colors. (C,D) The differing kinetics of the AF647 and the ATTO647N DNA pointer allows adjusting the temporal resolutions when tracking both pointer systems separately to 250 ms and 75 ms for the AF647 and the ATTO647N pointer, respectively, optimizing the spatiotemporal resolution separately for both tracked emitters.

Supplementary Section 11. Monte-Carlo simulations on pMINFLUX lifetime multiplexing in the FRET range and Distance Calibration

For pMINFLUX lifetime multiplexing, with AF647 and ATTO647N, two emitters with similar spectral properties are used. The resulting overlap in the absorption and emission spectra (see Supplementary Fig. 4) causes the occurrence of FRET, both from AF647 to ATTO647N and from ATTO647N to AF647 if the emitters are in close proximity to each other. To study the effect this has on the accuracy of the pMINFLUX lifetime multiplexing approach, we performed custom written kinetic Monte Carlo simulations simulating the fluorescence response of AF647 and ATTO647N placed at different distances from each other.

In these simulations, we assumed a gamma-shaped excitation pulse and an excitation probability p_{ex} corresponding to the extinction coefficient of each emitter. Once excited, the emitter has multiple pathways. It can return to its non-fluorescent ground state either by fluorescence, by FRET or by a non-radiative pathway in probabilities described by the rates k_f, k_{FRET} and k_{nr}, respectively.

The rates are coupled to photophysical properties such as the fluorescent lifetime τ, the quantum yield of the fluorescent state ϕ:

$$k_f = \tau_{noDNA}^{-1} \cdot \phi$$

where τ_{noDNA} is the fluorescence lifetime of the fluorophore without DNA modification. The modification with DNA only affects the non-radiative rate. The radiative rate remains the same thus can be calculated from manufacturer specifications. The non-radiative rate needs to be calculated from the experimental fluorescence lifetime with the corresponding buffer and DNA modification.

$$k_{nr} = \tau_{DNA}^{-1} - k_f$$

The FRET rate is strongly inter-dye distance r dependent as well as on the lifetime of the donor τ_D , as well as the Förster radius *R* characteristic for the dye pair:

$$k_{FRET} = \tau_D^{-1} \left(\frac{R_0}{r}\right)^6$$

As both dyes have similar spectral properties, both dyes can act as a donor hence, both FRET rates are needed.

Using the four rates for either dye (excitation, fluorescent emission, non-radiative relaxation and FRET), kinetic Monte-Carlo simulations[5] are performed for different distances. In the Monte-Carlo simulations we save where the photon is absorbed and where and when the photon is emitted. The kinetic Monte-Carlo framework is extended for pMINFLUX simulations. To this end, the excitation probability is modified according to the four vortex-beam excitation pattern and adding all four pMINFLUX excitations to one microtime window.

This framework is used to cross-check the experimental pMINFLUX lifetime multiplexing results with Monte-Carlo simulation for distances between 20 and 3 nm.

Rebinning the simulated photons according to their maximal microtime bin in each excitation window results in a single fluorescence decay (Supplementary Fig. 10A). The corresponding microtime decays show a distinct biexponential decay for large distances which becomes less distinct for smaller distances. In the simulations also the fraction of the photons absorbed and emitted by AF647 is determined (Supplementary Fig. 10B,C). As expected, the resulting fractions are strongly distance dependent and can be fitted by an adapted FRET relation:

$$E_{adapted} = E_{range} \cdot \left(1 + \left(\frac{d}{R_{50}}\right)^{6}\right)^{-1} + E_{low}$$

The fit results in $R_{50} = 7.8\,\mathrm{nm}$, $E_{range} = 19\%$ and $E_{low} = 48\%$ for the absorbed photons. This ratio is important to calculate the distance of the individual dyes to the center of mass of the MINFLUX measurement from the inter-dye distance. We then used photon packages of 2500 microtimes to calculate the phasor coordinates corresponding to the distances (Supplementary Fig. 10D,E). In simulations, the populations of AF647 and ATTO647N at distances of 10, 9, 8, 7, 6, 5 and 4 nm in the phasor plot can be easily differentiated. From of the phasor plot effective phasor coordinates can be calculated as the geometric mean of s and g.

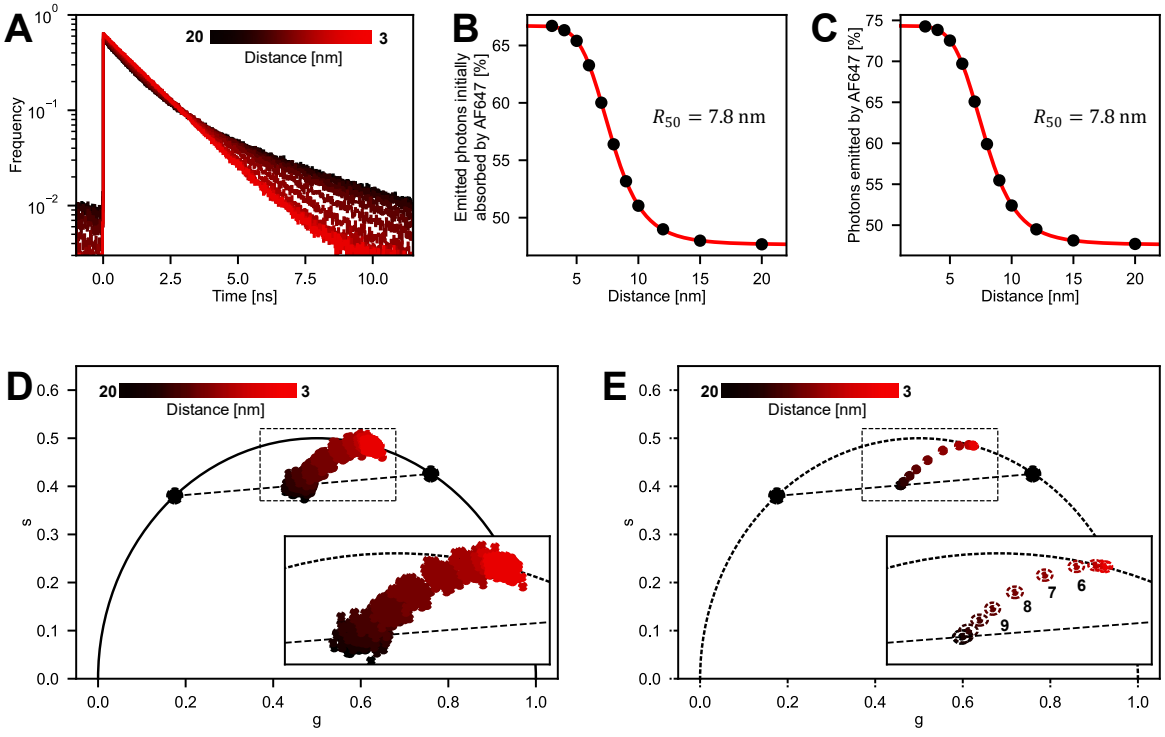

Supplementary Figure 10: Phasor approach for distance determination in the FRET range – Monte Carlo simulations. (A) Simulated fluorescence microtime decays of AF647 and ATTO647N placed at distances between 20 nm and 3 nm from each other in pMINFLUX experiments. The microtimes of the pMINFLUX simulations were extracted for each of the four excitation windows and then rebinned according to their maximal microtime bin in each excitation window, resulting in the shown single histogram (B,C) Fraction of photons absorbed (B) and emitted (C) by AF647 for different inter-fluorophore distances (black dots). Fitting with the adapted FRET equation revealed an apparent

Förster radius of $R_{50} = 7.8\,\mathrm{nm}$. (D, E) Simulated phasor plot of AF647 and ATTO647N placed at distances between 20 nm and 3 nm from each other in pMINFLUX experiments. The bold black dots correspond to the fluorescence of pure ATTO647N and AF647 (left and right dots), respectively. Datapoints on the dashed black line between them indicate inter-dye distances without interactions. The inset shows a zoom-in of the dashed box. Both a scatter plot of individual data points for all simulated distances (D) as well as a plot showing the mean phasor coordinates (dots) as well as the corresponding standard deviations (ellipses) for each simulated distance (E). The numbers in the inset of (E) correspond to the inter-dye distances in nanometer simulated for the respective data points. Simulations were carried out with a uniform background signal (overall SBR = 40) and using N = 2500 photons for calculating phasor data points in D,E.

The simulated data shows that the distance dependence of the phasor data follows the expected adapted FRET relation (Supplementary Fig. 11A). Using the same model for experimental data, also shows good agreement between fit and data. (Supplementary Fig. 11B). Thus, the fitted relation can be used as a calibration to calculate the distance out of the experimental phasor data used in Figure 4 (Supplementary Fig 11B black line).

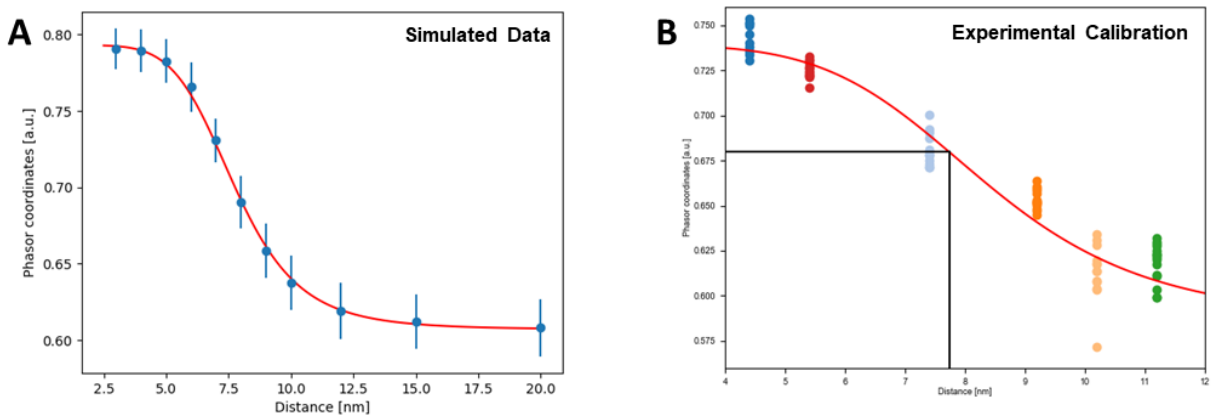

Supplementary Figure 11: Calibration curve for distance determination via the phasor approach in the FRET range. (A). The calibration curve of the simulated phasor coordinates and inter-dye distance. The red line represents the fit with the adapted FRET relation, used for calibration. (B). Color coded are the experimental phasor coordinates for samples of different inter-dye distances. The red line represents the fit with the adapted FRET relation, used for calibration. The black lines indicate the experimental measured phasor coordinate used in Figure 4 and its corresponding distance.

Microtime-Gating in pMINFLUX

For localizations in which AF647 and ATTO647N were in distances smaller than ~10 nm, we exploited the microtime information offered in pMINFLUX to determine the vector along which both fluorophores were located. In the following, the concept is illustrated using Monte Carlo simulations.

An easy approach to partially separate the fluorescence of AF647 and ATTO647N is the application of two small microtime gates, directly after each pulsed excitation beam and at the end of the corresponding microtime window. As the fluorescence lifetimes of AF647 (τ = 1.1 ns) and ATTO647N (τ = 4.3 ns) differ, the early photons can be predominantly attributed to AF647 whereas the late photons mainly are emitted from ATTO647N.

We thus performed the standard pMINFLUX localization algorithm using only photons arriving in the respective early and late microtime gates, yielding two separate localizations. We then gradually increased the length of both microtime gates in steps of 250 ps to include larger fractions of photons emitted from both fluorophores (Supplementary Fig. 12A,B). With increasing microtime gate length, the resulting localizations are displaced further towards the center of mass of both fluorophores. Fitting a linear function to the localizations of the different microtime gates revealed correctly the vector defined by the actual positions of the two fluorophores (Supplementary Fig. 12C). This vector can be used in combination with the phasor distance. However, with smaller distance FRET gets stronger, and more photons get emitted by the fluorophore with lower fluorescence lifetime. Thus, in the MINFLUX one fluorophore is weighted more, moving the center of mass towards the fluorophore with lower fluorescence lifetime. This is directly proportional to the intensity ratio of Supplementary Figure 10B, which can be used to recover the dye-center of mass distance.

By combining all three parts: the vector connecting both dyes, the previously fitted phasor distance calibration (Supplementary Figure 11A) and the dye-center of mass distance, the individual fluorophores can be localized. In simulations the localized positions are in good agreement with the true positions, thus confirming the validity of the approach.

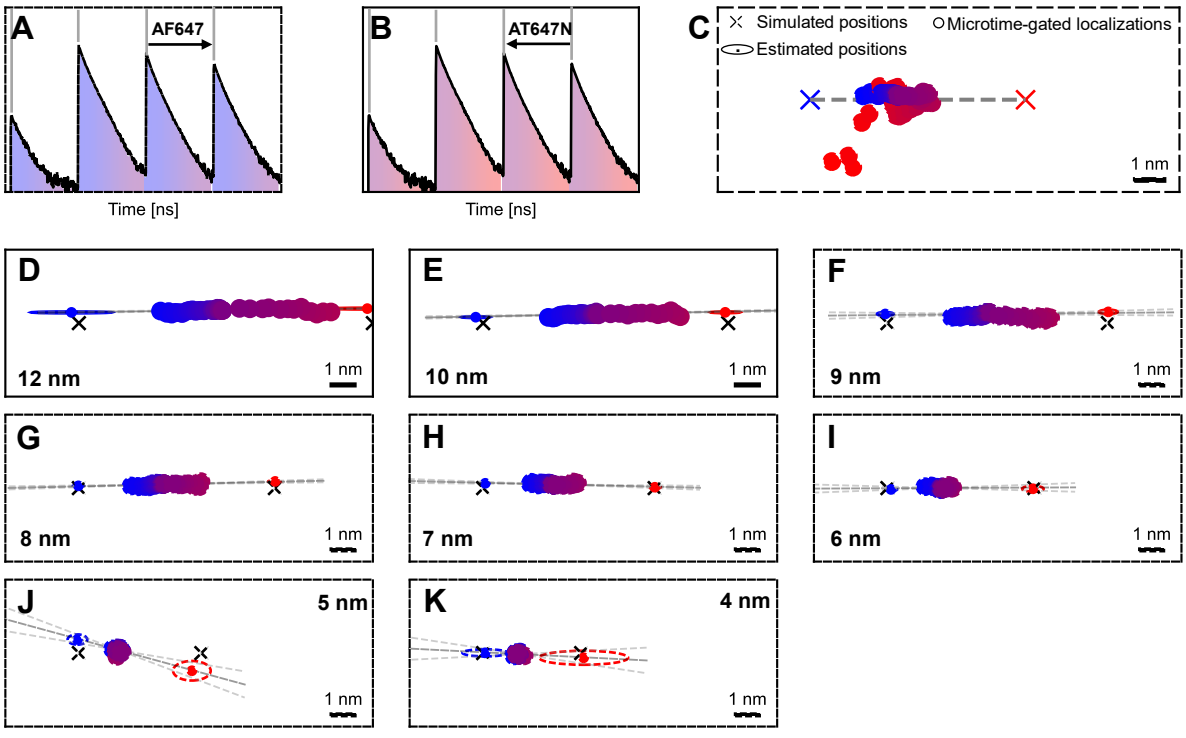

Supplementary Figure 12: Microtime-Gating in the FRET range in pMINFLUX – Monte Carlo simulations. (A, B) Simulated pMINFLUX microtime decays for AF647 and ATTO647N in a distance of 7 nm. For pMINFLUX localizations, only photons arriving in microtime gates right after each excitation pulse (A) or at the end of the corresponding microtime window (B) were considered. For determining the orientation of AF647 and ATTO647N to each other, the length of the microtime gates was gradually increased (color gradient to purple, black arrow). (C-K) Means of all localizations for the different gate lengths (circles) of the microtime decay shown in A,B (C) and AF647 and ATTO647N in distances between 12 nm and 4 nm. The color code corresponds to the different gate lengths illustrated in A,B. The large scattering in the mean localizations of late microtime gates in C (red circles) is caused by the increasingly shortened fluorescence lifetime of ATTO647N due to FRET and the resulting low number of photons/ high SBR in the late microtime gates. To circumvent this scattering, localizations performed with microtime gates filtering out more than 25% of the initial 8000 photons were discarded (D-K). The gray line indicates the fitted orientation vector. The dashed gray lines show the corresponding error margins. The blue and red dots and corresponding ellipses indicate the positions found for AF647 and AT647N with the phasor/ microtime-gating approach. Simulations were carried out with a uniform background signal (overall SBR = 40) and using N = 8000 photons for each localization. Initial microtime gate lengths were set to 0.25 ns and 3 ns for the early and the late photons, respectively. The gate lengths were increased in steps of 0.25 ns until they included the full microtime windows of the separate beam pulses. The SBR used for localizations was recalculated separately for each gate length to account for the different number of photons arriving in the different gates. For all distances, the microtimes of ~800 000 photons were simulated.

Due to the increasing indistinguishability of photons emitted from AF647 and ATTO647N due to FRET at small distances, the error of the determined vector direction; i.e. the slope of the linear fit, increases with decreasing distance (Supplementary Fig. 12D-K, Supplementary Tab. 1) The precision of the fit drops at distances of 5 nm and below, however still being accurate within 3 standard deviations.

Supplementary Table 1: Slope of the Microtime-Gating Fit corresponding to the vector along which AF647 and ATTO647N are determined to be orientated. The slope obtained from the ground truth of the simulations has a value of 0.

Distance [nm]	Slope
12	0.013 ± 0.005
10	0.019 ± 0.006
9	0.009 ± 0.019
8	0.022 ± 0.010
7	-0.02 ± 0.014
6	0.005 ± 0.03
5	-0.3 ± 0.10
4	-0.05 ± 0.10

Experimental data was analyzed accordingly.

Supplementary Section 12. Simulations on spectral multiplexing

An alternative approach to pMINFLUX multiplexing via the fluorescence lifetime utilizes the spectral information of the emitters. Here, emitters with similar absorption spectra but differences in their emission spectra are used. This allows exciting both emitters with the same excitation beam wavelength and still being able to partially separate their emission spectrally.

In spectral multiplexing, the fluorescence emission in MINFLUX experiments is spectrally split into two detection channels in each of which arriving photons are detected with an avalanche photon diode (APD0 and APD1, Supplementary Fig. 13A) using a dichroic mirror. The dichroic mirror optimally splits the fluorescence emission at a wavelength directly between the maxima in the emission spectra of the utilized emitters. This creates a contrast in the brightness with which both emitters are detected at the different APDs and allows their simultaneous localization.

In Supplementary Figure 13B the concept of spectral multiplexing is visualized using simulated pMINFLUX data of two emitters based on the fluorescent properties of ATTO542 and Cy3B which indicate that they could form a suitable emitter pair for spectral multiplexing in the green excitation range.

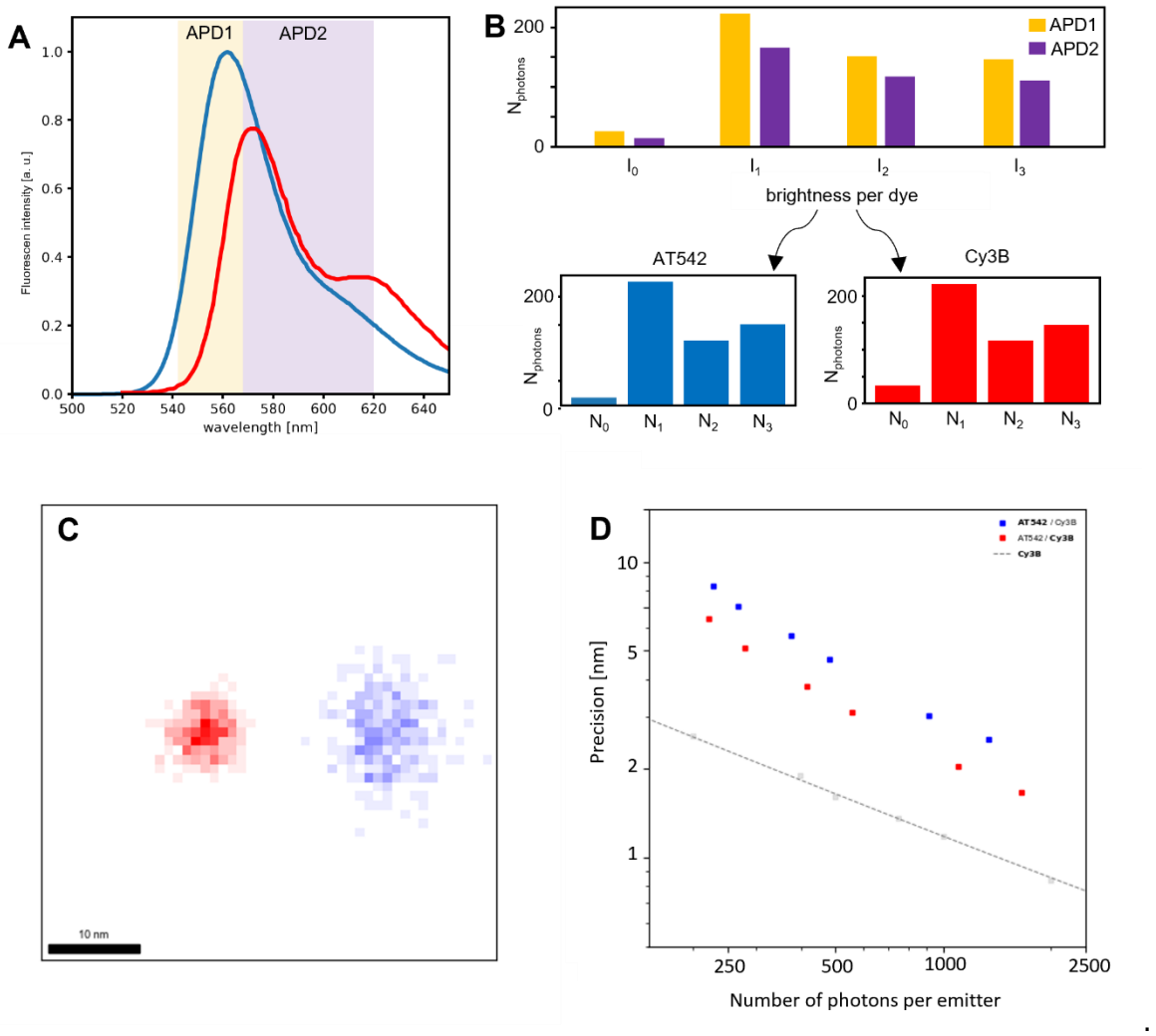

Supplementary Figure 13: MINFLUX multiplexing via Spectral Splitting. (A) Brightness normalized emission spectra of ATTO542 and Cy3b split with a dichroic mirror at 568 nm. The resulting spectral detection ranges of APD0 (yellow) and APD1 (purple) are marked. (B) Schematic of the spectral splitting workflow. For each localization, each excitation has detected photons on both APDs (yellow and purple). By knowing the brightness of each dye on each APD, the number of photons for each dye and each excitation can be extracted. (C) Simulated data of two dyes with spectral properties comparable to ATTO542 and Cy3B in a distance of 20 nm. Parameters for the simulations are 1000 localizations, with SBR = 50 and N = 2000 photons. Spectral splitting results in localizations of ATTO542 (blue) and Cy3B (blue) in a distance of 20 nm. (D) For simulations analogue to c, the precision of the spectral splitting localizations in dependence of the number of photons is comparable for both dyes (ATTO542: blue and Cy3B red). The precisions of a single dye (grey) at the same conditions outperforms the spectral splitting.

To extract the number of photons corresponding to each dye, the spectral splitting approach relies on knowing the fluorescent intensity fraction each dye has on each APD.

The total intensity on APD0 is the sum of the effective brightness of both dyes ($b_{dye,\#APD}$ with dye = 0,1 and # APD = 0,1), each multiplied with an intensity factor α_i:

$$I_{APD\,0} = \alpha_0\, b_{0,0} + \alpha_1\, b_{1,0}$$

Similar for APD1:

$$I_{APD\,1} = \alpha_0\, b_{0,1} + \alpha_1\, b_{1,1}$$

The intensity factor is dependent on the position hence for each excitation beam different, but not on the APD channel.

Our effective measurement is the intensity ratio of both APDs:

$$r = \frac{I_{APD\,0}}{I_{APD\,1}} = \frac{\alpha_0\, b_{0,0} + \alpha_1\, b_{1,0}}{\alpha_0\, b_{0,1} + \alpha_1\, b_{1,1}}$$

$$\left(\alpha_0\, b_{0,1} + \alpha_1\, b_{1,1}\right) * r = \alpha_0\, b_{0,0} + \alpha_1\, b_{1,0}$$

$$\alpha_0\left(r\ b_{0,0} - b_{0,1}\right) = \alpha_1\left(b_{1,0} - r\ b_{1,1}\right)$$

$$\frac{\alpha_0}{\alpha_1} = \frac{b_{1,0} - r\ b_{1,1}}{r\ b_{0,0} - b_{0,1}}$$

By introducing the intensity fraction of each dye in the APDs $f_0 = \frac{b_{0,0}}{b_{0,0}+b_{0,1}} = \frac{b_{0,0}}{b_0}$ and $f_1 = \frac{b_{1,0}}{b_{1,0}+b_{1,1}} = \frac{b_{1,0}}{b_1}$ it follows:

$$\frac{\alpha_0}{\alpha_1} = \frac{f_1 b_1 - r * (1-f_1) b_1}{r\, f_0 b_0 - (1-f_0) * b_0} = \frac{f_1 - r + r f_1}{r\, f_0 - 1 + f_0}\frac{b_1}{b_0}$$

$$x = \frac{\alpha_0\, b_0}{\alpha_1\, b_1} = \frac{f_1 - r + r f_1}{r\, f_0 - 1 + f_0}$$

Here x is the absolute intensity ratio between both dyes.

$$x = \frac{N_0}{N_1}$$

It follows for the total number of photons for dye 0 (N_0):

$$N_0 = N - N_1 = N - \frac{N_0}{x} = \frac{x * N}{1 + x}$$

Using N_0 and N_1, the standard maximum likelihood approach of MINFLUX can be used. Hence only the expected fraction of a dye per APD needs to be known to calculate the number of photons corresponding to each dye out of the measured intensity ratio. This enables spectral multiplexing with a minimal number of parameters.

Next, we validated the spectral splitting approach in simulations. To this end two dyes spaced in a distance of 20.0 nm are simulated. Simulations parameter are a SBR of

50, 100 bins with each 2000 photons. The spectral splitting approach localized the dyes correctly in a distance of ~19.9 nm (Supplementary Fig. 13C). To characterize this method further simulations were performed, binning the localization with different number of photons. By measuring the precision for each of those simulation, the precision in dependence of the number of photons can be characterized analogue to Figure 3G (Supplementary Fig. 13D). The precision of the spectral splitting localizations is comparable for both dyes. The precision compared to simulations of a single dye with the same conditions shows a twofold reduction of the precision at the same number of photons. Compared to pMINFLUX multiplexing with a less than 1.5-fold reduction in precision at the same number of photons, spectral multiplexing is less photon efficient. However, spectral splitting is still considerably more photon efficient compared to widefield tracking methods. This makes spectral multiplexing attractive to implement in commercial continuous-wave MINFLUX setups.

Supplementary Section 11. DNA staple strands used for folding the DNA origami structures

Supplementary Table 2. Core staples from the 5‘ to the 3’ end for the L-shaped DNA origami structure used as a platform for the dynamic pointer systems.

Staple ID	Sequence (5’ to 3’)
37[96]	CTCAAATGTTCAGAAATGGAAGTTTCACGCGCATTACTTCAACTGGCT
23[120]	AAATTATTTGGAAACAGCCATTCGAAAATCGC
26[171]	TAGTTGCCAGTTGCGGGAGGTTTTGAAGATCAATAA
29[144]	AGCATGTACGAGAACAATCCGGTATTCTAAGAACGATTTTCCAGA
35[112]	CATTATACGGTTTACCCATAACCCTCGAAATACAATGTTTAAACAGGG
16[103]	CCCCCTGCGCCCGCTTTAGCTGTTTCCTGTGT
18[167]	CAAACCCTTTAGTCTTACCAGCAGAAGATAA
1[104]	GCAGCAAGCGGTCCACAAGTGTTTTGAGGCCA
36[127]	ATTCATATCAGTGATTTGGCATCAGGACGTTGTAACATAAACCAGACG
48[159]	AGGAGGTGGCGGATAAGTATTAAGAGGCTAAATCCTCTACAGGAG
13[104]	CTAGCTGATAAATTAACAGTAGGG
49[160]	CCAGAATGGAGCCGCCAATCAAGTTTGCC
3[72]	CGTGCCTGTTCTTCGCATCCAGCGCCGGGTTA
33[52]	TGTAGCTCAACATTTACCCTCGAAAGAC
32[79]	ATCAAAAAGTCATAAAACGGAACAACATTATCAACTTTAGTAGAT
12[119]	TATTTTTGAGAGATCTGCCATATTTCCTCTACTCAATTGA
43[128]	CCGGAACCGCAAGAAAGCAATAGCTATCTTACTCACAATCCGATTGAG
49[64]	CTGAGGCCAACGGCTACAGAGGTTTCCATT
26[79]	ATAAAAATATCGCGTTCTCCTTTTGATAAGAGCTATAT
15[88]	CAAAGGGCCTGTCGTGTGGCCCTGAGAGAGTT
23[152]	ATTGCGTTTAACAACATTTCAATTACCTGAGCAAAAGGGAGAAACAGGTTTAAGAT GATGG
32[111]	AGAAACAGCTTTAGAAGGAAGAAAAATCTACGATTTTAAGCATATAAC
5[104]	GGGGTCATTGCAGGCGGGAATTGACTAAAATA
34[172]	AGGAAACCGAGGACGTAGAAAAAGTACCG
31[160]	GCCTAATTATCATATGATAAGAGATTTAGTTAATTTCAT
42[63]	GACAGATGGACCTTCATCAAGAGCCCTGAC
20[135]	TTATACTTAGCACTAAAAAGTTTGTGCCGCCA
27[56]	GTTGTACCACCCTCATAAAGGCCGGAGACAG
11[136]	GGCTTAGGTTGGGTTAAGCTAATGATTTTCGA
2[87]	GAAATTGTTATCCGCTCACATTAAATTAATGA
47[80]	CACAGACATTTCAGGGATCTCCAAAAAAAAGGTTCTTAAAGCCGCTTT
9[72]	CCAGCCAGCTTTCCGGGTAATGGGGTAACAAC
12[87]	CATTGCCTGAGAGTCTTTATGACCATAAATCATTTCATTT
30[159]	CACTCATGAAACCACCTTAAATCAAGATTGAGCGTCTTTTTGTTT
17[56]	ATGAGTGACCTGTGCAGTTTCTGCCAGCACG
5[72]	CCAGCTTACGGCTGGAAACGTGCCCGTCTCGT
16[135]	ACATTCTGAAGAGTCTCCGCCAGCAGCTCGAA
51[104]	GGAGCCTTCACCCTCAGAGCCACC
6[151]	AACGTTATTAATTTTACAACTAATCAGTTGGC

8[151]	TGATTGCTTTGAATACAAACAGAATGTTTGGA
18[135]	AAATCAACACGTGGCATCAGTATTCTCAATCC
51[136]	TTGAGTAAGCCACCCTCAGAACCG
19[120]	GTAAGAATAGTTGAAACTTTCGCAAACACCGC
26[111]	CTTAATTGAGACCGGAAACAGGTCAGGATTAGAGGTGGCA
15[56]	GTCCACTAAACGCGCGGACGGGCAACAGCTG
32[143]	AACGTCAATAGACGGGGAATACCCAAAAGAACAAGACTCCGTTTTTAT
22[135]	TTTTTTAATGCACGTACAAGTTACCCATTCAG
20[167]	CAATTCATATAGATAATAAATCCTTTGCCCG
23[56]	GTTTTCCCGTAGATGGCAGGAAGATCGCACT
14[167]	GCCGATTAAGGAAGGGCGCGTAACCACCACA
30[127]	TTTCATCGAATAATATCCAGCTACAATACTCCAGCAATTTCTTTACAG
14[103]	CGGGAAACGAAAAACCTGATGGTGGTTCCGAA
45[56]	GTCGAAATCCGCGACCTGCTCCACCAACTTTTAGCATTC
10[87]	AAATCAGCTCATTTTTGTGAGCGAATAGGTCA
21[152]	GCCGTCACAATATAAAAGAAACCACCAGAAGGAGCGGACTCGTATTACATTTGTC AAATAT
43[96]	GGCACCAAAACCAAAAGTAAGAGCAACACTATAGCAACGTAAATCGCC
24[103]	TAATAGTATTCTCCGTGCATTAAATTTTTGTT
17[152]	AACCGTTTCACACGGGAAATACCTACATTTTGACGCTAAACTATCACTTCTTTAAC AGGAG
46[172]	TTCTGAAACATGAAAGTGCCGGCCATTTG
43[160]	CCTCAGAGCACAAGAAGAAAAGTAAGCAG
49[96]	TGCGGGATAGCAGCGACGAGGCGCAGAGAAACGGCCGCGGTAACGATC
50[79]	TACCGATAGTTGCGCTTTTTCA
0[87]	ATCGGCAAAATCCCTTACGTGGACTCCAACGT
12[151]	CTTCTGACCTAAATTTGCAGAGGCCAGAACGCAATTTACG
9[136]	GCAGAGGCGAATTATTTTTCATTTGCTATTAA
0[119]	AGGCGAAAATCCTGTTGTCTATCACCCCCGAT
42[95]	AAGGGAACCGGATATTCACTCATCTTTGACCCGTAATGCCATCGGAAC
4[87]	TGTTGCCCTGCGGCTGATCAGATGCAGTGTCA
4[151]	AACAGAGGTGAGGCGGCAGACAATTAAAAGGG
15[120]	TTAGAGCTATCCTGAGGCTGGTTTCAGGGCGC
30[63]	TTAGTTTGCCTGTTTAGGTCATTTTTGCGGATAGGAAGCCGACTATTA
42[127]	CCATTACCAAGGGCGACATCTTTTCATAGGCAGAAAGAATAGGTTGAG
16[71]	CTGCGCGGCTAACTCACAATTCCACACAACATACGAGTACCGGGGCTCTGTGGG TGTTCAG
45[128]	TCGATAGCAGCACCGTAAAATCACGTTTTGCT
8[119]	GCTGCGCAACTGTTGGCAGACCTATTAGAAGG
1[136]	GTACTATGGTTGCTTTTTTAGACACGCAAATT
16[167]	TTCACCAGGTAGCAATGGCCTTGCTGGTAAT
11[104]	GTATAAGCAAATATTTTAGATAAGTAACAACG
9[104]	GGAAACCAGGCAAAGCGTACATAAGTGAGTGA
19[56]	CAAATCGTCAGCGTGGTGCCATCCCACGCAA
25[56]	TCATCAACAAGGCAAATATGTACCCCGGTTG
24[135]	GCCTGTTTGCTTCTGTTACCTTTTAACGTTAA
50[143]	TGTACTGGTAATAAGTTCAGTGCC

18[103]	CACATCCTCAGCGGTGGTATGAGCCGGGTCAC
47[112]	TAAAGTTTAGAACCGCTAATTGTATCGCGGGGTTTAAGTTTGGCCTTG
3[104]	ACAGTTGAGGATCCCCAGATAGAACTGAAAGC
21[120]	TCTTTAGGCTGAATAATGCTCATTAGTAACAT
37[128]	AAGCGCATAAATGAAACAGATATAGAAGGCTTAGCAAGCCTTATTACG
6[119]	GCAGTTGGGCGGTTGTCCAGTTATGGAAGGAG
21[88]	CGCTGGCACCACGGGAGACGCAGAAACAGCGG
27[88]	CTTTTGCGTTATTTCAATGATATTCAACCGTT
39[51]	CAACTAATGCAGACAGAGGGGCAATACTG
10[119]	TATTTTGTTAAAATTCGGGTATATATCAAAAC
36[159]	AATAAGTTAGCAAAAACGCAATAATAACGAGAATTAAAAGCCCAA
44[111]	GCACCCTCCGTCAGGTACGTTAGTAAATGAATAGTTAGCGTCAATCAT
1[72]	ATTGCCCTTCACCGCCCCAGCTGCTTGCGTTG
13[72]	TCAAATCACCATCAATACGCAAGG
2[119]	TTCGTAATCATGGTCATCCATCAGTTATAAGT
7[104]	ATCAAACTTAAATTTCTGGAAGGGCCATATCA
6[87]	AAATCCCGTAAAAAAACGTTTTTTGGACTTGT
48[127]	CCACCCTCTGTTAGGAAGGATCGTCTTTCCAGCAGACGATTATCAGCT
51[168]	GCCCCCTGGTGTATCACCGTACTC
35[80]	TGAATTACCAGTGAATGGAATTACGAGGCATATAGCGAGAGAATCCCC
41[112]	AAAGACAAATTAGCAAGTCACCAATGAAACCA
7[72]	CTCTCACGGAAAAAGAACGGATAAAAACGACG
5[136]	CTGCAACAGTGCCACGTATCTGGTAGATTAGA
22[167]	AATTACATAGATTTTCAATAACGGATTCGCC
14[135]	ACGCCAGATGACGGGGCGCCGCTAGCCCCAGC
3[136]	CAGGAAAAACGCTCATACCAGTAAATTTTTGA
27[152]	GCCAGTACGTTATAAGGCGTTAAATAAGAATAAACACAAAT
51[72]	CGTTGAAAATAGCAAGCCCAATA
4[119]	GCCGGGCGCGGTTGCGCCGCTGACCCCTTGTG
24[71]	TACAGGCATTAAATTAACCAATAGGAACGCCATCAAAGTCAATCAGAATTAGCCTAAATCG
22[103]	AAACGGCGCAAGCTTTGAAGGGCGATCGGTGC
19[88]	CCTGCAGCCATAACGGGGTGTCCAGCATCAGC
20[71]	GAAACAACGCGGTCGCCGCACAGGCGGCCTTTAGTGACTTTCTCCACGTACAGACGCCAGG
49[128]	ATATTCACCGCCAGCATTGACAGGCAAAATCA
2[151]	ATCCAGAACAATATTAGTCCATCAGGAACGGT
10[151]	CATAGGTCTGAGAGACAAATCGTCGAATTACC
24[167]	ATAAACAATCCCTTAGTGAATTTATCAAAAT
15[152]	GCGAGAAAAGGGATGACGAGCACGTATAACGTGCTTTTCACGCTGAAGAAAGC
17[120]	CCGAGTAAGCCAACAGGGGTACCGCATTGCAA
26[143]	TACCAGTAACGCTAACAGTTGCTATTTTGCACCCCATCCT
50[111]	TGCTTTCGAGGTGAATCTCCAAAA
19[152]	ATGGCTACAATCAACTGAGAGCCAGCAGCAAATGAAAAACGAACCTAATGCGCTTGGCAGA
47[144]	CAGTACCATTAGTACCCAGTGCCCGTATAAATTGATGAATTAAAG
37[160]	CCCTGAACAAATAAGAAACGCGAGGCGTT

7[136]	TATCATTTTGCGGAACATCCTGATATAAAGAA
48[63]	GGAACCCAAAACTACAAACAGTTTCAGCG
27[120]	CCAACATGACGCTCAATGCCGGAGGAAATACC
36[63]	GAGAAACATTTAATTTTACAGGTAGAAAG
35[144]	CAGTATGTTTATTTTGCGAAGCCCTTTTTAATTGAGTTCTGAACA
18[71]	AGAACGTTAACGGCGTAATGGGTAAAGGTTTCTTTGCGTCGGTGGTGCTGGTCTTGCCGTT
41[144]	GGAGGGAAGAGCCAGCAATCAGTAGCGACAGACCAGAACCGCCTC
51[51]	TGCGAATAATAATCGACAATGTTCGGTCG
21[56]	CCGGCAAATCGGCGAAGTGGTGAAGGGATAG
20[103]	TGGAGCCGGCCTCCGGGTACATCGACATAAAA
31[128]	TCTTACCATAAAGCCATAATTTAGAATGGTTTAGGGTAGC
8[87]	GGGCCTCTTCGCTATTACGTTGTACCTCACCG
31[96]	AGCGAACCAGAAGCCTGGAGAATCACAAAGGCTATCAGGT
36[95]	TGCTCATTCTTATGCGTTAATAAAACGAACTATATTCATTGGCTTTTG
37[64]	CGGAATCTCAGGTCTGTTTTAAATATGCATGCGAACGAATCATTG
23[88]	GCCAGTGCGATTGACCCACCGCTTCTGGTGCC
25[152]	TTAATTTCATGTTCTATAACTATATGTAAATGCTGATGTCAATAGAATCCTTGACAAAATT
48[95]	ACCCTCATGCCCTCATTTTCTGTATGGGATTTAGTTAAAGCAGCTTGA
30[95]	AGTTGATTAGCTGAAAAGAGTACCTTTAATTGTTAATTCGGACCATAA
17[88]	CGCTCACTATCAGACGGTCCGTGAGCCTCCTC
29[112]	ACAAGAAATAGGAATCCCAATAGCAAGCAAATATAGCAGCATCCTGAA
13[136]	GACCGTGTGATAAATACAAATTCT
41[80]	ACAAGAACCGAACTGATGTTACTTAGCCGGAAAAGACAGCACTACGAA
14[71]	ATCGGCCTTAAAGAATAAATCAAAAGAATAGCCCGAGACCAGTGAGGGAGAGGGGTGCCTA
38[111]	ACGATAAACCTAAAACAAAGAATACACTAAAACATTACCCAACAAAGC
42[159]	GGAATTAGGTAAATTTTCGGTCATAGCCCCACCGGAACCACCACC
29[80]	GGGGCGCGCCCAATTCACTAAAGTACGGTGTCACGAGAATAGCTTCAA
31[64]	TTCAAATTTTTAGAAAAAACAGGAGCAAACAAGAGAATCGATGAAGGGTGAGATATTTTA
38[143]	TAATAAGAAGAGCCACCCTTATTAGCGTTTGCCATTCAACAATAGAAA
25[120]	ATAACCTTATCAACAAAAATTGTATAACCTCC
25[88]	CCGTCGGAGTAGCATTCAAAAACAGGAAGATT
38[79]	CAAAAGAATAAAATACCCAGCGATTATACCAAGCGCGAA
44[79]	GAGGGTAGTTGCAGGGTGCTAAACAACTTTCACGCCTGGAAAGAG
22[71]	CGTTGGTAGTCACGACGCCAGCTGGCGAAAGGGGGATATCGGCCTGCGCATCGGCCAGCTT
40[172]	TTTTCATCGGCATATTGACGGCACCACGG
0[151]	CCCGCCGCGCTTAATGAAAGCCGGCGAACGTG
44[143]	AGAGCCGCAAACAAATGAGACTCCTCAAGAGATTAGCGGGCAGTAGCA
11[72]	ATAATCAGAAAAGCCCAACATCCACTGTAATA
43[64]	AAACGGGGTTTTGCTACATAACGCCAAAAAAGGCTTGTAATCTTG
3[25]	TTTTCGGGCCGTTTTCACGG
41[36]	TTTTGGCGCATAGGCTGGCTAACGGTGTTAAATTGT
45[173]	TTTCGACTTGATCGAGAGGGTTGATATAAGTATTTT
45[31]	TTTTTATCATCGCCTGAACAGACCATTTT

35[36]	TTTTATTGGGCTTGAGATGGCCAGAACGATT
18[192]	TTTTACCTTGCTGAACCAGG
19[179]	CTGATAGCCCTAAAACTTTT
20[192]	TTTTTTCCTGATTATCACGT
22[192]	TTTTAAACATCAAGAAAAAA
4[178]	CCGAATCTAAAGCATCTTTT
38[192]	TTTTGCTAATATCAGAGAGATAACCCCGCCACCGCG
28[187]	TTTTCCCGACTTACAAAATAAACAGTTTT
8[178]	TCGAAGATGATGAAACTTTT
20[44]	CATGTTTACCAGTCCCTTTT
15[176]	GAAAGGAGCGGGCGCTAGGTTTT
11[25]	TTTTTTTTTTTTAAAACTAG
43[36]	TTTTCTTTTTCACAACGGAGATTTGTTTT
0[178]	CGGCCTCGTTAGAATCTTTT
32[192]	TTTTCCATATTATTTATCCCAATCCAAAGTCAGAGA
13[25]	TTTTGTGTAGGTAAAGATTC
44[192]	TTTTCCCTCAGAGCCACCACCCTCAGAAAGCGCTTA
8[198]	TTTTAACAGTACCTTTTACA
0[198]	TTTTGCGCTGGCAAGTGTAG
39[173]	ATACGCAAAGAAAATTATTCATTAAAGGTGAATTTT
10[198]	TTTTGATTAAGACGCTGAGA
14[192]	TTTTAGAGCGGGAGCTAGAT
23[179]	CAGATGAATATACAGTTTTT
14[44]	TTTGCGTATTGGGCGCTTTT
40[187]	TTTTACTGTAGCCTCAGAACCGCCATTTT
36[192]	TTTTCATATAAAAGAAAGCCGAACATTTT
7[45]	AGATGAAGGGTAAAGTTTTT
33[31]	TTTTATTGCTGAATATAATACATTTTTTT
27[28]	TTTTGCCTCAGAGCATAAAGAAAATTAAGCAATAAATTTT
2[178]	CTCCAATCGTCTGAAATTTT
34[50]	ATTATAGCGTCGTAATAGTAAAATGTTTTTT
18[44]	TCAGCAGCAACCGCAATTTT
32[47]	TAGTCAGAAGCAAAGCGGATTTT
10[178]	AGAGCAAATCCTGTCCAGATACCGACAAAAGGTAATTTT
2[198]	TTTTTGCCTGAGTAGAAGAA
37[36]	TTTTTAGACTGGCATCAGTTGAGATTTTTT
17[31]	TTTTGTGTAAAGCCTGGCGG
7[25]	TTTTGGAATTTGTGAGAGAT
42[192]	TTTTTTATCACCGTCACAGCGTCAGTTTT
49[36]	TTTTACGCATAATGAGAATAGAAAGTTTT
29[36]	TTTTCGCAAATGGTCAATAAACCATTAGATGC
12[200]	TTTTAGAACGCGAGAAAACTTT
17[179]	TAGTAATAACATCACTTTTT
21[179]	ATTTAGAAGTATTAGATTTT
9[25]	TTTTTTGAGGGGACGACGAC
11[45]	CATAATAATTCGCGTCTTTT

13[45]	AAAACGGTAATCGTTTTTTT
46[50]	GAGCCGATATAACAACAACCATCGCCCTTTTTTT
16[44]	TGCGGCCAGAATGCGGTTTT
5[25]	TTTTGAATGCCAACGGCAGC
48[192]	TTTTTAGCCCGGAATAGCCTATTTCTTTT
31[25]	TTTTTTGCATCAAAAGCCTGAGTAATTTT
26[47]	AATGCAATAGATTAAGGGCTTAGAGCTTATTTT
22[44]	CCGTGCATCTGCCAGTTTTT
25[179]	ACATAGCGATAGCTTATTTT
21[31]	TTTTTAAACGATGCTGATGG
15[31]	TTTTTTGTTCCAGTTTGGAACAAGA
50[192]	TTTTACCGTTCCAGTAAGCGTCATACATGGCTTCAGTTAAT
5[45]	ACCTCGTCATAAACATTTTT
12[178]	TTCCGGAATCATAATTTTTT
47[36]	TTTTGTTTCGTCACCAGTACTGTACCGTAAT
9[45]	AGTGTGCTGCAAGGCGTTTT
4[198]	TTTTATCGCCATTAAAAATA
46[187]	TTTTGGAACCTAAGTCTCTGAATTTTTTTTTT
3[45]	TCACCGGAAGCATAAATTTT
1[45]	TTCATAGGGTTGAGTGTTTT
33[173]	TTAATTAAACCATACATACATAAAGGTGGCAATTTT
26[192]	TTTTACTAGAAAAAGCCTGTT
1[25]	TTTTCAGGGTGGTTTTTCTT
23[31]	TTTTATTAAGTTGGGTACGC
16[192]	TTTTTGGATTATTTACAGAA
25[31]	TTTTTGGCCTTCCTGTATAA
12[171]	ATATATATAAAGCGACGACATCGGCTGTCTTTCCTTATCATTTTT
39[31]	TTTTTTAGGAATACCACAGTAGTAATTTT
51[31]	TTTTGAACAACTAAAGGAACACTGATTTT
24[195]	TTTTAGTAATTCAATCGCAAGACAATTTT
30[192]	TTTTTCCAAGAACGGGTGCGAACCTTTTT
19[31]	TTTTCCCTTACACTGGTTGC
40[55]	ACAAAGTATGAGGAAGCTTTGAGGACTAAAGATTTT
34[187]	TTTTAAGTTACCAGGGTAATTGAGCTTTT
6[178]	ACAAATTATCATCATATTTT
6[198]	TTTTCTTTACAAACAATTCG

Supplementary Table 3. Biotinylated staples for surface-immobilization of the L-shaped DNA origami structure.

Sequence (5‘ to 3‘)	Function
biotin-TACCAGTAACGCTAACAGTTGCTATTTTGCACCCCATCCT	immobilization

biotin-AGAGCCGCAAACAAATGAGACTCCTCAAGAGATTAGCGGG CAGTAGCA	immobilization
biotin-GAGGGTAGTTGCAGGGTGCTAAACAACTTTCACGCCTG GAAAGAG	immobilization
biotin-ATAAAAATATCGCGTTCTCCTTTTGATAAGAGCTATAT	immobilization

Supplementary Table 4. Staples for introducing the dynamic FRET pointer system with three protrusions in distances of 6 nm to each other to the L-shaped DNA origami structure.

Sequence (5‘ to 3‘)	Function
GGCACCAAAACCAAAAGTAAGAGCAACACTATAGCAACGTAAATCGCC TTTTTTTTTCGGGCATTTA-**ATTO542**	Pointer-ATTO542 at 3’
AGAAACAGCTTTAGAAGGAAGAAAAATCTACGA TTTTA-Cy5	Cy5 FRET acceptor
AACGAATCATTGTGAATTACCTTTTTTAAATGCC	Protrusion 1
GGCACCAAAACCAAAAGTAAGAGCAACACTATAGCA ACTTTTAAATGC	Protrusion 2
AGCGTCAATCATAAGGGAACCGGTTTTAAATGCC	Protrusion 3
GCACCCTCCGTCAGGTACGTTAGTAAATGAATAGTT	Exchange staple
TGCTCATTCAGTGAATGGAATTACGAGGCATATAGCG AGAGAATCCCC	Exchange staple
ATATTCACTCATCTTTGACCCGTAATGCCATCGGAAC	Exchange staple
ATATTCACCGCCAGCATCGATAGCAGCACCGTAAAAT CACGTTTTGCT	Exchange staple
CGGAATCTCAGGTCTGTTTTAAATATGCATGCG	Exchange staple
GTAAATCGCCAAAGACAAATTA	Exchange staple
GCAAGTCACCAATGAAACCATTGACAGGCAAAATCA	Exchange staple
ATGCGTTAATAAAACGAACTATATTCATTGGCTTTTG	Exchange staple

Supplementary Table 5. Staples for introducing the dynamic double pointer system with each two protrusions in a distance of ~12 nm to each other to the L-shaped DNA origami structure.

Sequence (5‘ to 3‘)	Function
GCTGCGCAACTGTTGGCAGACCTATTAGAAGGTGGAGCCGCCATTTTTT TTTCGGGCATTTA-**AF647**	AF647 pointer

ATCAAACTTAAATTTCTGGAAGTTTTTAAATGCC	AF647 protrusion
GGGCCTCTTCGCTATTACGTTGTACCTCACCGTTTTTAAATGCC	AF647 protrusion
GGCACCAAAACCAAAAGTAAGAGCAACACTATAGCAACGTAAATCGCC TTTTTTTTTCGGGCATTTA-**ATTO647N**	ATTO647N pointer
AAACGGGGTTTTGCTACATAACGCCAAAAAAGGCTTTTTTTTTAAATGC	ATTO647N protrusion
TGCCATTCAACAATAGAAAATTCATATGGTTTTTTTTTAAATGC	ATTO647N protrusion
TGCCCTGACGAGAAACATTTAATTTTACAGGTAGAAAG	Exchange staple
TAATAAGAAGAGCCACCCTTATTAGCGTT	Exchange staple
CATTATACCAGTGATTTGGCATCAGGACGTTGTAACATAAACCAGACG	Exchange staple
TTACCCATAACCCTCGAAATACAATGTTTAAACAGGG	Exchange staple
GACAGATGGACCTTCATCAAGAGTAATCTTG	Exchange staple
GGCCATATCAAAATTATTTGGAAACAGCCATTCGAAAATCGC	Exchange staple
GCCTCCGGGTACATCGACATAAAA	Exchange staple
CGGGAGACGCAGAAACAGCGG	Exchange staple
CCAGCTTACGGCTGGAAACGTGCCCGTCTCGTCGCTGGCA	Exchange staple

Supplementary Table 6. Core staples from the 5‘ to the 3’ end for the rectangular DNA origami structure used as a static platform for placing AF647 and ATTO647N in different distances to each other.

Staple ID	Sequence (5‘ to 3‘)
NRO-1-1	CATAAATCTTTGAATACCAAGTGTTAGAAC
NRO-1-2	GATGTGCTTCAGGAAGATCGCACAATGTGA
NRO-1-3	GCAATTCACATATTCCTGATTATCAAAGTGTA
NRO-1-4	GATTTAGTCAATAAAGCCTCAGAGAACCCTCA
NRO-1-5	TCACCAGTACAAACTACAACGCCTAGTACCAG
NRO-1-6	CCAATAGCTCATCGTAGGAATCATGGCATCAA
NRO-1-7	GCTTTCCGATTACGCCAGCTGGCGGCTGTTTC
NRO-1-8	AAAGGCCGGAGACAGCTAGCTGATAAATTAATTTTTGT
NRO-1-9	AAATTAAGTTGACCATTAGATACTTTTGCG
NRO-1-10	AAGCCTGGTACGAGCCGGAAGCATAGATGATG
NRO-1-11	TCATTCAGATGCGATTTTAAGAACAGGCATAG
NRO-1-12	GCCATCAAGCTCATTTTTTAACCACAAATCCA
NRO-1-13	TATAACTAACAAAGAACGCGAGAACGCCAA
NRO-1-14	TTGCTCCTTTCAAATATCGCGTTTGAGGGGGT

NRO-1-15	GTATAGCAAACAGTTAATGCCCAATCCTCA
NRO-1-16	AAAGTCACAAAATAAACAGCCAGCGTTTTA
NRO-1-17	GGCCTTGAAGAGCCACCACCCTCAGAAACCAT
NRO-1-18	TTAACGTCTAACATAAAAACAGGTAACGGA
NRO-1-19	AGTATAAAGTTCAGCTAATGCAGATGTCTTTC
NRO-1-20	TCAAATATAACCTCCGGCTTAGGTAACAATTT
NRO-1-21	TTTCGGAAGTGCCGTCGAGAGGGTGAGTTTCG
NRO-1-22	GAGGGTAGGATTCAAAAGGGTGAGACATCCAA
NRO-1-23	TATTAAGAAGCGGGGTTTTGCTCGTAGCAT
NRO-1-24	GCCCTTCAGAGTCCACTATTAAAGGGTGCCGT
NRO-1-25	ATGCAGATACATAACGGGAATCGTCATAAATAAAGCAAAG
NRO-1-26	AGCCAGCAATTGAGGAAGGTTATCATCATTTT
NRO-1-27	TAAATGAATTTTCTGTATGGGATTAATTTCTT
NRO-1-28	AAACAGCTTTTTGCGGGATCGTCAACACTAAA
NRO-1-29	CGGATTCTGACGACAGTATCGGCCGCAAGGCGATTAAGTT
NRO-1-30	GCGCAGACAAGAGGCAAAAGAATCCCTCAG
NRO-1-31	AGAGAGAAAAAAATGAAAATAGCAAGCAAACT
NRO-1-32	GACAAAAGGTAAAGTAATCGCCATATTTAACAAAACTTTT
NRO-1-33	ACACTCATCCATGTTACTTAGCCGAAAGCTGC
NRO-1-34	CTACCATAGTTTGAGTAACATTTAAAATAT
NRO-1-35	TATATTTTGTCATTGCCTGAGAGTGGAAGATTGTATAAGC
NRO-1-36	CGGATTGCAGAGCTTAATTGCTGAAACGAGTA
NRO-1-37	TAAATCATATAACCTGTTTAGCTAACCTTTAA
NRO-1-38	GTACCGCAATTCTAAGAACGCGAGTATTATTT
NRO-1-39	TCTTCGCTGCACCGCTTCTGGTGCGGCCTTCC
NRO-1-40	GCAAGGCCTCACCAGTAGCACCATGGGCTTGA
NRO-1-41	ATTACCTTTGAATAAGGCTTGCCCAAATCCGC
NRO-1-42	CTTATCATTCCCGACTTGCGGGAGCCTAATTT
NRO-1-43	TTATACCACCAAATCAACGTAACGAACGAG
NRO-1-44	GTAATAAGTTAGGCAGAGGCATTTATGATATT
NRO-1-45	CAACCGTTTCAAATCACCATCAATTCGAGCCA
NRO-1-46	GATGGTTTGAACGAGTAGTAAATTTACCATTA
NRO-1-47	GCACAGACAATATTTTTGAATGGGGTCAGTA
NRO-1-48	AGCAAGCGTAGGGTTGAGTGTTGTAGGGAGCC
NRO-1-49	TCCACAGACAGCCCTCATAGTTAGCGTAACGA
NRO-1-50	ATTATACTAAGAAACCACCAGAAGTCAACAGT
NRO-1-51	TAAGAGCAAATGTTTAGACTGGATAGGAAGCC
NRO-1-52	ATACATACCGAGGAAACGCAATAAGAAGCGCATTAGACGG
NRO-1-53	CAACTGTTGCGCCATTCGCCATTCAAACATCA
NRO-1-54	GATGGCTTATCAAAAAGATTAAGAGCGTCC
NRO-1-55	TAGGTAAACTATTTTTGAGAGATCAAACGTTA
NRO-1-56	AGGCAAAGGGAAGGGCGATCGGCAATTCCA
NRO-1-57	ATTATCATTCAATATAATCCTGACAATTAC
NRO-1-58	GAAATTATTGCCTTTAGCGTCAGACCGGAACC
NRO-1-59	AATGGTCAACAGGCAAGGCAAAGAGTAATGTG
NRO-1-60	ATACCCAACAGTATGTTAGCAAATTAGAGC

NRO-1-61	ATAAGGGAACCGGATATTCATTACGTCAGGACGTTGGGAA
NRO-1-62	CACCAGAAAGGTTGAGGCAGGTCATGAAAG
NRO-1-63	ATCCCAATGAGAATTAACTGAACAGTTACCAG
NRO-1-64	CATGTAATAGAATATAAAGTACCAAGCCGT
NRO-1-65	CCAACAGGAGCGAACCAGACCGGAGCCTTTAC
NRO-1-66	GCTATCAGAAATGCAATGCCTGAATTAGCA
NRO-1-67	GACCTGCTCTTTGACCCCCAGCGAGGGAGTTA
NRO-1-68	AGGAACCCATGTACCGTAACACTTGATATAA
NRO-1-69	CAGCGAAACTTGCTTTCGAGGTGTTGCTAA
NRO-1-70	ACAACTTTCAACAGTTTCAGCGGATGTATCGG
NRO-1-71	CAGCAAAAGGAAACGTCACCAATGAGCCGC
NRO-1-72	ACCTTTTTATTTTAGTTAATTTCATAGGGCTT
NRO-1-73	CGATAGCATTGAGCCATTTGGGAACGTAGAAA
NRO-1-74	GCCCGAGAGTCCACGCTGGTTTGCAGCTAACT
NRO-1-75	ATTTTAAAATCAAAATTATTTGCACGGATTCG
NRO-1-76	ACCTTGCTTGGTCAGTTGGCAAAGAGCGGA
NRO-1-77	CTGAGCAAAAATTAATTACATTTTGGGTTA
NRO-1-78	CCTGATTGCAATATATGTGAGTGATCAATAGT
NRO-1-79	TCAATATCGAACCTCAAATATCAATTCCGAAA
NRO-1-80	CTTTAGGGCCTGCAACAGTGCCAATACGTG
NRO-1-81	AATAGTAAACACTATCATAACCCTCATTGTGA
NRO-1-82	TCACCGACGCACCGTAATCAGTAGCAGAACCG
NRO-1-83	GCCCGTATCCGGAATAGGTGTATCAGCCCAAT
NRO-1-84	TGTAGCCATTAAAATTCGCATTAAATGCCGGA
NRO-1-85	TCGGCAAATCCTGTTTGATGGTGGACCCTCAA
NRO-1-86	TGACAACTCGCTGAGGCTTGCATTATACCA
NRO-1-87	CCACCCTCTATTCACAAACAAATACCTGCCTA
NRO-1-88	CCCGATTTAGAGCTTGACGGGGAAAAAGAATA
NRO-1-89	AAGTAAGCAGACACCACGGAATAATATTGACG
NRO-1-90	CACATTAAAATTGTTATCCGCTCATGCGGGCC
NRO-1-91	TTAAAGCCAGAGCCGCCACCCTCGACAGAA
NRO-1-92	ATATTCGGAACCATCGCCCACGCAGAGAAGGA
NRO-1-93	TTCTACTACGCGAGCTGAAAAGGTTACCGCGC
NRO-1-94	AACGTGGCGAGAAAGGAAGGGAAACCAGTAA
NRO-1-95	GAATTTATTTAATGGTTTGAAATATTCTTACC
NRO-1-96	AGCGCGATGATAAATTGTGTCGTGACGAGA
NRO-2-1	AACGCAAAGATAGCCGAACAAACCCTGAAC
NRO-2-2	GCCTCCCTCAGAATGGAAAGCGCAGTAACAGT
NRO-2-3	AAAGCACTAAATCGGAACCCTAATCCAGTT
NRO-2-4	GCCAGTTAGAGGGTAATTGAGCGCTTTAAGAA
NRO-2-5	AAGGCCGCTGATACCGATAGTTGCGACGTTAG
NRO-2-6	TTTTATTTAAGCAAATCAGATATTTTTTGT
NRO-2-7	CTTTTGCAGATAAAAACCAAAATAAAGACTCC
NRO-2-8	CCTAAATCAAAATCATAGGTCTAAACAGTA
NRO-2-9	AGACGACAAAGAAGTTTTGCCATAATTCGAGCTTCAA
NRO-2-10	AGAAAACAAAGAAGATGATGAAACAGGCTGCG

NRO-2-11	CGCGCAGATTACCTTTTTTAATGGGAGAGACT
NRO-2-12	CACAACAGGTGCCTAATGAGTGCCCAGCAG
NRO-2-13	GCGGAACATCTGAATAATGGAAGGTACAAAAT
NRO-2-14	TAAAAGGGACATTCTGGCCAACAAAGCATC
NRO-2-15	AATTGAGAATTCTGTCCAGACGACTAAACCAA
NRO-2-16	GCGAAAAATCCCTTATAAATCAAGCCGGCG
NRO-2-17	AACACCAAATTTCAACTTTAATCGTTTACC
NRO-2-18	TAAATCAAAATAATTCGCGTCTCGGAAACC
NRO-2-19	GAAACGATAGAAGGCTTATCCGGTCTCATCGAGAACAAGC
NRO-2-20	GCGAACCTCCAAGAACGGGTATGACAATAA
NRO-2-21	TTAGGATTGGCTGAGACTCCTCAATAACCGAT
NRO-2-22	ATCGCAAGTATGTAAATGCTGATGATAGGAAC
NRO-2-23	GCGGATAACCTATTATTCTGAAACAGACGATT
NRO-2-24	AAGGAAACATAAAGGTGGCAACATTATCACCG
NRO-2-25	ACCCTTCTGACCTGAAAGCGTAAGACGCTGAG
NRO-2-26	ATATTTTGGCTTTCATCAACATTATCCAGCCA
NRO-2-27	TCAAGTTTCATTAAAGGTGAATATAAAAGA
NRO-2-28	TCTAAAGTTTTGTCGTCTTTCCAGCCGACAA
NRO-2-29	TTCCAGTCGTAATCATGGTCATAAAAGGGG
NRO-2-30	AATACTGCCCAAAAGGAATTACGTGGCTCA
NRO-2-31	TTTATCAGGACAGCATCGGAACGACACCAACCTAAAACGA
NRO-2-32	TTGACAGGCCACCACCAGAGCCGCGATTTGTA
NRO-2-33	CTGTGTGATTGCGTTGCGCTCACTAGAGTTGC
NRO-2-34	GCGAGTAAAAATATTTAAATTGTTACAAAG
NRO-2-35	TAGAGAGTTATTTTCATTTGGGGATAGTAGTAGCATTA
NRO-2-36	CGAAAGACTTTGATAAGAGGTCATATTTCGCA
NRO-2-37	TCATCGCCAACAAAGTACAACGGACGCCAGCA
NRO-2-38	TTAACACCAGCACTAACAACTAATCGTTATTA
NRO-2-39	TTATTACGAAGAACTGGCATGATTGCGAGAGG
NRO-2-40	ACAACATGCCAACGCTCAACAGTCTTCTGA
NRO-2-41	CATTTGAAGGCGAATTATTCATTTTTGTTTGG
NRO-2-42	TGAAAGGAGCAAATGAAAAATCTAGAGATAGA
NRO-2-43	TGGAACAACCGCCTGGCCCTGAGGCCCGCT
NRO-2-44	TACCGAGCTCGAATTCGGGAAACCTGTCGTGCAGCTGATT
NRO-2-45	GTTTATTTTGTCACAATCTTACCGAAGCCCTTTAATATCA
NRO-2-46	ACAAACGGAAAAGCCCCAAAAACACTGGAGCA
NRO-2-47	GTTTATCAATATGCGTTATACAAACCGACCGTGTGATAAA
NRO-2-48	ACGGCTACAAAAGGAGCCTTTAATGTGAGAAT
NRO-2-49	GACCAACTAATGCCACTACGAAGGGGGTAGCA
NRO-2-50	CTCCAACGCAGTGAGACGGGCAACCAGCTGCA
NRO-2-51	ACCGATTGTCGGCATTTTCGGTCATAATCA
NRO-2-52	CAGAAGATTAGATAATACATTTGTCGACAA
NRO-2-53	TGCATCTTTCCCAGTCACGACGGCCTGCAG
NRO-2-54	TTAGTATCACAATAGATAAGTCCACGAGCA
NRO-2-55	GTTTTAACTTAGTACCGCCACCCAGAGCCA
NRO-2-56	TTAATGAACTAGAGGATCCCCGGGGGGTAACG

NRO-2-57	CTTTTACAAAATCGTCGCTATTAGCGATAG
NRO-2-58	ATCCCCCTATACCACATTCAACTAGAAAAATC
NRO-2-59	AGAAAGGAACAACTAAAGGAATTCAAAAAAA
NRO-2-60	AGCCACCACTGTAGCGCGTTTTCAAGGGAGGGAAGGTAAA
NRO-2-61	AACAAGAGGGATAAAAATTTTTAGCATAAAGC
NRO-2-62	GCCGTCAAAAAACAGAGGTGAGGCCTATTAGT
NRO-2-63	TGTAGAAATCAAGATTAGTTGCTCTTACCA
NRO-2-64	GAGAGATAGAGCGTCTTTCCAGAGGTTTTGAA
NRO-2-65	CCACCCTCATTTTCAGGGATAGCAACCGTACT
NRO-2-66	CTTTAATGCGCGAACTGATAGCCCCACCAG
NRO-2-67	CCAGGGTTGCCAGTTTGAGGGGACCCGTGGGA
NRO-2-68	CAAATCAAGTTTTTTGGGGTCGAAACGTGGA
NRO-2-69	ACGCTAACACCCACAAGAATTGAAAATAGC
NRO-2-70	TACGTTAAAGTAATCTTGACAAGAACCGAACT
NRO-2-71	TAATCAGCGGATTGACCGTAATCGTAACCG
NRO-2-72	TTTTCACTCAAAGGGCGAAAAACCATCACC
NRO-2-73	GCCTTAAACCAATCAATAATCGGCACGCGCCT
NRO-2-74	AATAGCTATCAATAGAAAATTCAACATTCA
NRO-2-75	CATCAAGTAAAACGAACTAACGAGTTGAGA
NRO-2-76	CAGGAGGTGGGGTCAGTGCCTTGAGTCTCTGAATTTACCG
NRO-2-77	AAATCACCTTCCAGTAAGCGTCAGTAATAA
NRO-2-78	CTCGTATTAGAAATTGCGTAGATACAGTAC
NRO-2-79	TTTACCCCAACATGTTTTAAATTTCCATAT
NRO-2-80	GTCGACTTCGGCCAACGCGCGGGGTTTTTC
NRO-2-81	CGTAAAACAGAAATAAAAATCCTTTGCCCGAAAGATTAGA
NRO-2-82	AGGCTCCAGAGGCTTTGAGGACACGGGTAA
NRO-2-83	GAGAAGAGATAACCTTGCTTCTGTTCGGGAGAAACAATAA
NRO-2-84	TTTAGGACAAATGCTTTAAACAATCAGGTC
NRO-2-85	AATACGTTTGAAAGAGGACAGACTGACCTT
NRO-2-86	CTTAGATTTAAGGCGTTAAATAAAGCCTGT
NRO-2-87	TAAATCGGGATTCCCAATTCTGCGATATAATG
NRO-2-88	AACAGTTTTGTACCAAAAACATTTTATTTC
NRO-2-89	CTGTAGCTTGACTATTATAGTCAGTTCATTGA
NRO-2-90	AACGCAAAATCGATGAACGGTACCGGTTGA

Supplementary Table 7. Staples from the 5‘ to the 3’ end for introducing AF647 and ATTO647N statically placed at different distances to each other on the rectangular DNA origami. The distances labelled 4, 5, 7, 9, 10, 11 and 14 correspond to inter-fluorophore distances of 4.4 nm, 5.4 nm, 7.4 nm, 9.2 nm, 10.2 nm, 11.2 nm and 14.6 nm, respectively.

Sequence (5‘ to 3‘)	Function
TTAAAGCCAGAGCCGCCACCCTCGACAGAAT-**AF647**	AF647 for distances 4, 5, 7

AF647-TCCTTTAGCGTCAGACCGGAACC	AF647 for distances 9, 10, 11, 14
TCAGAAACCATCGATAGCAGCACCGTAATC-**ATTO647N**	ATTO647N for distance 4
TCAGAAACCATCGATAGCAGCACCGTA-**ATTO647N**	ATTO647N for distances 5, 9
CAGCAAAAGGAAACGTCACCAATGAAACCATCGATAGCAGC-**ATTO647N**	ATTO647N for distance 7,11
TCAGAAACCATCGATAGCAGCACC-**ATTO647N**	ATTO647N for distance 10
GGCCTTGAAGAGCCACCACCCTCAGAAACCAT-**ATTO647N**	ATTO647N for distance 14
GTGCCGTCGAGAGGGTGAGTTTCG	Exchange staple for distances 4,5,7, 9, 10,11
AACAAATACCTGCCTATTTCGGAA	Exchange staple for distances 4,5,7, 9, 10,11
AAGGAAACATAAAGGTGGCAACATTATCA	Exchange staple for distances 4,5,7, 9, 10,11
GAAATTATTCATTAAAGGTGAATATAAAAGA	Exchange staple for distances 9, 10, 11, 14
CCTCGACAGAATCAAGTTTG	Exchange staple for distances 9, 10, 11, 14
TTAAAGCCAGAGCCGCCAC	Exchange staple for distances 9, 10, 11, 14
AGTAGCAGAACCGCCACCCTCTATTCACA	Exchange staple for distances 4, 7, 11
CCGTCACCGACTTGAGCCATTTGGGAACGTAGAAA	Exchange staple for distances 4, 5, 9, 10
GGCCTTGAAGAGCCACCACCC	Exchange staple for distances 4, 5, 9, 10
ATCAGTAGCAGAACCGCCACCCTCTATTCACA	Exchange staple for distances 5, 9
GTAATCAGTAGCAGAACCGCCACCCTCTATTCACA	Exchange staple for distance 10
ACCGTAATCCCGTCACCGACTTGAGCCATTTGGGAACGTAGAAA	Exchange staple for distances 7, 11
GGCCTTGAAGAGCCACCACCCTCAGAGCCGC	Exchange staple for distances 7, 11

biotin-CGGATTCTGACGACAGTATCGGCCGCAAGGCGATTAAGTT	immobilization
biotin-ATAAGGGAACCGGATATTCATTACGTCAGGACGTTGGGAA	immobilization
biotin-GAGAAGAGATAACCTTGCTTCTGTTCGGGAGAAACAATAA	immobilization
biotin-TAGAGAGTTATTTTCATTTGGGGATAGTAGTAGCATTA	immobilization
biotin-AGCCACCACTGTAGCGCGTTTTCAAGGGAGGGAAGGTAAA	immobilization
biotin-GAAACGATAGAAGGCTTATCCGGTCTCATCGAGAACAAGC	immobilization

References

(1) Masullo, L. A.; Steiner, F.; Zähringer, J.; Lopez, L. F.; Bohlen, J.; Richter, L.; Cole, F.; Tinnefeld, P.; Stefani, F. D. Pulsed Interleaved MINFLUX. *Nano letters* **2021**, *21* (1), 840–846. DOI: 10.1021/acs.nanolett.0c04600. Published Online: Dec. 18, 2020.

(2) Gordon, M. P.; Ha, T.; Selvin, P. R. Single-molecule high-resolution imaging with photobleaching. *Proceedings of the National Academy of Sciences of the United States of America* **2004**, *101* (17), 6462–6465. DOI: 10.1073/pnas.0401638101. Published Online: Apr. 19, 2004.

(3) Qu, X.; Wu, D.; Mets, L.; Scherer, N. F. Nanometer-localized multiple single-molecule fluorescence microscopy. *Proceedings of the National Academy of Sciences of the United States of America* **2004**, *101* (31), 11298–11303. DOI: 10.1073/pnas.0402155101. Published Online: Jul. 26, 2004.

(4) Ram, S.; Ward, E. S.; Ober, R. J. Beyond Rayleigh's criterion: a resolution measure with application to single-molecule microscopy. *Proceedings of the National Academy of Sciences of the United States of America* **2006**, *103* (12), 4457–4462. DOI: 10.1073/pnas.0508047103. Published Online: Mar. 1, 2006.

(5) Voter, A. F. INTRODUCTION TO THE KINETIC MONTE CARLO METHOD. In *Radiation Effects in Solids*; Springer, Dordrecht, 2007; pp 1–23. DOI: 10.1007/978-1-4020-5295-8_1.

Peer-Reviewed Publications

* authors contributed equally

1. Michael Scheckenbach*, Julian Bauer*, **Jonas Zähringer***, Florian Selbach, and Philip Tinnefeld
DNA origami nanorulers and emerging reference structures, *APL Materials* 8, 110902 (2020). https://doi.org/10.1063/5.0022885
2. Luciano Masullo*, Florian Steiner*, **Jonas Zähringer**, Lucía Lopez, Johann Bohlen, Lars Richter, Fiona Cole, Philip Tinnefeld and Fernando D. Stefani
Pulsed Interleaved MINFLUX, *Nano Letters* 2021 Vol. 21 Issue 1 Pages 840-84., https://doi.org/10.1021/acs.nanolett.0c04600
3. Kateryna Trofymchuk*, Viktorija Glembockyte*, Lennart Grabenhorst, Florian Steiner, Carolin Vietz, Cindy Close, Martina Pfeiffer, Lars Richter, Max Schütte, Florian Selbach, Renukka Yaadav, **Jonas Zähringer**, Qingshan Wei, Aydogan Ozcan, Birka Lalkens, Guillermo P. Acuna, and Philip Tinnefeld
Addressable nanoantennas with cleared hotspots for single-molecule detection on a portable smartphone microscope, *Nat Commun* **12**, 950 (2021). https://doi.org/10.1038/s41467-021-21238-9 ;
4. Izabella Kamińska*, Johann Bohlen*, Renukka Yaadav, Patrick Schüler, Mario Raab, Tim Schröder, **Jonas Zähringer**, Karolina Zielonka, Stefan Krause, Philip Tinnefeld
Graphene Energy Transfer for Single-Molecule Biophysics, Biosensing, and Super-Resolution Microscopy. *Adv. Mater.* 2021, 33, 2101099. https://doi.org/10.1002/adma.202101099
5. **Jonas Zähringer**, Fiona Cole, Johann Bohlen, Florian Steiner, Izabela Kamińska, Philip Tinnefeld
"Combining pMINFLUX, Graphene Energy Transfer and DNA-PAINT for Nanometer Precise 3D Super-Resolution Microscopy", *Light: Science and Applications*, 70 (2023). https://doi.org/10.1038/s41377-023-01111-8
6. Fiona Cole*, **Jonas Zähringer***, Johann Bohlen, Tim Schröder, Florian Steiner, Fernando Stefan and Philip Tinnefeld
Super-Resolved FRET and Co-Tracking in pMINFLUX, *bioRxiv* 2023.03.24.534096. https://doi.org/10.1101/2023.03.24.534096, in revisions
7. **Jonas Zähringer**, Michael Scheckenbach and Philip Tinnefeld
The Art of Molecular Programming – Optical Control, book chapter accepted.

Patent Applications

8. Philip Tinnefeld, **Jonas Zähringer**, Johann Bohlen, Fiona Cole
Binding Hierarchies for accelerated superresolution, European patent application AF4294 EP S5

Manuscripts in preparation

9. Jonas Binder, Joshua Winkeljann, Katharina Steinegger, Lara Trnovec, Daria Orekhova, **Jonas Zähringer**, Andreas Hörner, Valentin Fell, Philip Tinnefeld, Benjamin Winkeljann, Wolfgang Frieß, and Olivia Merkel
Closing the bridge between experiment and simulation – a holistic study on complexation of small interfering RNAs with polyethyleneimine

Conferences and Presentations

09/2019 Poster presentation at CeNS/CRC235 Workshop 'Evolving Nanosciences': "MINFLUX with pulsed interleaved excitation", Venice, Italy.

09/2021 Oral Presentation at PicoQuant's 26th Single Molecule Workshop: "Exploiting Fluorescence Lifetime in Pulsed Interleaved MINFLUX", Berlin, Germany.

11/2021 Poster presentation at e-conversion Graduate Retreat: "pMINFLUX – Imaging Energy Transfers on the Nanometer Scale", Ettal, Germany.

12/2021 Oral Presentation at the CENS seminar Science Rocks: "pMINFLUX - Donut worry, be superresolved!", Munich, Germany.

04/2022 Oral presentation at the Focus on Microscopy Conference: "Exploiting Fluorescence Lifetime in Pulsed Interleaved MINFLUX", online.

08/2022 Poster presentation at the 11th Single Molecule Localization Microscopy Symposium: "Exploiting Fluorescence Lifetime in Pulsed Interleaved MINFLUX", Paris, France.

09/2022 Poster presentation at the CeNS-MCQST Workshop 'Bridging the gap': "Exploiting Fluorescence Lifetime in Pulsed Interleaved MINFLUX", Venice, Italy.

09/2022 Oral Presentation at 17th Conference on Methods and Applications in Fluorescence: "Exploiting Fluorescence Lifetime in Pulsed Interleaved MINFLUX", Gothenburg, Sweden.

Acknowledgements

There are many people who supported me over the years of my PhD, and I would like to thank everyone who made this work possible.

First of all, I would like to thank Philip for giving me an interesting project and providing such an outstanding work environment. While you always gave me freedom to develop my own research ideas, you also refocused me to generate high impact science. Your broad knowledge and insightful discussions were always very insightful. Also, you gave me opportunity to present my scientific work at conferences and get new ideas there.

Don, who provided invaluable knowledge and insights about the world of fluorescence. And this despite being not a fan of MINFLUX. Especially the MAF conference with you was fun!

Achim Hartschuh, Ralf Jungmann, Jan Vogelsang and Olivia Merkel for joining my thesis committee.

The people who proofread parts of this manuscript, Tim, Tatjana, Flo and Fiona. I am very grateful that you took time to read this manuscript.

Flo for starting the MINFLUX project, organizing almost everything, kept most of the bureaucracy away from me and always had an ear when I had a problem at the MINFLUX setup. You always pushed me towards new ideas beside the traditional biological application!

Johann, who gave such an amazing first impression that I knew that I should join Philip's group. Beside amazing socializing, your scientific input was maybe even greater. Only the reviews/book chapter and the NP paper are without any clock measurement. I hope you're not (too) mad I did not include a certain person in my committee.

Tim for all the socialization and your knowledge about everything. You know probably everything someone has ever done in this group. Together with Johann, Mario and Ija it was like all the knowledge was already in the room, so why bother reading books or paper? I hope you don't hate me for going over to the green (biological) side.

Fiona, who made working at the MINFLUX fun despite endless hours in the dark. I am grateful to have been working with you, let's hope we can make the kinesin story work. Beside working I had a lot of fun together with you, Martina, Luna and Xaverl. Thanks for keeping my head straight.

I also have to thank the "informal discussion group": Tim, Johann, Mario, Lars, Kristina, Stefan, Kateryna, Frank, Patrick and Evelyn for way too much beer events.

Michi who always was fun to discuss anything with him. Thank you also for the smooth projects with you and Julian. Julian for many scientific discussions, despite sometimes being at not so opportune times ;). I think we had quite a fun time in Paris with lots of Champagne.

Evelyn for giving always insightful advice. It was fun working with you, especially in PC1, which was an interesting experience to give a lecture.

Stefan who made the corona time very memorable if one remembers. I still regret that we didn't make the highest impact experiment work using the moon as an excitation source for nanoantenna...

Carsten for always being available for some question, dyes or beer.

Frank "Gauss" for being my counterpart at lambs, tracking molecules with gaussian beams instead of donuts still hurts! Also, Adrian for sharing pain and stories about a similar complicated setup.

Luciano for showing me together with Flo how to align donuts.

Alan for leading such a competent SR subgroup and Patrick for such a competent Mensa group.

I am grateful to all my office mates who created a supportive, joyful working atmosphere which I really enjoyed: Tim, Johann, Ija, Mario, Ece, Julian, Lars, Karina, Alan and Bosong.

Iza who provided many graphene samples thus I did not have to fish.

Angelika who so competently kept the lab running. I am grateful that you also were always around to grab a coffee and just chat.

Ben for a project which has nothing to do with MINFLUX.

The students I had the privilege to supervise, especially Fiona Daria and Chris, or whatever his real name is ;).

I am grateful to Moritz Ehrl, Silke Steger and Hilde for their help regarding all formal stuff and providing tips to track through the German bureaucracy.

For all the others I did not yet mention who providing sweets, cake and generating a nice working environment: Lorena, Giovanni, Andres, Merve, Sarah, Lorena, Melanie, Gereon, Flosel, Lennart, Cindy, Ece, Renukka

The mechanic workshop for all their fast and competent work, especially with the optical tables and also the electronic workshop. Also the infrastructure guys for a at least during non-construction times a stable air conditioning.

Thanks to the whole working group for the social events like hiking, drinking, eating and swimming, you rock!

My quidditch team, with which I made many great memories and supported my sanity during my PhD. It was an amazing journey from a small team predicted to come second to last, to winning multiple tournaments and playing competitive European quidditch.

My friends from studies in Freiburg and school with whom I could always reconnect as if no time passed.

My family who was always supportive of my studies and gave me the opportunity to do as I wanted.

Thanks to Tatjana all the motivation, cheerfulness and all the trips we made. Thanks for all the great time we had together. Hopefully we will have many more trips and years together.